2011

Droplet motion on miniaturized ratchets

Jeong Tae Ok
Louisiana State University and Agricultural and Mechanical College

DROPLET MOTION ON MINIATURIZED RATCHETS

A Dissertation

Submitted to the Graduate Faculty of the
Louisiana State University and
Agricultural and Mechanical College
in partial fulfillment of the
requirements for the degree of
Doctor of Philosophy

in

The Interdepartmental Program in
Engineering Science

by

Jeong Tae Ok
B.S., Sunmoon University, Korea, 1995.
M.S., Sunmoon University, Korea, 1998.
M.S., Louisiana State University, United States, 2007

May 2011

Acknowledgements

I would like to acknowledge the support and guidance provided by my major professor, Dr. Sunggook Park during the course of this study. I would like to thank the members of my graduate committee, Dr. Jin-Woo Choi, Dr. Harris Wong, Dr. Dimitris E. Nikitopoulos, and Dr. Michael C. Murphy for their support and guidance, and Dr. Sukhamay Kundu, for acting as the Dean's representative.

This work would not have been possible without the extensive help and guidance provided by Dr. Steve Soper, Dr. Daniel S. Park, Dr. Byoung Hee You, Dr. In-Hyouk Song, Dr. Namwon Kim and Dr. Taehyun Park.

Thanks to all members in Nanosystems Lab, especially to those who collaborated with me, Eugene Lopez-Oña, Benoit Laveau, Bahador Farshchian, Lance Brumfield, Steven Maxwell Hurst, Junseo Choi, Alborz Amirsadeghi and Jiahao Wu.

I wish to acknowledge the constant help, guidance, and love provided by my wife Bokyung Park in pursuing my Ph.D. degree.

Table of Contents

List of Tables

List of Figures

Abstract

The main objective of this study is to evaluate the feasibility of using miniaturized asymmetric structures to move liquid droplets and understand the driving mechanism. We developed the fabrication process for large area topological ratchets with the period ranging from millimeter down to sub-micrometer using micromachining techniques. Non-wetting superhydrophobic surfaces were successfully fabricated using soft UV or thermal nanoimprint lithography, reactive ion etching by oxygen plasma, and chemical surface modification by fluorinated silane vapor deposition. An accurate and reproducible experimental setup equipped with high speed camera and automatic injection system was established. Image processing tools allowed us to obtain various critical information related droplet motion and behavior along the ratchets surface. Various influences on the motion such as the surface temperature, ratchets dimension, surface wettability, droplet volume, kind of liquid, initial impact speed of droplet, polymer additive, and surface slope were systematically investigated for miniaturized non-wetting asymmetric ratchets. It is observed that the droplet motion on the ratchets is strongly dependent on the ratchets dimensions as well as the surface temperature. Extremely fast water droplet motion was achieved from the sub-micrometer ratchets near the Leidenfrost temperature. Even though the Leidenfrost-miniaturized ratchets system can be considered as an efficient pumping and cooling component, further intensive study to reduce the operating temperature and drive the liquid motion within microchannel is required for the broad range of applications.

Chapter 1 Introduction

1.1 General Background

Recently, there have been significant evolutions in micropumping techniques of liquid to have a proper answer for the question, "How can liquid be more efficiently moved in microfluidic systems?" Motion of matter needs to satisfy two conditions: application of asymmetric potential and fluctuation to overcome the pinning of liquid to the surface. Fluids are conventionally driven by applying macroscopic net asymmetric potentials large enough to overcome the pinning of the liquid to the surface. Examples are a pressure gradient by a pump or compressor and an electric field between two electrodes. Net asymmetric potentials produced by an imbalance of surface tension forces (Marangoni effect) via a chemical (Gallardo, Gupta et al. 1999; Garnier, Grigoriev et al. 2003), thermal (Jun and Kim 1998; Geng, Yuan et al. 2001; Song and Zhao 2001; Darhuber, Valentino et al. 2003; Tseng, Tseng et al. 2004; Yokoyama, Takeda et al. 2004), or electrical gradient (Matsumoto and Colgate 1990; Lee and Kim 1998; Lee, Moon et al. 2002; Ren, Fair et al. 2004) also have been used. However, these methods either require an external power source or have a limitation in the displacement due to a finite length of the gradient that can be produced. On the other hand, spatially periodic systems with localized asymmetric structures (topological ratchets) can induce directed transport of liquid/particles in the absence of net force and thus have recently received much attention as means of rectifying motion for many applications.

Ratchets have been used for quantum tunneling ratchets (Linke, Humphrey et al. 1999; Linke, Humphrey et al. 2002), dielectrophoretic rectification of Brownian motion (Hughes 2004) and action of molecular motors (Julicher, Ajdari et al. 1997; Kulic, Thaokar et al. 2005). Topological ratchet structures were also used as a rectifier that forces the otherwise random mechanical

motion of droplets into a specific direction by means of localized asymmetric potential (Gorre, Ioannidis et al. 1996; Sandre, Gorre-Talini et al. 1999; Ajdari 2000; Bico and Quere 2000; Daniel and Chaudhury 2002; Marquet, Buguin et al. 2002; Stroock, Ismagilov et al. 2003; Linke, Aleman et al. 2006; Ding, Song et al. 2007; Shastry, Taylor et al. 2007; Duncombe, Kumemura et al. 2009). To initiate motion, topological ratchet structures that rectify the direction of motion need to be combined with a fluctuation to overcome the pinning of the droplet to the surface. Such a fluctuation of droplet height occurs when millimeter scale saw-tooth surface profiles machined into brass were heated to the Leidenfrost regime (the film-boiling regime), as demonstrated by Linke et al. (Linke, Aleman et al. 2006) As liquid evaporates at the bottom surface of the droplet due to heating of the ratchet surface, the pressure that levitates the droplet pushes out the vapor laterally and the ratchet surface partially rectifies this vapor flow, exerting a net viscous force on the droplet. With the millimeter scale ratchets, the droplet velocity of a few cm/s was achieved. Despite the demonstration of using ratchets to drive motion of droplets, however, there have been no efforts to extend this driving mechanism to micro and nanometer scale ratchets, which is one of the core objectives for this dissertation work.

The fluctuating force provided by the vapor layer underneath liquid droplets in the Leidenfrost regime has a critical limitation in that the liquid droplets can be driven at a high temperature. Even though simple chemical surface modification can partially help to reduce the operation temperature, an alternative method to provide a fluctuation force is required to use the local asymmetric potential provided by surface ratchets for driving liquids at room temperature. A superhydrophobic surface is considered as non-wetting, which has near 180° static water contact angle as well as contact angle hysteresis close to 0°. Recently, there have been many efforts to understand water repellency in various superhydrophobic surfaces, not only upon

uniformly textured surfaces (Wang, Lopez et al. 2007; Jung and Bhushan 2008; Deng, Varanasi et al. 2009) but also upon surfaces with engineered non-uniformities (Malouin, Koratkar et al. 2010). In fact, millimetric water droplet has a unidirectional rebound on the non-uniformly textured surface with local roughness gradients by Si micropillars due to the significant local surface tension gradient. Similar behavior of liquid droplets is highly possible upon the superhydrophobic miniaturized ratchets due to the local irregular asymmetry. The directed rebounding by superhydrophobic ratchets has many potential applications such as self-cleaning, surface driven flows, wear on turbine blades, and heat transfer (Keller and Miksis 1983; Blossey 2003; Malouin, Koratkar et al. 2010). Therefore, in depth understanding of the impact and motion behavior of droplets upon superhydrophobic miniaturized ratchets is imperative.

1.2 Goal and Objectives of This Study

The goal of this study is to elucidate the potential of using miniaturized ratchets in driving liquids. The technical objectives to achieve the goal include:

1. Establish fabrication process to produce large area miniaturized ratchets with various types of material, period, aspect ratio, ridge shape, and wettability by combining micro- and nanomachining techniques.
2. Study impact and motion of liquid droplets deposited on various types of non-wetting ratchet surfaces under various conditions such as surface temperature, ratchet period and aspect ratio, ridge shape, surface tilting, kind of liquid, liquid volume, impact speed of liquid droplet, and surface wettability.
3. Reveal the mechanism behind the unidirectional droplet motion on the non-wetting ratchet surfaces.

This work consists of eight chapters. In Chapter 2, a literature review regarding the background information on the work including various pumping methods, Leidenfrost phenomenon, and superhydrophobic surface will be presented. Detailed fabrication process for various miniaturized ratchets, metrology methods for structural analysis, and experimental setups and specific procedures for characterization of droplet impact and motion will be described in Chapter 3. The driving mechanism of liquid droplets along the miniaturized ratchets of millimeter down to sub-micrometer period on elevated temperatures near or above the Leidenfrost temperature will be systematically examined using primitive experimental apparatus in Chapter 4. Chapter 5 will show the experimental results obtained using the enhanced experimental system equipped with a high speed camera for closer observation of the droplet impact and motion. The influence of droplet impact velocity and a polymer additive on the motion will also be investigated. In Chapter 6, further detailed study about the characteristics of the Leidenfrost droplets on various miniaturized ratchets will follow, as investigated with the enhanced set up. The experimental parameters include the ratchet dimension (period and depth), shape of ratchet ridge, tilted ratchet surface, surface temperature and wettability. Chapter 7 will mainly discuss rebounding behavior of millimetric water droplet on such various superhydrophobic surfaces as natural elephant ear leaf, UV-resin biomimetic micropyramid array, PMMA miniaturized asymmetric ratchets, and symmetric microratchets with local wetting gradient at room temperature. Finally, a summary of this study and future works will be given in Chapter 8.

Chapter 2 Literature Survey

2.1 Introduction

This study concerns the motion of liquid droplets on two different non-wetting miniaturized ratchets. The first non-wetting situation was achieved by heating metallic ratchets near or above the Leidenfrost temperature of the liquid used. The other non-wetting situation was obtained at room temperature by integrating superhydrophobic structures into miniaturized ratchets. In order to understand and analyze the unique behavior of directional motion of the millimetric droplet on these surface, diverse fields of knowledge are required such as fundamental mechanisms of liquid pumping, ratchet effect, the Leidenfrost phenomenon, various factors influencing the Leidenfrost droplet, superhydrophobic (water repellent) surface. This chapter summarizes the literature survey on these topics.

2.2 Pumping of Liquid

2.2.1 Conventional Methods to Mump Liquid in Microfluidics

Conventional methods of pumping fluids in microfluidics can be divided into two categories: pressure-driven and electrically-driven pumps. The pressure-driven pumps exerts oscillatory or rotational pressure forces on the working fluid through a moving solid-fluid (for vibrating diaphragm, peristaltic, rotary pumps), or fluid-fluid boundary (for ferrofluid, phase change, gas permeation pumps). All of these pumping methods use the motion of a solid or fluid to generate the pressure gradient over the length of microchannels, which are needed to move a fluid. The pressure-driven flow has characteristics of a smooth parabolic velocity profile caused by the no-slip condition at the channel wall. This parabolic velocity profile leads to hydrodynamic dispersion, which is undesirable in separation applications (Pennathur 2008). The pressure-

driven pumping methods can be further categorized into four different types based on the mechanisms applying pressure: diaphragm displacement, fluid displacement, rotary, and peristaltic micropumps.

Electrically-driven pumps convert electrical energy directly into fluid motion. They use both static and dynamic electric field for pumping. Different electrically-driven pumping schemes have been developed based on the actual implementation and the type of fluid. These pumping schemes provide a direct energy transfer to pumping power and generate constant and steady flows due to the continuous addition of energy such as electrohydrodynamic (EHD) and electrokinetic (EK) forces. These pumping techniques rely on creating an attractive force for some of the ions in the liquid, and the remaining liquid is dragged along to form a bulk flow. These kinds of dynamic pumps are valveless, therefore the pumping direction depends on the direction of the applied force.

Considering the scaling properties of these pumping methods, it is apparent that electrically-driven pumping methods are more appropriate for miniaturized applications. When the channel diameter is reduced the pressure-driven flow rate decreases as the cross-sectional area squared, whereas the electrically-driven flow rate decreases proportional to the cross-sectional area, for fixed volume and pressure drop, respectively (Hardt 2007). Typical pressure-driven pumps have employed a pressure gradient between the inlet and outlet of fluid as a driving force with the flow rate in the range from 10 μL/min to several mL/min. For electrically-driven pumps, the electrical energy is introduced for more accurate fluid control (flow rate less than 10 μL/min). Besides the scaling behavior, there are several advantages of electrically-driven pumps such as virtually plug-flow profiles in straight channels and pulse-free flows. However, there are also several disadvantages such as high voltages, Joule heating and undesirable electrochemical

reaction at the electrodes. They can only pump specific fluids (Pamme 2006). Therefore, many practical microfluidic systems employ seemingly unfavorable pressure-driven pumps induced by mechanical means, such as a syringe, peristaltic and diaphragm pump, and pressurized chamber.

Despite the wide use in microfluidic systems, pressure- and electrically-driven pumps have critical drawbacks. It requires an external device component, which usually comprises most of volume and mass of microfluidic systems and thus limits their applications such as military and space applications where light weight is a critical requirement. As a result, a potential gradient is created over the entire fluidic path of a microfluidic device, e.g. between two electrodes for electrical potential and between inlet and outlet for pressure gradient. In order to overcome such a drawback, methods to drive liquid droplets without an external device such as imbalance in surface tension forces (Marangoni effect) via a chemical, thermal, or electrical gradient, have been developed.

2.2.2 Pumping Driven by Surface Tension

According to the scaling law, forces that are functions of the surface area decrease more slowly than forces that depend on the volume. Thus, surface tension effects are dominant over inertial effects in micro or nanoscales. Surface tension gradient can be used as a driving force at these miniaturized scales. Surface tension driven pumping is based on capillary effects. A droplet on a solid substrate with high surface energy (hydrophilic) has a small water contact angle, forming a ‘wet’ surface. It has a puddle shape, or spreads on the entire surface. When a droplet is put on a solid substrate with low surface energy (hydrophobic), it has a large water contact angle and becomes a ball-like spherical shape except for the bottom area which is flat. The contact angle of the droplet on the solid surface depends on interfacial energies between the solid and liquid, the solid and gas, and the liquid and gas via Young’s equation (Luo, Fu et al. 2009):

$$\cos\theta = \frac{\gamma_{SG}-\gamma_{SL}}{\gamma_{LG}} \quad (2.1)$$

where, Υ_{SG}, Υ_{SL}, Υ_{LG} are surface tensions between solid and gas, solid and liquid, liquid and gas, respectively. If there is a gradient of surface energy along the interface between solid and liquid, bulk liquid or droplet spreads to the direction of more hydrophilic area. Various surface tension driven pumps have been developed based on this capillary effect.

Liquids can be dislocated passively either by the capillary effect (Tseng, Lin et al. 2004) or by transpiration concept (Namasivayam, Larson et al. 2003). Passive capillary umps are the simplest devices for liquid filling in microfluidic systems. A liquid needs to be in contact with another liquid, gas, or solid to function. Their efficiency is mainly determined by three factors; 1) surface tensions, 2) geometry of the interface between different phases, and 3) geometry of the solid phase at the border line between the three phases (liquid, gas and solid) (Wereley 2006). F. G. Tsenget et al. successfully implemented the capillary pumping method to microchannels in PDMS and SU-8 to transport blood and enzyme solution for glucose detection (Tseng, Lin et al. 2004). When the microchannel is completely filled with the liquid, it is inclined to stop flowing. In nature, however, water can be continuously supplied from roots to leaves due to transpiration effect. Vaporized water through pores on the leaf surface is refilled by a new feeding. V. Namasivayam developed transpiration micropumps, in which liquid flow can be controlled by the evaporation rate through the pores (Namasivayam, Larson et al. 2003).

Liquid pumping is also possible through active control of surface tension. There are various effects to control surface tension actively. Thermocapillary effect utilizes the temperature dependence of surface tension (Takagi, Maeda et al. 1994; Ozaki 1995; Jun and Kim 1998; Geng, Yuan et al. 2001; Song and Zhao 2001; Darhuber, Valentino et al. 2003; Tseng, Tseng et al. 2004; Yokoyama, Takeda et al. 2004). For most liquids the surface energy increases as the temperature

increases. Typical thermocapillary pumps consist of an array of microchannels and microheaters (Luo, Fu et al. 2009). The microheater raises the temperature locally and thus generates a temperature gradient. As a result, a surface tension gradient is formed. Therefore, the droplet flows from the high temperature zone (low surface energy) to low one (high surface energy). Electrocapillary or electrowetting controls the surface energy by electrostatic forces (Matsumoto and Colgate 1990; Lee and Kim 1998; Lee, Moon et al. 2002; Ren, Fair et al. 2004). Electrochemical (Gallardo, Gupta et al. 1999) or photochemical capillary effects (Garnier, Grigoriev et al. 2003) use the dependence of surface tension on the concentration of surfactants which is controlled by electrochemical or photochemical reactions. Compared to the thermocapillary flows, electrocapillary flows are much more energy efficient, with a much faster speed of operation. Speeds more than 10 cm⁄s were achieved with electrowetting micropumps, in contrast to a typical speed of only about 1 mm⁄s with thermocapillary micropumps (Li 2008).

In relation to this study, the asymmetry of the substrate geometry by topological ratchets makes macroscopic water contact angles at both rapidly and slowly inclined sides of a droplet different, where rapidly inclined sides generally have higher contact angles. Therefore, the effect of the surface tension gradient may play a role in the droplet motion and needs to be considered when the droplet is in direct contact with the ratchet surface.

2.2.3 Other Pumping Methods

There are other methods for liquid flow that have recently been given attention. Acoustically-driven pumps use high frequency surface acoustic waves (SAW) on the surface of a microchip (Yeo and Friend 2009). They have several advantages comparing with other actuation mechanism. The acoustic wave can be used for both continuous flow and discrete droplets. It can be also employed for both micropumps (Zhu and Kim 1998; Nguyen and White 1999) and active

micromixers (Nguyen, Meng et al. 2000; Acikalin, Raman et al. 2003). Moreover, SAW devices can be used as sensors to detect biological substances through a biological recognition system (Lange, Blaess et al. 2006). Magnetically-driven pumps employ the Lorentz force to move ions in liquids and to generate flow through a dragging force. This mechanism produces relatively larger force and is suitable for pumping a large volume of liquid (Luo, Fu et al. 2009). Bubble-driven pumps induce liquid flow with bubbles, which are produced with high frequency acoustic waves, lasers and pressure difference. Although this mechanism is not appropriate for real applications due to the difficulty in generating reproducible bubbles, it can be used as a system to understand the behavior of two phase flow (Pennathur 2008). Gravity can also be used to pump liquid in microchannels (Zhu, Chu et al. 2004; Chen, Lee et al. 2008). Recently, horizontal reservoir replaced vertical reservoir to obtain a constant flow rate of liquid (Zhu, Chu et al. 2004). In this system, the internal diameter of the fluid reservoir is critical to maintain the liquid within the reservoir as well as to prevent the fluid from filling the reservoir (Zhu, Chu et al. 2004). Biological organisms such as kinesin protein motors and bacterial carpets have also been demonstrated to create liquid flow (Pennathur 2008).

2.2.4 Pumping Driven by Ratchet Surfaces

Ratchets, which are spatially or timely periodic asymmetric potential or structures, have received much attention as a means of rectifying motion in the absence of net force. This ‘net force-free’ large-scale motion produced by ratchets is actually due to local asymmetric forces that are averaged to be zero over space and time. Ratchets have been used for a number of applications including quantum tunneling ratchets (Linke, Humphrey et al. 1999; Linke, Humphrey et al. 2002), dielectrophoretic rectification of Brownian motion (Hughes 2004), molecular action (Julicher, Ajdari et al. 1997; Kulic, Thaokar et al. 2005) and cellular motors

(Mahmud, Campbell et al. 2009). Some ratchet mechanisms use geometric asymmetry (Gorre, Ioannidis et al. 1996; Sandre, Gorre-Talini et al. 1999; Ajdari 2000; Bico and Quere 2000; Brown, Smith et al. 2001; Daniel and Chaudhury 2002; Marquet, Buguin et al. 2002; Stroock, Ismagilov et al. 2003; Linke, Aleman et al. 2006; A. Shastry, D. Taylor et al. 2007; Z. Ding, Song et al. 2007; T. A. Duncombe, M. Kumemura et al. 2009). Others rely on local asymmetry in applied force, provided that the average force is zero (Ajdari 2002). Non-equilibrium in a ratchet can be due to a thermal (Stroock, Ismagilov et al. 2003; Linke, Aleman et al. 2006), capillary (Prakash, Quere et al. 2008), wettability gradient (Bico and Quere 2000; Daniel, Sircar et al. 2004), asymmetry of surface waves (Eddi, Terwagne et al. 2008) and it can also be due to a periodic alteration of the system over time, such as switching on and off a local force (Brown, Smith et al. 2001; Buguin, Talini et al. 2002).

Brownian ratchets normally transport particles or molecules within a continuous carrier fluid (solvent) without dislocating the fluid itself. For example, colloidal particles entrained in solution move when an electric potential with periodic ratcheted profile is applied to the solution successively (Rousselet, Salome et al. 1994). Similarly, mesoscopic particles were selectively filtered through a micro-fabricated macroporous silicon membrane with etched one-dimensional asymmetrical bottleneck-like pores under the application of an oscillating pressure gradient (Kettner, Reimann et al. 2000; Muller, Birner et al. 2000; Matthias and Muller 2003). Brownian ratchets also represent the principle mechanism of molecular motors that are responsible for the active transport of molecules along filaments in biological cells (Julicher, Ajdari et al. 1997; Reimann and Hanggi 2002). There have been several ways to keep the Brownian ratchet system out of equilibrium for colloidal transportation and fractionation, such as a chemical reaction (Julicher, Ajdari et al. 1997), an oscillating pressure (Matthias and Muller 2003) or an electric

potential (Rousselet, Salome et al. 1994) that is periodically switched on and off. Theoretical approaches are very well developed for Brownian ratchets related to particle transport (Reimann and Hanggi 2002). Detailed studies have been reported for various types of ratchets e. g. entropic ratchets (Slater, Guo et al. 1997; van Oudenaarden and Boxer 1999; Tessier and Slater 2002), drift ratchets (Kettner, Reimann et al. 2000), inertia ratchets (Jung, Kissner et al. 1996; Lindner, Schimansky-Geier et al. 1999; Chen, Wang et al. 2005), ratchets with non-coherent switching (SchimanskyGeier, Kschischo et al. 1997).

Most devices using ratchets have been employed to transport or fractionate tiny colloidal particles or molecules as a kind of sieves. Recently, several novel studies have proved that ratchets also have a considerable potential for transportation of bulk fluid. The ferrofluids are colloidal suspensions of ferromagnetic nanoparticles. A. Engel et al. reported that the Brownian motion of magnetic particles in ferrofluids, drives carrier liquid via viscous coupling when an magnetic field oscillates the device (Engel, Muller et al. 2003). This driving mechanism is very similar to the Brownian ratchets for colloids transportation.

A net, global flow in the liquid is also caused by viscous coupling itself without the motion of colloidal particles. Thermally driven Marangoni–Bénard convection over a solid substrate with asymmetric grooves induces a net secondary flow in the plane of the layer of convective liquid, besides primary recirculating flow. The key parameters of the mean flow direction and velocity are the thickness of the liquid layer and the temperature gradient across the layer (Stroock, Ismagilov et al. 2003).

There have also been different approaches to use ratchet geometries for liquid droplet transportation. Droplets placed on a micro-ratcheted surface (A. Shastry, D. Taylor et al. 2007; T. A. Duncombe, M. Kumemura et al. 2009) or in a ratcheted microchannel move when the droplet

shape or wetting properties are periodically alternated by various methods, such as mechanical substrate vibration (Buguin, Talini et al. 2002; A. Shastry, D. Taylor et al. 2007; Z. Ding, Song et al. 2007), on/off electric field across the channel (Buguin, Talini et al. 2002), low-frequency electric field of zero mean value along the channel (Buguin, Talini et al. 2002) and electrowetting on dielectric (EWOD) (T. A. Duncombe, M. Kumemura et al. 2009).

Recently, G. Mahmud et al. demonstrated that random motile cells also could be rectified by micropatterned ratchets. The interactions between the live cells and asymmetric micro geometries (micro-ratchets) guide the cells polarization and drive their directional migration (Mahmud, Campbell et al. 2009).

Another important study has been reported by Linke et al., where a liquid droplet is placed on a hot geometric ratchets surface in the film boiling (Leidenfrost) regime and thus the liquid is fully levitated from the surface (Linke, Aleman et al. 2006). The periodic macroscale ratchet geometry (period: 1.5 mm, depth: 0.3 mm) induces a unidirectional motion of the levitating droplet. This self-propelled motion is observed for various liquids in a wide temperature range in their film boiling regime. They concluded that the driving mechanism of the droplet is a viscous force generated by asymmetric vapor flow between the ratcheted solid and liquid droplet. Based on their observation, a vapor flow model for the ratchets system was developed by solving Navier-Stokes equation under lubrication approximation, neglecting incompressibility of the fluid and inertia. According to the vapor flow model, the driving force of the motion of a Leidenfrost droplet on macro ratchets is given by:

$$F = \left(-\frac{h}{2}\frac{\partial P}{\partial x} - \mu\frac{v_{droplet}}{h}\right) A_{eff} \cos\theta_{ratchet} \tag{2.2}$$

where h is the thickness of the vapor layer parallel with the droplet bottom surface and slowly inclined part of ratchets, ($\frac{\partial P}{\partial x}$) pressure gradient of vapor, μ viscosity of the vapor, $v_{droplet}$ droplet

velocity in the direction of lateral motion (x direction), A_{eff} area of the droplet bottom surface interacting with ratchets, and $\theta_{ratchet}$ ratchet angle as shown in figure 2.1.

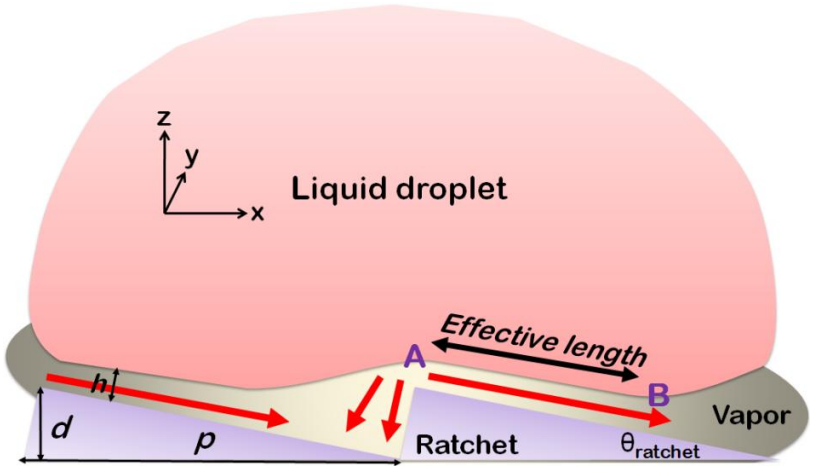

Figure 2.1 Schematic diagram of moving droplet on macro ratchets by asymmetric vapor flow in Leidenfrost regime.

In the figure, red arrows represent the direction of vapor flow, black arrow an amount of liquid surface (l) that is approximately parallel to the ratchet slope. The symbols of d and p represent depth and period ratchets, respectively. It is plausible that the driving force is mainly due to frictional force between the bottom surface of droplet and parallel vapor layer. The first term of equation (2.2) represents a driving "ratchet force" caused by a pressure gradient (Poiseuille flow) while the second term represents a dissipative "drag force" caused by viscous drag (Couette flow) (Taormina 2006). An important factor on the driving force is the area of droplet bottom surface which interacts with ratchets, A_{eff}. It was obtained by tailoring vapor flow model on flat surface into that of ratchets surface. Based on the geometry of ratchets system in figure 2.1, A_{eff} could be defined as:

$$A_{eff} \equiv \frac{l}{\sqrt{p^2+d^2}} A_{flat} \tag{2.3}$$

where, A_{flat} is the surface area of a droplet interacting with a flat surface. l can be experimentally measured by high speed camera with the magnification of the bottom area of the droplet. p and d are known according to ratchet dimensions. For 1.5 mm period ratchets, A_{eff}/A_{flat} was determined to be ~ 0.6 for water (Linke, Aleman et al. 2006).

2.3 Levitating Droplet on Hot Solid Surface

2.3.1 Leidenfrost Phenomenon

When a liquid droplet is placed on a hot solid surface at temperatures much higher than the boiling point of the liquid, a continuous vapor layer is formed around the bottom surface of droplet. The vapor layer acts as an insulating layer to hinder direct heat transfer between the droplet and solid surface. As a result, the droplet does not boil but slowly evaporates, levitating over its own vapor layer. Such behavior was first reported by J. G. Leidenfrost using a hot iron spoon in 1756 and hence it is well known as Leidenfrost phenomenon (Leidenfrost 1966). The Leidenfrost temperature (T_L) is defined as the minimum liquid/solid interface temperature required to provide Leidenfrost (film boiling) regime on a surface or the temperature where the lifetime of the droplet is longest (Gottfrie, Lee et al. 1966).

A levitating droplet can be considered as nonwetting because there is no direct contact between the droplet and the substrate surface. The droplet experiences competing forces due to gravity and surface tension. Gravity tends to flatten them out, but surface tension prefers a spherical shape to minimize the surface area. For example, if the droplet radius is smaller than the capillary length ($a = \sqrt{\gamma/\rho g}$, where γ, ρ, and g are the liquid surface tension, density and gravity, respectively) of a liquid, the droplet is nearly spherical from the lateral view except for the droplet bottom where it is flattened by the contact with the substrate surface. Droplets larger than the capillary length form a disk-like (pancake or puddle) shape, flattened by gravity (Biance,

Clanet et al. 2003).

A better understanding of the interactions between the droplet and hot surface well above the film-boiling regime not only enables development of an improved modeling for two-phase flows, but it will also help improve performances of diverse industrial processes such as combustion processes upon fuel injection, quenching, spray cooling of nuclear reactor cores, inkjet printing, heat sink and etc (Rein 1993; Fan, Lau et al. 2001; Ge and Fan 2006). For examples, improper deposition of fuels in engines causes inhomogeneous and incomplete combustion of the fuel, which reduces the performance of the engine and increases the pollutant emissions. In steel industry, the vapor layer from liquid deteriorates the cooling rate of glowing metals. For inkjet technology, liquid droplet should be controlled not to be disintegrated (Karl and Frohn 2000). Leidenfrost reactors cooled by liquid nitrogen were used for low temperature polymerization (Zsuga, Kennedy et al. 1988). An advanced nano-patterning technique was developed using moving droplet of water containing metal nanoparticles on a silicon surface above the Leidenfrost temperature (Elbahri, Paretkar et al. 2007).

2.3.2 Heat Transfer Mechanism

There have been many efforts to describe the heat transfer mechanism of Leidenfrost droplets. The heat transfer coefficient in the film boiling regime is considerably smaller than other boiling regimes such as nucleate and transition boiling because low conductivity of the vapor layer with the thickness in the range of 10 – 100 μm induces a large resistance to heat flow. Three different heat transfer mechanisms involved in the Leidenfrost droplet include contact, bulk air convection, and radiative heat transfer, as discussed by several groups (Liu and Yao 1982; Deb and Yao 1989; Delcorio and Choi 1991). According to their experimental results, the dominant mechanism is the heat transfer by contact. S. Deb and S. C. Yao found that the radiative heat transfer had

almost negligible contribution up to the surface temperature of ~ 1000 ℃, except for the case with high surface emissivity (Deb and Yao 1989).

Baumeister et al. developed a model to calculate the evaporation rate of a Leidenfrost droplet with a flat bottom by simultaneously solving the momentum, energy and continuity equations for 2-D radial symmetry (Baumeister, Hamill et al. 1966). Gottfried et al. (Gottfrie, Lee et al. 1966) and Wachters et al. (Wachters.Lh, Bonne et al. 1966) separately developed models for a Stokes-type plate-parallel flow by balancing simple forms of mass, momentum and energy without considering radiative transfer. Most of other models developed are based on above three models in order to solve specific problems. Basically, a vapor film is generated at the bottom surface of a droplet via evaporation and flows downward due to the gravity. They only consider the heat from the hot surface that is diffused across the vapor film. For smaller droplets ($R < a$, where R is radius of droplet), the heat brought to the liquid per unit time is proportional to the surface area $\pi\frac{R^4}{a^2}$, the thermal conductivity of the vapor κ, and the temperature gradient over the vapor layer thickness $\Delta T/h$ (where h is the thickness of the vapor layer). By introducing the latent heat of evaporation L, the evaporation rate is given by

$$\frac{dm}{dt} = \frac{\kappa}{L}\frac{\Delta T}{h}\pi\frac{R^4}{a^2} \tag{2.4}$$

Then, the gravity by droplet weight is considered, which generates a radial Poiseuille flow of vapor. Applying lubrication approximation due to very thin vapor layer), the flow rate scales as $\frac{h^3 2\gamma a}{\eta R^2}$, where η is viscosity of the vapor. Integrated over the contact length R^2/a, a mass per unit time is given (in absolute value)

$$\frac{dm}{dt} = \frac{4\pi\rho_v\gamma h^3}{3\eta R} \tag{2.5}$$

In a steady state condition, the mass flow rate of the vapor generated from the droplet and

flowing out due to the radial Poiseuille flow should be same. Thus, *h* is deduced using Eqs. (2.4) and (2.5):

$$h = \left(\frac{3\kappa\Delta T\eta}{4L\rho_v\gamma a^2}\right)^{1/4} R^{5/4}. \quad (2.6)$$

The thickness of vapor layer *h* for smaller droplets mainly varies as $R^{5/4}$ (Biance, Clanet et al. 2003). The vapor layer thickness for Leidenfrost droplets experimentally determined is in the range of 10 – 100 μm.

2.3.3 Factors Influencing Droplet on Hot Solid Surface

2.3.3.1 Effect of Surface Roughness

Surface roughness is usually quantified by the vertical deviations of a real surface from its ideal form. If these deviations are large, the surface is rough; if they are small, the surface is smooth. It has been known that T_L depends on surface roughness as well as the thermal properties of the solid (Temple-Pediani 1970).

Prat et al. found by a theoretical investigation that surface roughness significantly affects the vapor flow field beneath a levitating droplet on an impermeable hot solid surface (Prat, Schmitz et al. 1995). The flow field in the vapor region was determined by solving the Navier-Stokes equation around three different surface roughness elements: rectangular, semi-cylindrical, and triangular. The vapor flow penetrated into the roughness cavities in all cases. Sizable recirculation regions exist in the cavities only for rectangular roughness geometry. These recirculation regions gradually disappear as the roughness size decreases. The thickness of the vapor film above the roughness elements increases as the size of the droplet relative to the size of the roughness increases, in other words, as the number of surface roughness elements under a levitating droplet increases. This effect was more significant for the triangular roughness, which is similar to the ratchet structures used in this study. They also estimated through the simulation

that the thickness of the vapor layer increases as the height of the roughness elements decreases. Bernardin and Mudawar further developed a new mechanistic model for T_L by considering a cavity activation and bubble growth on it (Bernardin and Mudawar 2002). Even though this model is for smooth surface where the radii of surface cavities are in the range of 100 nm - 1 μm, it could be applied for rougher surfaces to predict T_L with good accuracy. Surface roughness and contamination would induce higher T_L by requiring a thicker vapor layer to avoid liquid-solid contact (Bernardin and Mudawar 1999).

Avedisian and Koplik investigated the effect of the surface porosity on a film boiling droplet (Avedisian and Koplik 1987). They investigated the evaporation of methanol on a polished stainless steel surface and ceramic (alumina) surfaces with three different porosities of 10%, 20%, and 40%. It was observed that T_L increases as the porosity increases. Even the droplet could not be levitated on the alumina surface with 40% porosity. It was attributed to the fact that the vapor film thickness on a porous surface is thinner than that on an impermeable surface due to adsorption and flow of the vapor within the ceramic material. Consequently, for porous surface the heat transfer rate through the vapor film into levitating droplet increases and evaporation rate also increases. These induce a higher surface temperature required for droplet levitation on a porous surface. A theoretical analysis was also carried out by allowing slip of the vapor flow on the porous surfaces. Chandra and Avedisian also demonstrated that porosity suppresses the Leidenfrost phenomenon with further work on the impact dynamics of n-heptanes droplet on porous surface (Chandra and Avedisian 1992). They introduced an important parameter which is the ratio of the contact diameter on the solid surface to the initial diameter of the spherical droplet for the same droplet volume. This ratio increases as the droplet spreads until reaching a maximum, and then starts decreasing with the progress of evaporation. For low temperature

below 100 ℃, the ratio from porous ceramic surfaces was higher than that from impermeable stainless steel. At higher temperatures, the droplets initially have smaller ratio for porous surface, however as time goes it becomes higher. The maximum ratio was estimated by means of an energy balance.

2.3.3.2 Surface Wettability

There have been several studies on the effect of surface wettability on Leidenfrost droplet. Young's equation in (2.1) needs to be corrected to apply on rough surface because the actual area of solid-liquid interface increases with the increase in roughness. Wenzel's equation is employed for contact angles on rough surface:

$$\cos\theta_r = r\cos\theta = \frac{r(\sigma_S - \sigma_{SL})}{\sigma_L} \tag{2.7}$$

where θ_r is the contact angles on a rough surface and r the roughness factor ($r > 1$). For hydrophilic surface where $\theta < 90°$, further rough surface decreases the contact angle, making the surface more hydrophilic while the surface becomes more hydrophobic with increasing surface roughness if $\theta > 90°$. Briefly, the surface roughness develops further the hydrophilicity or hydrophobicity.

Hidaka et al. investigated evaporation time of small water droplets (diameter $D < 3$ mm) and wetting limit temperatures (T_{WL}, the minimum evaporation time point) with large contact angle variation in the range of $0 - 170°$ using titania (TiO_2) surface (Hidaka, Yamashita et al. 2006). For contact angles below 90 °, as θ_r decreases T_{WL} increase dramatically because the solid-liquid contact area or heat transfer rate increases with smaller θ_r. For contact angles above 90 °, water droplet evaporates slowly at or even above T_{WL} due to either unstable vapor film formation or complete separation from solid. Especially for a contact angle of 170 °, neither T_{WL} nor T_L is recognized from the evaporation curve due to monotonous decrease in evaporation time with the

increase in T_s. Takata et al. also observed that T_L decreases with increase in θ (ΔT_L = 20K with $\Delta\theta$ = 60 °) (Takata, Hidaka et al. 2005).

2.3.3.3. Other Effects

Temple-Pediani experimentally studied on fuel droplets for a large range of external pressures (Temple-Pediani 1970). He reported that the delay time for the droplet to rebound after initial contact increases with pressure. At higher pressure, the levitating droplet deforms and spreads more because of its lower density and surface tension. However, the variation of the droplet spread is not significant, resulting in only 16% increase at 20 atm and 7% decrease at 0.01 atm (Issa 2003). As pressure decreases, the Leidenfrost effect occurs at relatively lower temperature due to the smaller gravity and buoyancy. Especially in the gravity free zone, there is an absence of normal nucleate boiling, hence a much lower T_L can be achieved (Agrawal and Menon 1994).

Even though most researches on droplet evaporation has been done with pure liquid, there also have been important studies in particle-liquid mixtures (Avedisian, Ioffredo et al. 1984), emulsions (Avedisian and Fatehi 1988), and binary liquids (Godleski and Bell 1966; Mann and Walker 1975). Avedisian et al. experimentally investigated Leidenfrost droplet evaporation of coal-water mixtures (coal volume fraction of 14% and 26%) on polished brass surface, which has temperatures ranging from 127 ℃ to 427 ℃ (Avedisian, Ioffredo et al. 1984). The evaporation time of coal-water mixed droplet was shorter than that of pure water droplet for a same volume. Heavier total weight of mixed droplet caused faster evaporation rate due to the enhanced heat transfer. They also included theoretical study to predict total evaporation time of the droplet. It was observed that the vapor layer collapsed in the final stage of evaporation. They suggested that the collapse might be generated due to the formation of a porous structure at the bottom area of

the droplet. As a result, the supplementation of the mass lost by evaporation slows down. Avedisian and Fatehi observed the film boiling evaporation of water-fuel emulsion drops (10%, 20%, 35%, and 50% water in heptanes and in the decane) (Avedisian and Fatehi 1988). The emulsions exhibited preferential evaporation of one of the components. For water-heptane emulsion the hydrocarbon is completely evaporated first, while for water-decane emulsion water is completely evaporated before decane evaporates.

Oscillation of a droplet exists due to the radial vapor flow underneath the droplet especially when the droplet size is large (Thimbleby 1989). As vapor escapes radially from under the droplet, drag causes the horizontal diameter of the droplet to increase. As one part of the droplet spreads out, another part of the droplet tends to shrinks in order to conserve the volume. However, for smaller spherical droplets constrained by surface tension, small interfacial area between droplet and hot flat surface generates much less oscillation. In this study, relatively small volume of droplets in the range of 3-12 μL have been used in order to avoid the large oscillation behavior during droplet motion on miniaturized ratchets. The droplets have been generated at lower needle height to minimize vertical variation of droplets.

2.3.4 Droplet Impact on Hot Surface

The literature review on droplet impact on hot surfaces is also required due to the nature of droplet injection method used in our experiments. Liquid droplets are released from a pipette or syringe pump away from the hot surface. Therefore, the kinetic energy that the droplet gains before the impact on the surface will influence initial behavior of the droplet motion. The problem of droplet impact on a hot surface above the film boiling regime has been actively investigated for applications such as fuel combustors, spray quenching, fire protection systems, etc (Chiu and Lin 2005). Many investigators examined the droplet to wall interaction, especially

in a thermal and dynamic view of the large contribution to heat transfer during the contact between droplet and hot solid surface.

Raising the impact velocity can enhance the net heat transfer in the non-wetting state (Pedersen 1970). The greatest heat transfer takes place upon impact when the droplet pushes against the solid during the rebounding process (Groendes and R. Mesler 1982). T_L increases when the impact speed to the surface wall increases due to the shorter time to form a vapor film around the droplet (Karl and Frohn 2000). Thus, a higher temperature (called as dynamic Leidenfrost temperature) is required to isolate liquid from the surface wall during an impact. Horizontally and vertically impinging sprays onto a hot surface were compared. Vertically impinging sprays to a horizontal surface leaded to a greater heat transfer rate than the horizontal spray on a vertical surface in the film boiling regime. It was observed that for the Weber number *We* < 350, as *We* increases the breakup of a droplet into secondary small droplets is greater. Here, *We* is the ratio of kinetic energy to surface energy of a droplet ($We = \frac{\rho D_0 {v_0}^2}{\gamma}$, where ρ, D_0, v_0 and γ is density, initial diameter, initial velocity and surface tension, respectively). However, no such relationship was found for *We* > 350 (Choi and Yao 1987). Droplet heating was also observed during an interaction above T_L due to the enhanced heat transfer between droplet and the wall, which is caused by high pressure of the vapor layer. The temperature change of droplet during an impact mainly depends on impact speed. However, the influence of droplet impact on wall temperature was almost negligible (Castanet, Liénart et al. 2008).

Generally, the dynamic behavior of droplet after an impact is mainly influenced by normal momentum of a falling droplet, not by the wall temperature (Yao and Cai 1988). When a droplet impacts on a hot wall, it deforms and spreads until reaching its maximum extension, then it retracts and elongates in the vertical direction due to the elasticity. It actively vibrates as it rises,

then reaches maximum height. The resident time, defined as the time from impact to departure from the hot wall, is almost independent of the impact speed, instead rapidly increases as droplet size increases, as $R^{3/2}$ (Biance, Chevy et al. 2006). This observation is very similar to the bouncing behavior of droplet on superhydrophobic water repellent surface (Richard, Clanet et al. 2002). The maximum radius is a function of *We* number ($R_{max} \sim We^{1/4}$) (Biance, Chevy et al. 2006). Large deformation corresponds to large *We* number. Another important parameter for the interaction of liquid droplet in Leidenfrost regime is the loss of momentum *L*. According to the empirical observations, the loss of momentum normal to the heated wall is quite considerable ($L = 0.263We^{0.257}$ for $0 \leq We \leq 25$) but tangential loss is almost negligible (Karl and Frohn 2000). This behavior is independent of viscosity of droplet liquid. In order to quantify the elasticity of impinging Leidenfrost droplet, restitution coefficient ($e=v_0'/v_0$) was deduced, which is defined as the ratio between the speeds of its center of mass after and before the impact. The impact speed v_0 is $\sqrt{2gH}$, where g is acceleration of gravity and *H* falling height of droplet. The take-off speed v_0' ($=gt/2$) is calculated from the flight time of droplet because it is subject only to gravity. At low *We* number (< 1), the shock is quasi-elastic ($e \sim 1$). For smaller droplets with 5 μL volume, more than 1000 consecutive rebounds were observed because they rose almost to the same height (Biance, Chevy et al. 2006). *e* values larger than 1 were also observed due to the oscillation of droplet. However, at large *We* number, the elasticity sharply drops ($e \sim We^{-1/2}$) due to the loss of energy associated with the shock in a liquid. This behavior occurred because of dissipation during the spreading at the impact and partition of the energy between droplet oscillation and translation at take-off.

A very small amount [of the order of 100 parts per million (ppm)] of flexible polymer additives (polyethylene oxide, PEO) to liquid significantly reduces both rebounding and

secondary atomization (SA) of droplet on heated surface, with negligible changes of the density, surface tension, and shear viscosity on the fluid (Bergeron, Bonn et al. 2000; Bergeron 2003; Bertola and Sefiane 2005). The liquid mixed with polymer additives becomes viscoelastic. When polymer molecules are at rest, they are coiled in a minimum energy conformation. They unfold under the hydrodynamic forces with larger resistance to deform (Degennes 1974). Therefore, this viscoelastic liquid mixed with PEO (200 ppm) significantly reduces the critical temperature for which SA completely disappears (more than 50℃ for *We*: ~ 28). As well, it avoids rebounding behavior of droplet. The incorporation of small amount of PEO into de-ionized water is expected to significantly influence the threshold temperature (T_{th}) for the motion of droplet as well as both vertical and horizontal mobility of droplet.

2.4 Superhydrophobic Surface

2.4.1 Hierarchical Structures and Surface Chemistry

It is well known that the naturally superhydrophobic surface such as butterfly wings, lotus leaf and bird feather, is covered by wax crystals; a mixture of large hydrocarbon molecules and it also has a very rough surface composed of a dual scale roughness (Barthlott and Neinhuis 1997; Bhushan, Jung et al. 2009). In fact, the combination of surface chemistry and surface topography effects is the cause of water repellency of those surfaces. There are two requirements for a superhydrophobic surface. It should have a very high contact angle (>150°) and very low contact angle hysteresis (Sun, Luo et al. 2005; Guo and Liu 2007; Roach, Shirtcliffe et al. 2008). In Wenzel's state water droplet wets the surface completely and therefore it cannot easily slide on the surface. In Cassie's state the droplet is in contact with solid only on top of asperities, thus reducing the frictional force applied on the droplet. As the result, the droplet can easily move on the surface at a low sliding angle. Therefore, only Cassie state can achieve both requirements for

a superhydrophobic surface.

Superhydrophobic or water repellent surface shows industrial applications such as contamination prevention, anti-oxidation, and pressure drop reduction (Cortese, D'Amone et al. 2008). Their self cleaning nature is desirable in photovoltaics, and their ability to produce a shear-free air-water interface along which liquids may flow drastically reduces the drag force in microfluidics (Rothstein 2010). These widespread applications have motivated recent efforts to improve superhydrophobic surface fabrication techniques. Bio-inspired superhydrophobic surfaces can be fabricated using different method such as solvent induced phase separation (Xie, Fan et al. 2004), electrochemical deposition (Wang, Feng et al. 2005), electrohydrodynamic (Jiang, Zhao et al. 2004), template synthesis (Lee, Park et al. 2007), growth of carbon nanotubes (Lau, Bico et al. 2003) and sol-gel processing (Xiu, Hess et al. 2008). A summary of techniques used for fabrication of superhydrophobic surfaces can be found in the reviews (Feng and Jiang 2006; Roach, Shirtcliffe et al. 2008; Xue, Jia et al. 2010).

In this study, soft UV-nanoimprint lithography (NIL) and thermal 3-D molding process that have been developed in our research group were used to generate microscale roughness on ratchet surfaces (Farshchian, Ok et al. 2009; Farshchian, Ok et al. 2010). Transparent negative PDMS replica was used as a mediate stamp. Reactive ion etching by oxygen plasma makes nanoscale surface roughness on microstructured polymers. The polymer surface is chemically modified by fluorinated silane vapor deposition.

2.4.2 Rebounding of Water Droplet on Superhydrophobic Surface

Water repellency of the solid surface can be evaluated by investigating the surface reaction to water droplet impact. When the capillary number, the ratio of viscosity and surface tension, is small enough ($\ll 1$), surface energy dominates viscous force and liquid droplet can rebound like

a spring depending on the degree of impact (Reyssat, Richard et al. 2010). However, on extremely high impact speed (≥ 2.8 m/s), splashing occurs. Generally, if liquid droplet rebounds off the surface at lower impact, it could be considered as the more water repellent surface. Complete rebounding is only observed when the contact angle values are the larger than 150 − 160 ℃(Quere 2005). The restitution coefficients (the ratio of the velocities after and before impact) as large as 0.91 were observed on excellent superhydrophobic surfaces (Richard and Quere 2000). Even in the small *We* regime (≤ 2.5) droplet impacting multiscale rough surfaces of carbon nanofiber jungles (CNFJ) (θ_s > 155±3 ℃) showed four different impact events, which include nonbouncing "Fakir" droplet, complete rebound, sticky wetting droplet, and partial rebound (Tsai, Pacheco et al. 2009). These events generally occurred in the order as *We* gradually increased. When a water droplet is very slowly released, it maintains "Fakir" state with air trapped underneath the bottom surface of water due to small kinetic energy. Therefore, higher contact angles between water and solid surface keep for the whole impacting procedures. A complete rebound can be induced by the nonwetting nature of the superhydrophobic surface, which limits droplet spreading. When the kinetic energy overcomes the surface energy, the wetting transition such as sticky wetting droplet and partial rebound occurs. For CNFJ surfaces, the wetting transition was observed even from *We* ~1. Bouncing pesticides for practical agricultural spray is one of critical issues. Small amount of polymer additive can prevent droplet from rebounding due to the higher elongational viscosity, which means good resistance of the liquid to large extensions (Bergeron, Bonn et al. 2000; Amarouchene, Cristobal et al. 2001). In this study, rebounding behavior of millimetric water droplet will be mainly investigated upon various superhydrophobic surfaces, which include natural leaf, biomimetic pyramid array (UV-resin), various dimensions of asymmetric microratchets (PMMA), and symmetric microratchets

with local wetting gradient for large range of *We*.

2.5 Conclusion

Numerous studies have been evolved to drive liquid motion more efficiently in micro and nanofluidic devices. Conventionally, pressure driven and electrically driven methods have been dominated. Both of those have critical benefits as well as limitations for specific dimensions and applications. Many creative ideas have been invented such as using surface tension gradient, high frequency surface acoustic waves, magnetic force, bubble, gravity, and biological organisms. Most recently, "force free or self-propelled" pumping concept, which employs periodically asymmetric potential (ratchets) and small friction flow on non-wetting surface (Leidenfrost effect), has been introduced as a strong candidate of a next generation of pumping mechanism. Ratchets were used for asymmetric potential while Leidenfrost effect was to overcome pinning droplet on the ratchets. Ratchets are spatially or timely periodic asymmetric potential or structures. They have been widely used to selectively transport and filter tiny colloidal particles or molecules without moving the fluid itself. They also have a considerable potential to transport bulk fluid because of their rectifying capability from the random motion. The Leidenfrost droplet, levitated by insulating vapor film from the hot surface, has various characteristics depending on such factors as surface temperature, roughness, permeability, wettability, its size, viscosity, falling height and etc. Polymer superhydrophobic ratchets are seriously considered to overcome the Leidenfrost limit. Based on the literature study, we are going to systematically study the motion of liquid droplet on both non-wetting miniaturized ratchets.

Chapter 3 Experimental Methods

3.1 Introduction

This chapter mainly contains the methodology, which are mainly divided into three aspects: fabrication methods, metrology (methods for structural analysis) and methods to characterize droplet motion on non-wetting miniaturized ratchets.

3.2 Fabrication of Miniaturized Ratchets

Various micromachining techniques such as micromilling, nanoimprint lithography (NIL), photolithography, electroplating are employed to produce large area ratchets with period ranging from millimeter down to sub-micrometer. Three different types of micro scale ratchets were fabricated and used to investigate the motion of droplet: (1) original brass ratchets milled by a micromilling machine, (2) replicated Ni ratchets, and (3) PMMA superhydrophobic ratchets. The replication of ratchets mainly consists of three different procedures: thermal NIL, electroplating and post-electroplating processes. For sub-micron ratchets, commercially available polymer-based optical gratings with ratchet structures were purchased and used as original masters. These were replicated into Ni via electroplating to be used for the study of droplet motion. A Ni microratchets with round ridge was implemented via 3-D molding process (Farshchian, Hurst et al. 2011). PMMA superhydrophobic ratchets were fabricated using thermal NIL, reactive oxygen plasma etching, and fluorinated silane vapor deposition process. The overall process flows for the designed experiments is shown in figure 3.1. One critical requirement for the fabrication of ratchets is that the ratcheted surface area has to be large enough to observe the development of rectified droplet motion after initial impact on the surface. The areas of the ratcheted surface fabricated were 5×10 cm^2, 5.2×5.2 cm^2, or 1×3 cm^2. Different ratchet aspect ratios, defined

as the ratio of depth-to-period, used in the experiments were 1:4, 1:5 and 1:10.

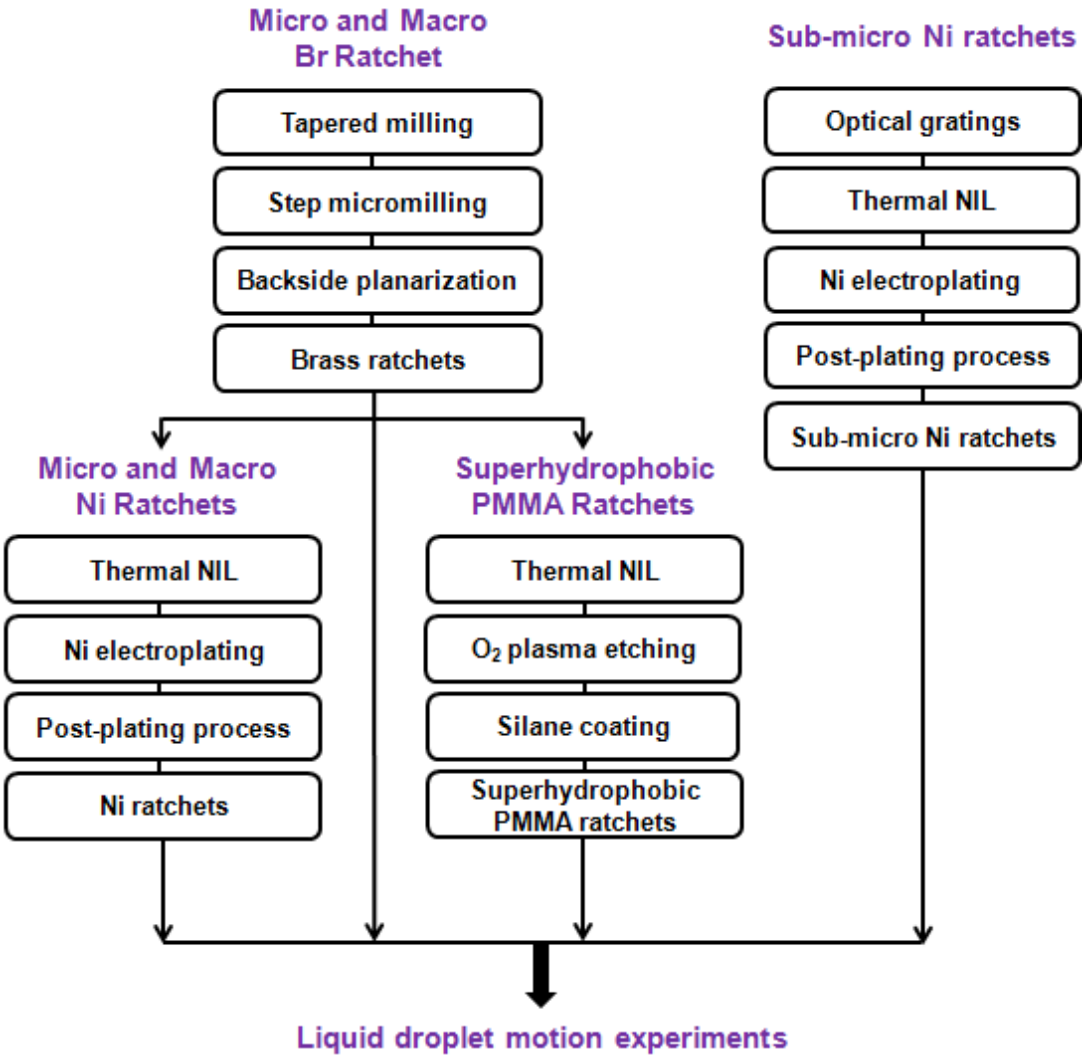

Figure 3.1 Fabrication flows of the miniaturized ratchets and their applications.

3.2.1 Original Brass Ratchets by Micromilling

The micromilling process is characterized by the use of milling tools of 100 μm or less in diameter. These tools can create miniature features in plastics and some soft metals, typically with a very low material removal rate. In this study, micromilling process was employed to fabricate asymmetric ratchet profiled surfaces on bulk brass, which have period in the range of a few micrometers to a few millimeters.

Figure 3.2 shows a schematic diagram for the fabrication of ratchets via micromilling, which consists of three steps: tapered milling, step micromilling and backside planarization. First, a brass (Br) bar (5 × 2 × 1 inch^3, Alloy 353, McMaster-Carr, Atlanta, GA) was milled with a tapered angle determined by the aspect ratio (depth-to-period) of the designed ratchets to fabricate using a CNC milling machine (CNC Hass VF-2YT, CA). The tapered angles were 11.3 ° and 5.7 ° for 1:5 and 1:10, respectively. This step is needed to reduce the process time for the subsequent micromilling process. The resolution of position and repetition by the CNC milling machine was in the range of 30 – 50 μm. A 1/2 inch solid carbide end mill was used as a tool. Spindle and milling speeds were 3000 rpm and 18 inches per minute, respectively.

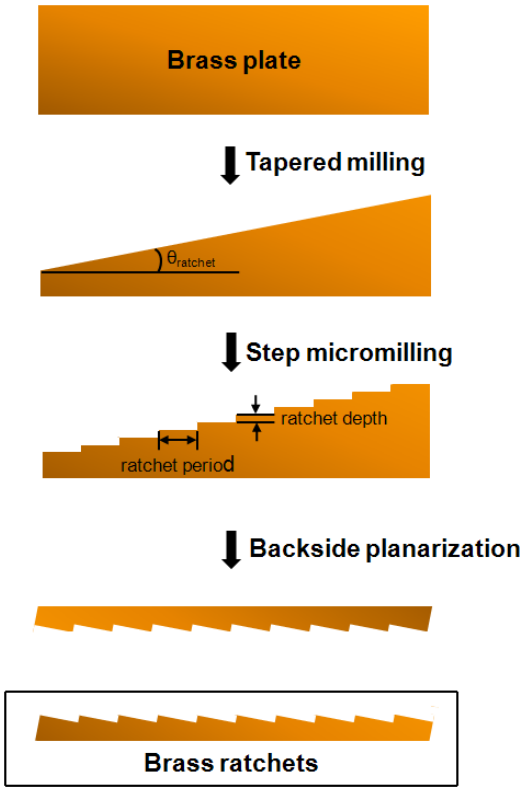

Figure 3.2 Fabrication methods of brass micro and macro ratchets.

The second step is to produce micro to millimeter scale steps in the CNC-milled, tapered brass bar using a micromilling machine (KERN MMP2522, KERN Micro- und Feinwerktechnik

GmbH & Co. KG, Germany). The photograph of the micromilling machine used is shown in figure 3.3 (a). The micro milling bit (radius 100 – 1500 μm) was carried on a spindle at a maximum rpm of 40,000 and the resolution of position and repetition was ±1 μm. The used spindle speed for micro milling was 3500 rpm. The micro milling speed was in the range of few tens to hundreds mm/min, which was carefully decided according to ratchets dimensions. The root mean square roughness for the surfaces produced by the micro-milling technique was typically ~ 300 nm (Kim, Murphy et al. 2008). As a last procedure, backside planarization was done with the conventional milling process while protecting micromilled step surface with a piece of thick (1/2 inch) silicone rubber sheet (NSF-certified silicone rubber sheet, Mcmaster-Carr, Atlanta, GA). Figure 3.3 (b) shows the photograph of Br micro ratchets with 768.1±3.0 μm period and 127.6±2.6 μm depth ($5 \times 2 \times 1/4$ inch^3) after completing whole milling procedures.

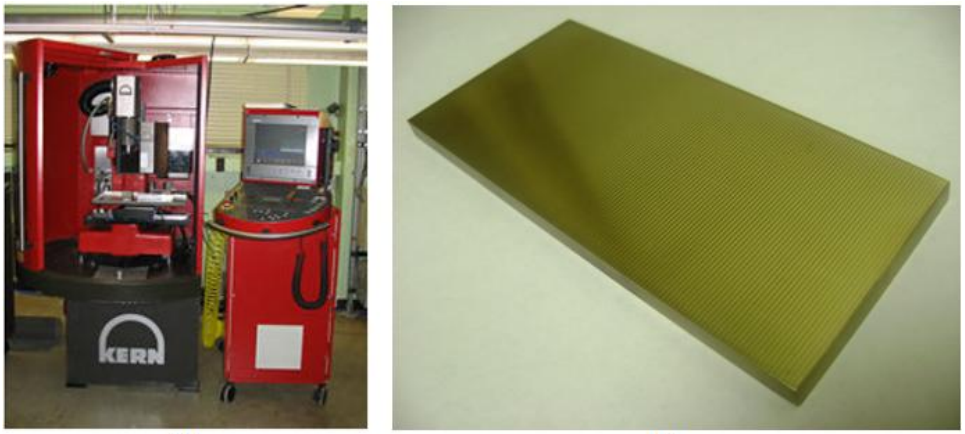

Figure 3.3 Photographs of (a) Kern MMP Micromilling machine in Center for Bio-Modular Multi-Scale systems (CBM^2) of Louisiana State University and (b) micromilled brass micro ratchets (*p*: 768.1±3.0 μm, *d*: 127.6±2.6 μm).

3.2.2 Replicated Nickel Ratchets via NIL and Electroplating

During investigating droplet motion on the micromilled brass ratchets at an elevated temperature, we found that the brass surface becomes oxidized with time and this influences the

droplet motion by reducing the heat flux from the ratchet surface to droplets. Therefore, in order to minimize the influence of surface oxidation on the droplet motion, the micromilled brass ratchets were replicated into Ni via the series of replication process. Figure 3.4 shows the process scheme for the replication process. The replication process mainly consists of thermal NIL on a thermoplastic polymer, poly (methyl methacrylate) (PMMA), deposition of a metallic seed layer on the imprinted polymer ratchets, Ni electroplating and post-electroplating process. Post-electroplating process includes the water-jet cutting, backside surface planarization and removal of the polymer plating template. The purchased optical gratings (Richardson Grating Laboratories) with ratcheted structures of sub-micron (800 nm) period were also copied into Ni via electroplating.

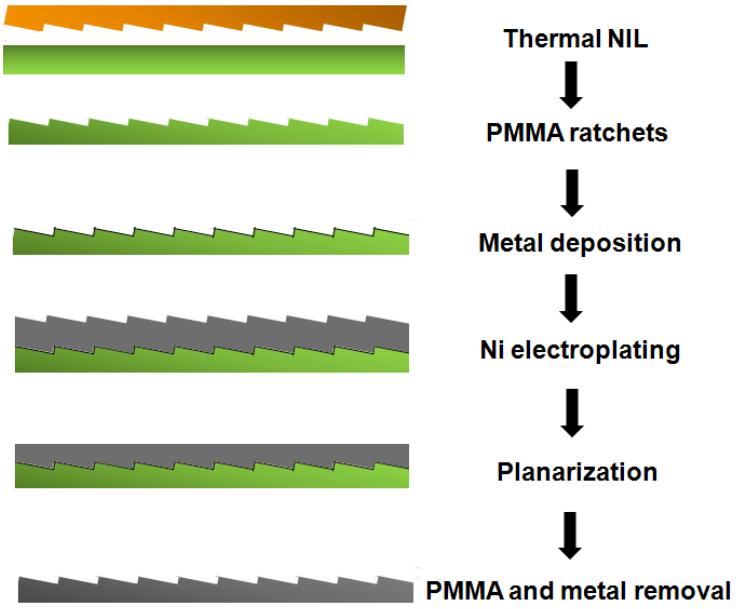

Figure 3.4 Replication process flows

3.2.2.1 Nanoimprint Lithography

NIL is a low cost, high-throughput, and high resolution process to pattern micro and nano structures on thermoplastic polymers using mechanical molding. The thermal NIL process

consists of three steps in sequence; molding, cooling and demolding, which altogether determine the fidelity of replication and the mechanical stability of the patterns. The polymer to be imprinted was a bulk polymer sheet. After stacking a stamp on a substrate and placing them on the stage of the NIL system, the first step in NIL is heating above the glass transition temperature of the polymer T_g. The increased temperature significantly reduces viscosity of the thermoplastic polymer, especially when the temperature is above T_g. Then, a metallic ratchet stamp is pressed into a substrate so that the polymer can flow into the cavities of the stamp structures. A piece of silicone rubber sheet placed on the top surface of the stamp ensures homogenous distribution of pressure. After conformal molding, the molded polymer becomes hardened by cooling the stamp/substrate assembly down to below T_g of the polymer while maintaining the pressure. In the demolding step, pressure is released and the stamp is separated from the substrate during demolding. Since thermal NIL does not utilize high energy beams such as UV light, its resolution does not depend on the factors such as light diffraction and beam scattering (del Campo and Arzt 2008). The theoretical minimum feature size that can be produced by NIL is related the radius of gyration of the polymer chain, which is defined as the average distance from the center of the gravity to the chain segment (Zhou and Yan 1997). The radii of gyration of PDMS and PMMA used in this study are in the range of 0.12.0 – 28.4 Å based on their molecular weight. Thermal NIL has demonstrated sub-10 nm features in polymer substrates (Chou, Krauss et al. 1995; Chou, Krauss et al. 1996). The smallest feature that have been reported was 6 nm in line width, as produced via UV-NIL using a stamp fabricated by molecular beam epitaxy (MBE) of GaAs and AlGaAs bilayers and the subsequent selective etching (Austin, Zhang et al. 2005). In practice, the minimum feature size for NIL relies only on the ability of fabricating smaller structures for the stamp.

There are basically two important requirements for a successful imprinting. First, the resist should easily flow and completely fill the structures on the stamp during imprinting. Second, the stamp needs to be easily removed from replicated patterns at the demolding step, without any unacceptable defects. In order to improve the polymer filling, higher imprint temperature and longer imprinting time are preferred. However, higher imprint temperature gives rise to increased deformation of the molded substrate such as warping. Thus, an optimal imprint temperature needs to be found. Maintaining homogeneous pressure is important in order to achieve uniform patterns over the entire patterning area. For successful demolding it is critical to apply a surface coating on the stamp surface to reduce adhesion at the stamp/polymer interface.

In this study, abrasion resistant acrylic sheets (PMMA, T_g = 95 ℃, 1/8" thickness, Champion Plastics, Baton Rouge, LA) were used as substrate material. Prior to the thermal NIL, brass or Ni stamp surfaces were coated by a fluorinated silane molecule, 1H,1H,2H,2H−Perfluorodecyltrichlorosilane ($C_{10}H_4Cl_3F_{17}Si$) in a custom made chemical vapor deposition (CVD) chamber (figure 3.5). This molecule consists of a head group with three chlorosilanes and a fluorinated, long carbon chain (C_{10}) and is known to form a covalent bonding to hydroxylated Si (HO-Si-) surface. The silane may form a similar bonding with the brass or Ni surface due to the presence of an oxide layer at the surface. The bonding strength is expected to be much lower than that with the hydroxylated Si surface. Before coating the fluorinated silane, either brass or Ni ratchets stamp was cleaned sequentially with acetone, isopropyl alcohol, and deionized (DI) water in an ultrasonic bath (Branson 3510) for 5 min and then exposed to O_2 plasma at 150 watts and 250 mTorr for 30 seconds in order to activate the surface. The stamp is blow-cleaned by N_2, then loaded into the custom-designed CVD chamber to be exposed to the vapor of the hydrophobic silane for 5 − 10 min.

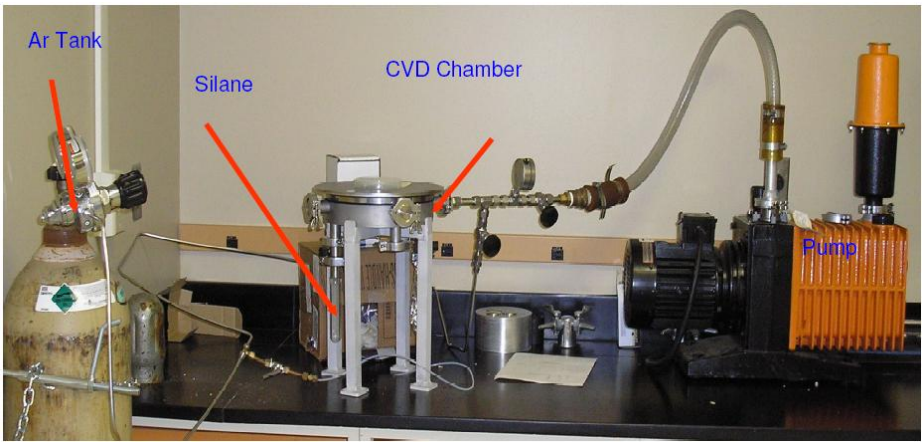

Figure 3.5 CVD system for hydrophobic silane coating (Roychowdhury 2007).

For imprinting of millimeter and micro scale ratchets, a mechanical press equipped with two heating platens or shortly a hot press (Atlas Press Power T25 and Series Heated Platens, Specac Inc., Atlanta, GA) was used while for imprinting of sub-micron ratchets a commercial NIL system (Obducat 6") was used. It is because the Obducat 6" NIL system permits overall thickness of the stamp/substrate assembly of 2 mm and thus ~ 6 mm thick brass ratchets cannot be introduced in the system. Figure 3.6 (a) shows the photography of the NIL system used. The imprinting parameters used for imprinting into a PMMA sheet with the two systems was are shown in table 3.1. Under these conditions, the brass or Ni stamp/substrate assembly was easily demolded even without using a sharp blade for separation, mostly thanks to the low aspect ratio of ratchet structures and the anti-adhesion, fluorinated silane coating. In order to minimize the structural deformation during demolding, force was applied parallel to the direction of ratchet grooves. All the operations were performed in a 10,000× class modulus clean room (refer Figure 3.6 (b)).

(a) (b)

Figure 3.6 (a) Obducat 6” NIL system (b) 10,000× class modulus clean room (Song 2007).

Table 3.1 Optimized imprinting conditions of custom-designed hot press and Obducat nanoimprint system for PMMA sheet.

	Custom-designed Hot press	Obducat 6” NIL system
Molding temperature	150 ℃	150 ℃
Weight/pressure	3 ton	40 bar
time	20 min	20 min
Demolding temperature	70 ℃	70 ℃

3.2.2.2 Electroplating

The replicated ratchets into a PMMA sheet were further copied into Ni via electroplating. As a seed layer, 10 nm thick Cr and 30 nm thick Au were deposited on the imprinted PMMA ratchets using an electron beam evaporator (Temescal BJD-1800 E-Beam Deposition System) at the Center for Advanced Microstructures and Devices (CAMD), Louisiana State University. Prior to plating, the sample was treated with an oxygen plasma at a working pressure of 250 mTorr and an incident power of 150 Watt for 1 min in an reactive ion etching (RIE) machine (Technics Micro-RIE series 800 reactive etcher) in order to avoid bubble generation on metal coated PMMA substrate and to remove organic contaminations on the surface. Then, Ni over-plating was carried out in a custom-designed electroplating setup using a Ni sulfamated solution

(Park, Hupert et al. 2008). Table 3.2 shows chemical composition of the electroplating solution and conditions for electroplating. The E-form (electronic grade sulfamate nickel concentrate, 180 g/L), boric acid (minimum purity of 99.8%) and E-liminate pit (wetting agent) were purchased from DisChem Inc. (Ridgway, PA).

Table 3.2 Chemical composition of the nickel sulfamate electroplating solution and the electroplating conditions used (Park, Hupert et al. 2008).

Chemicals and parameters	Contents and conditions
Ni^{2+} from $Ni(SO_3 \cdot NH_2)_2$ (sulfamate Ni)	89 g/L
H_3BO_3 (boric acid)	45 g/L
Wetting agent	0.3% volume/L
Total solution volume	70 L
Plating temperature	50 ℃
pH	3.8 − 4.2
Current density	7 – 40 mA/cm^2

A custom-designed electroplating bath for large area plating template, which consist of a polypropylene electroplating tank, a DC power supply (Tequipment.net, Long Branch, NJ), was assembled as shown in figure 3.7 (a). The electroplating solution was continuously circulated and filtered using a commercially available filtration system (Technic Inc., Cranston, RI) with two different sizes of polypropylene filters (10 μm and 1 μm, Technic Inc.) in figure 3.7 (b). Sulfur depolarized nickel crown pellets (Inco "S" rounds, Belmont Metal Inc., Brooklyn, NY) were used to maintain a supply of nickel ions during electroplating. The pellets were encased in a 250 mm by 213 mm titanium anode basket (Vulcanium Corp., Northbrook, IL) to ensure an anode-to-cathode area ratio of 1:1 or greater for maximum plating efficiency. The anode basket was bagged in a napped polypropylene bag (Baker Bags, Tamworth, NH). An electroplating jig with proper insulation was made of polysulfone (McMaster-Carr, Atlanta, GA) to hold the 150

mm diameter substrates immersed in the electroplating tank. The electrical current path for electroplating was established between the seed layer of the PMMA substrate and the stainless steel bottom plate of the jig using conductive copper tape. The plating jig and the anode basket were supported by titanium bars and immersed in a conductive nickel sulfamate solution as shown in Figure 3.7 (c). In order to control process quality, the operating conditions of Ni electroplating system were evaluated. The appropriate parameters shown in table 3.2 were maintained after completing every plating by carrying out standard tests following the DisChem's operating manual such as internal stress test with copper (Cu) sample, measurement of surface tension, Ni amount and pH value of the Ni solution. For example, sulfamic acid 60 g in 2 L of DI water needed to be added into the Ni solution to control pH as well as to activate anode. Low pH increases the rate of anode corrosion and efficiency. High pH also should be avoided since it reduces anode dissolution and efficiency, causing anode passivation to occur. 60 g sodium hydroxide (NaOH) in 1 L of DI water needs to be added into the tank to increase the pH value of Ni solution by around 2 – 3. Tensile stress can be significantly reduced by particle and carbon filtration.

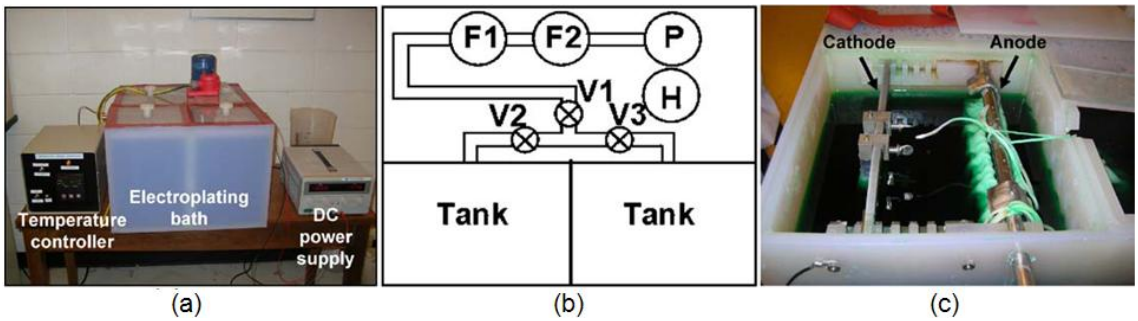

Figure 3.7 Custom-designed electroplating setup: (a) Overall view of the setup including the electroplating bath, a temperature controller, and a DC power supply; and (b) Schematic top view of the electroplating bath (F1 and F2 filters, P pump, H heater, and V1, V2, and V3 valves). (c) Photographs of a top-view of the electroplating tank showing the plating jig and the anode basket immersed and held by titanium bars in a conductive nickel sulfamate solution (Park, Hupert et al. 2008).

The current density for electroplating was initially set at $7 - 10$ mA/cm^2, and increased to 20

-40 mA/cm^2 to complete the overplating of the base of the large area ratchets. Upon completion of electrodeposition, post-plating processes followed, which include backside surface planarization of the overplated Ni ratchets, water jet cutting to a rectangular (5×10 cm^2) or square (5.2×5.2 cm^2) shape and removal of the imprinted PMMA templates with acetone.

3.2.3 Integration of Micro and Nanostructures on Ratchets

One of the technical objectives of this work is to reveal the effect of additional surface roughness elements on micro and nano ratchets because surface roughness is known to significantly influence the film boiling behavior such as Leidenfrost temperature (T_L). In addition, surface roughness is a critical factor influencing the wettability of surfaces together with surface chemistry. In order to integrate designed micro and nano structures on micro scale ratchets, a modified thermal NIL process called 3-D molding was employed (Farshchian, Ok et al. 2009; Farshchian, Hurst et al. 2011). 3-D molding is a simple and low cost process which allows for producing micro and nanostructures on non-planar substrates. Figure 3.8 shows the process scheme for 3-D molding to pattern micro and nano structures on the ratchets surface.

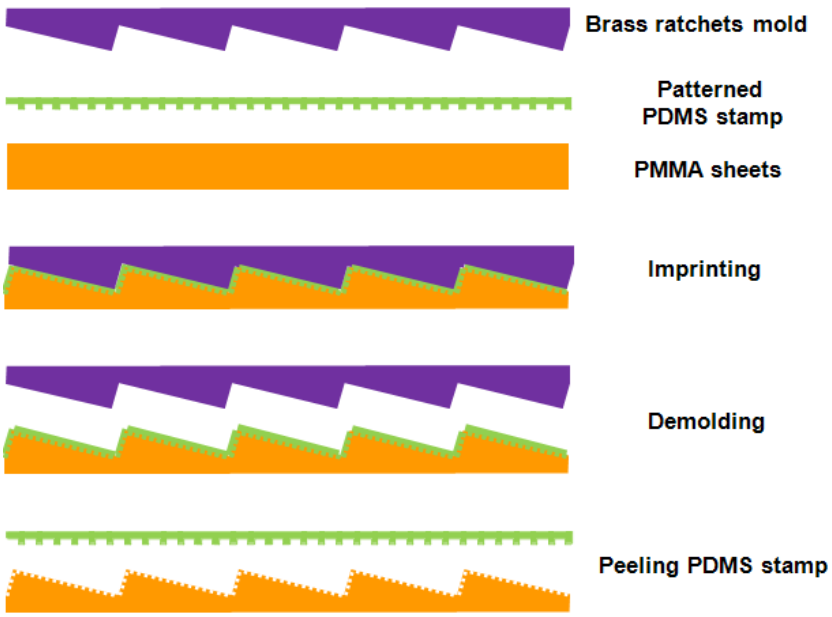

Figure 3.8 Schematic illustration of the 3-D molding process to fabricate micro gratings and micro pillars on top of the ratcheted surface.

3.2.3.1 Fabrication of PDMS Intermediate Stamp for 3-D Molding

The key of the process is the use of a flexible thin PDMS with micro or nano patterns as intermediate stamp, which was placed between a brass mold and a PMMA sheet for conventional NIL or hot embossing. PDMS was chosen as the intermediate stamp material because of its elasticity, flexibility and hydrophobicity. PDMS can stretch during 3-D molding and restore to its original dimension after demolding due to its elasticity. Therefore, it can be used repeatedly. The thickness of the PDMS layer can be easily controlled by time and speed of spin coating. The flexibility of the PDMS stamp reduces adhesion between the stamp and the substrate as the adhesion is related to the Young's modulus of stamp and substrate materials, making demolding easier (Pollock, Maugis et al. 1978). Moreover, PDMS has low interfacial energy due to its hydrophobicity and thus it can be easily released even without the use of an anti-adhesion agent.

The PMDS intermediate stamps have been fabricated by spin-coating PDMS into pre-patterned molds which were produced by two different methods. Molds with micro gratings and pillars were produced in an epoxy-based negative photoresist SU-8 (MicroChem Corp., Newton, MA) by photolithography while molds with micro and submicron ratchets were fabricated by NIL into PMMA with the brass or Ni ratchets produced in Chapter 3.2.1 and 3.2.2.

For SU-8 molds with micro gratings and pillars, SU-8 was spin-coated over 4" Si wafers (University Wafers, Boston, MA) and pre-baked in two steps at 65 and 95 ℃ on a hot plate. SU-8 has been widely used due to its excellent UV sensitivity, high resolution, thermal and chemical stability. For the samples with thick SU-8 (> 50 μm), flycutting (Optimum 120, Precitech Inc., Keene, NH) was used to reduce the total thickness variation of the film. Then, the SU-8 layer was exposed to UV light in a UV exposure system (Quintel Ultraline 7000 series mask aligner, Morgan Hill, CA) that is equipped with a 1 kW broadband mercury UV lamp and an UV filter

(Kopp 9345, Kopp Glass Inc., Pittsburgh, PA). The UV filter was used to avoid the formation of excessive cross-linking at the top surface of the SU-8 layer because the SU-8 exposure process is optimized with near UV wavelength in the range of 350 – 400 nm. The UV exposure was followed by two step post-baking process at 65 and 95 ℃ on a hot plate. Then, the sample was developed in SU-8 developer, propylene glycol methyl ether acetate (PGMEA, MicroChem Corp., Newton, MA).

The SU-8 mold with micro gratings and pillars was first spin-coated with a very thin layer of PMMA (less than 1 μm) as a sacrificial layer (MW 75k, 10 wt% diluted in Ethyl L-lactate, 98%, from Sigma-Aldrich) at 1000 rpm for 60 seconds prior to spin-coating of PDMS. This step was not necessary when PMMA molds with micro and sub-micron ratchets were used. For PDMS coating, Sylgard 184 silicon elastomer and curing agent were purchased as a kit from Dow Corning and used without any modification. PDMS was mixed in a 10:1 mass ratio of silicon elastomer to curing agent. Air bubbles were removed from the mixture by degassing in vacuum for 15 minutes. Then, PDMS was spin-coated on the mold or PMMA coated mold at 1000 rpm for 20 seconds, followed by curing at 65 ℃ for 24 hours and separating from the substrate by dissolving the PMMA sacrificial layer in acetone. By scratching near the edge of the sample, a thin PDMS film patterned with micro/nano structures was spontaneously released from the mold within a few seconds. The minimum thickness of PDMS stamps used was ~ 100 μm. A thinner PDMS stamp less than 100 μm in thickness can also be produced. However, it becomes torn and crumbled easily, making it difficult to handle.

3.2.3.2 3-D Molding Process

In 3-D molding, a flexible and thin intermediate PDMS stamp with micro/nano patterns was placed between a brass mold and a PMMA substrate. The whole system was heated at 200 ℃ for

20 minutes, followed by imprinting at 200℃ and 3 ton for 20 minutes using a hot press. Demolding of the brass mold was manually performed at 70℃, which was followed by the second demolding step by peeling off the PDMS thin stamp from the imprinted PMMA pattern. With the 3-D molding process, patterning of micro and nano scale gratings and pillars on the entire sidewalls and bottom surfaces of millimeter and micro scale channels has been demonstrated (Bahador Farshchian, Steven Max Hurst et al. 2010). In this study, only plain (without pattern) thin intermediate PDMS stamp was used to make microratchets with round shape of ridges.

3.2.4 Polymer Superhydrophobic Surface

Two different polymer materials were selected to fabricate hierarchical superhydrophobic surfaces; UV-resin and PMMA. Soft UV-nanoimprint lithography was employed for UV-resin superhydrophobic structures (Farshchian, Choi et al. 2011). Transparent negative PDMS replica was used as a mediate stamp. For PMMA superhydrophobic ratchets, thermally imprinted PMMA ratcheted surface was modified by reactive ion etching and fluorinated silane coating.

For the fabrication of UV-resin superhydrophobic textures, the elephant ear leaf (Colocasiaesculenta) and hierarchical pyramids were used as a template. Elephant ear leaf was cut with the size of 20 mm × 20 mm, pasted to a flat piece of PMMA sheet and was used as a master. In order to fabricate hierarchical pyramids on UV-resin a multistep process was followed. P-type silicon (100) wafers with a resistivity of 1-10 Ω cm were used for the experiments. Si master stamps with pyramid-shaped grooves in a (100) Si wafer deposited with 100 nm thick layer of silicon nitride using LPCVD (Low-Pressure Chemical Vapor Deposition) were fabricated using a combination of photolithography and wet etching techniques. First, a 1.3 μm thick layer of positive photoresist (S1813, Shipley Co.) was spin-coated at 3500 rpm for 45 sec

on the substrate, which was treated with oxygen plasma in order to modify its surface and dehydrated at 110 ℃, and subsequently a pre-exposure bake was performed at 115 ℃ for 60 sec. Photolithography was done with a custom designed photomask (Advance Reproductions Co.) in a UV exposure station (UL7000-OBS Aligner and DUV exposure, Quintel Co.) at class 100 clean room. The exposed wafer was then developed in MF319 developer solution (Rohm and Haas Co.) for 90 sec, followed by washing with deionized water for 5 min and drying with N_2 gas. Any residual layer in the recessed area of the resin patterns was removed by etching with oxygen plasma for about 10 sec. Then, the nitride layers were patterned into square etch masks using a plasma etching process by SF_6 gas at 400 mTorr the RIE power was set at 150 watt. The wet etching was performed in a glass beaker at 80 ±1 ℃ in 35 - 50 wt% KOH solution added 5 wt% isopropyl alcohol (IPA). The solutions were made by dissolving KOH pellets (85%, Fisher Scientific Inc.) in deionized water. In order to prevent the change in concentration of the KOH solution because of evaporation, the top of the beaker was closed with an aluminum foil. Subsequently, the barrier nitride layer on the silicon surface was removed by hydrofluoric acid (48%, EMD Chemicals Inc.) and it was cleaned in acetone, isopropyl alcohol and deionized water of sonication bath for 5 min each.

Then silicon was used as stamp for pattern transfer to UV-resin coated on the surface of glass slide. Prior to pattern replication, the silicon master surfaces were treated 20 minutes with a fluorinated silane molecule (heptadecafluoro-1, 1, 2, 2- tetrahydrodecyl) trichlorosilane ($C_{10}H_4C_{l3}F_{17}Si$) purchased from Gelest in the vapor phase using a home built vacuum chamber in order to reduce to reduce adhesion to the resin. Pattern imprinting was tried using a UV-curable polymer blend (resin) containing tripropylene glycol diacrylateas oligomer from Aldrich co., trimethylolpropanetriacrylate (TMPTA) as the crosslinking agent from Aldrich co. and Irgacure

651 as the photo initiator from Ciba. The weight ratio of oligomer, crosslinking agent and curing agent were 49 wt%, 49 wt% and 2 wt% respectively. Taking advantage of the low viscosity of the polymer, it was manually dispensed on the surface of glass slide. The Si stamp was placed over the surface of glass which was previously coated with the UV-resin. Finger pressure was applied to the Si stamp to provide contact with the substrate. The UV-resin was exposed to UV light from slide glass side for 10s using a UV-lamp having the intensity of 1.8 W/cm^2. After UV exposure Si stamp was manually demolded from the printed UV- resin. Then oxygen plasma etching process was performed to treat surface of UV-resin pyramids using Reactive Ion Etch Series 800 Plasma System (Technics 800 Micro RIE). The reactive ion etching (RIE) power and oxygen pressure were set at 150 W and 150 mTorr respectively and the surface of UV-resin pyramids were treated for 20 minutes. The RIE treated UV-resin structures were treated for 20 minutes with a fluorinated silane molecule described earlier to reduce their surface energy.

The PDMS elastomer that we used was Sylgard ™ 184 purchased from Dow Corning. It is supplied as a two-part kit: a liquid silicone rubber base (i.e. a vinyl-terminated PDMS) and a catalyst or curing agent (i.e. a mixture of a platinum complex and copolymers of methylhydrosiloxane and dimethylsiloxane) (Xia and Whitesides 1998). Silicon rubber base and curing agent were mixed in a 10:1 mass ratio. In order to remove air bubbles from the mixture it was vacuumed for 20 minutes. After removing air bubbles, the PDMS was casted on the surface of leaf or hierarchical pyramid template. PDMS on surface of leaf and hierarchical pyramids were then cured at room temperature and 65 °C in oven for 24 hours and four hours respectively. Then the liquid mixture becomes a solid, cross-linked elastomer via the hydrosilylation reaction between vinyl (SiCH=CH2) groups and hydrosilane (SiH) groups (Xia and Whitesides 1998). Once PDMS was cured, it was peeled off from the superhydrophobic template manually.

The PDMS stamp was placed over the surface of PMMA sheet with the size of 20 mm × 20 mm which was previously sanded with sand paper with grit number of 240, cleaned with the air-gun and coated with the UV-resin. Gentle finger pressure was applied to the PDMS stamp to provide a conformal contact with the substrate. The UV-resin was exposed to UV light from top of PDMS stamp for 10s using a UV-lamp having the intensity of 1.8 W/cm^2. After UV exposure PDMS stamp was manually peeled off from the printed UV-resin. Sanding of PMMA will avoid peeling off the imprinted UV-resin from PMMA substrate during peeling off PDMS from imprinted UV-resin structures.

For PMMA superhydrophobic ratchets, the procedures are much simpler than those of UV-resin superhydrophobic textures. Thermal NIL process allows direct ratchets replication on the PMMA template, which is previously well described in chapter 3.2.2. The generation of nanoscale surface roughness and chemical surface modification are exactly same as those for UV-resin superhydrophobic surfaces.

3.3 Metrology

The fabricated micro and nano ratchets, micro pillars, micro gratings were characterized using various methods such as optical microscope, surface profilometer, scanning electron microscope (SEM) and atomic force microscope (AFM), depending on their dimensions and material properties such as electrical conductivity.

3.3.1 Scanning Electron Microscopy (SEM)

Scanning electron microscope (SEM) is an electron microscope that images a sample surface with high resolution by scanning it with a high energy electron beam. SEM was performed using a Hitachi S-3600N SEM system in secondary electron and topographic mode at 5 − 25 kV accelerating voltage, 5 − 20 mm working distance, automatic contrast and brightness. SEM

images were captured at different magnifications in the range of 30 − 15,000× depending on sample dimensions. In case of polymer structures, a several tens of nanometer thick Au layer was deposited on polymer samples by sputtering in order to increase the conductivity. A low accelerating voltage of 5 kV was used to avoid blurring of images due to surface charging by electrons.

3.3.2 Surface Profilometer

A surface profilometer is usually used to quantify surface roughness by scanning a sharp tip or focused light probe over the sample surface. Vertical resolution is in the nanometer scale (10 Å), but lateral resolution is relatively poorer. In this study, both of stylus (contact type, Tencor P-11) and optical (non-contact, Nanovea ST400) surface profilometers were used to measure profiles, roughness and flatness (or vertical variation) of millimeter/micro ratcheted surfaces. Both profilometers scan samples by moving their stages while keeping constant position of stylus or optical probe. For each sample, scanning was carried out along four different directions: lengthwise, widthwise, inner diagonal and outer diagonal directions. An overall vertical variation and RMS surface roughness generated by micromilling process was in the range of 100 − 300 μm and 150 − 300 nm for the entire sample sizes, respectively.

3.3.3 Atomic Force Microscopy (AFM)

Atomic force microscopy (AFM) can provides a precise 3D profile of nano structures, using force between a sharp tip attached to a flexible cantilever and surface at a very short distance. While the tip scans over the sample surface, the deflection of the cantilever is recorded, that is converted into an image representing the 3-D shape of the sample surface. In this study, AFM was performed using an Agilent 5500 system in an AC (non-contact) mode. In AC mode, the tip does not contact the sample surface while oscillation of the cantilever with the amplitude is

maintained by piezoelectric actuation. When the tip comes close to the surface, the amplitude of the oscillating cantilever is changed. Changes in the vibration amplitude are measured during scanning the tip over the sample surface, which are converted into a topographic image of the sample surface by software provided by Agilent. A non-contact mode AFM tip (the pointprobe-plus® silicon-SPM-sensor, Inc. Nanosensors) was used; material: n+ silicon; resonance frequency; 146 − 236 kHz and tip height; 10 − 15 μm). Since the maximum height that can be probed by the AFM scanner is 8 μm, only sub-micron imprinted polymer and replicated Ni ratchets were inspected by AFM.

3.3.4 Contact Angle Measurement

A contact angle is an angle formed at the air/liquid/solid interface and is a measure of wettability of a surface. A static contact angle can be measured by gently depositing a liquid droplet on a solid surface. A contact angle analyzer (FTA 125, First Ten Ångstrom, Inc. Portsmouth, Virginia) shown in figure 3.9 was used to measure static contact angles on the samples used in this study. It mainly consists of four parts: a sample stage, a digital camera, an illuminator, and image processing software. The sample to measure contact angle is placed on the sample stage and adjusted to an appropriate level by lifting manually. A droplet is dispensed on the sample by pushing a button of the pipette and turning a knob slowly. The image is captured immediately after the droplet is placed on the sample for accurate and consistent observation. The software analyzes the drop shape and computes the contact angle. In this study, the contact angle values are used as an index of surface wettability of such various implemented structures as different dimensions of ratchets, micro pillars and various roughness elements on micro ratchets. At least ten measurements were performed for each sample and the average values were used for each data point. The volume of the droplets used was 5 μL.

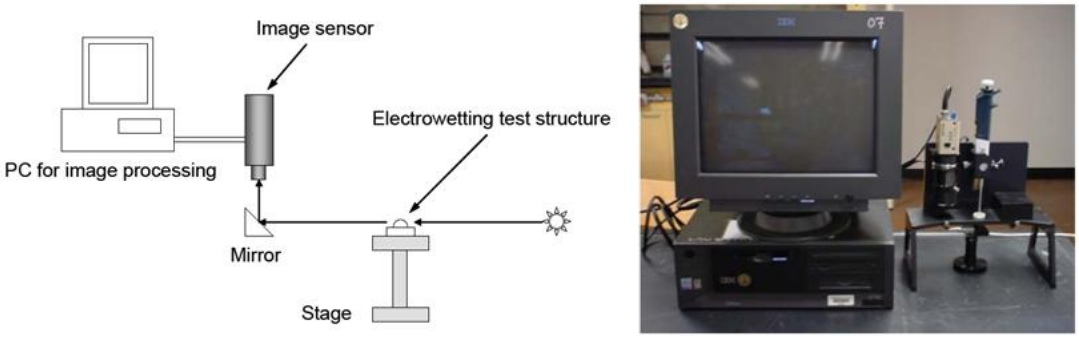

(a) (b)

Figure 3.9 Contact angle measurement system: (a) schematic diagram and (b) photograph of the system (Park 2007).

3.4 Characterization of the Motion of Leidenfrost Droplets on Ratchets

After the fabrication and characterization of ratchets, the impact and motion of droplets on the ratchets were systematically investigated. At the beginning stage of this study, a simple experimental setup consisting of a low resolution video camera and a hot plate was used to obtain mean velocities of droplet motion in the film boiling regime. After initial results, a more sophisticated experimental setup with a high speed camera and a syringe pump for injection was developed and used. The image sequence captured by high speed camera was processed by the software. In order to investigate the droplet motion on ratchets further specifically, overall modification of the system was required. This section mainly describes about the experimental setup and procedures.

3.4.1 Initial Experimental Eetup for Droplet Motion

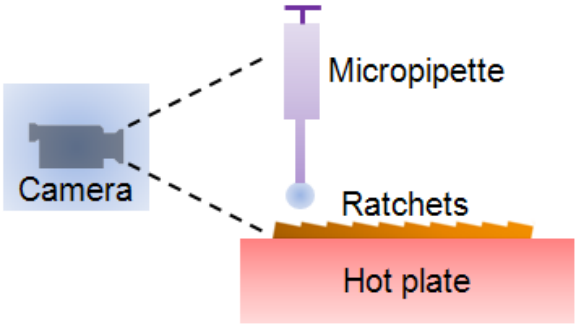

Figure 3.10 Schematic diagram of primitive experimental setup to investigate motion of Leidenfrost droplet on ratchets.

The initial experimental setup shown in figure 3.10 consists of three parts: a micropipette for injection of droplets, a hot plate for heating, and a video camera for recording. The video camera used (Sony DSC-V1) has a low frame rate of 16 fps. A droplet is generated by slowly pushing a button of micropipette (Eppendorf, adjustable range of volume: 1 – 10 μL) and is released on top of the ratchets surface at a height of 1 – 3 mm above the heated ratchet surface, to minimize the influence of the gravity.

The volume of droplets was manipulated by adjusting the knob of the pipette. The actual droplet volumes generated by the micropipette were measured using a contact angle analyzer (FTA 125). Figure 3.11 shows the measured droplet volumes versus the volumes set in the micropipette for DI water, acetone, and IPA (2-propanol). For the droplet volume in the range of 3 – 6 μL, the set and measured volumes are fairly similar to each other with variances of 0.5 – 1 μL.

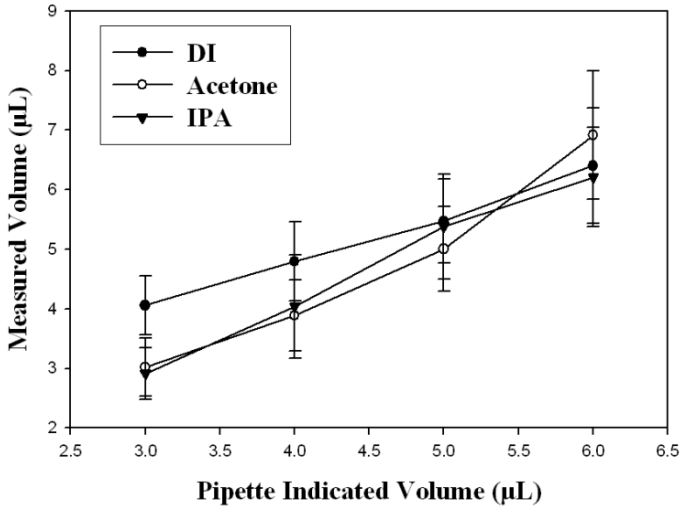

Figure 3.11 Droplet volume measured by a contact angle analyzer (FTA 125) versus set volume in the micropipette. Volumes of at least ten droplets were measured and the average value was used for each data point.

A hot plate (Isotemp, Fisher Scientific) with set temperature in the range of 20 – 400 ℃ was used to heat ratchets. Since the hot plate set temperature is usually different from the temperature in ratchets, we have measured temperatures at two additional locations: ratchet surface

temperature was measured by putting a thermocouple on top of the substrate surface while ratchet bulk temperature was taken by inserting a thermocouple into a circular hole drilled into substrate bulk. Table 3.3 and figure 3.12 show the measured temperature at the two locations versus hot plate set temperature. Measuring the ratchet bulk temperature may lead to more consistent results over the ratchet surface temperature due to negligible effects from convective heat flux near ratchets and the intimate contact of a thermocouple to the ratchet in the hole. However, it was not possible to drill a hole for bulk temperature measurements for all samples because the overplated Ni samples are usually too thin. Therefore, in this study, we measured ratchet surface temperatures from five locations on a sample (four corners and the center) and the average value was used as the ratchet surface temperature.

Table 3.3 Measured temperature values on the top surface and inside circular groove of brass bar (1/2" ×2" ×4") by using a K-type thermocouple (TP 873, EXTECH).

Hot plate set T (℃)	20	50	100	150	200	250	300	350
Surface Temperature (T_s) (℃)	20	38	83	124	171	224	263	306
Bulk Temperature (T_b) (℃)	20	42	93	142	193	243	294	341

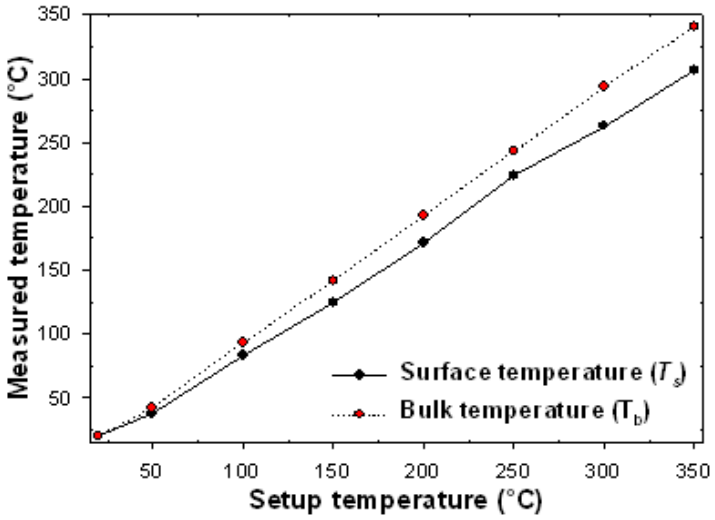

Figure 3.12 Measured temperatures versus hot plate set temperature (Graph from table 3.3).

3.4.2 Experimental Setup with High Speed Camera

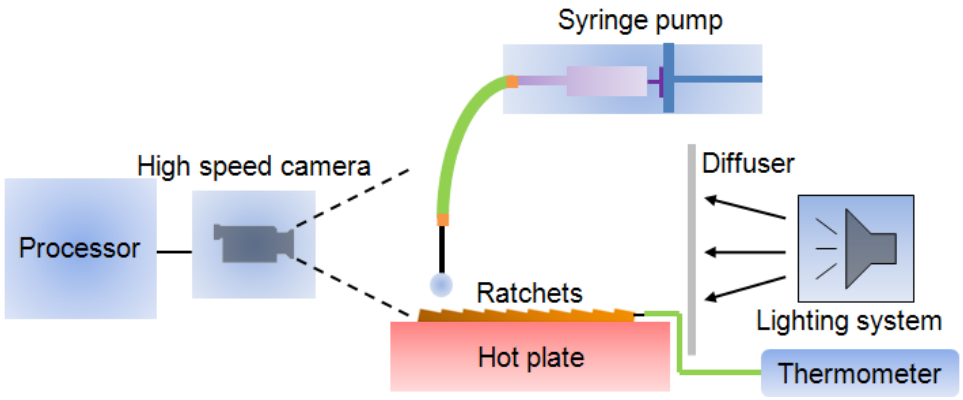

Figure 3.13 Schematic diagrams of modified experimental apparatus.

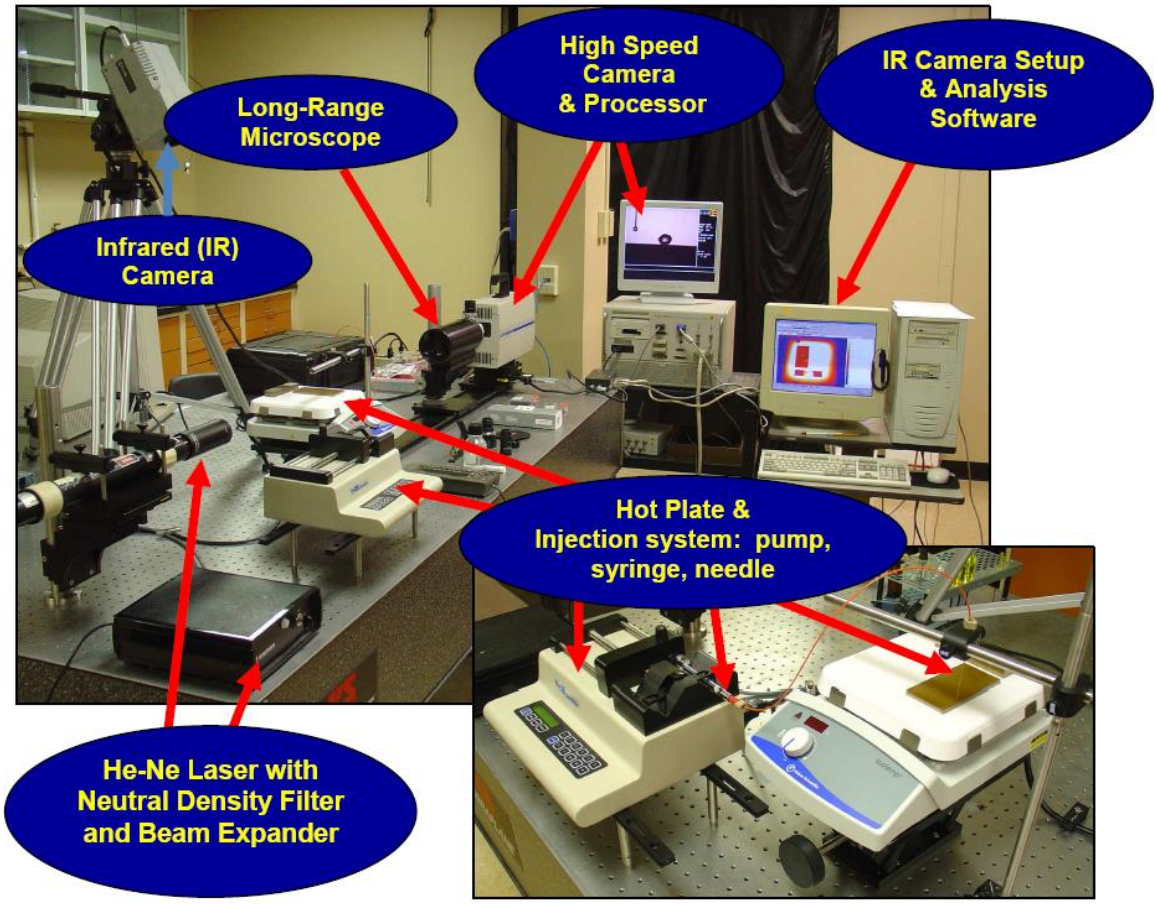

Figure 3.14 Photo of modified experimental apparatus by B. Gaveau (Laveau 2008).

In order to obtain in-situ images of dislocating droplets, to process captured pictures and to extract relevant data such as droplet velocity, acceleration and geometric shape, the initial and

primitive experimental apparatus needed to be modified. The modified apparatus should include an accurate data acquisition system and provide good repeatability. Figure 3.13 and 3.14 show the schematic and photograph of the modified setup. In addition to a hot plate, the system includes a syringe pump and a high speed camera with a lighting system. After acquisition of a video sequence with the high speed camera, image processing tools which were developed in-house using commercial softwares Optimas and Matlab were used to capture the physics relevant to the droplet motion.

3.4.2.1 Recording System

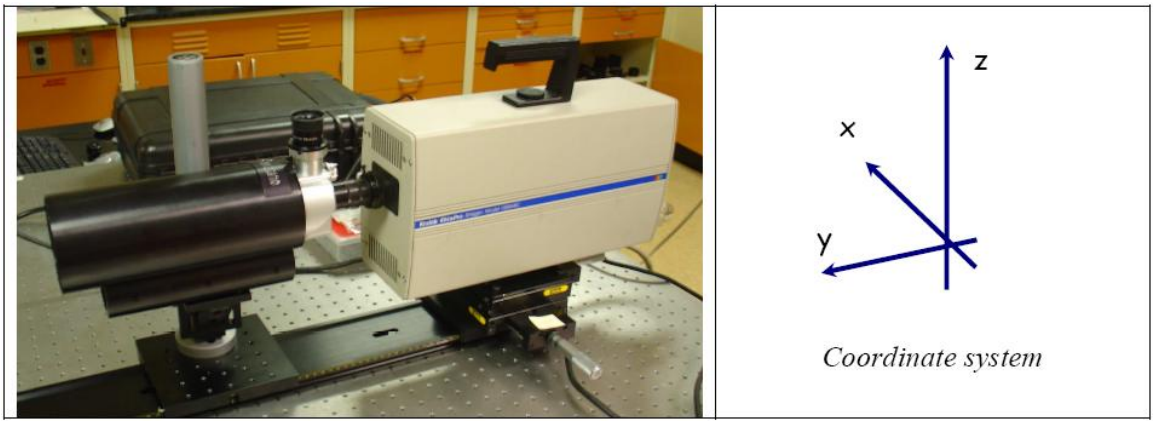

Figure 3.15 The Installed high speed camera in the positioning system and coordinate system (Laveau 2008).

The recording system consists of a high speed camera, lighting system, and accessories. The high speed camera (Kodak Ektapro 1000HRC) has a maximum frame rate of 1000 fps and minimum exposure time of 50 μs. In addition, a camcorder (Canon HG10 high definition (HD) video camcorder, 60 fps and 1920 × 1080 resolution) was employed to capture droplet motion over the entire ratchets from a wide view. Different magnifications are possible for the high speed camera just by inserting a set of spacers (C-Mount Nikon spacers of 5, 10, 20 and 40 mm) between the lens and the CCD sensor. A long range (LR) microscope (Questar) was used for further magnification and can be directly connected to the camera. This LR microscope has a

short field of focus and a short field of view, so that it should be used only for analysis requiring a high magnification. The camera needs a positioning system to achieve high quality of pictures and for handful and precise focusing. It is composed of an optical rail, two micro-positioning platforms and an adapter to screw the camera on top of this system. The two platforms allow position in two directions as shown in figure 3.15:

- On the x axis: to place the camera in a different part of the droplet trajectory such as injection, middle and end part.
- On the y axis: to obtain a precise focusing on the droplet outline.

A lighting system is also required to obtain clear pictures by the high speed camera. The emitted light should be strong enough to get clear images at the fastest frame rate with the shortest exposure time, and especially for LR microscope**.** The homogeneous background and contrast among background, needle, droplet and ratchet surface are very critical for the post image processing. Silver Bullet Wallylight (575W lamp, Cinemills Inc., CA) for big light and HeNe laser (Uniface, CA) for narrow light are selected. The former provides enough light for clear view of every experimental component for droplet motion and could be easily used with a neutral density filter (called diffuser) and give a clear and uniform background. The latter should have been the best way to light this system for narrow area but the beam cannot expand enough to light uniformly the whole recorded area (Edmond optics).

3.4.2.2 Heating System

For most of liquids except refrigerant R134a, Leidenfrost effect could not be generated without heating. The heat supplier used in the modified apparatus is a ceramic hot plate (Isotemp, Fisher Scientific), which could provide enough thermal energy to maintain it up to the hot plate set temperature of 550℃. One of the major issues in this study is to measure the surface

temperature of ratchets, which significantly influences the droplet behavior on the ratchets. The main problem encountered with the initial experimental setup was the sample damage generated by the direct contact with a thermocouple during measuring. Moreover, it is almost impossible to get good thermal contact between thermocouple and ratchets because of their geometric mismatches. Bulk temperature measurements by inserting a thermocouple into a drilled groove was only possible for thick brass ratchet samples, not for thin replicated Ni ratchet samples whose thicknesses are in the range of thickness from sub-millimeter to a few millimeters. Therefore, an infrared (IR) camera (FLIR ThermaCam SC500) is used to measure the ratchet surface temperature for improved setup. It provides real time visualization of temperature at 60 frames per second. It is easily controlled by the software which enables to set parameters describing the experimental configurations such as working distance and the surface emissivity. It is an analysis and visualization tool by generating various data such as the temperature on a spot, a temperature profile along a line, an average on defined area and a time evolution monitoring. The use of an IR camera is much more reliable than the use of a thermocouple especially on a ratcheted surface but the calibration process has to be carefully done, with a great attention given to the emissivity parameter. Detail calibration process of the temperature measuring system by IR camera is described in (Laveau 2008).

3.4.2.3 Injection System

The main purpose of the injection system is to generate droplets with a controllable manner. This system is assembled with an electronic syringe pump (NE-300, New Era Pump Systems Inc.), a syringe (1 mL, Hamilton), a needle (Hamilton) and the fitting system (Upchurch Scientific Inc.). The electronic syringe pump is programmable. Different parameters need to be provided such as syringe type and size, volume to inject and injection rate. In fact, the droplet

volume to be released is directly related to the injection rate and needle size. The fitting system connects the syringe and the needle in a flexible way. Different sizes of needles are prepared to manipulate droplet size in the range of 2 – 12 μL. As a preliminary experiment, performance of the injection system was evaluated at room temperature. The liquid used was DI water. The high speed camera was set at its highest frame rate (1000 fps) to record pictures of the droplet just leaving the needle. The two parameters examined were needle size and injection rate which were programmed in the electronic syringe pump. Ten droplets were used for each condition and an average value of droplet volume was calculated by Matlab. The necessary parameters could be estimated through this preliminary experiment as shown in table 3.4. The measure volumes slightly deviate from the set volume because of the surface tension which plays a role when a droplet is exited from the needle and the hot ratcheted surface just beneath the needle. It is expected that convective flow of air due to a thermal gradient between the needle and heated ratchets accelerates the evaporation of droplet. Therefore, in order to avoid this limitation, parameters with relatively higher injection rate are selected.

Table 3.4 Parameters identified for the generation of a droplet with a specific volume through preliminary experiment (Laveau 2008).

Volume (μL)	Needle	Injection rate (μL/min)
2	33	500
4	27	1600
	32	200
6	27	800
10	22	1000
12	22s	200

Injection configuration is also a critical factor for the creation of droplets as well as introduction on the ratchets. For the purpose of minimizing the bounce of droplets influenced by

gravity, M. Taormina (Taormina 2006) and H. Linke et al (Linke, Aleman et al. 2006) employed a tilted ramp for their droplet injection system. It provides droplets with an initial velocity due to the slope before entering ratchets. Then the droplet decelerates then stops and accelerates in the opposite direction. Though using a sloping surface is a good way for droplet injection, there is a problem in focusing caused by irregular and random places of droplets, which makes post image processing extremely difficult. Therefore, in this study droplet injection by a vertically aligned needle was chosen because of the lowest uncertainty on the droplet volume.

3.4.3 Procedures

Two different procedures are used for primitive and modified setups.

3.4.3.1 Initial Setup

A detail procedure to measure the velocity of droplet motion using primitive experimental setup is described. A ratcheted sample was placed on a hot plate without heating. Leveling was done with a bubble valance measurer on top of the ratchet surface. Then, the sample was heated by setting up a set temperature for hot plate. It takes around half an hour to reach an equilibrated temperature. Then, the ratchet surface temperature was measured at four corners and the center with a K-type thermocouple. The averaged temperature is used as the ratchets surface temperature (T_s). Usually the difference for temperatures measured at the five spots is in the range of 0 – 15°C. Droplet trajectory was captured by using a video camera and the Windows Movie Maker (Microsoft) software was used for tracking and processing the captured videos. Since the acceleration of the droplet could not be properly monitored with the video camera used due to its poor resolution, the averaged velocity of droplet motion is obtained based on the time interval from the point when the droplet starts to move to the point just before the droplet escaped from the ratchet surface. The trajectories of 10 droplets are captured for each T_s and the

velocity values are averaged to obtain a data point.

3.4.3.2 Modified Setup with High Speed Camera

A specific procedure for droplet motion and impact experiments with the modified setup is described as below. Prior to carrying out every experiment, several parameters have to be chosen such as droplet size, the magnification used for the picture and so on. Depending on the selected parameters, appropriate frame rate of the camera should be used. Lower frame rate (250 or 500 fps) is useful for the trajectory characterization. The highest frame rate (1000 fps) is recommended for specific measures such as the volume or the curvature of the droplet bottom.

The first step is to place a sample on the hot plate and position it. Leveling is done with a spirit level (Digital Torpedo Level, Craftsman, IL) and an alignment of the camera can also be done with the laser. The emitted light and the high speed camera forms an optical axis and the sample surface must be perpendicular to this axis otherwise the ratchet shape creates blurred patterns on the picture recorded. This perpendicularity could be checked directly by observing the picture recorded or with the laser. Then the desired temperature was set and monitored with the infrared camera. The emissivity has to be set at this time.

During the heating process, the injection system, high speed camera and lighting were set up and configured. First, the injection system has to be set up by programming the injection rate of the electronic pump as well as by placing the needle above the hot plate as close as much from the sample edge. Focusing on the needle has to be done by adjusting a knob for a micro-position platform while monitoring injection and bouncing of droplets by the high speed camera. However, the focusing of the camera lens should be avoided for this task. Camera lens is set as infinity, otherwise the size of the field of view would change and a calibration would be needed for each record. Thanks to the grids displayed on the monitor, the needle could be well aligned

and positioned. When the camera is well focused on the needle or the droplet outline, it's ready to record the pictures and the experiment could begin.

For most of the experiments, two magnifications were recorded. One with the 5 mm spacer was to record the entire motion of the droplet on a ratchet surface and the other with the 30 mm spacer to record picture and determine the volume. Pictures from the latter and higher magnification could also be used to study more precisely the behavior of droplet in injection area. The last part of the procedure is the picture recording, saving and then their download on a computer (Laveau 2008).

3.4.4 Image Processing

3.4.4.1 Image Processing by Optimas

After recording all the pictures with the high speed camera, the next step is to extract information contained in every picture. The image processing software Optimas was used to identify droplets, extract their geometrical features and to collect parameters, which are required for subsequent analysis of droplet motion by Matlab. The image processing by Optimas is based on arithmetic operation between a picture containing a droplet and a clear field (picture without droplet).

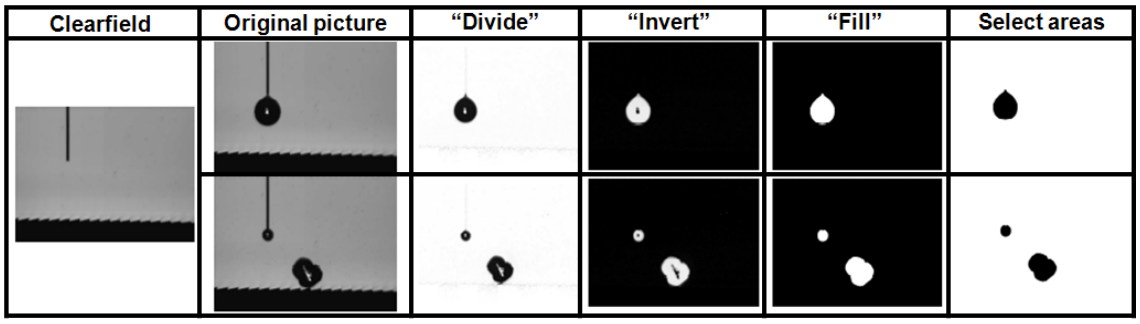

Figure 3.16 The separation process by Optimas (Laveau 2008).

The Optimas process is divided into three different steps: the separation, extraction, tracking and computation. In the separation step, the process separates the droplet from the needle, the

ratchets and the background. The basic set of operation is the division of the picture by a clear field, followed by binary inversion, then the white area is filled to remove black holes, finally the software identifies and selects automatically the black droplet. These operations are illustrated for injection area by figure 3.16.

When the droplet is not in the injection area, the set of operation is reduced and the time origin is set to the first picture containing an identified droplet. After the area of droplet is selected and the macro (*mainDroplet.mac*) could extract such the information requested as area, perimeter, position of the centroid (x, z), circularity (defined as $\frac{1}{4\pi}\frac{perimeter^2}{area}$), breadth, surrounding box (x_{min}, x_{max}, z_{min}, z_{max}), outline of droplet and etc. The next step is the tracking of the droplet through different pictures by another macro (*DataAnalysisDrop.mac*). The last step of Optimas is the computation of the droplet motion based on the position of the droplet centroid by third macro (*AccelVelDropl.mac*). The output excel file contains the outline description, position, geometrical features and motion information of moving droplet. All these information is ready to implement a statistical treatment and to visualize them by Matlab.

3.4.4.2 Data Processing by Matlab

The Excel file generated by Optimas is now read by a script (*GUIdroplet.m*) written in Matlab language. As a first step, the script organizes the data in a three dimensional matrix containing all the geometrical features and position information organized by droplet, where the third dimension is the number of droplet). Next, the script calculates the volume of each droplet and this allows us to select only those to be tracked. Unreliable droplets should be deleted based on the calculated droplet volume. The third step is the position and outline filtering. The resolution of the high speed camera is limited to 384 × 512 pixels, therefore sometimes two successive points of the outline or position are only two adjacent pixels, thus they get the same x

or z coordinate. A smoothing has to be done otherwise the data could not be used for any interpolation or extrapolation of new point. The filter used is: $p(i) = \frac{p(i)+p(i+1)}{2}, i = 0\ to\ n-1$, $p(n) = \frac{p(n)+p(0)}{2}$, where the vector of points *p* and its length *i*. Then the list of information which is organized by frame is now turned in a time based array. The flag marking the frame where the droplet leaves the needle is now used. The origin of the time and knowing the time step (1 over the frame rate) the time evolution of the droplet is now accessible. The forth step is to prepare the statistical processing. A choice has been made concerning the time origin and now every single droplet is considered with the same reference. The statistic process calculates the mean and the 95% confidence interval with the Student T distribution.

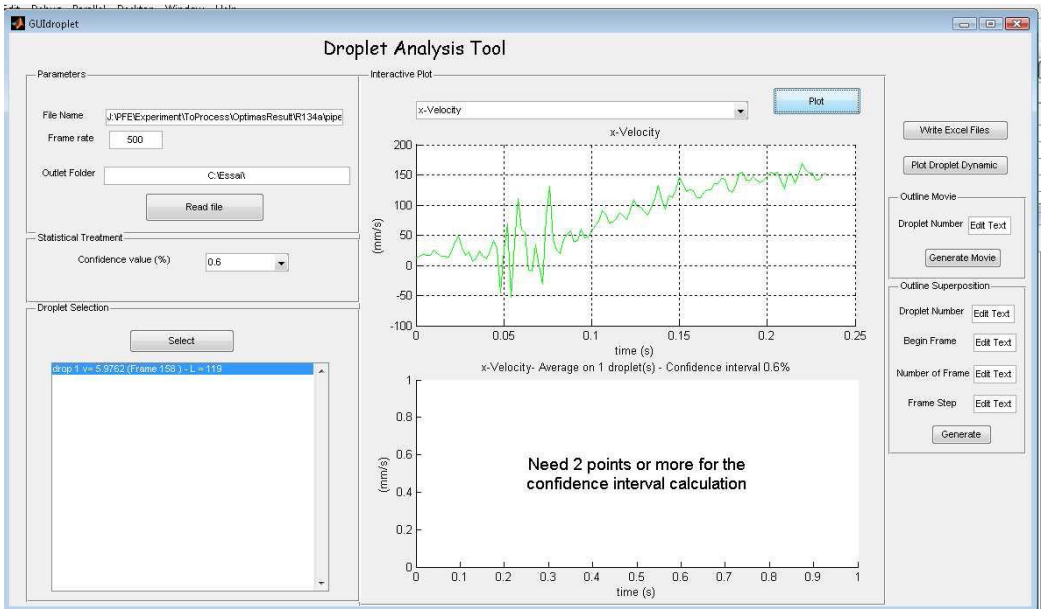

Figure 3.17 Graphic user interface for the data processing by *GUIdroplet.m* (Laveau 2008).

Now the data are loaded and another menu give us many possibilities to use them: plot the trajectory and the dynamic of the droplet, write Excel files with all the results, compute the volume of the droplet in another list of frames, see a movie of one droplet outline, plot a superposition of outline to see the deformation of the droplet during its motion, calculate the motion of one particular point of the droplet outline (giving an angle) and etc. An interactive

GUI interface has been developed with Matlab and allow the data processing in an easier way as shown in figure 3.17.

3.5 Conclusions

Various micro and nanofabrication techniques such as micromilling, NIL, photolithography, 3-D molding, and electroplating were used to fabricate various types of large area topological ratchets down to sub-μm scales. The fabrication methods for various dimensions of ratcheted structures were established by either series of milling and replication processes. The microratchets with round shape of ridges were fabricated by 3-D molding, which is a modifying thermal NIL process with a thin flexible PDMS stamp. Various polymer superhydrophobic surfaces were fabricated by replication, RIE, and chemical surface modification. All morphologies of fabricated structures were inspected using such various metrology equipments as surface profilometer, SEM and AFM according to their surface properties. The methods to characterize the motion of Leidenfrost droplet on ratchets has been evolved by using high speed camera and developing image processing tool.

Chapter 4 Characteristics of Leidenfrost Droplets on Miniaturized Ratchets

4.1 Introduction

According to the model of droplet motion discussed in Chapter 2.2.4, where the vapor flow under a droplet is responsible for the rectified motion on a millimeter scale ratchet surface in the Leidenfrost regime (Linke, Aleman et al. 2006), various parameters including the thickness of vapor layer (h), pressure gradient of vapor along the surface of ratchets ($\frac{\partial P}{\partial x}$), viscosity of the vapor (μ), initial velocity of droplet ($v_{droplet}$), droplet area interacting with ratchets (A_{eff}) and aspect ratio (depth-to-period) of ratchets, influence the motion of droplet (Linke, Aleman et al. 2006; Taormina 2006). Among the various factors, this Chapter especially focuses on the period of ratchets which ranges from 800 nm to 1.5 mm while maintaining the aspect ratio similar to each other. Table 4.1 summarizes experimental parameters used in this Chapter.

Table 4.1 Experimental parameters in Chapter 4.

Subject	Parameter
Ratchet material	Brass (Br), Nickel (Ni)
Ratchet size	p: 800 nm (Ni), 15 (Br), 75 (Br), 150 μm (Br), 1.5 mm (Br)
Ratchet ratio	$d : p$ = 1 : 4 (Ni ratchets) or 1 : 5 (Br ratchets)
Temperature (T_s)	Room temperature - 350 ℃
Liquid type	DI water, acetone, IPA, R134a
Volume of liquid	3 - 6 μL (R is smaller than a)
Surface treatment	With and without fluorinated silanes

4.2 Structural Analysis for Miniaturized Ratchets

Prior to the study of impact and motion of droplet, morphologies of the fabricated ratchet surface were inspected using various metrology tools such as optical microscope, surface

profilometer, scanning electron microscope (SEM) and atomic force microscope (AFM). Figure 4.1 shows definition of ratchet dimensions used in this study. *l* and *h* represent the period and depth used to design and fabricate steps with micromilling while *p* and *d* are the period and depth for the final ratchets after backside planarization. Ratchet dimensions were obtained by measurements with a stylus or optical profilometer except for 800 nm period ratchets where AFM was used.

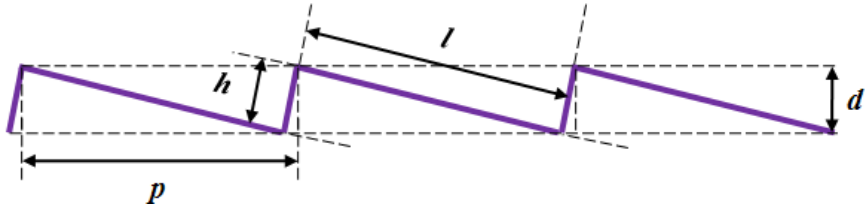

Figure 4.1 Ratchet dimensions to be used, where *d*, *p*, *h* and *l* are ratchet depth, ratchet period, step depth and step period with the slope of a certain ratchet angle.

Figure 4.2 (a) – (d) shows SEM images of micromilled brass ratchets with 1.5 mm, 150 μm, 75 μm and 15 μm periods, respectively. All SEM images were taken after tilting the sample stage with an angle of 17.5 °to observe the ratchet morphologies more clearly. The surface morphology of nickel ratchets with 800 nm period, replicated from optical gratings, is presented in figure 4.3 (e), observed by SEM and AFM. Figure 4.3 (f) shows a photograph of the 800 nm Ni ratchets (*p*: 800 nm, *d*: 200 nm and size: 5.1×5.1×0.2 cm^3) after completing post-plating processes. In addition to ratchet structures with a saw-tooth profile, surface roughness is clearly visible.

The root mean square roughness for brass surfaces produced by the micromilling process was usually 150 − 300 nm (Kim, Murphy et al. 2008), which is the case for the slowly-inclined side of the micromilled ratchets. The surface roughness on the highly-inclined side of ratchets is usually higher than that on the slowly-inclined side. Even some milling marks in the direction of ratchet gratings are seen in the SEM images. Further inspection of the ratchets was carried out using a stylus surface profilometer (contact type, Tencor P-11).

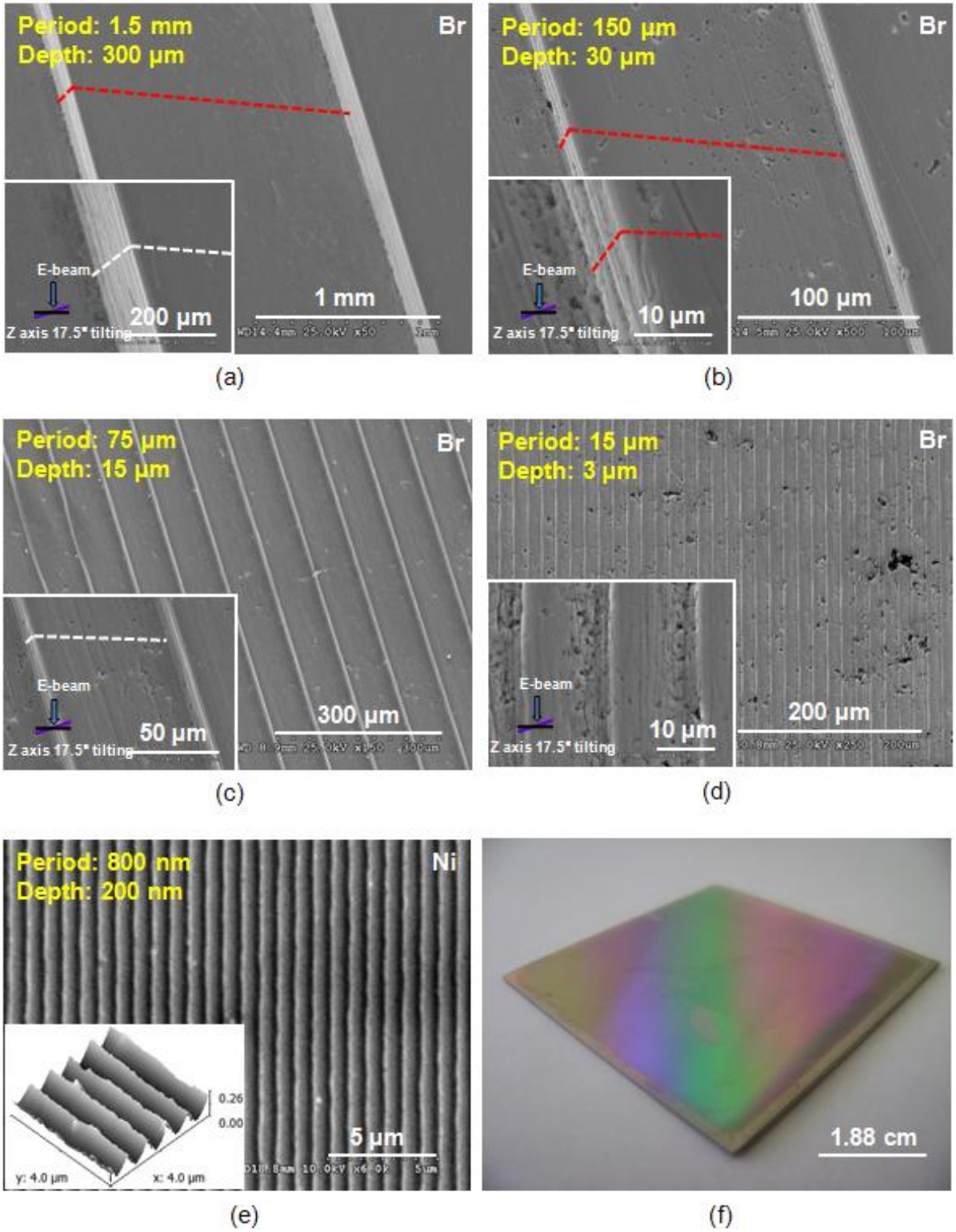

Figure 4.2 (a) – (d) Scanning electron micrographs of micromilled brass ratchets with their periods of 1.5 mm, 150 µm, 75 µm, and 15 µm, respectively, which have depth to period aspect ratio 1:5. (e) Scanning electron, atomic force micrographs and (f) photograph of replicated nanometer scale ratchets with their period 800 nm and depth 200 nm.

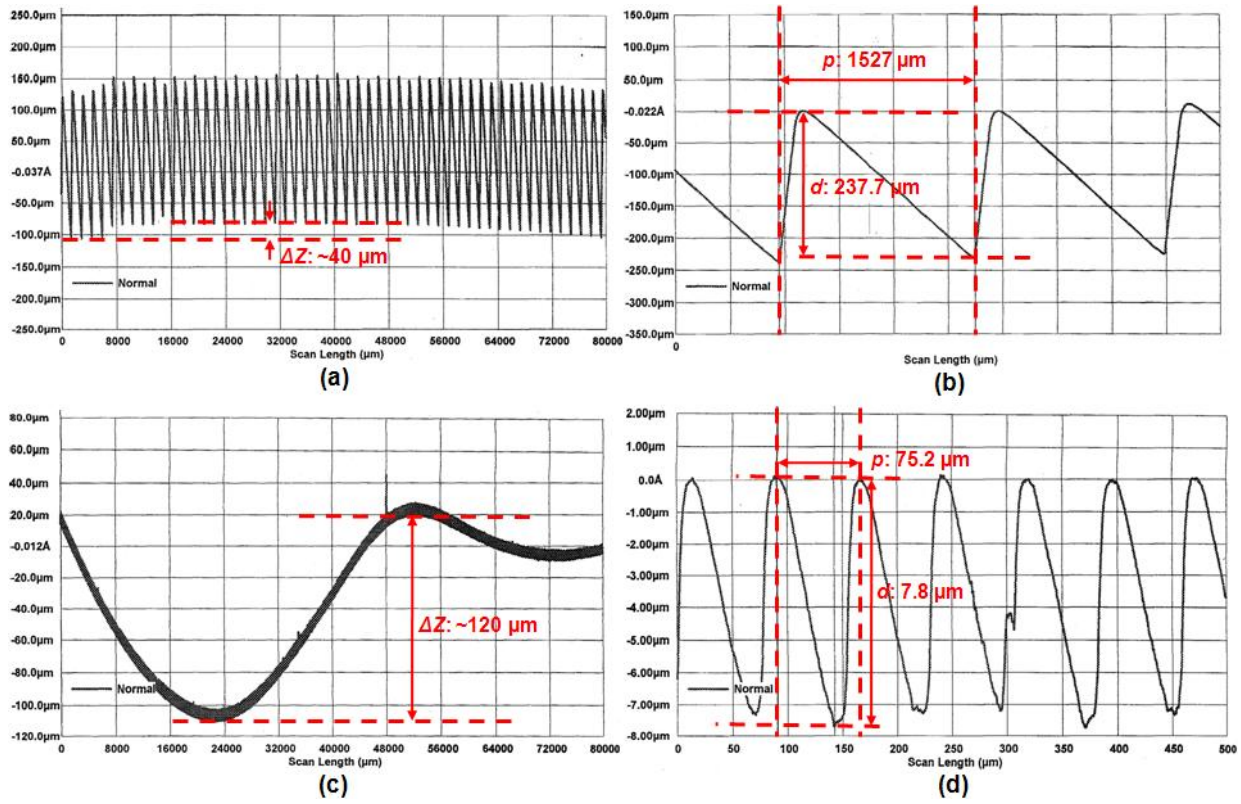

Figure 4.3 Surface morphologies of Br 1.5 mm (a) and (b), and 75 μm period of ratchets (c) and (d) scanned by stylus surface profiler (Tencor P-11). *ΔZ* is defined as the maximum vertical variation for overall sample size.

Figure 4.3 shows examples of cross-sectional profiles for two brass ratchets with 1.5 mm (a), (b) and 75 μm (c), (d) periods. For each sample, one large scan over the entire ratchet surface (with scan lengths of 4 cm for 800 nm ratchets and 8 cm for other micromilled ratchets) and one high resolution scan over reduced area were made. From the measured large scan profiles, maximum vertical variations (*ΔZ)* were obtained as the differences between the maximum and minimum heights. The ratchet dimensions *l*, *h*, *p*, and *d* were deduced from high resolution surface profiles.

Table 4.2 summarizes the dimensions of miniaturized ratchets designed and measured after fabrication. Each value in the table was obtained by averaging from three different measurements. As mentioned in Chapter 3, it is easier to fabricate steps on a tapered substrate rather than

directly produce ratchet structures in micromilling process. The periods designed for the steps in micromilling (l) are 15, 75, 150, and 1500 μm, with the step height (h) determined in order to keep the ratio of h/l constant at 0.2.

Table 4.2 Surface morphologies of miniaturized ratchets fabricated by micromilling or replication process. ΔZ has varied scan lengths due to the different sample sizes: 4 cm for sub-microratchets with 800 nm period and 8 cm for all others.

Sample name	Designed					Measured						
	l **(μm)**	***h*** **(μm)**	***p*** **(μm)**	***d*** **(μm)**	***d/p***	***l*** **(μm)**	***h*** **(μm)**	***p*** **(μm)**	***d*** **(μm)**	***d/p***	***ΔZ*** **(μm)**	***RMS*** **(μ-inch)**
800 nm	−	−	0.8	0.2	0.25	−	−	0.8	0.2	0.25	~85	2.2
15 μm	15	3	15.3	2.9	0.19	15.3±0.4	2.7±0.1	15.3±0.2	2.4±0.2	0.16	~140	33.7
75 μm	75	15	76.5	14.7	0.19	75.4±0.0	12.9±0.2	76.7±1.1	12.0±0.1	0.16	~120	169.9
150 μm	150	30	153	29.4	0.19	146.0±0.6	27.7±0.1	150.4±1.8	24.3±1.6	0.16	~100	336.8
1.5 mm	1500	300	1529.7	294.2	0.19	1486±13.1	281.5±8.1	1499±15.7	230.5±2.3	0.15	~40	3346.2

The measured depth (d) and period (p) of fabricated ratchets after backside planarization were slightly deviated from the designed values due to uncertainties and errors involved in different fabrication steps. The measured aspect ratio values were also varied slightly, showing 0.25, 0.16, 0.16, 0.16 and 0.15 for the ratchet periods of 0.8, 15.3±0.2, 76.7±1.1, 150.4±1.8, and 1499±15.7 μm, respectively, but they were still in the similar range around 0.2. Sample names (most left column in table 4.2) will be used to identify ratchets dimension as a matter of convenience from now.

Despite slight variations between designed and measured ratchet dimensions, the saw-tooth like ratchet shape is clearly visible, enough for a droplet bottom to see the effect of the asymmetric structure, thus rectifying motion of the droplet levitated by vapor. Vertical variations for the sample surfaces (ΔZ) generated by series of milling process including backside planarization, were low, in the range of 40 − 140 μm over 4 or 8 cm scanning length. Thus, the

influence of the surface slope on the droplet motion can be neglected.

4.3 Characteristics of Leidenfrost Droplets on Miniaturized Ratchets

4.3.1 The Influence of Surface Temperature and Ratchet Period

With the fabricated ratchets of various periods, a systematic study to understand the influence of ratchet surface on droplet put on the surface in elevated temperatures was carried out. A ratchet sample was heated to a temperature on a hot plate and then droplets were dispensed from a commercial micropipette (Eppendorf, adjustable range of volume: $1 - 10$ μL) at a distance of $1 - 3$ mm from the ratchet surface. The droplet behavior on the ratchets was characterized by a video camera (Sony DSC-V1, 16 fps). For experimental details, see Chapter 3.4.1 and 3.4.3.1.

When the ratchet surface temperature is low, a droplet put on the ratchet surface was spread and remained at or near the same location, forming a certain contact angle at the three phase (droplet/air/ratchet) interface region depending on their surface energies and surface roughness. A rectified motion of the droplet starts to occur when the temperature of the ratchet surface reaches a critical temperature. We define this temperature as the threshold temperature (T_{th}) for droplet motion. T_{th} is usually close to but not necessarily same as the Leidenfrost temperature (T_L) of the liquid, which is defined as the temperature where the droplet lifetime is the longest. In the Leidenfrost regime, a liquid droplet on a hot surface produces an insulating vapor layer around it, keeping the droplet from boiling rapidly. For water, T_L was reported to be in the range of $155 - 515$ ℃, depending on solid material, surface cleanness and surface roughness (Bernardin and Mudawar 1999). While the rectified motion was driven by a saw-tooth shaped surface topology, the vapor layer provides the fluctuating force vertical to the ratchet surface to overcome the pinning of droplet to the surface.

Figure 4.4 shows an example of a video sequence for the motion of a 5 μL DI water droplet

on a 1.5 mm period brass ratchets at a ratchet surface temperature of 254 ℃. The mean droplet velocity was calculated simply by dividing moving distance by time. The moving time is defined as the time interval from the point when the droplet starts to move to the point just before the droplet escaped from the ratchets. The mean droplet velocity for a specific experimental condition was obtained by averaging the droplet velocities of 10 droplets.

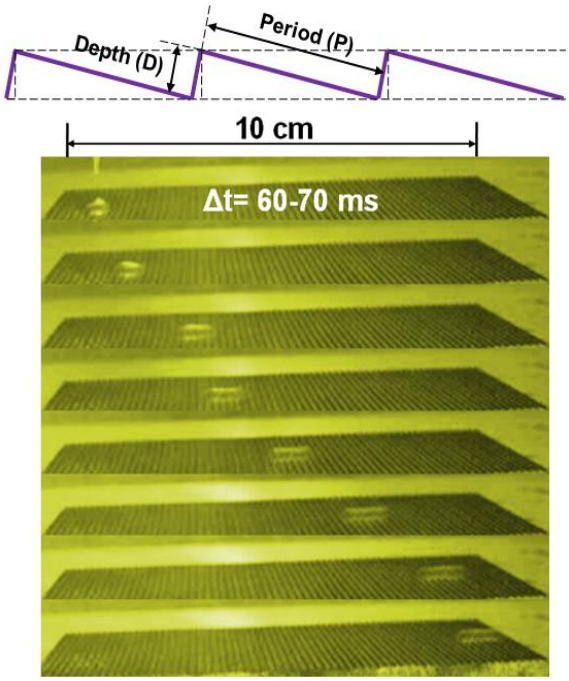

Figure 4.4 A video sequence (time interval: 60 – 70 ms) of a 5 μL droplet of DI on a horizontally leveled, brass macro ratchets with 1.5 mm period and 0.3 mm depth at 254 ℃.

Figure 4.5 shows the mean velocity for the motion (v_m) of 5 μL DI water droplets as a function of surface temperature (T_s) for different ratchet periods. As T_s increases beyond T_{th} for droplet motion, v_m first increases, reaches maximum, and then decreases until it attains almost a constant velocity. Regarding the dependence of ratchet period (p), two regimes can be distinguished. At relatively low T_s above T_{th} (L regime), a dramatic increase in v_m was observed with the decrease in p. It even reached over 40 cm/s for the ratchets with p = 800 nm. Such propulsion is unprecedented with any droplet motion driven by a surface tension gradient and

topological ratchets without external force application. The droplet velocities achieved with such surfaces have been in the range from a few mm/s (Chaudhury and Whitesides 1992; Daniel, Chaudhury et al. 2001; J. Yang, G. Mo et al. 2002; Stroock, Ismagilov et al. 2003) to a few cm/s (Dossantos and Ondarcuhu 1995; Linke, Aleman et al. 2006). Even in the cases of directly applying external forces on periodically asymmetric surfaces including mechanical vibration (Buguin, Talini et al. 2002; Shastry, Case et al. 2006; Ding, Song et al. 2007; Shastry, Taylor et al. 2007), light source (Ichimura, Oh et al. 2000) or electric field (Buguin, Talini et al. 2002; Duncombe, Kumemura et al. 2009), velocities above 10 cm/s have never been achieved so far because of the strong interaction between droplet and the surface. This thermally driven droplet pumping results using vapor flow as a driving force, clearly indicate that micro and nanometer scale ratchets dramatically enhance propulsion of liquid motion and thus are a good candidate as a propulsion mechanism.

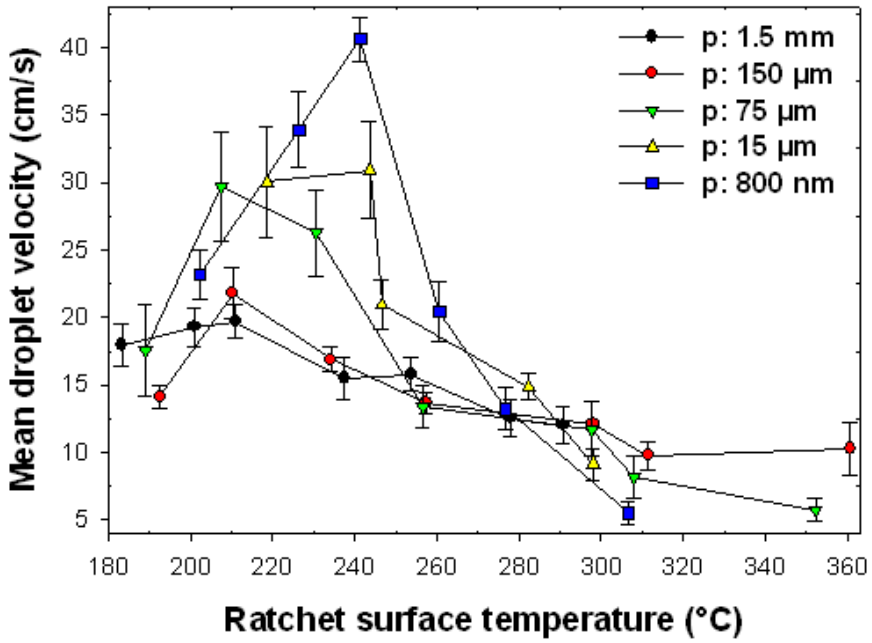

Figure 4.5 Mean droplet velocity of 5 µL DI water droplet motion (v_m) as a function of ratchet surface temperature (T_s) for ratchets with different periods (p).

However, when T_s is much higher than T_{th} (*H* regime), *p* does not enhance the mean droplet velocity v_m, instead maintaining constant values of a few cm/s. This is in agreement with the velocity value reported previously with millimeter scale ratchets (Linke, Aleman et al. 2006; Taormina 2006). These two regimes were also observed for other liquids including acetone (T_b = 52 ℃) and isopropyl alcohol (IPA, T_b= 82 ℃), which will be discussed precisely later (in section 4.3.5).

We propose a model to explain the droplet behavior of the two regimes whose schematics are shown in figure 4.6. The dependence of v_m on the ratchet *p* for the *L* regime can be understood by assuming that the droplet is almost in contact with top edges of the ratchets. This is justified because the droplet would not be fully supported by vapor or the vapor layer would be very thin in this relatively low temperature range. Due to the enhanced heat transfer through the direct local contacts or very thin vapor film, the liquid droplet evaporates mainly right above the peaks of the ratchets. The evaporated vapor is then split by the peak, flows down the two sides into the trenches, and then escapes along the trenches. The vapor on the less inclined side exerts more shear stress on the droplet bottom than that on the steeply inclined side. The enhanced heat transfer at the contacts, which was confirmed by observing nucleate boiling of liquid nitrogen droplet at a tape edge (Linke, Aleman et al. 2006), also enhances the thermocapillary flow along the bottom surface of the droplet, which reduces shear stress at the droplet/vapor interface. However, the thermocapillary effect is expected to be less effective for smaller ratchet periods because the temperature gradient along the bottom surface of the droplet also decreases. Therefore, a single ratchet generates a net driving force on the droplet and the total driving force will depend on the number of ratchets beneath the droplet.

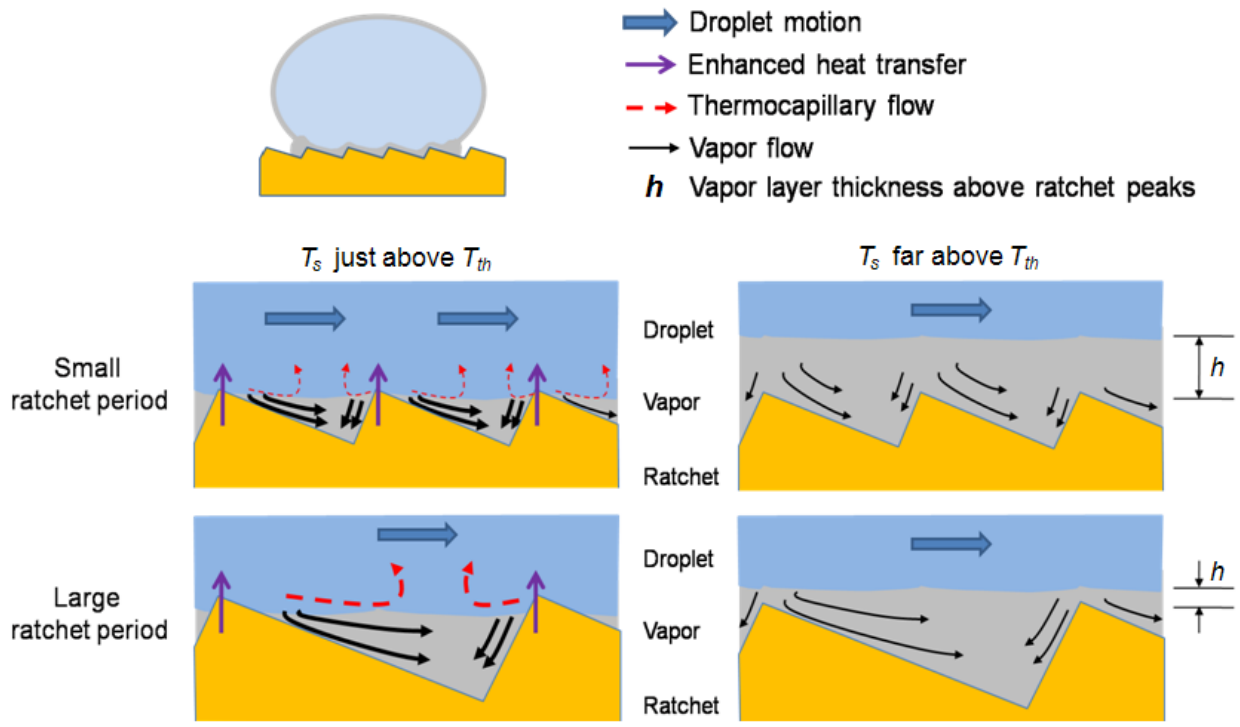

Figure 4.6 Schematics at the droplet/vapor/ratchets interface for two different temperature regimes; *L* and *H* regimes.

For the *H* regime, the vapor film beneath a droplet is thick enough to levitate droplet completely on ratchets (for 5 μL droplet, *h*: 38.7 μm at 300 ℃ and 44.0 μm at 400 ℃ by (Wachters.Lh, Bonne et al. 1966)). According to theoretical studies (Prat, Schmitz et al. 1995; Nagai and Nishio 1996; Bernardin and Mudawar 1999; Bernardin and Mudawar 2002), the presence of surface roughness significantly affects the flow field of the vapor underneath a fully levitating droplet mainly in three ways: first, the vapor flow penetrates into the roughness cavities and recirculation develops at the bottom of each cavity; second, as the size of the droplet relative to the size of the roughness element increases or as the size of the roughness element decreases while keeping the droplet volume constant, the thickness of the vapor layer (*h*) above the rough surface increases; and third, T_L increases. Thus, even though the increase in the number of ratchets may affect the droplet motion in a positive way, this will be cancelled by the negative effect of increasing vapor layer thickness above the ratchet peaks. This accounts for the

droplet behavior at the higher temperature regime in which no dependence of p was observed. In H regime, thermocapillary flow on the bottom of the droplet may exist but is negligible because the presence of a thin vapor layer diminishes the temperature gradient along the bottom of the droplet. The resistance of vapor flow underneath the droplet increases due to the increased vapor viscosity at higher temperature (Latto 1965), which is shown in the reduced saturated v_m of a few cm/s in H regime as compared to v_m in L regime.

Figure 4.7 shows the threshold temperatures (T_{th}) and ratchet surface temperatures (T_s) with maximum horizontal velocities (v_{max}) as a function of ratchet period (p). Both temperatures are the highest with 15 μm period brass ratchets. All other brass ratchets (p: 75 μm, 150 μm and 1.5 mm) have negligible variations (for T_{th}: ~ 9 ℃ and for T_s with v_{max}: ~ 3 ℃). One reason for higher temperature values of T_{th} and T_s with v_{max} from 15 μm period ratchets is believed to be induced by surface defects like undesirable cavities, which is supported by SEM images in figure 4.2. Another possible reason might be due to the surface roughness related with smaller ratchet dimensions (averaged ratchets depth, d: 2.4±0.2 μm).

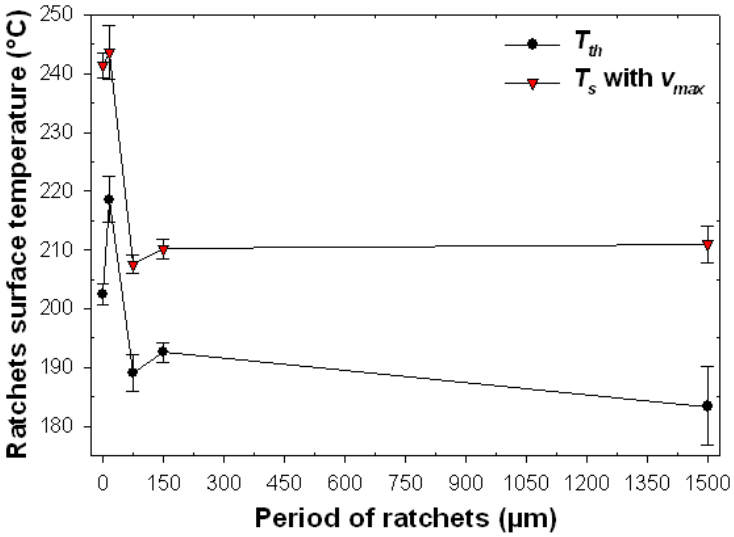

Figure 4.7 Threshold temperature (T_{th}) and surface temperature (T_s) with maximum horizontal droplet velocity (v_{max}) as a function of ratchets period.

Figure 4.8 plots v_{max} as a function of p. The increase in v_{max} follows a linear relationship with the logarithm of p. The contribution of each ratchet to the droplet motion was estimated simply by normalizing v_{max} by the effective number of ratchets underneath a droplet (N), which is shown in Figure 4.9. In calculating N, the droplet is assumed to be spherical except bottom area which is flat. This can be justified because the droplet radius (R ~ 1.06 mm) calculated from the dispensed volume is smaller than the capillary length of water at 100°C ($a = \sqrt{\gamma/\rho g}$ = 2.5 mm, where γ is surface tension, ρ density of water at 100°C and g the gravity). The flatten bottom area of the droplet in contact with the ratcheted surface is estimated to be ~ 0.51 mm^2, according to the effective area of levitating droplet $A_{eff} = 0.81\pi R^4/a^2$ for $R \leq a$ (Aussillous and Quere 2001; Biance, Clanet et al. 2003). From the calculated effective area A_{eff}, we can obtain the diameter of the circular perimeter based on the flat bottom area of the droplet in contact with the ratcheted surface, which indicate effective length of vapor layer underneath a droplet (l ~ 0.81 mm). Since the contact area is circular from the top view and the contribution of each ratchet to the motion is different depending on the location of the ratchet, every N with various p was achieved by normalizing the number of ratchets under the length by $\frac{A_{eff}}{l^2}$ (≈ 0.78). The values are given in table 4.3, which are used to normalize the mean droplet velocity to roughly estimate the contribution of each ratchet to the droplet motion.

It is reasonable that higher v_m is from smaller kinetic friction force. The kinetic friction force is proportional to the friction coefficient μ and normal force exerted between the contact surfaces. The normal force should be constant because 5 μL DI droplets are uniformly used. Therefore, μ is critical factors for varied values of v_m. If the surface is smooth enough to be considered as plain one, the friction force does not matter with surface area. However, for rough surface, μ significantly decreases with the increase in surface roughness (Elleuch, Elleuch et al. 2007). In

the case of ratchets, surface roughness decreases with shorter p or d. Thus, the net A_{eff} beneath the droplet significantly increases with the decrease in p. Thus v_{max} of nano ratchets is much faster than those of micro and macro ratchets due to its small amount of friction in the low temperature regime.

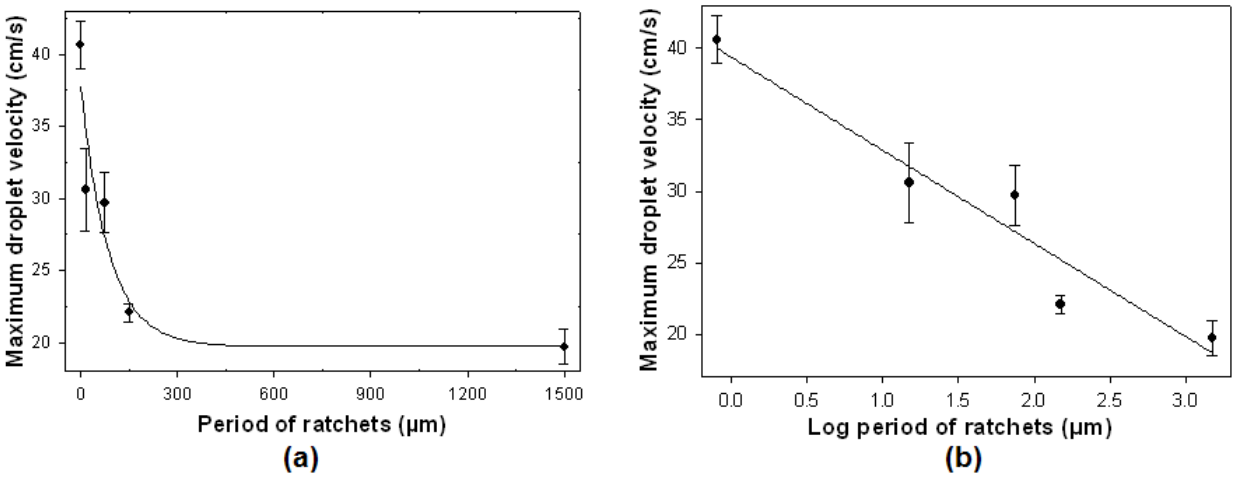

Figure 4.8 (a) Maximum droplet velocity (v_{max}) as a function of ratchet period. (b) A best logarithmic fit gives $v_{max}\left(\frac{cm}{s}\right) = -6.62 \times \log p(\mu m) + 39.37$.

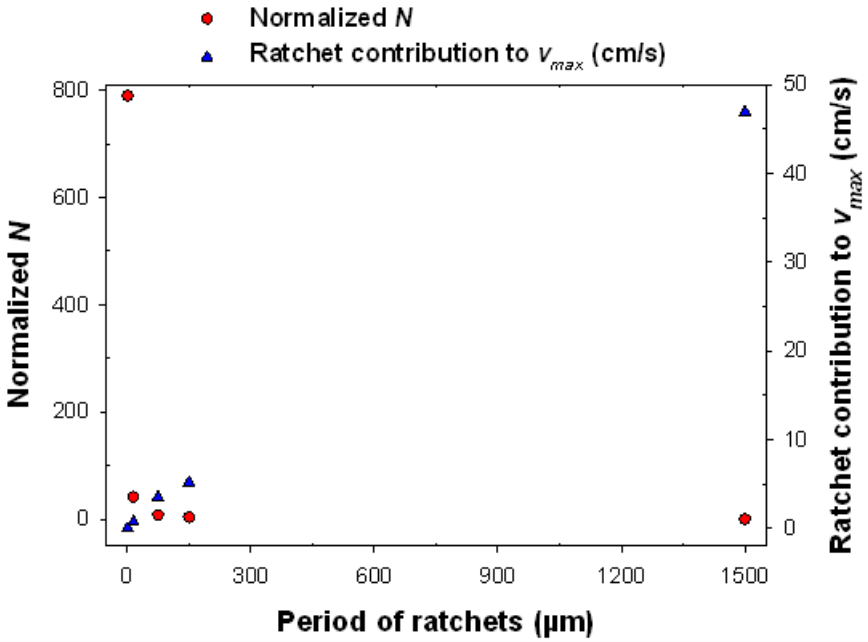

Figure 4.9 Normalized effective number of ratchets underneath a droplet and corrected velocity contribution from each ratchet to v_{max} as a function of ratchet period.

Table 4.3 The effective number of ratchets for different ratchet periods used to normalize the maximum velocity.

p (μm)	v_{max} (cm/s)	N in l	Normalized N	Ratchet contribution
0.8	40.60	1012.5	789.75	0.05
15	30.93	54	42.12	0.73
75	29.69	10.8	8.42	3.53
150	21.77	5.4	4.20	5.18
1500	19.71	0.54	0.42	46.93

The contribution of each ratchet to the overall droplet motion decreases linearly with decreasing p from millimeter to sub-micron scales. This is attributed to friction occurring while the vapor escapes from the bottom of the droplet along the ratchet trenches. The effective area for the triangle formed between the ratchet trenches and the droplet bottom surface through which the vapor escapes, decreases, as p decreases, resulting in an increase in friction and consequently a decrease in the contribution of each ratchet to the overall droplet motion (Ornatskii 1965). Nevertheless, the significant increase in the overall droplet velocity with decreasing ratchet period suggests that a decrease in the ratchet period to the real nanoscale may further increase propulsion of the droplet motion until the droplet sees the ratchets as a flat surface. Thus, it will be an interesting research topic to investigate the minimum ratchet period that still shows the propulsion of liquid droplets, which may depend on the aspect ratio, surface roughness, and wetting behavior of ratchets as well as the types of droplets. However, production of large area, nanoscale ratchets with defined geometries is still a great challenge and needs to be developed in order to pursue the limitation in the use of nanoscale ratchets for driving droplet motion.

4.3.2 The Influence of Droplet Volume

The influence of droplet volume on the motion of Leidenfrost droplets was investigated with micro ratchets. According to the observation on Leidenfrost droplets on a flat surface, the shape of droplets and the thickness of the vapor layer (h) are critically dependent on the size of droplets (Biance, Clanet et al. 2003; Linke, Aleman et al. 2006). Various volumes of droplets in the range of $3-6$ μL (corresponding to droplet radii R of $0.89-1.13$ mm) could be manipulated with the micropipette used. There are two factors that need to be considered regarding the volume of droplets: the capillary length of droplet and the size of ratchets underneath droplet. For a DI droplet, 65 μL is the critical volume corresponding to its capillary length a of 2.5 mm at its boiling temperature. When the droplet radius is smaller than a, the lateral shape of the droplet is almost spherical except at the bottom because surface tension of the droplet governs, which is the case for our experiments. They evaporate through the entire droplet surface. For the droplet radius larger than a, the droplet looks like a pancake or puddle flattened by their gravity. Evaporation occurs mostly through their bottom surface with lower evaporation rate than that of smaller droplets. For both of cases, h increases linearly as the droplet size increases. Another factor for droplet volume is that the droplet should be large enough, so that the droplet bottom covers at least one entire ratchet in order to induce unidirectional motion. This condition is met because the diameter for the smallest droplet volume used (2×0.89 mm for 3 μL volume) is still larger than the largest ratchet period of 1.5 mm.

Figure 4.10 (a) and (b) show mean velocity of DI droplets with different volumes ($3-6$ μL) as a function of surface temperature T_s for two brass micro ratchets and one macro ratchets with 75 μm, 150 μm and 1.5 mm period, respectively. In all temperature regimes, the effect of the droplet volume on v_m was negligible within the accuracy of the measurement. Intuitively one

could think that v_m increases with the increase of droplet volume because of the increased effective number of ratchets within the effective length. However, this effect seems to be cancelled out by the increase in the mass of the droplet to levitate.

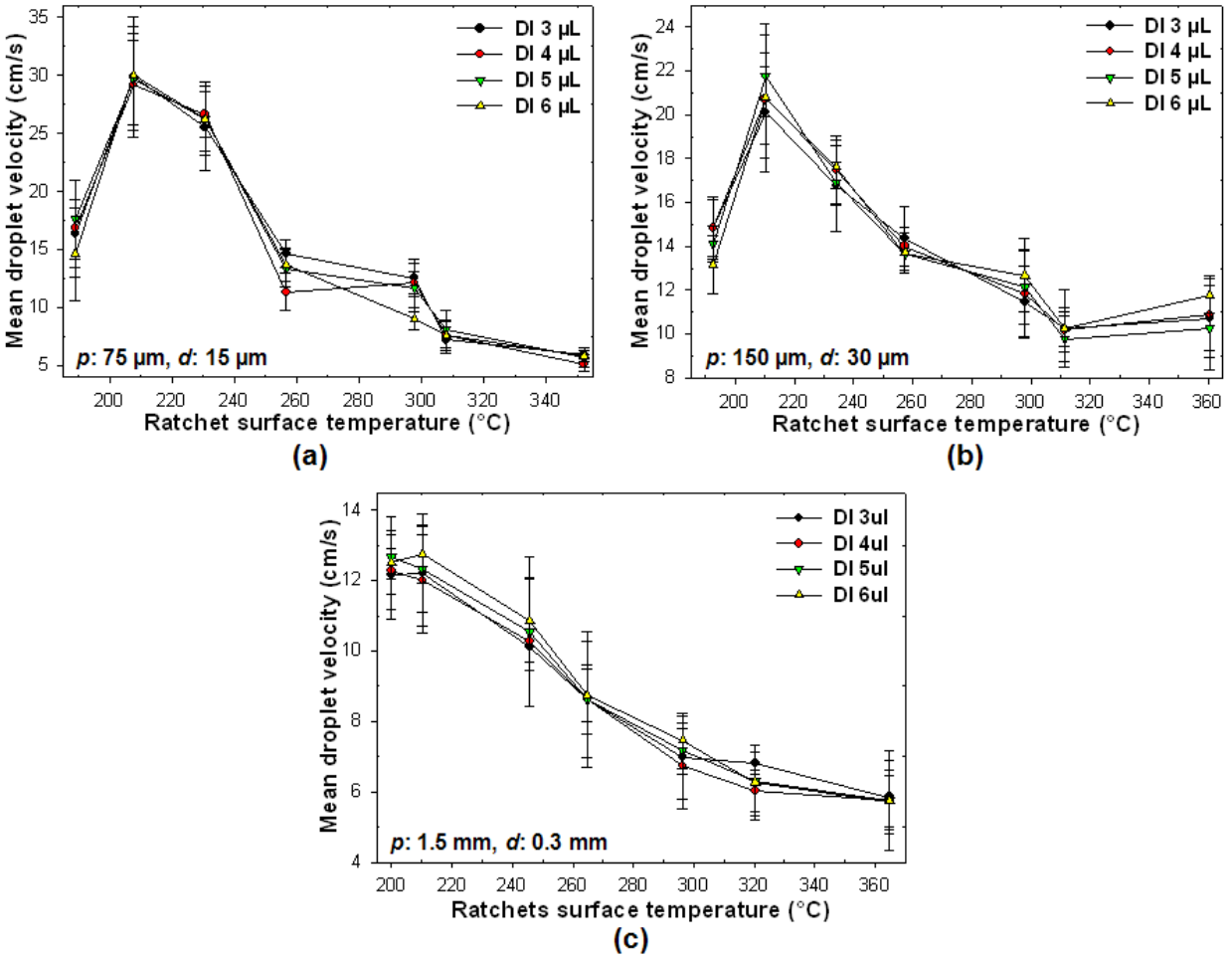

Figure 4.10 The influence of droplet volume on the motion of droplet: (a) v_m as a function of T_s for different DI droplet volumes in the range of 3 − 6 µL on brass micro and macro ratchets with 75 µm p, (b) with 150 µm p and (c) with 1.5 mm p.

Table 4.4 shows various parameters of levitating droplets for different desired volumes (3 − 6 µL) on micro ratchets with 75 µm and 150 µm periods. The calculated values were based on desired droplet volume. The experiment to evaluate the pipette accuracy in figure 3.11 showed that the measured DI droplet volume were in the range of 4 − 6 µL. The effective number of ratchets within the effective length (N in l) increases with increasing droplet size; $\Delta N_{p:75\,\mu m}$ in l and

$N_{p:150\mu m}$ in l are 4.54 and 2.26, respectively, for different desired volumes (3 − 6 μL). When the normalized effective numbers of ratchets within effective length are considered for both micro ratchets, there are considerable variations in the normalized $\Delta N_{p:75\mu m}$ (3.62) and $\Delta N_{p:150\mu m}$ (1.80) for different desired volumes (3 − 6 μL). However, v_m values obtained by droplet experiments in figure 4.9 have negligible variations for varied droplet volumes. The acceleration factor by the increasing effective number of ratchets within the effective length seems to be offset by increased resistance due to the increased mass and vapor layer thickness for larger droplets (Biance, Clanet et al. 2003).

Table 4.4 Various parameters of levitating droplets for different desired volumes (3, 4, 5 and 6 μL) on micro ratchets with 75 μm and 150 μm period.

Parameters\droplet volume	**3 μL**	**4 μL**	**5 μL**	**6 μL**
R **(mm)**	0.89	0.98	1.06	1.13
A_{eff} **(mm^2)**	0.26	0.38	0.51	0.66
l **(mm)**	0.58	0.70	0.81	0.92
$\frac{A_{eff}}{l^2}$	0.77	0.78	0.78	0.78
$N_{p:75\mu m}$ **in** l	7.73	9.33	10.80	12.27
normalized $N_{p:75\mu m}$ $(\frac{A_{eff}}{l^2})$	5.95	7.28	8.42	9.57
$N_{p:150\mu m}$ **in** l	3.87	4.67	5.40	6.13
normalized $N_{p:150\mu m}$ $(\frac{A_{eff}}{l^2})$	2.98	3.64	4.21	4.78

4.3.3 The Influence of Surface Wettability

In order to investigate the influence of surface wettability on droplet motion, the ratchet surface was coated with a fluorinated silane molecule 1H,1H,2H,2H−Perfluorodecyltrichlorosilane ($C_{10}H_4Cl_3F_{17}Si$), which consists of a head group with three chlorosilanes and a fluorinated, long carbon chain (C_{10}). The fluorinated silane coating

reduces wettability of the ratchet surfaces. In other words, their hydrophobicity increases with the silane coating. In order to evaluate the effect of the silane coating, water contact angles were measured for all the prepared miniaturized ratchets with and without hydrophobic surface treatment at room temperature.

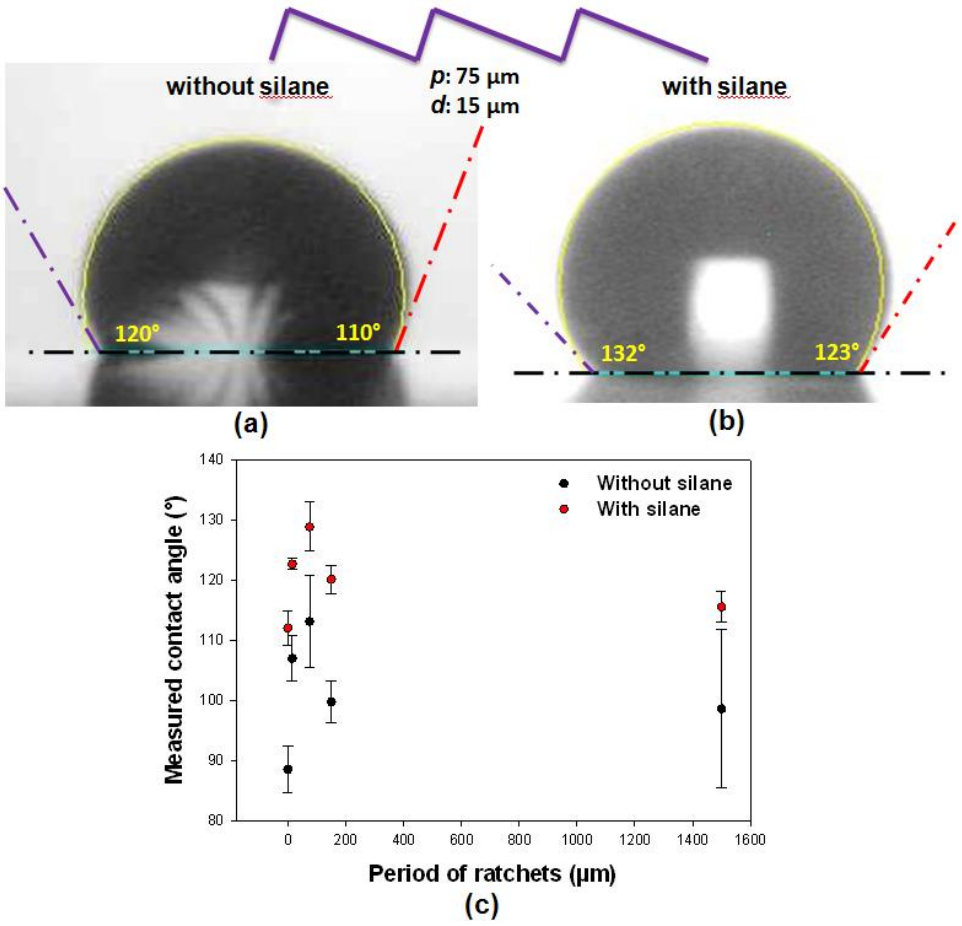

Figure 4.11 The result of contact angle measurement by FTA 125. The micrograph images are lateral views of DI 5 µL droplet on top of micro ratchets (*p*: 75 µm), (a) is from without silane, and (b) from with silane at room temperature. (c) The average contact angle values as a function of period of ratchets (*p*: 15 µm, 75 µm, 150 µm and 1.5 mm) for with and without fluorinated silane. Note that plain brass surface was considered as 0 µm period of ratchets.

Figure 4.11 (a) and (b) show an example of water contact angle change on the 75 µm period micro ratchets before and after the silane coating. The contact angles measured at the slowly inclined side of the ratchets (right side in the figure) are usually smaller than those at the steeply inclined (left side in the figure) side. Microscopically, the contact angle at both sides of the

water/air/surface interface should be the same. However, the geometrical asymmetry due to ratchets leads to different macroscopic contact angles that are measured by assuming a horizontal base line for the solid surface. Figure 4.11(c) shows the static contact angles of DI water droplets on top of various ratchet surfaces. The photographs taken during contact angle measurements show that water completely fills grooves of the ratchet, indicating a Wenzel's state. Significant increase in hydrophobicity on the ratchet surface was achieved after the coating with almost uniform increase of the contact angles by ~ 20 ° for all measured ratchets. The maximum contact angle was observed on the brass ratchets with 75 μm period regardless of the presence of the silane coating.

Then, the influence of surface wettability on the motion of Leidenfrost droplets was investigated. Figure 4.12 (a) plots the average velocities (v_m) of 5 μL DI droplet motion as a function of surface temperature (T_s) for 1.5 mm period ratchets (p: 1.5 mm, d: 0.3 mm) with and without hydrophobic silane coating. The impact of surface wettability was different for the two temperature regimes (L and H regime). The hydrophobic coating significantly affects the droplet motion in the L regime, decreasing T_{th} by ~ 30 ℃ and increasing the maximum velocity by ~ 4 cm/s. The maximum velocity appears at a lower surface temperature. In the H regime, there was no effect of the fluorinated silane coating on v_m. Figure 4.12 (b) also shows the v_m profile of 5 μL DI droplet motion as a function of T_s for sub-micron ratchets (p: 800 nm period, d: 200 nm) with and without the silane coating. A similar behavior with that of 1.5 mm period ratchets was observed. The maximum velocity reaches even ~ 50 cm/s, showing an outstanding ability of pumping liquid without net potential. But in this case, the maximum velocity for the silane coated ratchets appears at higher temperature than that without silane coating, which is different from the case with 1.5 mm period ratchets.

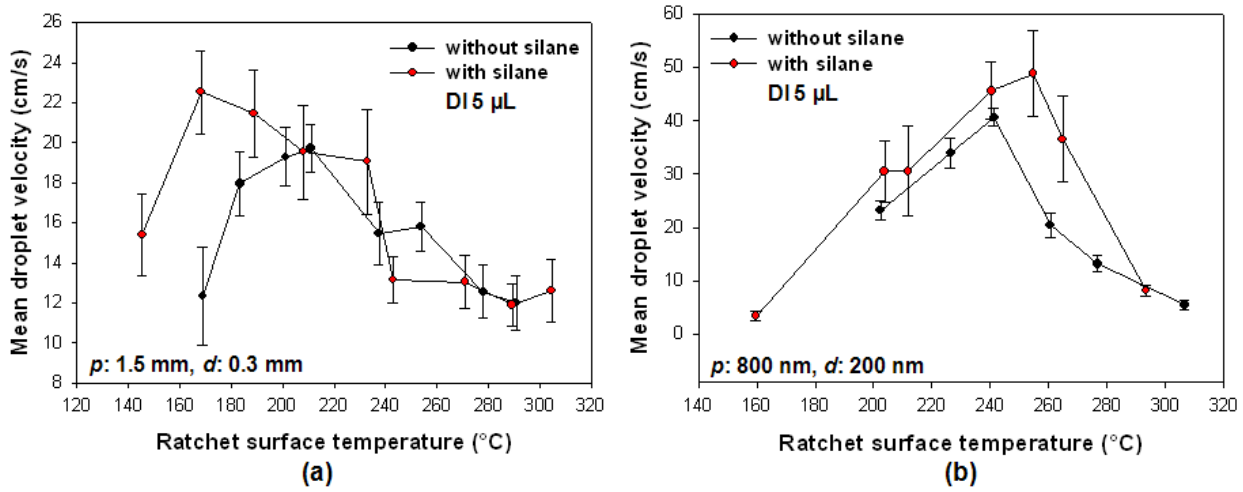

Figure 4.12 Mean droplet velocity of 5 µL DI water as a function of ratchet surface temperature (a) on 1.5 mm period of Br ratchets and (b) on 800 nm period of Ni ratchets with and without hydrophobic silane coating.

Figure 4.13 shows v_{max} as a function of logarithm of period with and without silane coating for DI 5 µL droplets. The values of v_{max} on silane coated ratchet surfaces are always faster than those on the ratchets without silane coating by 2 – 8 cm/s. Prat et al. theoretically investigated the effect of surface tension on the flow field in the vapor layer for fully levitating droplets (Prat, Schmitz et al. 1995). They found that the round-off of the droplet due to surface tension does not serious affect the flow field. Thus, the significant changes in the behavior of droplet motion upon the silane coating occurring in the *L* regime can only be explained by the fact that there are direct contacts between the droplet bottom and ratchet edges, and this modifies the three phase interface line or contact angle, changing the behavior of droplet motion. Takata et al. reported that T_L decreases with the increase in water contact angle. They manipulated the values of water contact angle by illuminating ultraviolet (UV) light on sputtered titania (TiO_2) (Takata, Hidaka et al. 2005). They observed that T_L decreases by ~ 20 ℃ from ~ 160 ℃ to ~ 140 ℃ with the increase in θ from 30 ° to 90 ° ($\Delta\theta$: 60 °). They interpreted their observation of decreasing T_L upon increasing hydrophobicity due to the decrease in the area of direct contact between droplet and

surface at the collision. This agrees with our observation that T_{th} decreases upon a hydrophobic coating of ratchet surfaces in the *L* regime.

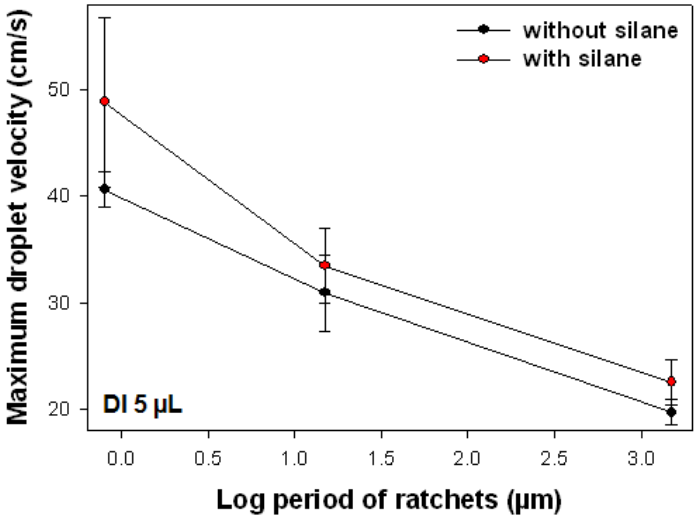

Figure 4.13 Maximum droplet velocities of 5 µL DI droplet as a function of log *p*.

In the *H* regime where the vapor layer thickness is large enough to fully levitate droplets, the change in surface tension does not make any influence, as predicted by Prat et al (Prat, Schmitz et al. 1995). This corroborates well with our model to explain the dependence of ratchet period on the droplet motion in Chapter 4.3.1.

4.3.5 The Influence of Liquid

Beside DI water, various liquids such as acetone, IPA and R134a were used to investigate motion of levitating droplets on miniaturized ratchets. Acetone and IPA are most popular solvents and R134a is a refrigerant. The physical properties of these liquids are given in table 4.5. Figure 4.14(a) shows the characteristics of the motion of acetone droplets on micro (*p*: 75 and 150 µm) and macro ratchets (*p*: 1.5 mm). Droplet volume used was 5 µL. The lateral shape of droplet is spherical except its bottom area, considering that the critical volume of acetone $V_{a,\ acetone}$ is 18.48 µL as shown in table 4.5. Overall, the v_m versus T_s curves show a similar behavior to that for DI water where v_{av} increases after T_{th}, reaches v_{max}, and decreases to a constant

velocity. The differences are three fold. First, v_{max} for various dimensions of ratchets was observed at slightly below 100 ℃. This is related to T_L of acetone. Second, the mean velocities (v_m) fall down sharply by increasing T_s only slightly above the temperature for v_{max}. Third, after v_m reach constant values, their variations are small. This observation means that the thickness of vapor film from acetone rapidly increases even with a small amount of superheat. This unique behavior might be due to the fast evaporation rate of acetone, which is highly volatile even at room temperature.

Table 4.5 Physical properties of liquids at their T_b (2004; Lide 2006). V_a is the critical volume of the liquid based on its a, which decides droplet shape as spherical or puddle.

Liquids\Properties	T_b (℃)	$\rho\left(\frac{\mathbf{kg}}{\mathbf{m^3}}\right)$	$\gamma\left(\frac{\mathbf{mN}}{\mathbf{m}}\right)$	a(mm)	V_a (μL)
Water	100	958.40	58.91	2.50	65.45
Acetone	56.0	747.06	19.65 (50 ℃)	1.64	18.48
IPA (2-propanol)	82.3	711.26	16.98 (75 ℃)	1.56	15.9
R134a	-26.1	1392.16	14.90	1.05	4.85

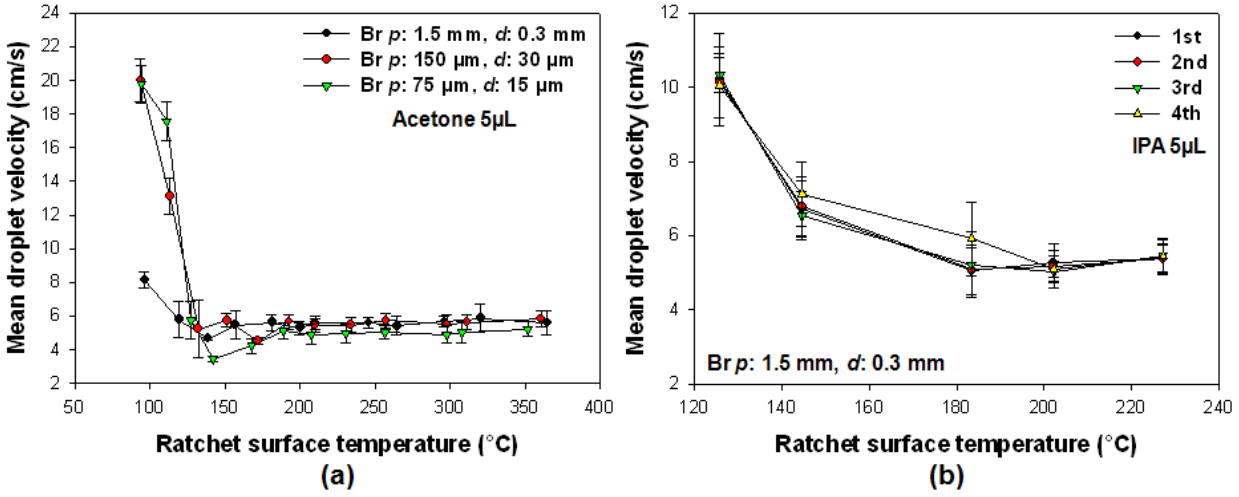

Figure 4.14 The motion of solvents droplets (5 μL): (a) v_m of acetone (T_b: 56.3 ℃) droplet as a function of T_s with micro and macro ratchets (p: 75, 150 μm and 1.5 mm) and (b) v_m of IPA (T_b: 82 ℃) droplet as a function of T_s with macro ratchets (p: 1.5 mm).

For IPA, a similar trend with that of acetone was observed with macro ratchets as shown in Figure 4.14 (b). Recurrence of the droplet motion was examined by repeating four cycles with the same droplet volume at each T_s. Each cycle is carried out with ten droplets and has a few minutes of time interval with the adjacent cycle. Almost negligible variations in average velocities of IPA 5 μL droplet motion for all different cycles were observed. The transition range from *L* to *H* regimes is short like acetone. The maximum average velocity of IPA droplets on macro ratchets is similar to that of acetone. Table 4.6 provides the comparison of maximum average velocities for different liquid droplets (for 5 μL) on various dimensions of ratchets. For both solvents, however, the directional motions of levitating droplets could not be observed for ratchet periods of 15 μm and 800 nm. Instead, droplets move randomly and slowly without direction, still keeping their levitation on top of those scales of ratchets.

Table 4.6 Maximum average velocities of different liquid droplets (5 μL) on various dimensions of ratchets.

Liquid\ $v_{max,\ p:\ x}$	**$v_{max,\ p:\ 75\ \mu m}$ (cm/s)**	**$v_{max,\ p:\ 150\ \mu m}$ (cm/s)**	**$v_{max,\ p:\ 1.5\ mm}$ (cm/s)**
Acetone	19.77±1.14	20.01±1.29	8.15±0.51
IPA	−	−	10.14±0.96
DI	29.69±3.98	21.77±1.87	19.71±1.19

Figure 4.15 shows the average velocity for R134a droplet motion at room temperature (T_s =25 ℃) as a function of ratchet period with and without a fluorinated silane coating. In the case of R134a, there was no directional motion of droplets only with 800 nm period of ratchets. The slowest motion of R134a droplet was obtained from 15 μm period brass ratchets. The maximum velocity appears with 75 μm period ratchets. Upon the silane coating, the droplet velocity increases by 2 − 5 cm/s. Both solvents and refrigerant have faster evaporation rates due to their higher volatilities. Therefore, the results indicate that there is a critical vapor layer thickness above

which the lateral vapor flow above the ratchet edges dominates over the asymmetric vapor flow within the ratcheted grooves and the droplet sees the surface as flat. Thus, the ratio of vapor layer thickness to ratchet depth seems to be the parameter to determine rectified motion of droplets.

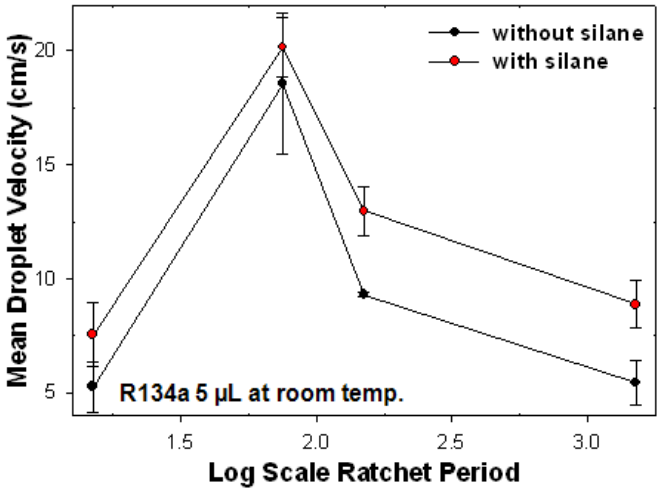

Figure 4.15 Average velocities of 5 µL R134a droplet as a function of log scale ratchet period at room temperature.

4.3.6 The Influence of Ratchet Material

Directional motion of Leidenfrost droplets was observed for the metal ratchets in the period range from sub-micrometer to 1.5 millimeter. However, when R134a droplets were put on ratchets made in polymer sheets which were fabricated by imprinting into poly(methyl methacrylate) (PMMA, glass transition temperature T_g= 95°C, 1/16″ thickness, Champion Plastics, LA) and Polycarbonate (PC, T_g=105°C, 1/16″ thickness, Champion Plastics, LA), or in a SU-8 (MicroChem., T_g>200°C after UV-cured) layer with the thickness larger than 100 µm coated on Si substrate, the droplet immediately spreads out and evaporates horizontally instead of forming Leidenfrost droplets and flowing with directional motion. Even after coating a thin metal (Au 30 nm/Cu 10 nm) on the polymer surface, Leidenfrost droplets of R134a could not be generated. This observation disagrees with Linke et al.'s observation that self-propelled

Leidenfrost droplet is independent of the ratchet material (Linke, Aleman et al. 2006). L. Melling observed motion of nitrogen droplets on plastic (Plexiglas or PMMA) macro ratchets (p: 1.5 mm, d: 0.2 mm) at room temperature for very short time around 0.3 second. Even though nitrogen droplets quickly evaporated on Plexiglas ratchets, the observed terminal velocities were in the range of 6 – 10 cm/s (Melling 2003). There are several possible reasons for this observation. For polymers, the levitating droplet cannot be generated due to their porous chain structures, poor thermal conductivities and the chain interaction which depends on liquid polarity.

4.4 Conclusions

A systematic study to understand the directional motion of levitating liquid droplets on the miniaturized ratchets was carried out with simple experimental apparatus. The motion of Leidenfrost droplets were characterized by mainly obtaining their mean velocities under various conditions. Regarding the dependence of ratchet period, two different regimes were distinguished. At the surface temperature just above the threshold temperature for droplet motion, v_m significantly increases with decreasing period of ratchets while in the higher temperature regime v_m remains constant at a few cm/s. These two regimes were also observed for other liquids including acetone and IPA. The hydrophobic coating of the ratchet surface significantly affects the droplet motion, decreasing threshold temperature for the droplet motion and increasing the maximum velocity. It has been observed that the directional motion of Leidenfrost droplets on all scale of metal miniaturized ratchets. However, for various polymer ratchets, the levitating droplet could not be generated due to their porous chain structures, poor thermal properties and the chain interaction depending on liquid polarity.

The results observed in this chapter show that driving levitating droplets using ratchets may be more effective in micro and nanofluidic environments because droplets are usually squeezed

by and thus touch the walls of micro and nanochannels. Thus, micro and nano ratchets can potentially be used as a component for micro and nanofluidic devices. One disadvantage of using the ratchet surface is the requirement of high threshold temperature. However, combining ratchets with superhydrophobic treatment (chemically, topologically or the combination thereof) may lower T_{th}, which may enable, for instance, droplet-based thermal cycling of biopolymers for amplification and ligation. The superhydrophobicity of the ratchet surface will also keep fluids from fully wetting micro and nanochannel surfaces, which is a prerequisite for this propulsion mechanism to work. An application with high operation temperature is envisioned in microscale heat pipes incorporated with nanoratchets as closed loop, two-phase cooling systems with no moving parts and no external power for microprocessors. Use of low boiling point materials such as R134 and liquid nitrogen will also allow room temperature operation. Broader applications are also found as a means of increasing efficiencies for film boiling heat transfer associated with droplets and spray by preventing stationary vapor films between the droplets and hot surface, such as fuel injection for combustion technology, stream generation for energy conversion in nuclear power energy converters, cooling systems for nuclear reactors, and spray quenching of heat treatable alloys. Transport of biomolecules such as molecular motor molecules is another interesting application with nano ratchets because fluctuation force will be provided via the transduction of chemical energy into mechanical work inherent to the motor molecules while the motion is rectified by the ratchets.

In summary, we have shown the effect of ratchet period down to sub-micrometer on the motion of water droplets dispensed on heated ratchet surfaces. The average droplet velocity significantly increased as the ratchet period decreased, reaching ~40 cm/s for sub-micron ratchets. The results suggest that even higher propulsion can be achieved with nanoscale ratchets and that nanoscale

ratchets can potentially be used as a mechanism to drive droplet motion in micro and nanofluidic environments.

Chapter 5 The Influence of Droplet Impact

5.1 Introduction

In Chapter 4, the motion of liquid droplets on miniaturized ratchets was systematically studied mainly by analyzing mean velocities of moving droplets, as obtained using a low resolution video camera, for various parameters such as ratchet dimensions, types of liquid, droplet size, surface temperature, and wettability. For sub-micron ratchets with the aspect ratio (*d/p*) of 0.25, a maximum mean velocity faster than 40 cm/s was achieved. Even though we could extract some valuable information with the primitive experimental apparatus used in Chapter 4, many important physics behind the droplet motion could not be captured due to the limitation of the experimental setup used. The low frame rate, slow exposure time and auto-focusing function of the camera used in the primitive experimental setup often made the images blurred and misty. The droplet generation and injection by manual micro-pipetting could not guarantee the consistent droplet volume and released height, which might affect the droplet mobility. Therefore, an enhanced experimental setup for both recording and injection system was developed. The recording system was replaced by a high speed camera system with a maximum frame rate of 1000 fps and a minimum expose time of 50 μs, which enabled more clear and precise capturing of mobile droplets. For the injection system, a programmable syringe pump and various dimensions of needles are connected with a flexible fitting system. For accurate and efficient data extraction, image processing tools were developed to extract meaningful information from the captured raw images of moving droplet along the ratchets.

The main objective of this chapter is to in-depth study of the behavior of droplet impact and motion on miniaturized ratchets using the enhanced experimental setup. The focus on this chapter will be to examine the reproducibility of the results by the enhanced experimental setup,

to investigate the influences of droplet impact speed as well as the polymer additive on the droplet motion. Parametric studies for various ratchet dimensions will be shown in the next chapter. Table 5.1 shows a summary of experimental parameters used in this chapter.

Table 5.1 Experimental parameters in Chapter 5.

Subject	Parameter
Ratchet material	brass, nickel
Ratchet size	p: 75 μm (brass), 150 μm (nickel),
Ratchet aspect ratio	$d : p = 1 : 5$
Surface temperature	From room temperature to 350 ℃
Liquid type	DI water, PEO 200 ppm resolved DI water
Size of liquid	~5 μL (R: ~1.1 mm)

5.2 Structural Analysis

Two different ratchets were used in this chapter. The micromilled brass microratchets (p: 76.7±1.1 μm, d/p: 0.16) was used to investigate the influence of polymer additive on droplet motion. The other replicated nickel micro ratchets (p: 150.5±0.6, d/p: 0.19) was used to evaluate the reproducibility of the new experimental setup as well as to examine the influence of droplet impact speed on the mobility. Brass ratchets were fabricated via three consecutive milling procedures: tapered milling, step micro milling and backside planarization, as shown in Chapter 3.X. Ni ratchets were replicated from the micro-milled brass ratchets through a series of replication processes, which mainly consists of thermal NIL, Ni electroplating process and post-processing. Figure 5.1 shows a photograph of the replicated Ni ratchets. The overall area and thickness of the sample were 10 × 5 cm^2 and 2 mm, respectively. Figure 5.2 (a) and (b) shows SEM images of both metallic micro ratchets. It can be seen that some surface defects were generated during the replication process. However, the deviation from the original mold shape

and dimensions was almost negligible.

Figure 5.1 Photograph of Ni replicated microratchets (p: 150.5 ±0.6, d/p: 0.19).

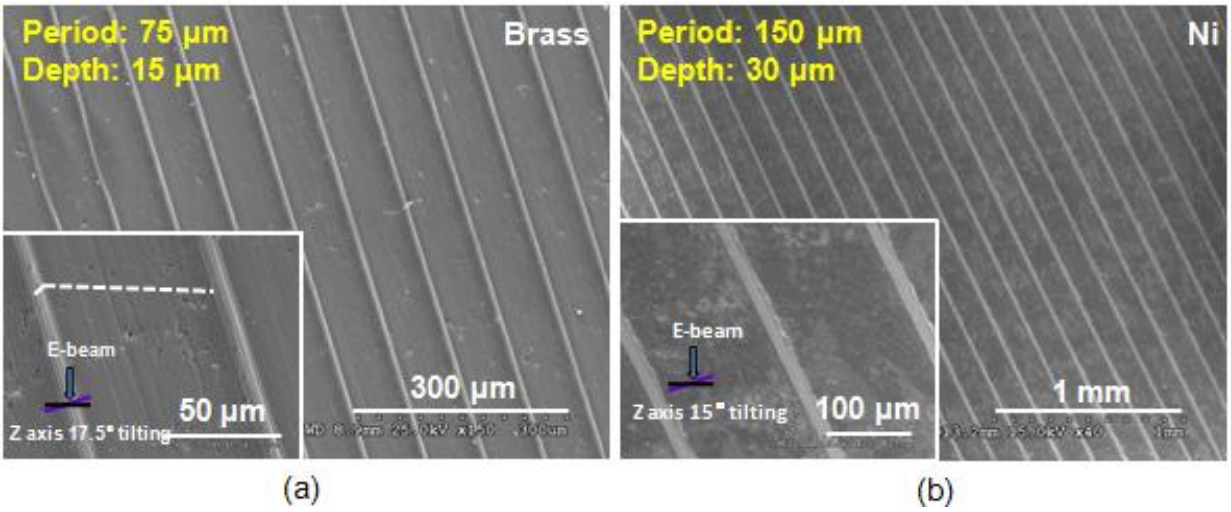

Figure 5.2 Scanning electron micrographs of (a) micro milled brass 75 µm period and (b) replicated Ni 150 µm period of ratchets, which have depth to period aspect ratio 1:5.

The stylus surface profiler is also used for more precise structural analysis of the miniaturized ratchets, as shown in figure 5.3. In table 5.2, the ratchet morphologies designed and measured by surface profilometer are summarized. Each value in the table was obtained by averaging from three different random measurements. Overall vertical variation or flatness of samples (ΔZ) generated by series of milling and replication processes, was in the range of 120 and 40 µm over 8 cm scanning length for brass 75 µm and Ni 150 µm ratchets, respectively. For the convenience sake, the ratchets were named with the material and designed step length to mill (l, most left column in table 5.2), instead of either the desired or measured period. For example, the measured period value of brass 75 µm period micro ratchets is 76.7 ±1.1 µm.

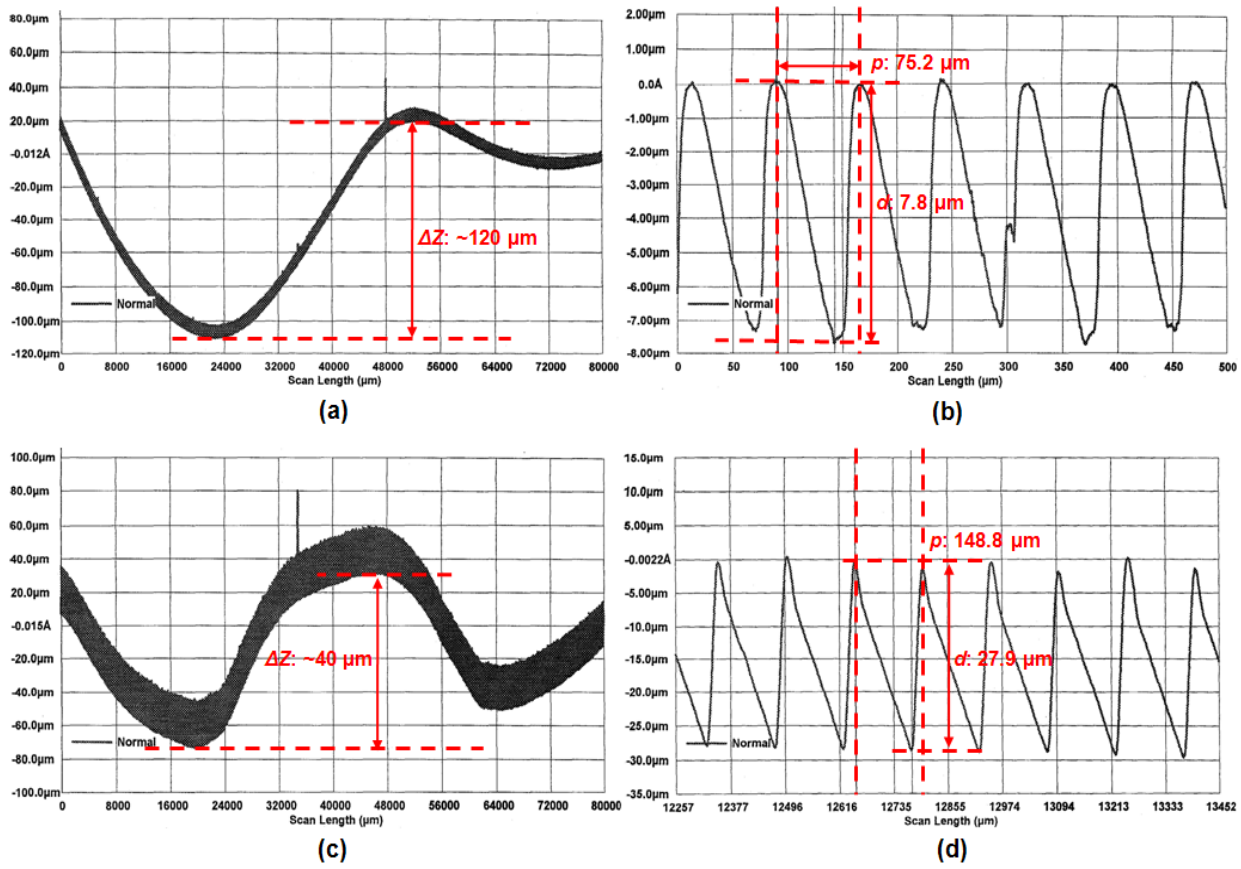

Figure 5.3 Surface morphologies of brass 75 μm (a) − (b), and Ni 150 μm period of ratchets (c) − (d) scanned by stylus surface profiler (Tencor P-11).

Table 5.2 Surface morphologies of miniaturized ratchets fabricated by micromilling or replication process. *ΔZ* is the maximum vertical variation for overall sample size (scan length: 8 cm).

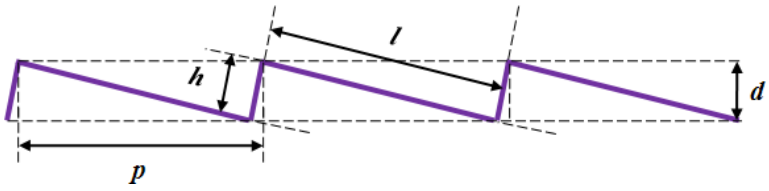

Designed						Measured					
l (μm)	*h* (μm)	*p* (μm)	*d* (μm)	*d/p*	*Mat.*	*l* (μm)	*h* (μm)	*p* (μm)	*d* (μm)	*d/p*	*ΔZ* (μm)
75	15	76.5	14.7	0.19	Brass	75.4 ±0.0	12.9 ±0.2	76.7 ±1.1	12.0 ±0.1	0.16	~120
150	30	153	29.4	0.19	Ni	147.1 ±1.0	30.0 ±0.2	150.5 ±0.6	29.1 ±0.6	0.19	~100

5.3 Characterization of Liquid Motion

The enhanced experimental setup allows for a more precise description of droplet behavior on miniaturized ratchet surfaces as well as acquisition of more accurate and reproducible data. Individual droplets are created at the tip of a metallic needle connected to a programmable screw-driven syringe dispenser. 5 μL DI water droplets were dispensed by using a needle with inner diameter of 0.21 mm and manipulating the injection rate according to preliminary experimental results (Chapter 3.4.2.3). The high speed camera system is equipped with a magnifying lens, a diffuser and a lamp for back-to-front illumination. A lower frame rate (either 250 or 500 fps) was used to evaluate the trajectory and velocity characteristics of droplet motion over the entire ratchet surface. A higher frame rate (1000 fps) was used to visualize the point of droplet impact on ratcheted substrates. In-house developed image processing tools using Optimas 6.5 and Matlab R2009a were used to extract appropriate data from captured pictures of droplet motion (Laveau 2008).

5.3.1 Reproducibility of Measurements

Prior to parametric study, reproducibility of the droplet motion taken by the high speed camera system was evaluated. Five consecutive droplets were dispersed on Ni ratchets with 150 μm period at 232.7±5.1 ℃, a temperature corresponding to the low temperature regime (*L* regime) where droplet motion is expected to be relatively fast due to direct contacts between the droplet and ratchet edges. Figure 5.4 shows a sequence of a dislocating droplet captured at a frame rate of 500 fps and an exposure time of 100 μs. The time interval between images is 40 ms. The needle height above the ratchet surface to release droplets (H_0) was 3.4 mm. Upon impact onto the surface, the droplet initially spreads, reaches a maximum width, and then bounces at an inclined angle, fully detached from the ratchet surface. Such a sequence repeats, which results in

a net motion toward the direction perpendicular to the ratchet grooves. As the droplet moves, the maximum height after each rebound decreases and finally it does not fully detach from the ratchet surface even though vertical oscillation still continues due to its elastic property. According to B. S. Gottfried et al. (Gottfrie, Lee et al. 1966), the critical surface temperature, above which secondary atomization (breakage of a droplet into more than one fragment) of an impacting droplet does not occur, is defined as dynamic Leidenfrost temperature (T_{DL}). The greatest heat transfer takes place upon impact when the droplet pushes against the solid surface during the rebounding process (Groendes and R. Mesler 1982). T_{DL} increases when the impact speed to the surface wall increases because a shorter time is required to form a vapor layer below the droplet (Karl and Frohn 2000). Under this condition with relatively low impact speed, secondary atomization did not occur. During the first couple of rebounds, the droplet shape continuously deforms much like an elastic ball. However, after a certain time interval, in this case at ~ 140 ms, the droplet keeps its oval lateral shape with almost negligible deformation.

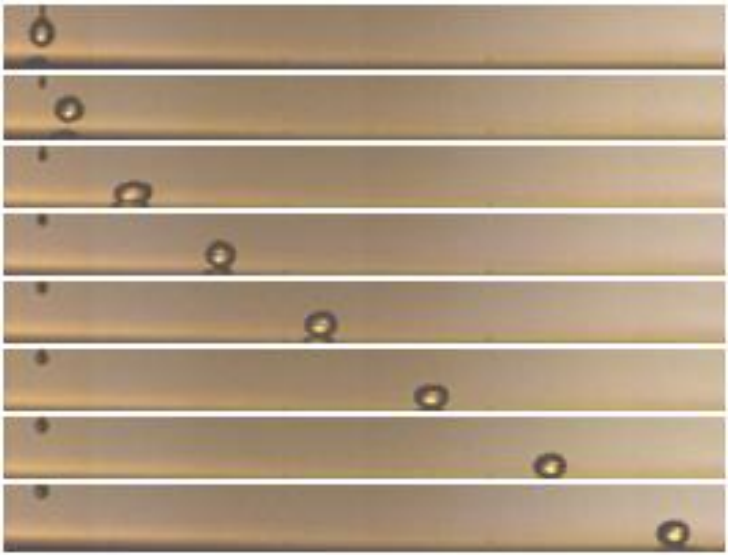

Figure 5.4 Time evolution of millimetric de-ionized water droplet (initial droplet volume, V_0: 4.8 μL) moving along Ni microratchets (p: 150.5±0.6 μm, d/p: 0.19) at 232.7±5.1 ℃, which is recorded at a frame rate of 500 fps and expose time of 100 μs. The sequence has 40 ms time interval.

Figure 5.5 shows a comparison of the video sequences for five droplets consecutively put on the Ni 150 μm period of ratchets under the same condition. Overall, the same behavior as described above was observed for the motion of all the droplets, with a slight difference in the time interval where the droplet acceleration starts to increase. The average overall passing time (t_{pass}) for the droplets to move the entire path (S) of 4.5±0.02 cm was 280±7.5 ms. The mean velocity of the droplet motion (v_m) calculated by S/t is 16.09±0.47 cm/s, which is similar to v_m of 16.89±0.93 obtained in Chapter 4 under the similar condition (at 234.2±2.2 ℃) by using primitive experimental setup. We also could measure initial diameters of water droplets (averaged D_0: 2.04±0.04 mm) using image processing software (Optimas 6.5) when they just left the needle. The average volume of initial droplets (V_0: 4.5±0.2 μL) was consistent, calculated based on D_0, by assuming that the droplets were spherical. The impact speeds of water droplets (v_0: 15.94±0.24 cm/s) was obtained using equation (5.1):

$$v_0 = \sqrt{2g(H_0 - D_0)}\,. \tag{5.1}$$

Then, v_0 values were used to obtain the impact Weber numbers (*We*: 0.85±0.02), which represents the indicative of the competition between kinetic energy and surface energy

$$We = \frac{\rho D_0 v_0^2}{\gamma} = \frac{2\rho g D_0 (H_0 - D_0)}{\gamma}, \tag{5.2}$$

where, ρ and γ are the density and surface tension of water droplet at its saturate temperature (ρ= 960 kg/m^3, γ= 59 mN/m at T_s=99 ℃).

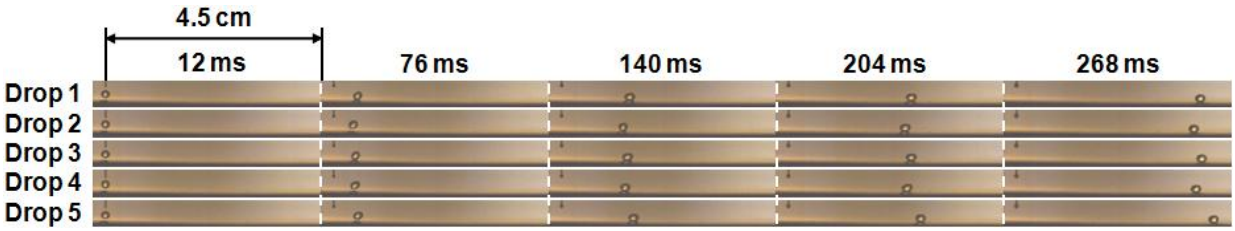

Figure 5.5 Sequences of five consecutive DI droplets dislocating along Ni 150 μm ratchets at 232.7±5.1 ℃, which are recorded at a frame rate of 500 fps and expose time of 100 μs.

Figure 5.6 shows the trajectories of the center of lateral droplet areas for all five droplets as the droplets horizontally dislocate along the ratchets surface. Figure 5.7 presents horizontal velocities $v_x(x)$ as functions of horizontal trajectories of every droplet. The vertical trajectory was plotted based on the ratchet surface while the zero position of horizontal trajectory corresponded to the point of droplet injection. Initially, the droplet vertically oscillates in the vertical position range of 1.0 − 2.4 mm, while moving horizontally with significantly increased horizontal velocity. The largest vertical variations of ~ 1.3 mm were observed in the injection area (near zero horizontal trajectories) because the first rebound is the strongest and fully detached from the surface due to their high kinetic energy at impact. All other small degrees of vertical fluctuations around 0.3 mm were generated by the self-oscillations of droplets while the droplet kept touching with the ratchet surface. The large oscillation of vertical trajectory due to the rebounding of droplets location continues up to ~ 5 mm horizontal position. Up to this point, the horizontal distance between two consecutive rebounds and frequency for the oscillations were fairly uniform at 3.25±0.35 mm and 0.31±0.03 number of oscillations/mm, respectively. The shape of rebounded droplets was significantly deformed from their spherical shape.

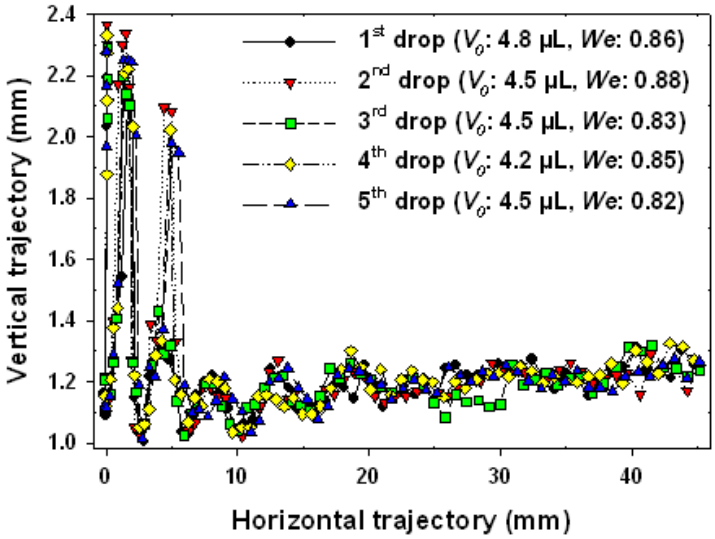

Figure 5.6 Trajectories of DI droplets on Ni 150 µm ratchets at 232.7±5.1 ℃.

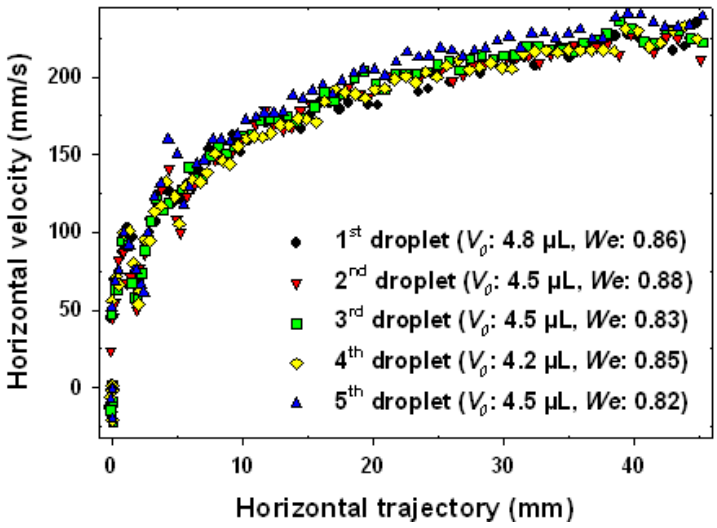

Figure 5.7 Horizontal velocity $v_x(x)$ profiles of DI droplet as a function of horizontal trajectory of droplet on Ni 150 μm ratchets at 232.7±5.1 ℃.

Before the horizontal position of droplets passes around 5 mm, the horizontal velocities first increase significantly. After around 5 mm horizontal positions of droplets, the velocities slightly enhanced with the increase of ~ 70 mm/s for ~ 40 mm paths. In the range of horizontal trajectories from ~ 10 to ~ 45 mm, the droplets keep their oval (or pancake) lateral shapes with almost negligible deformation due to the low and constant acceleration. In this region, the center of the vertical oscillations decrease up to 1.1 – 1.2 mm, attributed to the deformation of the droplets shape from near spherical to pancake-like. The horizontal distance between oscillations increases from 3.25±0.35 mm to 6.76±0.17 mm and the frequency of the oscillation changes to 0.15±0.01 number of oscillations/mm, which are accompanied with the increased horizontal velocities. The average terminal velocity (v_t), as obtained by averaging last five velocity values (for 20 ms), is 22.6±0.5 cm/s, which is ~ 5.7 cm/s faster than v_m.

Figure 5.8 shows vertical velocity $v_z(x)$ of droplet motion as a function of horizontal droplet position. The zero vertical velocity appears twice for a single droplet oscillation: when the droplet spreads to its maximum width and the droplet is at its highest position. Therefore, the frequency is doubled with respect to that shown in the corresponding vertical droplet trajectory.

The largest negative and positive velocities which are found near the injection area represent the droplet with maximum vertical kinetic energy right before the impact and right after droplet rebounds. Similar to the vertical droplet trajectory, the amplitude of the oscillation is strongest at its first rebound and is reduced to ~ 1.2 mm up to ~ 5 mm horizontal position, and further reduced to ~ 0.2 mm. The absolute values of maximum droplet velocity induced by bouncing were 10 – 15 cm/s, but by droplet oscillation below 5 cm/s. Using the horizontal $v_x(x)$ and vertical velocity $v_z(x)$ of every droplet, their kinetic energies ($K.E.(x) = \frac{m\{v_x(x)^2+v_z(x)^2\}}{2}$) as functions of horizontal locations x were obtained, which is shown in figure 5.9. All $K.E.(x)$ gradually increase as the droplets moves horizontally except for the values near the injection area (x: 0 − 5 mm), which are caused by higher absolute values of $v_z(x)$ due to the initial couple of rebounding.

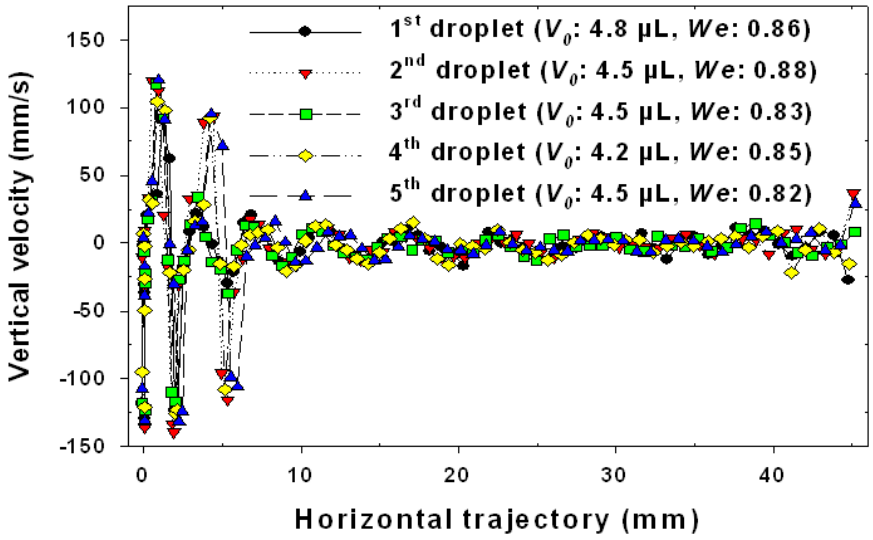

Figure 5.8 Vertical velocity $v_z(x)$ profiles of DI droplets as a function of their horizontal trajectories on Ni 150 µm ratchets at 232.7±5.1 ℃.

It was experimentally observed that the horizontal acceleration of droplet (a_x) linearly decreased with its velocity (v_x) (Linke, Aleman et al. 2006). This result indicates a possible drag force directly proportional to v_x, so that the net force could be written as:

$$F_{net} = F_{ratchet} - \beta v_x \tag{5.3}$$

where, β is the drag coefficient and $F_{ratchet}$ the driving ratchets force.

This is reasonable due to the fact that drag at low Reynolds numbers is usually linear in the velocity. The velocity fits well to the differential equation which is composed of a constant (velocity independent) ratchet force (*ma*) and a drag (retarding) force ($-\beta v_x$) that is linear in velocity:

$$m\frac{d^2x}{dt^2} = ma - \beta\frac{dx}{dt} \tag{5.4}$$

where, *m* is a mass of droplet (assuming a constant mass) and *a* the acceleration resulting from the ratchet force.

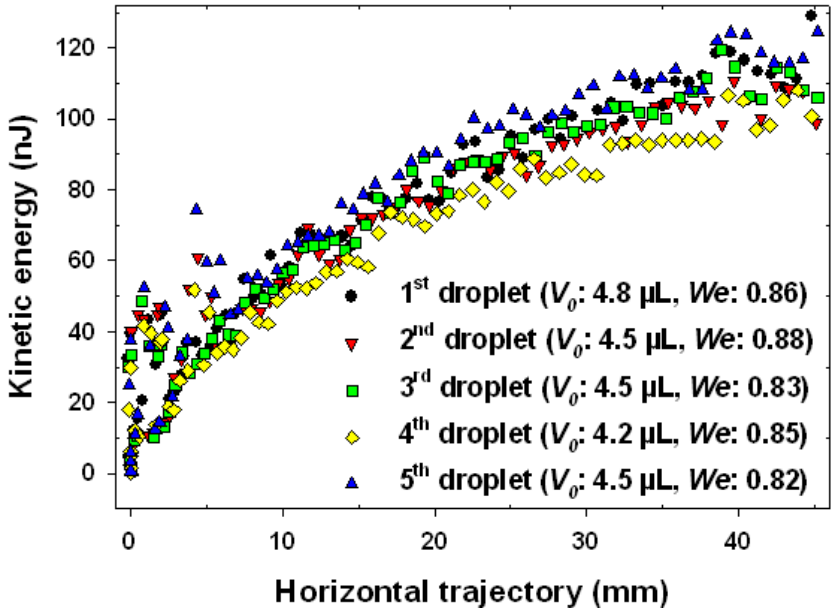

Figure 5.9 Kinetic energies of DI droplets as a function of the trajectory on Ni 150 µm ratchets at 232.7±5.1 ℃.

Solving equation (5.4), an expression for horizontal velocity of the droplet as a function of time $v_x(t)$ is obtained (see Appendix A):

$$v_x(t) = \left(v_x(0) - \frac{a}{\beta/m}\right)e^{-(\beta/\mathrm{m})t} + \frac{a}{\beta/m} \tag{5.5}$$

Here, t is time, $v_x(0)$ initial velocity caused by potential energy of droplet and $\frac{a}{\beta/m}$ terminal velocity. By extracting the velocities of a moving droplet in the Leidenfrost-ratchet system, the equation (5.5) can fit to the measured data from the image sequence and be employed to determine a and β/m.

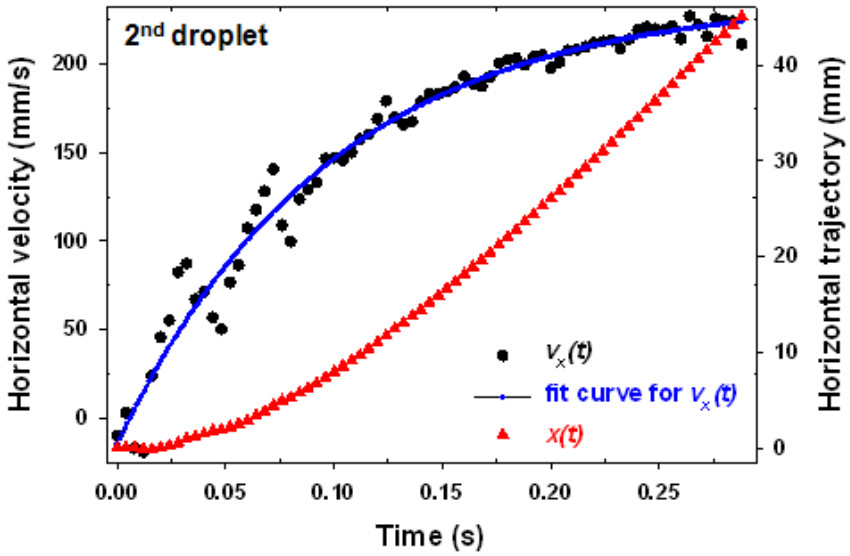

Figure 5.10 An example of fitting curve (blue spots, from fit equation $v_x(t) = -251.93e^{-(10.19)t} + 237.54$) from horizontal velocity (black circles) and horizontal trajectory (red triangle up) of 2nd droplet on Ni 150 μm ratchets at 232.7±5.1 ℃ as a function of time.

Figure 5.10 shows that the horizontal velocity profile of droplet on Ni 150 μm ratchets at 232.7±5.1 ℃, fits the equation quite well. Since the acceleration of droplet a mathematically is in equivalent to the second time derivative of its horizontal trajectory, a could be calculated directly from the trajectory. Under constant acceleration, the profile could be fit to a simple parabolic curve $x(t) = \alpha t^2 + \beta$, where $a = \ddot{x}(t) = 2\alpha$ provides the desired quantity. However, due to the presence of a drag term, $x(t)$ is not simply parabolic, except near negligible velocity (small drag), as shown in figure 5.10. The far deviation of $v_x(t)$ from the fit curve (color: blue spots) till ~ 80 ms might be mainly caused by the actively fluctuating vertical kinetic energy $v_z(t)$ due to the strong heat transfer via direct contact between bottom of droplet and top of the ratchet surface as

well as large deformation of droplet shape. In *L* regime the droplet on a ratchet is partially separated by a vapor layer, and nucleate boiling induces strong repulsion and elongation in the vertical direction *z*. Table 5.3 shows various experimental data and fit parameters with the equation (5.5). The injection system which is composed of an electronic syringe pump, a syringe, a needle and the fitting system (Upchurch Scientific Inc.) resulted in consistent values of V_0, *We* and *m*.

Table 5.3 Various experimental data and fit parameters of five consecutive DI droplets on Ni 150 μm ratchets at 232.7±5.1 ℃.

Drop #	V_0 (μL)	*We*	v_t (cm/s)	$v_x(0)$ (mm/s)	β/m (s^{-1})	a (m/s^2)	$\frac{a}{\beta/m}$ (cm/s)
1	4.8	0.86	22.3±0.5	-1.6	11.22	2.59	23.07
2	4.5	0.88	22.1±0.5	-14.4	10.19	2.42	23.75
3	4.5	0.83	22.7±0.5	-9.8	10.63	2.56	24.09
4	4.2	0.85	22.4±0.6	-7.7	10.04	2.40	23.91
5	4.5	0.82	23.4±0.6	-8.3	11.56	2.86	24.72
Av.	4.5±0.2	0.85±0.02	22.6±0.5	-8.4±4.6	10.63±0.65	2.57±0.18	23.91±0.60

The syringe pump was programmed with the feeding rate of 1 mL/min in order to obtain the desired DI water droplet volume of 5 μL according to the preliminary experimental results shown in Chapter 3. A little bit smaller size of droplets (4.5±0.2 μL) resulted, which might be caused by the influence of the hot ratchet surface. The motion of Leidenfrost droplets on the ratchets also shows a consistent behavior for all five times repetition, with slight variations in the initial horizontal velocity $v_x(0)$ and drag coefficient β. Besides trajectory, velocity, kinetic energy and acceleration of liquid droplet, other information such as circularity, breadth, perimeter, area, major axis length and major axis angle could be extracted by newly established experimental

apparatus.

In summary, the reproducibility of the enhanced experimental setup with the high speed camera was evaluated. For five successive DI water droplets on Ni micro ratchets at 232.7±5.1 ℃ (H_0: 3.34±0.04 mm, D_0: 2.04±0.04 mm, v_0: 15.94±0.24 mm/s), consistent results of their trajectories, velocities, kinetic energies and fit parameters were obtained.

5.3.2 The Influence of Droplet Impact Speed

Most studies related to droplet impact on hot surfaces have been carried out for cooling applications such as fuel combustors, spray quenching and fire protection system. In terms of heat transfer, as the impact speed increases the net heat transfer enhances in film boiling regime. The maximum heat transfer has been observed when droplet spreads most and start pushing against the wall (Groendes and R. Mesler 1982). Thus, higher temperature is required to isolate liquid droplet from the wall with an impact, which is called as dynamic Leidenfrost temperature (T_{DL}). For dynamics of Leidenfrost droplets, the kinetic energy effectively transfers to surface energy and then vice versa due to its elasticity. This temperature independent elasticity of Leidenfrost droplets strongly decreases with We ($e \sim We^{-1/2}$ for $We > 1$) (Biance, Chevy et al. 2006). In this section, the influence of initial droplet impact speed on the droplet motion along the ratchet surface is investigated in both *L* and *H* regimes by alternating the needle height where droplets are dispensed.

Figure 5.11 shows a video sequence of motion of DI water droplet (V_0: 4.2 μL) on 150 μm period Ni ratchets (with *d*/*p* aspect ratio of 0.19 and sharp ridges), recorded by high speed camera with 500 fps. The needle height (H_0) used to release droplet was 31.6 mm. H_0 is defined as the distance from the bottom of the needle to top of the ratchet surface. When a droplet impacts on the ratchet surface, it deforms and spreads until reaching its maximum extension,

then it retracts and elongates into the vertical direction due to the elasticity of Leidenfrost droplet, similar behavior often observed with Leidenfrost droplet on flat surface. It actively vibrates as it rises. It also moves into the horizontal direction (toward positive *x*, or rightward) due to the ratchet geometry. After the droplet experiences several rebounds (2 ~ 3), it keeps contact with the ratchet surface and moves toward +*x*. As the droplet moves, the maximum height after every rebound significantly decreases. Finally, it does not rebound from the ratchets surface. The amplitude of vertical oscillation of the droplet keeps reducing and seems to maintain constant values, so that the droplet velocity gradually increases and saturates. Secondary atomization and droplet split did not occur in this condition. However, when the droplet dispensed on the ratchets surface with long periods ($p \geq 375$ μm and *d/p*: 0.17 – 0.19) in similar H_0 and T_s, it split into two smaller droplets without secondary atomization upon the initial impact.

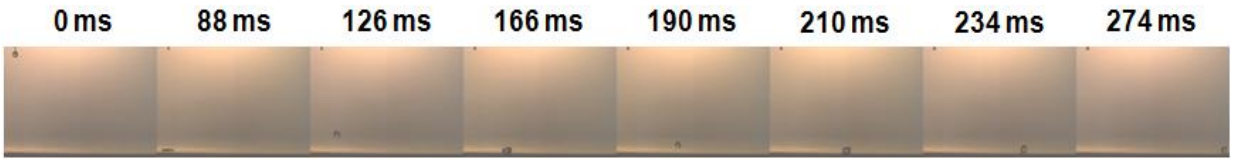

Figure 5.11 Image sequence of the motion of a 4.2 μL DI water droplet on Ni 150 μm ratchets at 214.0±1.7 ℃. The needle height to dispense the droplet was 31.6 mm (*We*: 18.81).

Figure 5.12 (a) and (b) present trajectories and velocities of the droplet when they are released from five different heights (H_0: 3.8 – 31.6 mm) in *L* regime (T_s: 214.0±1.7 ℃). DI water droplets were dispensed three to five times at a specific needle height. The observed motion of droplets was almost consistent in a condition. Figure 5.12 (a) and (b) show vertical trajectory and horizontal velocity as a function of horizontal trajectory for different needle heights or *We* numbers (*We*).The horizontally dislocated distance between rebounds and vertically rebounding heights of the droplets, increase as H_0 or *We* increases. However, horizontal velocities versus horizontal trajectory profiles are similar to every other, as shown in figure 5.12 (b). The

measured and calculated parameters related these experiments are given in table 5.4. It is noted that passing time *t* is defined as the interval between the moment when the droplet touches the ratchet surface and that when it reaches the end of path (*x*: ~46 mm).

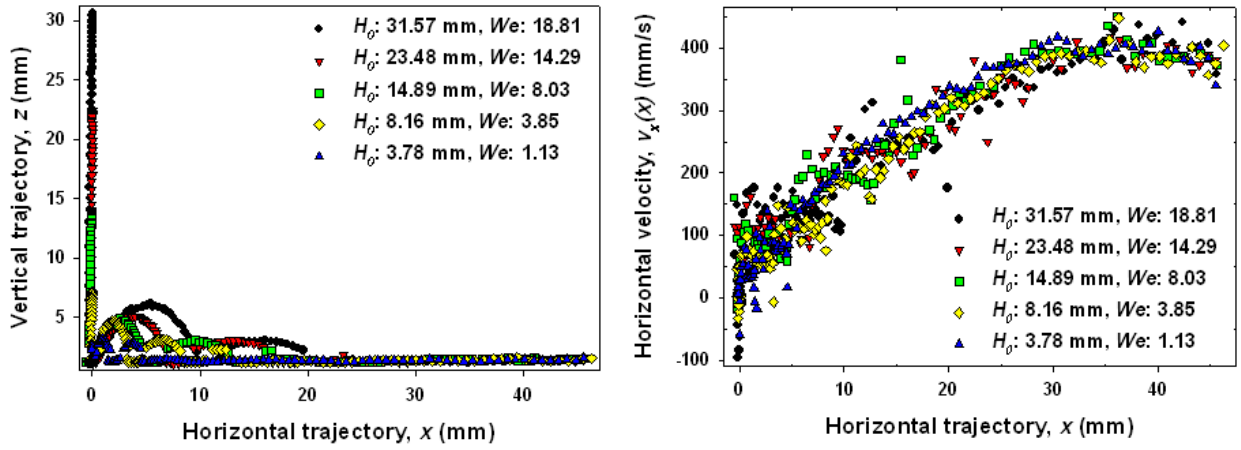

(a) (b)

Figure 5.12 (a) Vertical trajectories *z (x)* and (b) horizontal velocities $v_x(x)$ of DI droplet dispensed from five different needle heights along Ni 150 μm ratchets in *L* regime (T_s: 214.0±1.7 ℃).

Table 5.4 The values of relative parameters for figure 5.12.

H_0 (mm)	V_0 (μL)	D_0 (mm)	v_0 (cm/s)	*We*	*t* (ms)	*S* (cm)	v_{av} (cm/s)	v_t (cm/s)
3.78	4.5	2.04	18.43	1.13	224	4.56	20.36	39.07±2.24
8.16	3.8	1.94	34.89	3.85	234	4.63	19.79	38.46±1.37
14.89	3.8	1.94	50.38	8.03	204	4.56	22.35	39.03±1.19
23.48	4.8	2.09	64.75	14.29	194	4.56	23.51	38.63±1.23
31.57	4.2	1.99	76.13	18.81	188	4.56	24.26	40.83±2.37

Figure 5.13 (a) and (b) show vertical trajectory and horizontal velocity of droplet motion as a function of horizontal trajectory when they are dispensed from five different needle heights (H_0: 2.64 – 27.48 mm) at a temperature in *H* regime (T_s: 313.0±2.6 ℃). Compared to the behavior in *L*

regime, both the horizontally dislocated distances and vertically rebounding heights of droplets significantly decrease, indicating that the net heat transfer from the surface to the droplet decrease and thus the kinetic energy is much less than that in *L* regime. The values of $v_x(x)$ gradually decreased after reaching their maximum for all the varied impact velocity. One of critical reasons of these observations might be the absence of droplet fluctuation. The self-oscillation of droplet is always most significant near the injection area. As the droplet horizontally moves it does fluctuate gradually less. Finally, it moves maintaining almost the constant shape.

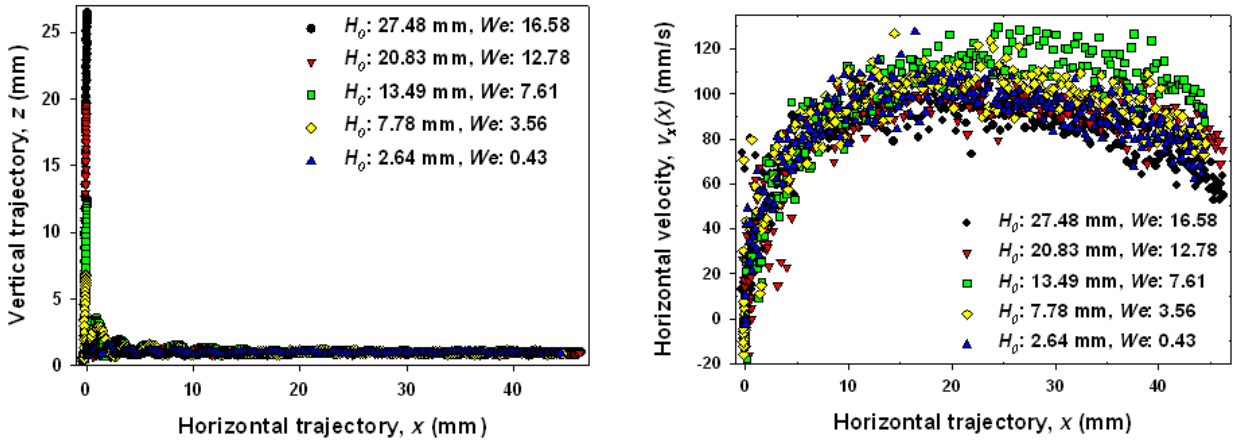

(a) (b)

Figure 5.13 (a) Vertical trajectories $z(x)$ and (b) horizontal velocities $v_x(x)$ of DI droplet dispensed from five different needle heights along Ni 150 μm ratchets in *H* regime (T_s: 313.0±2.6 ℃).

In *H* regime, it resembles a sphere, which is different in *L* regime (an oval). Therefore, $v_x(x)$ increased up to the horizontal trajectory of ~ 20 mm by enhanced heat transfer, especially when the droplet sank. It is reasonable that the droplet velocity would be saturated after the kinetic energy given by the impact completely disappears. The direct contacts between the bottom of droplet and the top of ratchet surface make the droplet in *L* regime more efficient than that in *H* regime, in terms of heat transfer as well as dynamics. There are also negligible variations of horizontal droplet velocities with all five different initial impact speed v_0. Table 5.5 shows

parameters related to figure 5.13.

Table 5.5 The values of relative parameters for figure 5.13.

H_0 (mm)	V_0 (μL)	D_0 (mm)	v_0 (cm/s)	*We*	*t* (ms)	*S* (cm)	v_m (cm/s)	v_t (cm/s)
2.64	3.8	1.94	11.67	0.43	530	4.44	8.38	7.55±0.96
7.78	3.6	1.89	33.97	3.56	502	4.45	8.86	7.90±0.44
13.49	4.8	2.09	47.26	7.61	484	4.44	9.17	9.71±0.46
20.83	5.2	2.14	60.52	12.78	594	4.61	7.76	7.87±0.44
27.48	4.5	12.04	70.61	16.58	628	4.63	7.37	5.82±0.39

Besides the Ni 150 μm period ratchets, we also investigated the effect of the initial impact speed on the motion of DI water droplets for 75 μm brass ratchets in *H* regime (H_0: 2.26, 4.09, 15.28 mm, and T_s: 273.3±0.6 ℃), 75 μm Ni ratchets in *L* regime (H_0: 2.42, 27.58 mm, and T_s: 237.3±2.5 ℃), and 750 μm brass ratchets in *L* regime (H_0: 6.09, 10.39 mm, and T_s: 186.3±3.2 ℃). For all samples, the initial impact speed shows a negligible effect on the horizontal velocity. Based on the experimental observation, we can conclude that the initial impact speed of released droplets does not affect its horizontal motion along the ratchet surfaces in both *L* and *H* regime.

5.3.3 The Influence of Polymer Additive

Addition of a very small amount [of the order of 100 parts per million (ppm)] of flexible polymer additives (polyethylene oxide, PEO) to liquid significantly reduces both rebounding and secondary atomization (SA) of the droplet on a heated surface, with negligible changes in the density and surface tension, and a minor change in the shear viscosity on the fluid as shown in table 5.6 (Bergeron, Bonn et al. 2000; Bergeron 2003; Bertola and Sefiane 2005). The liquid mixed with polymer additives becomes viscoelastic. When polymer molecules are at rest, they

are coiled in a minimum energy conformation. They unfold under hydrodynamic forces with large resistance to deform (Degennes 1974). Therefore, this viscoelastic DI water mixed with PEO (200 ppm) significantly reduces the critical temperature for which SA completely disappears on the mirror polished aluminum block (by more than 50 ℃ for *We*: ~ 28), comparing pure DI water (Bertola and Sefiane 2005). It also avoids rebounding of the droplet. The incorporation of a small amount of PEO into DI water is expected to significantly influence the threshold temperature (T_{th}) for the motion of droplet as well as both vertical and horizontal mobility of droplet. A high magnification recording was used to investigate T_{th} while a low magnification recording was used to investigate droplet mobility.

Table 5.6 Physical properties of DI water and PEO 200 ppm resolved DI water at 20 ℃, where ρ, η, and σ are the density, shear viscosity, and surface tension, respectively (Bertola and Sefiane 2005).

Fluid	ρ **(kg/m^3)**	σ **(mN/m)**	η **(mPa s)**
DI water	1000	72	1.0
DI water+200 ppm PEO	1000	68	1.3

Micromilled 75 μm period brass microratchets (*p*: 76.7 ±1.1 and *d*/*p*: 0.16) was used for this purpose as shown in figure 5.2 (a). Two different fluids were explored in the surface temperature range of 87 ±2.0 – 291.7 ±1.5 ℃: pure DI water and 200 ppm solution of PEO in DI water. The PEO (Sigma-Aldrich) had an average molecular weight of 4×10^6 amu and a typical density of 1.21 g/mL at room temperature. The PEO was dissolved into a beaker of DI water, where a magnetic stirrer kept generating a vortex at a low speed at room temperature. Injection tools were separately prepared to release two different liquids. Three consecutive droplets were released for each condition. An identical needle size (#27, Hamilton) and injection rate (1 mL/min) were

applied to generate droplets with a similar size for two different liquids (radius: ~1 mm). In this experiment, all liquid droplets were released at a low needle height (H < 3.5 mm).

A high magnification (with 80 mm spacer) and fast frame rate (1000 fps) recording was used to study the influence of a PEO additive on the threshold temperature for the directional motion of droplet. Figure 5.14 presents sequences of droplet impact on the heated 75 μm brass microratchets at different surface temperatures for both liquids. At low *Ts*, droplets put on the surface show slight vertical oscillation while neither rebounding nor rectified motion was observed. A reduced vertical oscillation was observed with DI water with PEO. At 138.0±1.0 ℃ and 161.3±1.5 ℃, severe SA or explosion events were observed, still without generating a rectified motion of the droplet. . Even at 191.7±1.2 ℃ where only a gentle SA event occurred, the droplet randomly moved with bouncing and then finally escaped the sample surface. The first directional motion with continuous rebounding was achieved at T_s of 218.3±2.3 ℃. Therefore, It is reasonable to conclude T_{th} of pure DI water on brass 75 μm period of ratchets exist somewhere between 191.7±1.2 ℃ and 218.3±2.3 ℃.

For DI water droplets containing PEO, the behavior was significantly different. As T_s increases the event changes from one where the droplet sticks to the ratchet surface to the other where it rebounds without SA. Slight SA was observed at intermediate T_s of 138.0±1.0 ℃. The droplet started to show a unidirectional (toward slowly sloped ratchet direction) motion at 161.3±1.5 ℃. Thus, the actual T_{th} is expected to lie between 138.0±1.0 ℃ and 161.3±1.5 ℃. An exceptional behavior was observed at T_s of 191.7±1.2 ℃, where the droplet slightly shifted toward opposite direction during the beginning stage after impact on the hot surface, and turned around the direction, and then finally kept following the right direction.

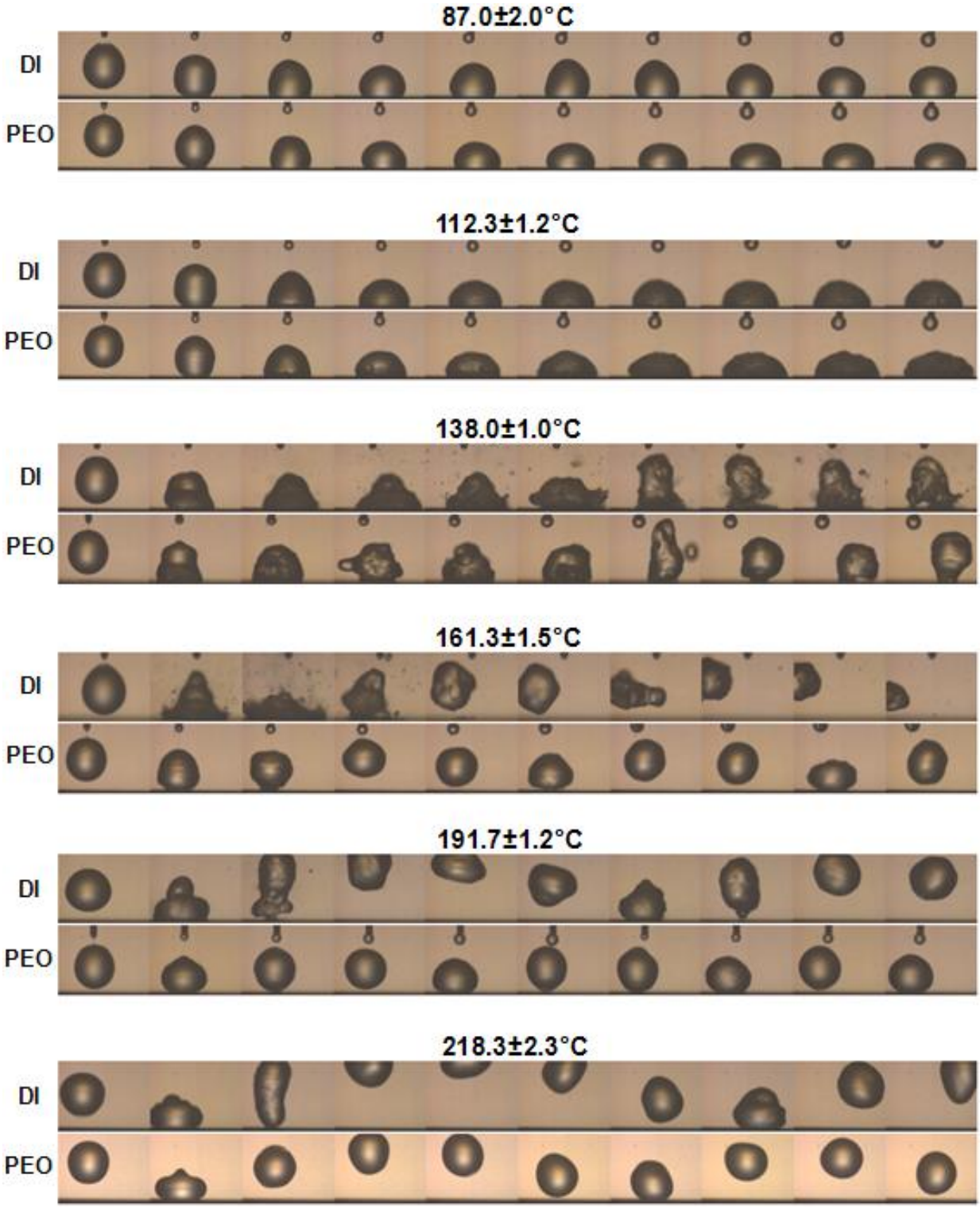

Figure 5.14 Time evolutions of droplet impacting on brass microratchets (p: 76.7±1.1 and d/p: 0.16) captured by high speed camera (Kodak Ektapro 1000HRC, magnification: 80 mm spacer, frame rates: 1000 fps, expose time: 100 μs) at varied surface temperatures (87±2.0 – 291.7±1.5 ℃). Horizontally successive images have 10 ms time interval.

The main reason of the huge difference in the threshold temperature (30°C < ΔT_{th} < 80 ℃) for two different liquids could be attributed to the viscoelastic property of the polymer additive solution (Bertola and Sefiane 2005), which is introduced in the beginning of this chapter (5.3.3). The presence of polymer improves the surface stability between the droplet and the surrounding atmosphere as well as that between the droplet and vapor layer (Bertola and Sefiane 2005). At the threshold temperatures for both liquids, it is expected that a continuous and stable vapor cushion does not exist between the liquid and the ratchets. The additive could significantly affect the growth, detachment, and the rise of vapor bubbles so that it avoids their bursting.

Figure 5.15 shows highly magnified sequences of two different liquid droplets impacting on heated brass microratchets at 245.7 ±1.2 ℃. There is no SA event for both liquids. Thus, they can be considered as Leidenfrost droplets. It can be easily distinguished that there are significantly different degree of droplet shape deformation for them. More severe deformation of droplet shape was observed from pure DI water. Much less deformation behavior of PEO dissolved DI water is caused by its higher elongational viscosity. It was reported that PEO dissolved droplet has a large resistance to droplet retraction after impact, thereby suppressing droplet rebound on hydrophobic surface at room temperature (Bergeron, Bonn et al. 2000). Even though a PEO dissolved water droplet rebounds in film-boiling regime due to the vapor cushion between the droplet and the ratchets surface, it is much less mobile for both vertical and horizontal directions than pure DI water.

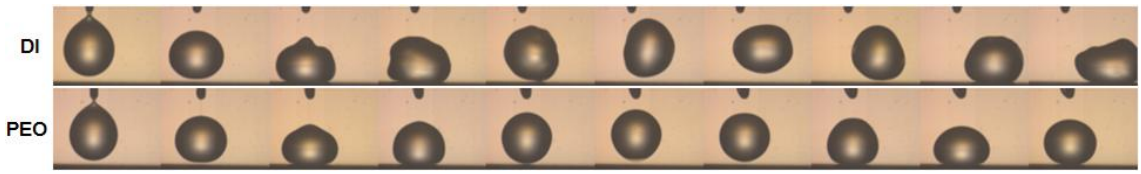

Figure 5.15 Time evolutions of droplet impacting on brass micro ratchets (p: 76.7 ±1.1 and d/p: 0.16) captured by high speed camera (Kodak Ektapro 1000HRC, magnification: 80 mm spacer, frame rates: 1000 fps, expose time: 100 μs) at 245.7 ±1.2 ℃. Horizontally successive images have 5 ms time interval.

Low magnification (with 5 mm spacer) and mediate frame rate (500 fps) of recording was used to obtain the information on droplet mobility over the long range of horizontal position. Figure 5.16 shows their trajectories. Figure 5.17 compares the droplet velocity as a function of time for the two liquids. The fitted curves to the equation 5.5 are also shown. The acceleration and the terminal velocity for the PEO added DI water droplet were 17.8 times and 6.1 times lower than those for the DI water droplet. The additive stabilizes the surface between the liquid droplet and the surrounding atmosphere as well as the surface between liquid droplet and vapor film (Bertola and Sefiane 2005). This stabilizing property could significantly reduce heat transfer between the liquid and ratchets surface. Much less deformable property of the droplet due to the viscoelasticity might induce smaller number of ratchets beneath the bottom surface of the liquid when the droplet in contact with the heated microratchets.

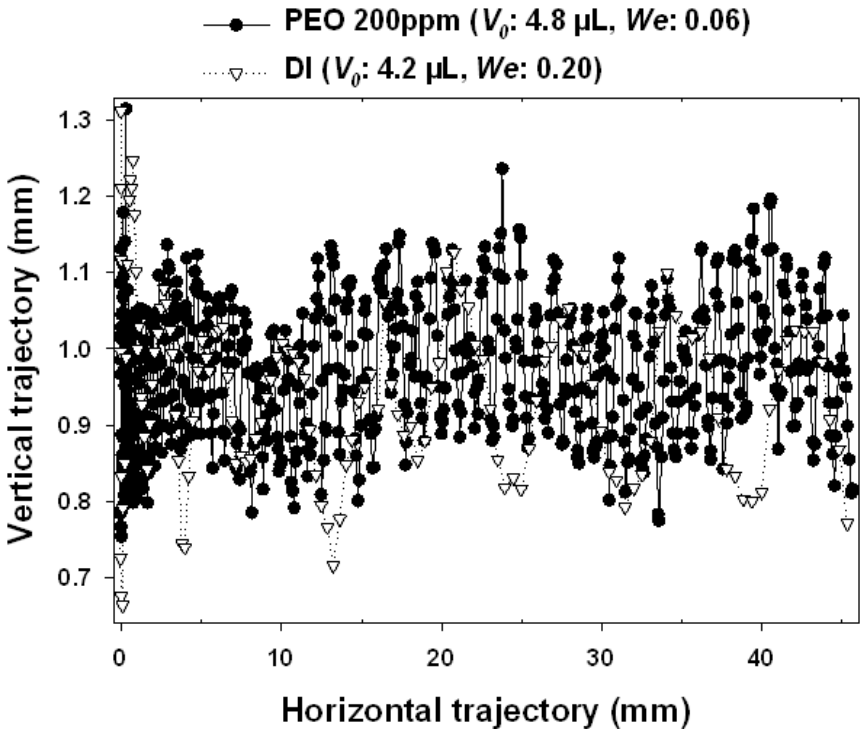

Figure 5.16 Trajectories of two different liquid droplets moving along the brass microratchets (*p*: 76.7 ±1.1 and *d*/*p*: 0.16) at 245.7 ±1.2 ℃.

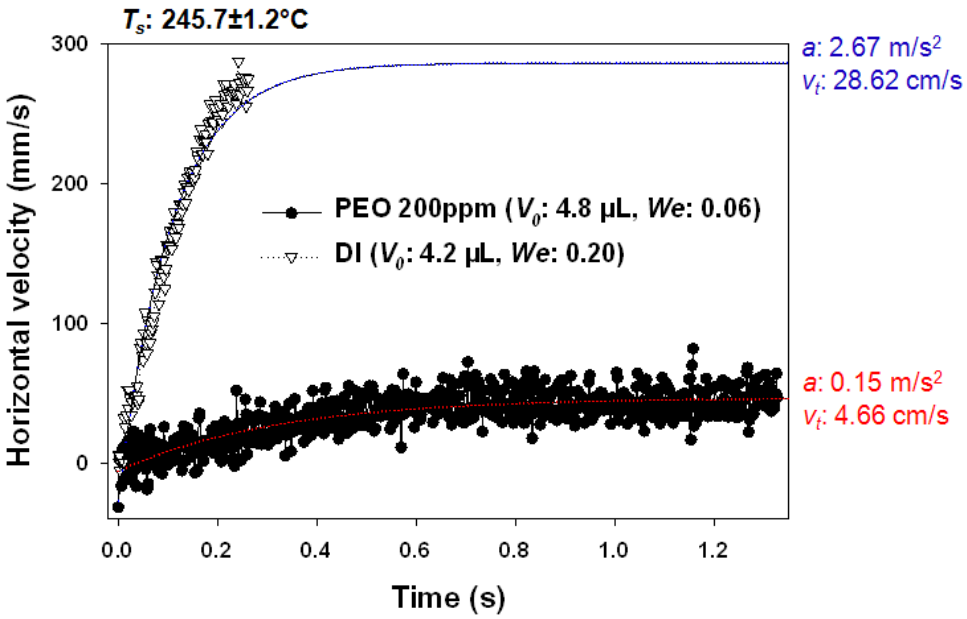

Figure 5.17 Time evolutional horizontal velocities of two different liquid droplets moving along the brass microratchets (*p*: 76.7 ±1.1 and *d*/*p*: 0.16) at 245.7 ±1.2 ℃.

Figure 5.18 depicts vertical trajectory versus horizontal trajectory for PEO dissolved droplets for different surface temperature. The vertical oscillation decreases with increasing surface temperature. Directional motion of the PEO dissolved droplet was only observed in the range of wall temperatures 161.3±1.5°C − 245.7±1.2°C. The droplet randomly moved at 291.7±1.5°C. However, at this temperature DI water droplets still showed directional motion. This can be attributed to the combined effect of the reduced droplet deformation with the PEO dissolved droplet and the large vapor layer thickness at high temperature, which results in the reduction in the asymmetric vapor flow and ultimately the loss of unidirectional motion.

Despite the reduction of vertical oscillation, the horizontal velocity of the PEO dissolved DI water droplet does not significantly vary with the surface temperature as shown in figure 5.19. At lower surface temperature, instant velocity values fluctuate due to the higher rebounding. The saturated horizontal velocities are consistently in the range of 3 – 5 cm/s, with the acceleration of 8.5 – 14.7 cm/s^2.

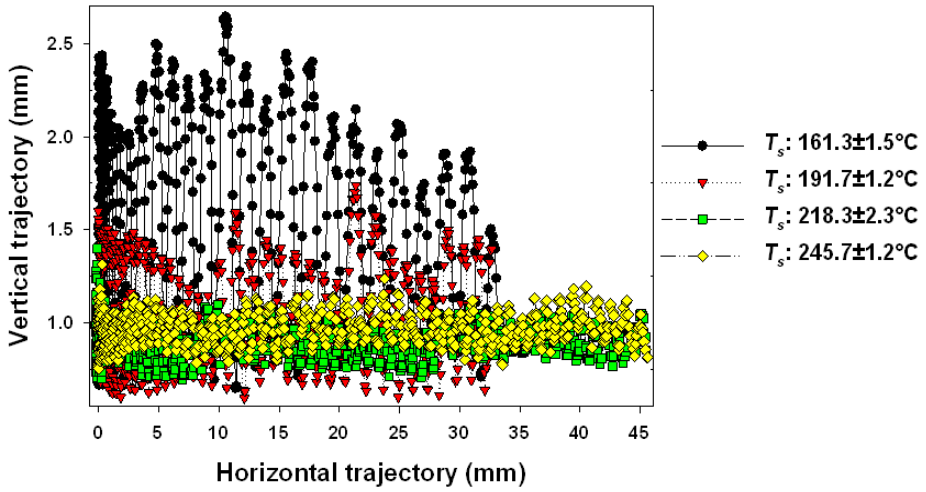

Figure 5.18 The influence of surface temperature on trajectory of the PEO 200 ppm resolved DI water droplet moving along brass microratchets (p: 76.7 ±1.1 and d/p: 0.16).

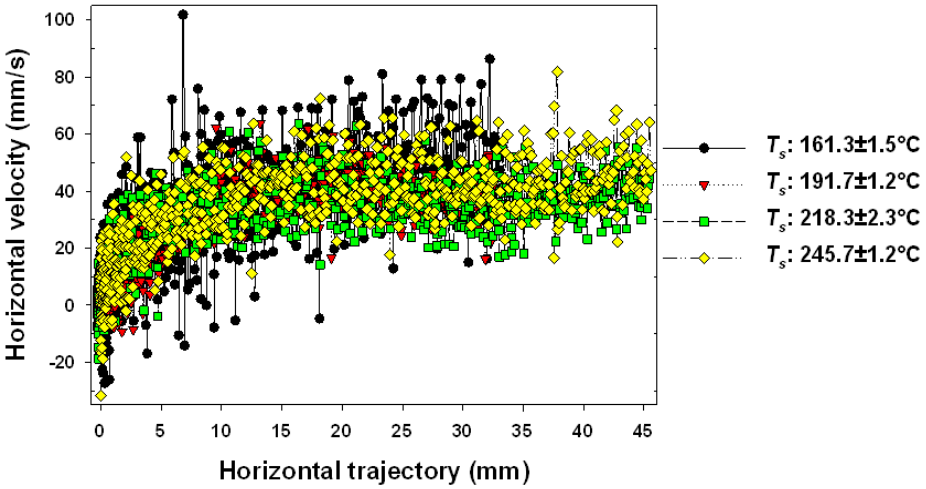

Figure 5.19 The influence of surface temperature on horizontal velocity of the PEO 200 ppm resolved DI water droplet moving along brass microratchets (p: 76.7 ±1.1 and d/p: 0.16).

5.4 Conclusions

The enhanced experimental setup equipped with a high speed camera and a modified injection system with a needle and a syringe pump was used to characterize the impact and motion of droplets on different ratchets under various conditions. The results show good reproducibility. The highest acceleration is always observed at the beginning of droplet motion. The vertical oscillation of droplets during horizontal motion was found to be related to how much

acceleration the droplet can receive from the ratchet surface. In *L* regime, the terminal velocities (v_t) are at least twice as high as the mean velocities (v_m) obtained by the primitive apparatus in Chapter 4. The impact speed of droplet does not significantly affect the droplet motion because of critical decrease of elasticity with *We* ($e \sim We^{-1/2}$). The polyethylene oxide (PEO) 200 ppm resolved DI water significantly reduced the threshold temperature for the motion. However, the motion is much less mobile.

Chapter 6 The Influence of Ratchet Geometries on Droplet Motion

6.1 Introduction

In Chapter 5, the performance of the enhanced experimental apparatus was evaluated. A high speed camera, automated injection system, and image processing tool allowed one to observe more accurate behavior of film-boiling liquid droplets on the heated miniaturized ratchets and extract valuable information from the captured video sequence. The main objective of this chapter is to investigate further in detail the behavior of film-boiling droplets on the heated miniaturized ratchets with the enhanced experimental setup. Experimental parameters were carefully selected based on the results obtained in the previous chapters, which include ratchet dimensions (period and depth), the shape of ratchet ridge, tilting angle of ratchet surface, surface temperature and wettability. Table 6.1 shows a summary of experimental parameters used in this chapter.

Table 6.1 Experimental parameters in Chapter 6.

Subject	Parameter
Ratchet material	Brass, Nickel (Ni)
Ratchet size	p: 75 μm (brass, Ni), 150 μm (Ni), 750 (brass, Ni), 1.5 mm (Ni)
Shape of ratchet ridge	Sharp (S) and round (R)
Ratchet aspect ratio	$d : p$ = 1 : 5 or 1 : 10
Surface temperature	From room temperature to 350 ℃
Liquid type	DI water
Size of liquid	~5 μL (R: ~1.1 mm)
Surface treatment	With and without fluorinated silanes

6.2 Structural Analysis

Figure 6.2 shows SEM images for all various dimensions of ratchets used in this study. Three different ratchet types used in this chapter include:

(1) 75 μm period Ni ratchets with sharp ridges and 1:5 aspect ratio (Figure 6.2(a)),

(2) 750 μm period brass and Ni ratchets with sharp ridges and 1:5 aspect ratio (Figure 6.2(b) and (c)),

(3) 750 μm period Ni ratchets with round ridges and 1:10 aspect ratio (Figure 6.2(d)),

(4) 750 μm period brass ratchets with sharp ridges and 1:10 aspect ratio (Figure 6.2(e)), and

(5) 1.5 mm period Ni ratchets with sharp ridges and 1:5 aspect ratios (Figure 6.2(f)).

By comparing samples (1), (2) and (5), the dependency of ratchet period can be investigated while the comparison of samples (2), (3) and (4) allows for decouple the influence of ratchet aspect ratio and ratchet shape. Some surface defects were generated during the replication procedures. However, the changes in the ratchet shape and dimension were negligible.

The Ni ratchets with round ridges and reduced depths were fabricated by employing 3-D molding process using a thin flexible PDMS intermediate stamp (see Chapter 3.2.3). A blank thin PDMS stamp without containing any structures was used. When the PDMS intermediate stamp was placed between the brass ratchets mold and PMMA sheet during NIL process, the elongational property of the PDMS film and incomplete filling of PMMA produced rounded ratchet ridges with reduced ratchet depth. Figure 6.1 (d) presents an SEM image of the microratchets with round ridges and reduced depths, which was produced with this method using the brass microratchets shown in Figure 6.1 (b). The stylus surface profiler is also used for the more precise structural analysis of the miniaturized ratchets, as shown in figure 6.2.

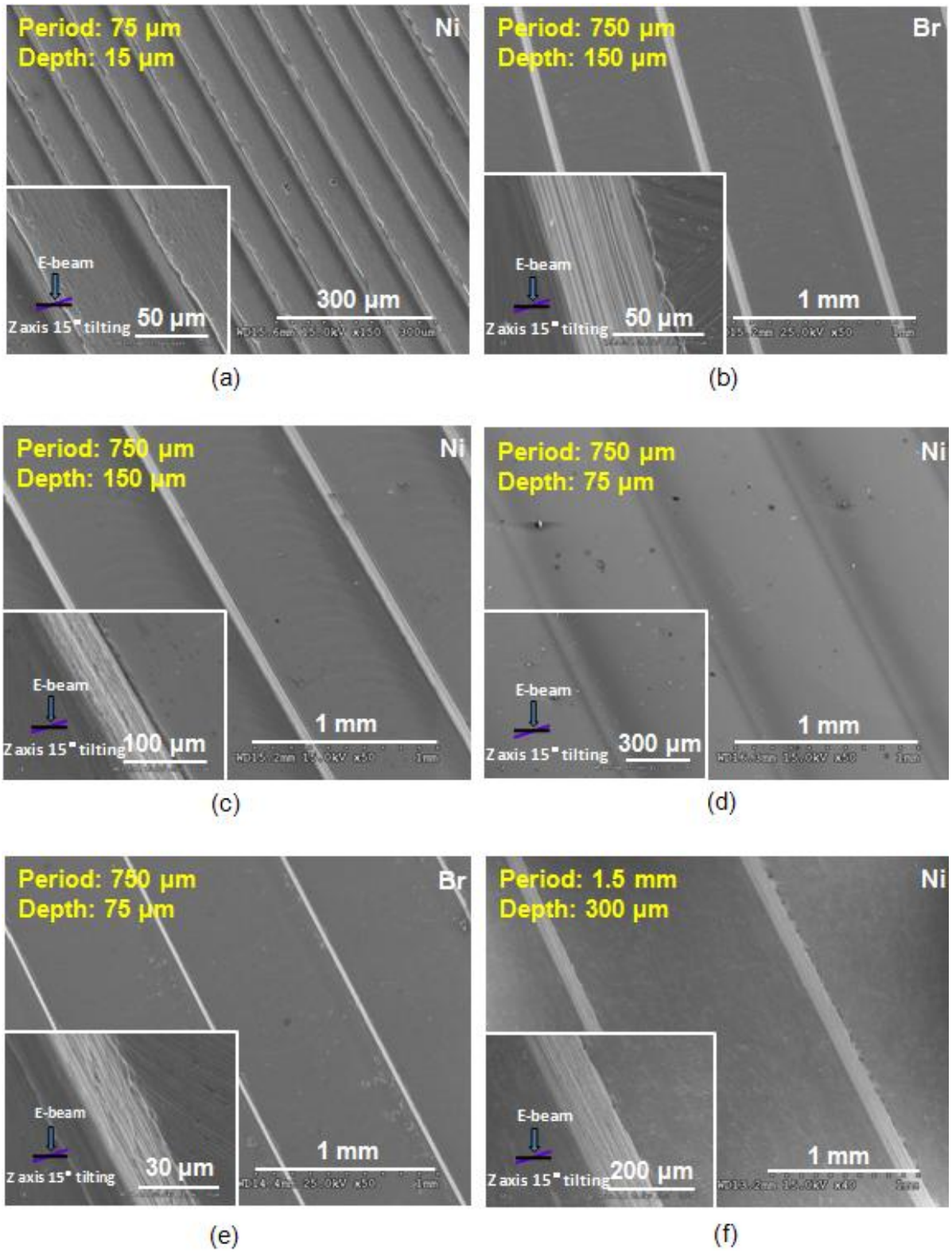

Figure 6.1 (a) – (f) Scanning electron micrographs of micro milled brass and replicated Ni ratchets with their periods of 75, 750 µm and 1.5 mm, respectively, which have depth to period aspect ratio 1:5 or 1:10 with sharp and round ridges of ratchets.

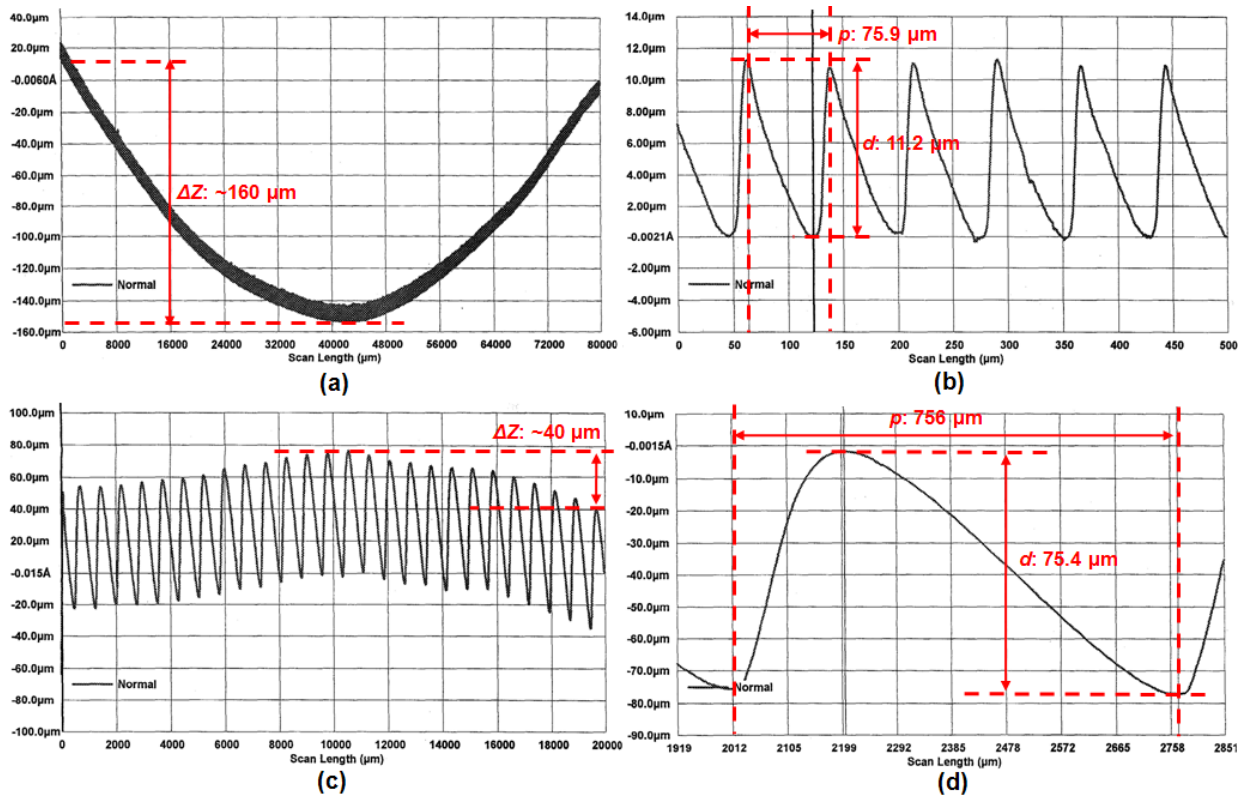

Figure 6.2 Surface morphologies of replicated Ni 75 μm ratchets (*p*: 76.3±0.6 μm, *d*: 11.1±0.3 μm) with sharp shape of edges (a) − (b), and 750 μm ratchets (*p*: 755.6±6.9 μm, *d*: 73.8±1.9 μm) with shallow depths and round shape of edges (c) − (d) scanned by stylus surface profiler (Tencor P-11). *ΔZ* is the maximum vertical variation for overall sample size (scan length: 8 cm).

In table 6.2, the ratchet dimensions designed and measured by surface profiler are summarized. Each value in the table was obtained from three different random measurements. Overall vertical variation or flatness of samples (*ΔZ*) generated by series of milling and replication processes, was in the range of 35 − 270 μm for 8 cm scanning length. Note that the application of 3-D molding process with a blank PDMS stamp reduced the ratchet depth from 130 to 74 μm. In addition, the shape of ratchet ridges was deformed into the round shape. For the convenience sake, the ratchets are identified with the material and desired length to mill (*l*, most left column in table 6.2), instead of either the desired or measured period. For example, even though the

measured period value of Ni 75 μm period of ratchets is 76.3±0.6 μm, it would be just called as Ni 75 μm period of ratchets, not Ni 76.3±0.6 μm period of ratchet.

Table 6.2 Surface morphologies of miniaturized ratchets fabricated by micromilling or replication process. *ΔZ* is the maximum vertical variation for overall sample size (scan length: 8 cm).

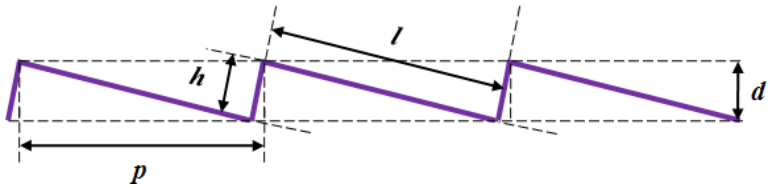

Designed						Measured							
l (μm)	*h* (μm)	*p* (μm)	*d* (μm)	*d/p*	*Mat.*	*l* (μm)	*h* (μm)	*p* (μm)	*d* (μm)	*d/p*	*ΔZ* (μm)	*Edge shape*	*RMS* (μ")
75	15	76.5	14.7	0.19	Brass	75.4±0.0	12.9±0.2	76.7±1.1	12.0±0.1	0.16	~120	sharp	169.9
75	15	76.5	14.7	0.19	Ni	75.4±0.5	14.9±0.2	76.3±0.6	11.1±0.3	0.15	~160	sharp	169.9
150	30	153	29.4	0.19	Ni	147.1±1.0	30.0±0.2	150.5±0.6	29.1±0.6	0.19	~100	sharp	336.8
750	150	764.9	147.1	0.19	Brass	757.6±2.6	149.6±2.3	768.1±3.0	127.6±2.6	0.17	~70	sharp	1674.4
750	75	753.7	74.6	0.1	Brass	748.1±5.2	72.5±0.6	753.3±0.0	70.5±1.0	0.09	~40	sharp	849.5
750	150	764.9	147.1	0.19	Ni	753.3±2.5	145.2±1.5	768.6±0.5	130.3±0.9	0.17	~270	sharp	1674.4
750	75	753.7	74.6	0.1	Ni	753.6±5.2	126.7±0.9	755.6±6.9	73.8±1.9	0.1	~35	round	-
1500	300	1529.7	294.2	0.19	Ni	1461.0±21.7	282.8±3.1	1513.0±17.8	249.8±1.4	0.17	~150	sharp	3346.2

6.3 Characteristics of Liquid Motion

The enhanced experimental setup equipped with a high speed camera was used to characterize millimetric DI water droplet motion along the various dimensions of heated metallic miniaturized ratchets. The detailed procedures are described in Chapter 3.4.2. Low frame rate (250 or 500 fps) and low magnification (with 5 mm or 30 mm spacer) recording was used to evaluate the trajectory and velocity characterization for droplet motion over the entire ratchet surface. High frame rate (1000 fps) and high magnification (with 80 mm spacer) recording was used to visualize the point of droplet impact on the ratcheted surface. In-house developed image processing tools using Optimas 6.5 and Matlab R2009a were used to extract appropriate data

from captured pictures of droplet motion (Laveau 2008).

6.3.1 The Influence of Surface Temperature

In Chapter 4, we observed different droplet behavior on miniaturized ratchet surface at different surface temperatures. In *L* regime, the mean velocity of liquid droplet (v_m) for the whole path increases as ratchet period (*p*) decreases, due to the direct contacts between ratchet top peaks and bottom of droplet. Fully levitating droplets by thick vapor layer in the *H* regime, however, does not show significant dependence on the ratchet period. In this section, the motion of DI water droplets were investigated using high speed camera at various surface temperatures in the range of 186 − 313°C for two different ratchet materials and periods (Ni 150 μm and brass 750 μm). The aspect ratios (*d/p*) for those ratchets used were similar each other in the range of 0.17 – 0.19.

The influence of the surface temperature was first investigated with the 750 μm period brass ratchets. Figure 6.3 (a) shows vertical trajectories of DI water droplets as they move horizontally along the ratchets at two different ratchet surface temperatures of 186.3±3.2℃ and 295±3.0℃. The two temperatures represent *L* and *H* regimes, respectively. Comparing the motion of droplets at two different surface temperatures, the number of vertical oscillations over the entire path of the droplet along the ratchets in the *L* regime is much fewer than that in *H* regime while the both oscillation amplitudes were reduced in a similar way. The frequencies for the bounces and oscillations are similar to each other at around 40±1.0 *Hz*. In all, the trajectories of droplets on the brass ratchets (*p*: 750 μm) are similar in both *L* and *H* regimes. The main difference between the two temperature regimes is the horizontal velocity, which is much faster in the *L* regime as shown in figure 6.3 (c). Figure 6.3 (b) shows the kinetic energy *K.E.(x)* of droplets as function of horizontal trajectory for both temperature regimes.

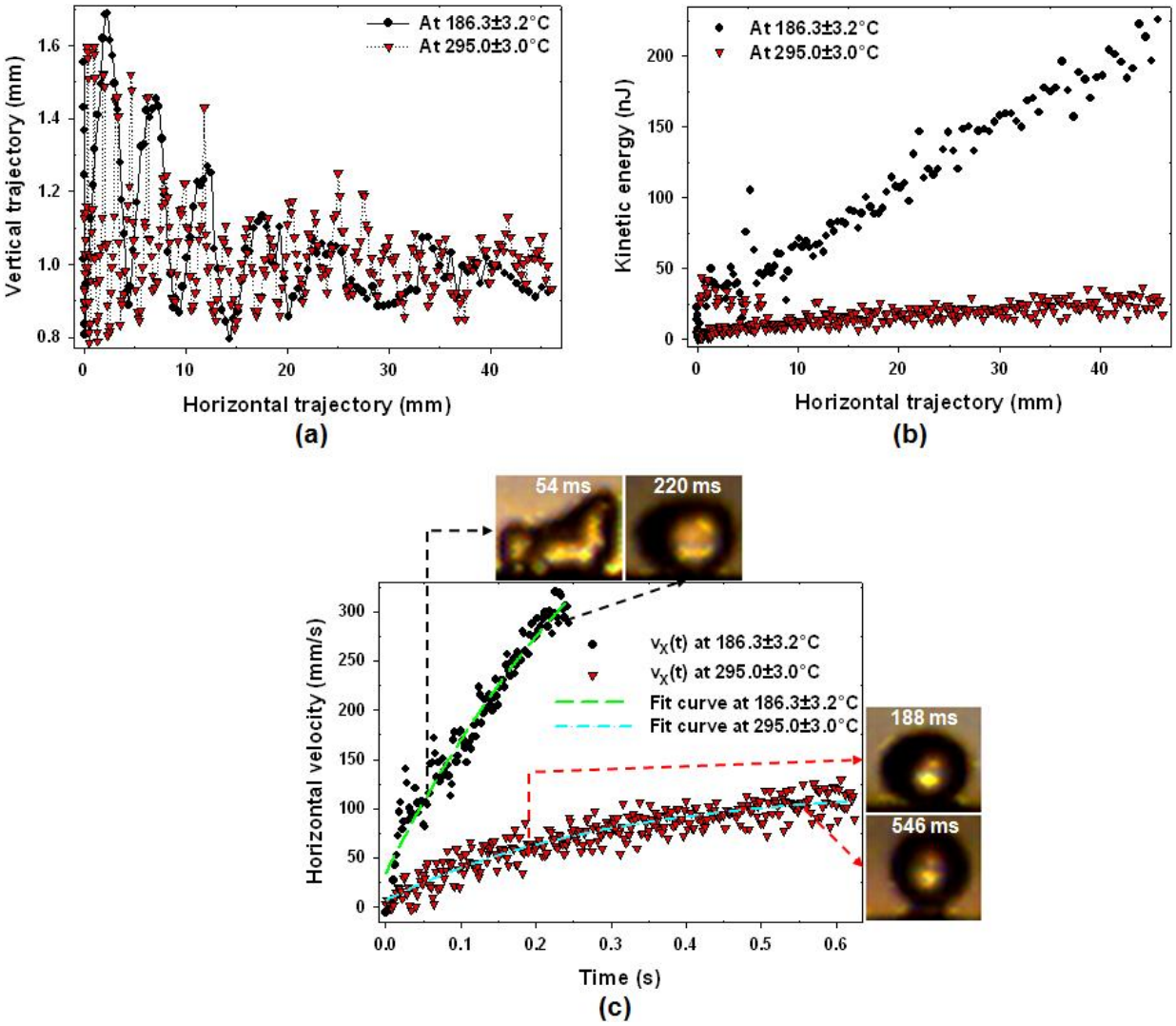

Figure 6.3 (a) Vertical trajectories *z(x)*, (b) kinetic energies *K.E.(x)* as functions of their horizontal trajectories and (c) horizontal velocities $v_x(t)$ of DI water droplets with brass 750 μm period of ratchets in *L* (186.3±3.2 ℃) and *H* (295±3.0 ℃) regimes. The fitting curves for the graphs in (c) are $v_x(t) = -603.73e^{-(2.54)t} + 638.10$ in *L* regime and $v_x(t) = -113.92e^{-(3.41)t} + 106.88$ in *H* regime.

Table 6.3 shows various parameters relevant to the experiments and derived by fitting the horizontal velocity versus time curve with equation 5.5. Slight different initial droplet volumes (V_0) of 4.5 and 5.9 μL were measured with the same target volume of 5 μL for the syringe pump. Also, a slight variation in the needle height from the ratchet surface (2.58 and 2.26 mm) was inevitable due to manual alignment, which results in slight different initial impact speeds (v_0: 8.2 and 2.0 cm/s) and Weber numbers (*We*: 0.34 and 0.01). However, such small differences in v_0 and

We do not influence the droplet motion significantly, as was previously shown in the Chapter 5.3.2. The terminal velocity (v_t) at 186.3±3.2 ℃ in the *L* regime is about three times faster than that at 295±3.0 ℃ in the *H* regime. Time (*t*) for the droplet to move the entire path (*S*) of 4.6 cm was 236 ms and 616 ms at these two temperatures, respectively. The mean velocity of the droplet motion (v_m) calculated by *S*/*t* was 19.45 (in *L* regime) and 7.47 cm/s (in *H* regime). Constant acceleration value of the motion at 186.3±3.2 ℃ which was obtained by fit equation (5.5) is almost forth times of that at 295±3.0 ℃.

Table 6.3 Experimental parameters for droplet motion on the brass 750 μm period of ratchets at two surface temperatures of 186.3±3.2 and 295±3.0 ℃.

T_s (℃)	V_0 (μL)	*We*	v_t (cm/s)	$v_x(0)$ (mm/s)	β/m (s^{-1})	a (m/s^2)	$\frac{a}{\beta/m}$ (cm/s)
186.3±3.2	4.5	0.35	30.3±1.2	34.1	2.54	1.62	56.94
295.0±3.0	5.9	0.01	10.9±1.1	7.0	3.41	0.41	10.69

Two different net acceleration values ($\frac{dv_x}{dt}$ or $\frac{d^2x}{dt^2}$) experienced by the droplet, can be extracted and compared from the curves: initial and final acceleration. Initial net acceleration can be obtained from the sharp slope in the horizontal velocity versus time curve near the injection area while the slow slope of the linear region gives final net acceleration. The initial net acceleration values in *L* and *H* regimes are 6.24 and 0.86 m/s^2, respectively. Droplet in *L* regime accelerate about 7 times faster than that in *H* regime, the ratio of which was similar for the final net acceleration values of 0.89 and 0.11 m/s^2.

When a droplet impinges on a surface with a kinetic energy, the kinetic energy is dissipated by viscosity as the drop spread on the surface, in particular owing to the moving contact lines close to which viscous losses are enhanced (Rein 1993). For Leidenfrost droplets, a remarkable dynamic characteristic is shown: upon impact the droplets bound. Since there is no contact line,

kinetic energy efficiently converts to surface energy and then to kinetic energy again, allowing the system to behave as an elastic spring (Biance, Chevy et al. 2006). The rebounding of droplet is more elastic (called as quasi-elastic) when the impact speed is small. This characteristic is independent of the surface temperature in the range of 166 − 375°C. In the *L* regime where there are direct local contacts between the droplet bottom and ratchet top edges, both mechanisms (viscous loss and conversion into surface energy) may play a role upon droplet impact. In addition to the two mechanisms, thermal energy will be transferred from the surface into the droplet through ratchet top edges, which is the main mechanism to accelerate the droplet motion. The amount of viscous loss increases as the effective area of the direct contacts between the droplet bottom and ratchet top edges increases. Therefore, significant reduction in the amplitude of the oscillation upon initial impact can be attributed to the viscous loss due to the increased contact area at a high initial impact speed. The high effective contact area in turn increases the heat transfer into the droplet, showing high initial acceleration. Such behavior occurs at a couple of initial oscillations where droplets fully rebound from the surface.

After initial rebounding, the amplitude of vertical oscillation keeps decreasing by viscous loss while the droplet is moving in one direction. The high acceleration occurs when the amplitude of the vertical oscillation was significantly reduced. From this observation, it can be deduced that vertical oscillation of droplet increases the resistance to droplet motion. This can be easily understood because the downward motion of droplet in partial contact with ratchets surface gives rise to additional normal force to overcome for lateral droplet motion. Only after the vertical oscillation is significantly reduced, then the droplet can receive full acceleration. At high surface temperature in *H* regime, the acceleration either continuously decreases or remains at a similar amplitude. We attributed this behavior to the thick vapor layer present beneath the

droplet, which reduces the viscous loss upon rebounding. Therefore, a sudden decrease of oscillation amplitude is prevented.

We investigated the motion of water droplet on the brass 750 μm ratchets only in typical *L* and *H* regimes. In order to understand the influence of ratchet surface temperature on the motion of droplet in depth, we investigated the droplet motion for various surface temperatures. For this purpose, the replicated Ni 150 μm period of ratchets was employed and the motion of droplet was characterized with five different temperatures in the range of 214 − 313°C. The surface temperatures were varied by 18 − 34°C. The droplets with similar volumes (V_0: 3.8 – 5.2 μL) were released at a similar needle height (H_0: 2.28 – 3.69 mm). Three to five droplets were repeated at each temperature. All the droplet motion at different temperatures was consistent and reproducible in a similar degree to that described in Chapter 5.3.1.

Figure 6.4 (a) shows the horizontal velocity as a function of their horizontal trajectory for five different surface temperatures. All data, except those at 214.0±1.7 ℃, fit well with equation (5.5). The horizontal velocity $v_x(x)$ at 214.0±1.7 ℃ does not show a saturated value by the end of the ratchet path, unlike the profiles of $v_x(x)$ at other temperatures, where after a steep increase of the horizontal velocity near the injection area (to ~5 mm), the velocity increase slows down and reaches a constant speed at the end of the path. At 214.0±1.7 ℃, the significant deformation of the lateral shape of the droplet continued until $v_x(x)$ saturated near the end of the whole path, as shown in the inset of figure 6.4 (a). The upper sequence is obtained at T_s 214.0±1.7 ℃ while the lower one at T_s 313.0±2.6 ℃. From this observation, it can be deduced that when extremely high acceleration *a* exists, the resistance to the droplet motion also increases.

Figure 6.4 (b) shows terminal velocity v_t, mean velocity v_m and acceleration *a* of droplet as a function of surface temperature. v_t, v_m, and *a* decreases as T_s increases. This result is consistent

with the data from the micromilled brass 150 μm ratchets as shown in Chapter 4 (see Figure 4.5). v_t and a rapidly decrease in lower T_s ranges (214.0±1.7 to 232.7±5.1 ℃) and then gradually decrease in other ranges of T_s (232.7±5.1 to 313.0±2.6 ℃). It is speculated that real contact area between bottom surface of the droplet and top of the ratchets ridges significantly decreases around 232.7±5.1 ℃. The reason for the slow decrease between 232.7±5.1 ℃ to 313.0±2.6 ℃ might be the temperature dependence of vapor film thickness ($h \propto \Delta T^{1/4}$, where $\Delta T = T_s - T_b$) and vapor viscosity (ν). Table 6.4 shows parameters relevant to the experiments. Higher accelerations (a) and lower drag parameters (β/m) were obtained at lower temperatures.

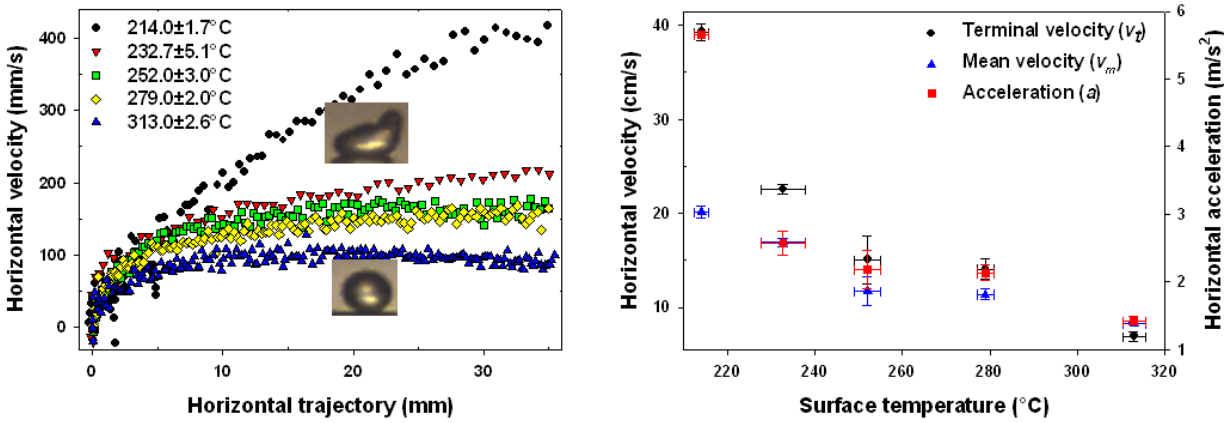

(a) (b)

Figure 6.4 (a) Horizontal velocity v_x of droplet as a function of horizontal trajectory x at five different surface temperatures and (b) terminal velocity v_t, mean velocity v_m and acceleration a of droplet as a function of surface temperature for Ni 150 μm ratchets.

Table 6.4 Relative parameters for figure 6.4 (b) (Ni 150 μm ratchets with varied T_s).

T_s (℃)	V_0 (μL)	*We*	v_m (cm/s)	v_t (cm/s)	$v_x(0)$ (mm/s)	β/m (s^{-1})	a (m/s^2)	$\frac{a}{\beta/m}$ (cm/s)
214.0±1.7	4.7±0.4	1.12±0.05	20.2±0.6	39.3±0.9	-707.0±0.0	10.5±0.0	5.66±0.00	54.0±0.0
232.7±5.1	4.5±0.2	0.85±0.02	16.9±0.4	22.6±0.5	-8.4±4.6	10.7±0.7	2.57±0.18	23.9±0.6
252.0±3.0	4.8±0.0	0.26±0.00	11.7±1.5	15.1±2.6	-28.1±4.9	14.0±0.4	2.19±0.28	15.6±2.5
279.0±2.0	5.2±0.0	0.09±0.01	11.4±0.6	14.1±1.0	-3.7±3.5	14.8±1.5	2.14±0.12	14.5±1.3
313.0±2.6	3.8±0.0	0.50±0.10	8.3±0.1	6.9±0.5	-4.0±31.0	14.8±0.5	1.43±0.06	9.6±0.7

6.3.2 The Influence of Ratchet Period

Now, let us consider the influence of ratchet period on the droplet motion. Based on previous observation using primitive experimental setup in Chapter 4, the droplet velocity is significantly affected by the ratchet period in *L* regime while it shows almost negligible effect in *H* regime. Figure 6.5 shows vertical trajectory and horizontal velocity of a moving droplet on Ni micro ratchets with two different periods (*p*: 150 μm and 1.5 mm) in *L* regime. The specific parameters and extracted data are given in table 6.5. For the trajectory of droplet on 1.5 mm period Ni ratchets, the droplet moves along the ratchets without rebounding. Vertical fluctuation of droplet trajectory comes from the ratchet geometry and its oscillation. But for the trajectory of the droplet on 150 μm period Ni ratchets, vertical fluctuations are induced by both rebounding and its oscillation. For 150 μm period Ni ratchets, the needle height could not be reduced below certain level (~ 3.7 mm) at 214.0±1.7 ℃ because the released droplet tended to bounce back from the ratchets and attach to the needle. The motion of droplet on 150 μm period Ni ratchets is much faster than that on Ni 1.5 mm period of ratchets due to the different number of ratchets beneath a droplet.

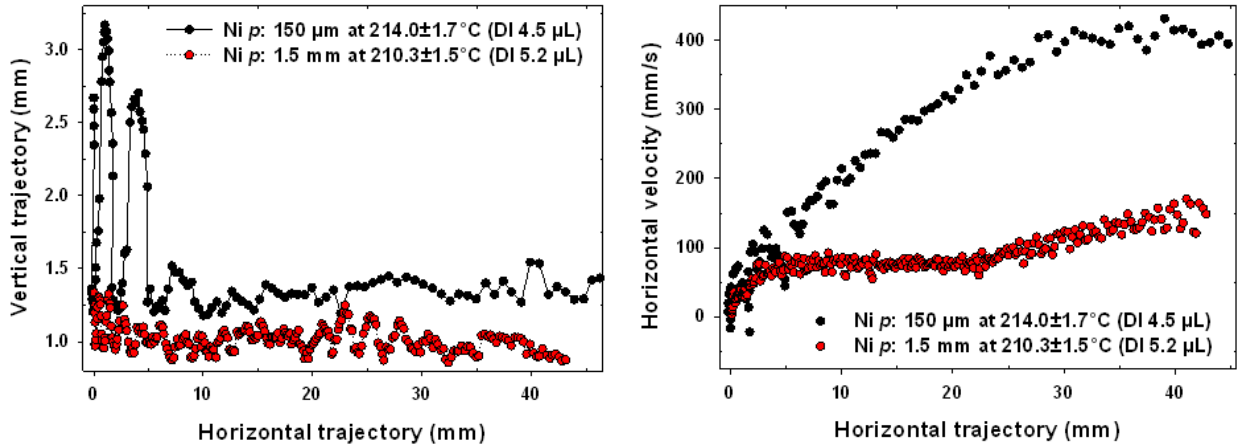

(a) (b)

Figure 6.5 Comparison of droplet behavior on Ni miniaturized ratchets with 150 μm and 1.5 mm periods in *L* regime: (a) vertical trajectory of droplet *z(x)* and (b) horizontal velocity of droplet $v_x(x)$ as a function of horizontal trajectory of droplet.

Table 6.5 The values of relative parameters for figure 6.5 (Ni miniaturized ratchets in *L* regime, *p*: 150 μm, 1.5 mm).

p (μm)	T_s (℃)	V_0 (μL)	We	v_m (cm/s)	v_t (cm/s)	$v_x(0)$ (mm/s)	β/m (s^{-1})	a (m/s^2)	$\frac{a}{\beta/m}$ (cm/s)
150	214.0±1.7	4.5	1.07	20.67	40.3±1.6	-707.02	10.48	5.66	54.04
1500	210.3±1.5	5.2	0.04	8.26	15.0±2.2	3.49	14.22	1.21	8.51

Figure 6.6 (a) shows the trajectories of droplets on the two miniaturized ratchets with different dimensions (*p*: 150 μm and 1.5 mm) in *H* regime. Relatively large vertical fluctuation of droplet on 1.5 mm period ratchets by rebounding and self oscillation is believed to be formed by the higher ratchet depth (~250 μm), which is almost ten times higher than that of 150 μm period ratchets (~29 μm), more significantly deforming the droplet shape. Figure 6.6 (b) shows horizontal velocities of moving droplets along these ratchets in *H* regime. Even though both values of v_m and v_t from different ratchets have within ~ 1.6 cm/s differences as shown in table 6.6, their velocity profiles are pretty similar each other. However, acceleration values from fit equation (5.5) still have ~ 1.7 times difference.

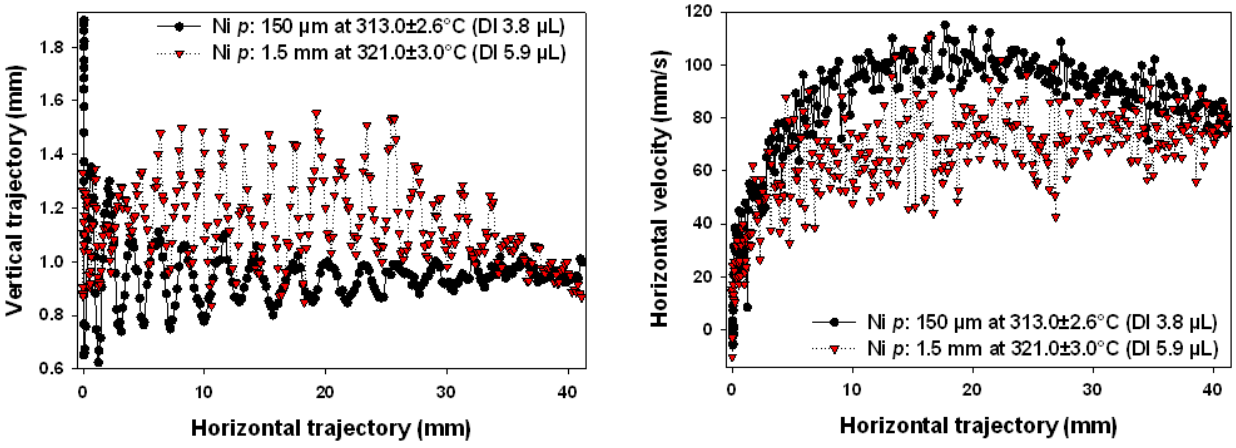

(a) (b)

Figure 6.6 Comparison of miniaturized ratchets with Ni 150 μm (*d/p*: 0.19) and Ni 1.5 mm period (*d/p*: 0.17) in *H* regime: (a) vertical trajectory of droplet and (b) horizontal velocity of droplet as a function of horizontal trajectory of droplet.

Table 6.6 The values of relative parameters for figure 6.6 (Ni miniaturized ratchets, *p*: 150 and 1500 μm in *H* regime).

p (μm)	T_s (℃)	V_0 (μL)	We	v_m (cm/s)	v_t (cm/s)	$v_x(0)$ (mm/s)	β/m (s^{-1})	a (m/s^2)	$\frac{a}{\beta/m}$ (cm/s)
150	313.0±2.6	3.8	0.57	7.92	8.1±0.4	-25.57	14.88	1.36	9.14
1500	321.0±3.0	5.9	0.15	6.35	7.7±0.4	1.21	10.82	0.80	7.4

In summary, the influence of surface temperature and ratchet period on the motion of small water droplets with R < *a*, having almost spherical shapes from the lateral view, was reevaluated by the enhanced setup. The results are consistent with those by the primitive one, showing ratchets scaling only effective in *L* regime, but not significant in *H* regime.

6.3.3 The Influence of Ratchet Aspect Ratio and Shape of Ratchet Ridge

6.3.3.1 Low Magnification Analysis

The influence of ratchet aspect ratio and shape of ratchet ridges on the droplet motion was investigated with two different micro ratchets having similar periods of 768.6±0.5 μm and 755.6±6.9 but different depths (130.3±0.9 μm and 73.8±1.9 μm) and ridge shapes (sharp and round). SEM images of the samples used in this study are shown in figure 6.1 (c) and (d). Table 6.2 presents their scanned surface data, where ΔZ is the maximum vertical variation over 80 mm and 20 mm scanning lengths for the sharp and rounded ratchets, respectively.

Figure 6.7 shows experimental results on the influence of ratchets aspect ratio and their ridge shape at a temperature in *L* regime. When shallow and rounded ratchets were used, the droplet continuously rebounded while moving over the entire path of the ratchet surface. This is different from the case of deep and sharp ratchets where the amplitude of vertical trajectory gradually decreases. Such motion with successive rebounds was observed in the range of surface temperature 192 − 248°C. Below this temperature zone, the injected droplets were dispersed and

quickly evaporated. Above this zone, the droplets moved in random directions, not guided by ratchets. The terminal velocity v_t from the shallow, rounded ratchets was 4.2±0.7 cm/s, which was lower than half of that from normal-sharp ratchets (10.9±1.6 cm/s). We speculate that the loss of sharpness at ratchet ridges reduces viscous loss during impact of droplet on the surface. In addition, the low aspect ratio for the shallow ratchets also reduces the local pressure gradient of the vapor flow below the droplet. As a result, the droplet bounces more elastically with reduced horizontal velocity.

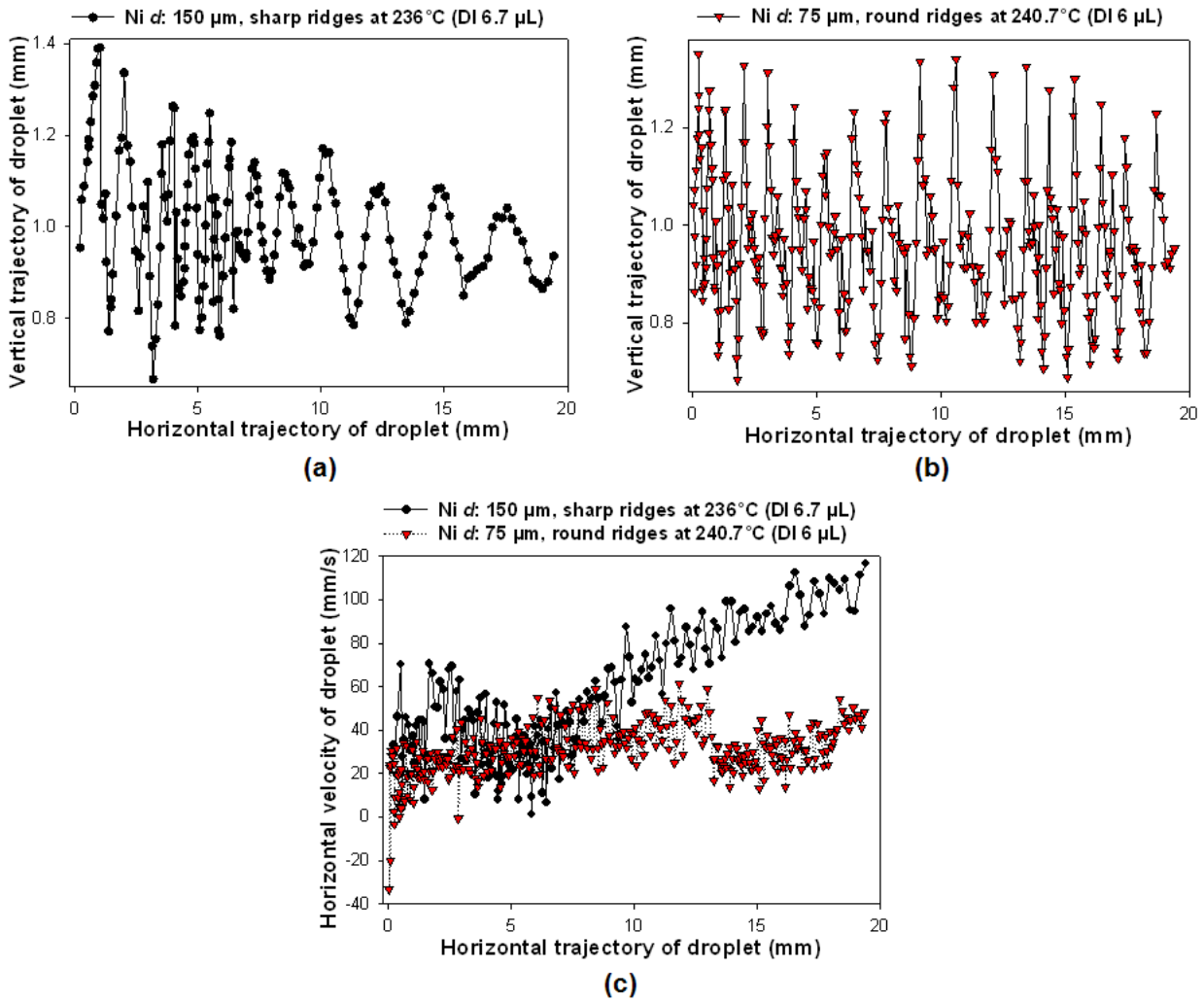

Figure 6.7 The influence of aspect ratio and roundness: vertical trajectory of the droplet on (a) microratchets (*p*: 768.6±0.5 µm, *d*: 130.3±0.9 µm) with sharp ridges, (b) microratchets (*p*: 755.6±6.9 µm, *d*: 73.8±1.9 µm) with round ridges and (c) horizontal average velocity of droplet on both of microratchets as a function of horizontal trajectory of droplet.

The restitution coefficients (e) of rebounding droplet, defined as $e = v_0'/v_0$, where v_0 and v_0' are impact and take-off velocity of droplet, respectively (Biance, Chevy et al. 2006), are very close to unity (~ 1) for all rebounds, which is very similar behavior observed with film boiling droplets on flat smooth surface (Biance, Chevy et al. 2006).

6.3.3.2 High Magnification Analysis

It is useful to investigate the behavior of droplet in the injection area with high magnification. Figure 6.8 shows video sequences of droplet motion on three different ratchets: 750 μm period Ni ratchets with deep and sharp ratchet ridges ($p = 768.6 \pm 0.5$ μm, $d = 130.3 \pm 0.9$ μm, aspect ratio = 0.17), 750 μm period Ni ratchets with shallow and rounded ratchet ridges ($p = 755.6 \pm 6.9$ μm, $d = 73.8 \pm 1.9$ μm, aspect ratio = 0.1) and 75 μm period Ni ratchets with deep and sharp ratchet ridges ($p = 76.3 \pm 0.6$ μm, $d = 11.1 \pm 0.3$ μm, aspect ratio = 0.15). All experimental conditions, except the ratchet shapes and dimensions, were kept similar to each other (similar surface temperature T_s, needle height H_0, initial droplet volume V_0). For both 750 μm period ratchets with sharp and round ridges, small secondary atomization, i.e. defragmentation into small droplets, upon initial impacts are seen as black mist around the droplets. Also, the droplets are significantly deformed. Secondary atomization is usually observed with Leidenfrost droplets when the surface temperature is lower than dynamic Leidenfrost temperature (Bertola and Sefiane 2005). This happens by bursting on droplet surface of vapor bubbles generated at contact points between the liquid and the hot surface. On the other hand, for 75 μm period ratchets with deep and sharp ridges, no secondary atomization was observed and the droplet deformation upon impact was relatively small.

In order to decouple the influence of ratchet geometries from the influence of elevated temperature, we repeated the experiments at room temperature. Figure 6.9 shows image

sequences showing the progressive motion of ejected droplets on three different ratchets. All ejected droplets were gradually spread out along the ratchets surface without any secondary atomization and rebound. The degree of droplet deformation is in the decreasing order of 750 μm deep and sharp ratchets, 750 μm shallow and rounded ratchets, and 75 μm deep and sharp ratchets. We can conclude that the degree of droplet deformation is mainly determined by the ratchet geometries, increasing with large surface roughness (RMS roughness parameter: 75 μm deep-sharp ratchets = 528, 750 μm shallow-rounded ratchets = 3247.2 and 750 μm deep-sharp ratchets = 5614.4), while the second atomization is related to the boiling phenomenon at elevated temperature.

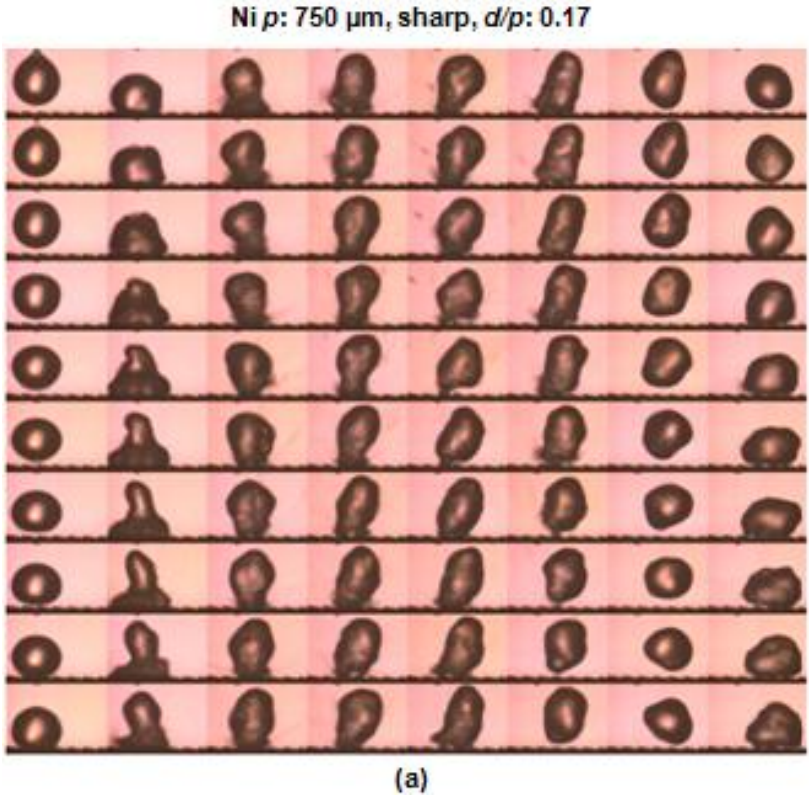

Figure 6.8 The video sequences recorded by high speed camera (Kodak Ektapro 1000HRC, magnification: 80 mm spacer, frame rates: 1000 fps, expose time: 1 ms and time interval between successive images: 1 ms): (a) Ni 750 μm ratchets with sharp ridges (*p*: 768.6±0.5 μm, *d/p*: 0.17) at 234.3±0.6 ℃ (80 frames), (b) Ni 750 μm ratchets with round ridges (*p*: 755.6±6.9 μm, *d/p*: 0.1) at 238.7±2.1 ℃ (80 frames), (c) Ni 75 μm ratchets with sharp ridges (*p*: 76.3±0.6 μm, *d/p*: 0.15) at 237.3±2.1 ℃ (50 frames).

(Figure 6.8 continued)

Ni *p*: 750 µm, round, *d*/*p*: 0.1

(b)

Ni *p*: 75 µm, sharp, *d*/*p*: 0.15

(c)

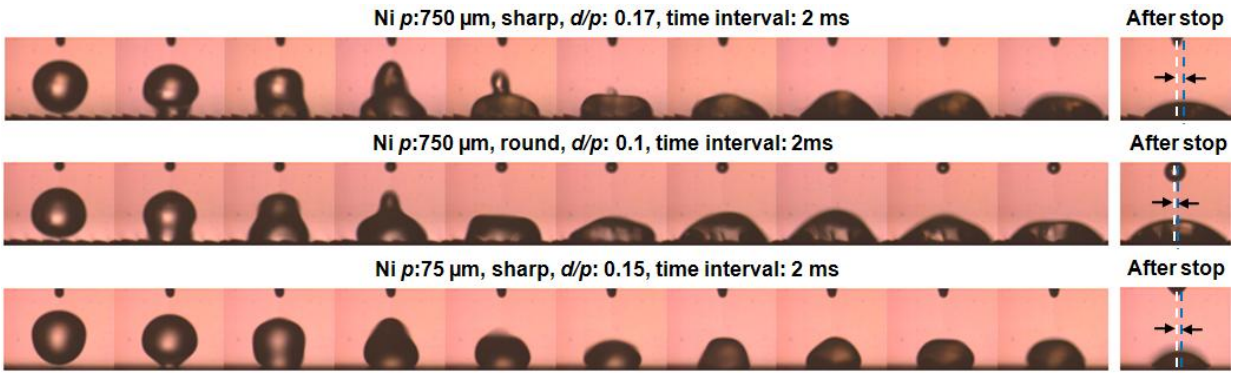

Figure 6.9 The video sequences recorded by high speed camera (magnification: 80 mm spacer, frame rates: 1 kfps, expose time: 1 ms and time interval between successive images: 1 ms): (top) Ni 750 µm ratchets with sharp ridges (*p*: 768.6±0.5 µm, *d/p*: 0.17), (middle) Ni 750 µm ratchets with round ridges (*p*: 755.6±6.9 µm, *d/p*: 0.1), (bottom) Ni 75 µm ratchets with sharp ridges (*p*: 76.3±0.6 µm, *d*/*p*: 0.15) at room temperature.

When a water droplet was put on ratchets surface at room temperature, there was always a slight lateral shift of the center of mass of droplet after its initial impact toward slowly inclined surface of ratchets. The rightmost pictures of figure 6.9 show the photographs after the motion of droplet is completed. White (or bright) dot lines correspond to the horizontal positions of the center of mass of droplets where they release. Blue (or dark) dot lines are indicative of the center of mass after completing their dynamic behavior. The maximum shift (~ 380 µm) was observed with the 750 µm deep-sharp ratchets while negligible shifted length from the 750 µm shallow-rounded ratchets. From the top view, released liquids have an oval shape, which are longer along the wide ratchet grooves [into and out of the page in figure 6.9].

6.3.3.3 The Influence of Surface Temperature on Shallow and Rounded Ratchets

In order to explore the continuous bouncing of droplets observed with 750 µm shallow-rounded ratchets, we performed additional experiments at different surface temperatures in the range of 192 − 248°C. Figure 6.10 (a) – (c) show vertical trajectory and horizontal velocity (d) versus horizontal trajectory for three different surface temperatures. Table 6.7 provides the parameters related to figure 6.10. For all temperatures, the droplet continuously rebounds until it

completely leaves the sample surface. The rebounding frequencies were also in a similar range of 25.1 – 28.7 Hz. The main difference is the terminal velocity, which decreases as T_s increases.

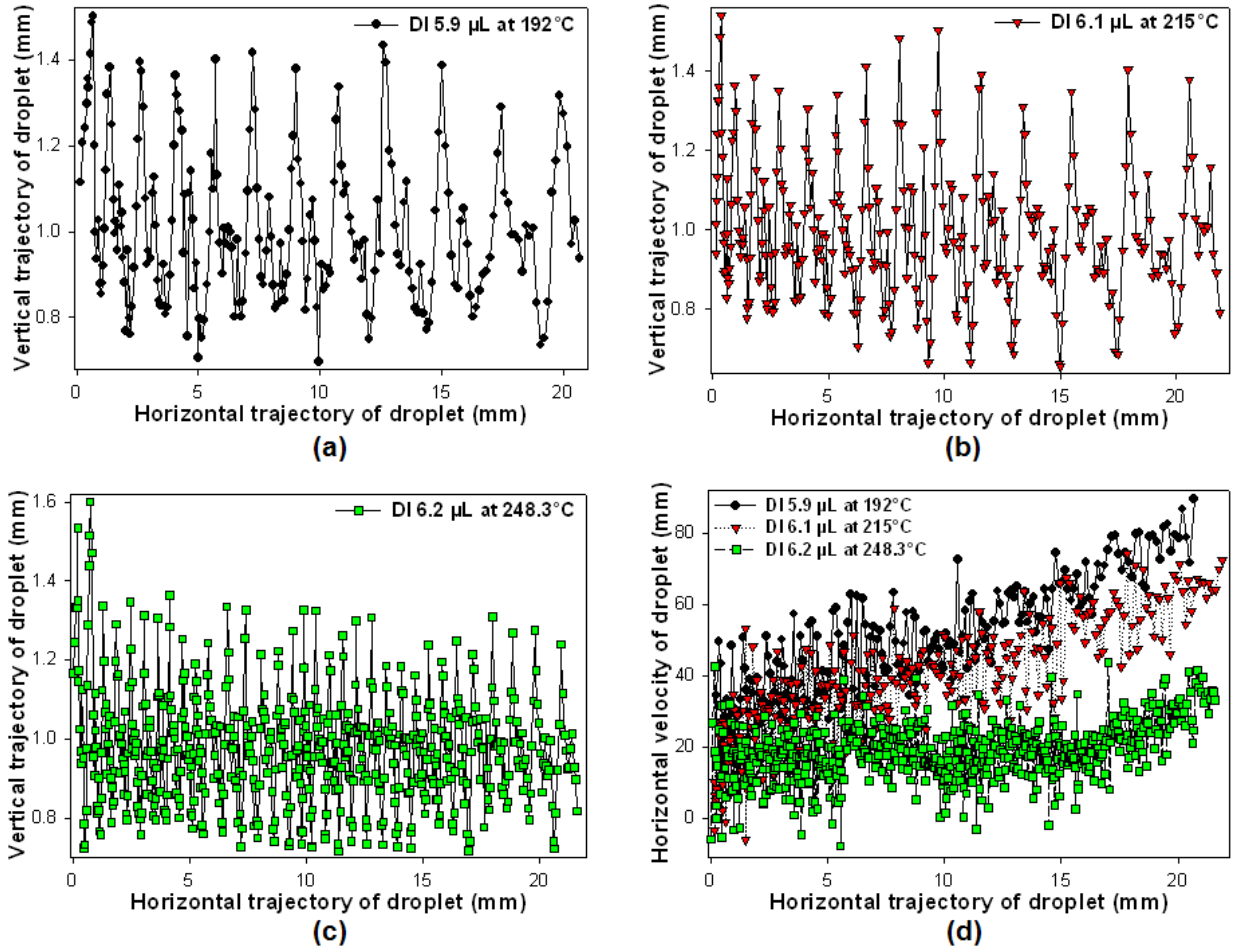

Figure 6.10 Temperature dependence of DI droplet motion on Ni 750 µm shallow-rounded ratchets: trajectory of droplet (a) at 192±1.0 ℃, (b) at 215±1.0 ℃, and (c) at 248.3±0.6 ℃, (d) horizontal velocity as a function of horizontal trajectory at three different temperatures.

Table 6.7 Temperature dependent parameters of droplet motion on Ni 750 µm shallow-rounded ratchets (*p*: 755.6±6.9 µm, *d/p*: 0.1) for figure 6.10, *We*: Weber number, *t*: passing time, *N*: number of rebounds for whole path, *f*: rebounding frequency (*N*/*t*).

T_s (℃)	V_0 (µL)	D_0 (mm)	H_0 (mm)	v_0 (cm/s)	*We*	*t* (ms)	*N*	*f* (Hz)	v_t (cm/s)
192.0±1.0	5.9	2.24	3.09	12.91	0.61	418	12	28.71	7.7±0.7
215.0±1.0	6.1	2.27	3.19	13.43	0.67	558	14	25.09	6.4±0.6
248.3±0.6	6.2	2.28	3.19	13.36	0.65	1,158	33	28.50	3.3±0.5

Figure 6.11 (a) shows residence time and flying time as a function of surface temperature. Residence time is defined as the time interval from the instant when droplet reaches the ratchet surface to the instant when it leaves the ratchet surface for each bounce. Flying time is the time duration when droplet is detached from the surface upon rebounding. Both show temperature-independent characteristics. Averaged horizontal v_t, calculated from the last 20 horizontal droplet velocities, decreases with T_s as shown in figure 6.11 (b). Similar vertical variations by rebounds for all observed T_s and temperature independent flying time support that restitution coefficient (e) is very close to unity (quasi-elastic behavior). The large deviated data for the flying time of droplet by every rebound might be partially related to the uncertainty in the measurement and the oscillation of the droplet.

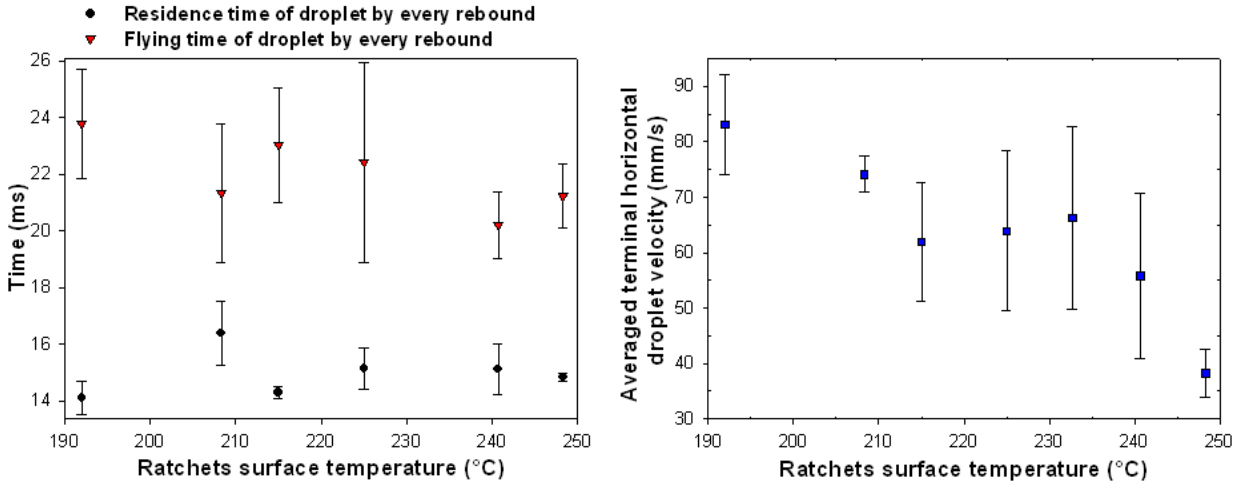

(a) (b)

Figure 6.11 Temperature dependence (a) of residence and flying time of droplet by every rebound, (b) of averaged terminal velocity (v_t) of droplet on Ni 750 μm shallow-rounded ratchets (p: 755.6±6.9 μm, d/p: 0.1).

6.3.4 The Influence of Ratchet Depth

In the previous experiments, the use of rounded ratchet ridges and low aspect ratio (d/p ~0.1) resulted in continuous rebounding with reduced horizontal velocity with respect to ratchets with the same period but with sharp ridges and high aspect ratio (d/p ~0.2) In order to able to

decouple the effect of the ridge shape from that of the ratchet aspect ratio, we have fabricated additional brass ratchets with the same period (p = 750 μm) but with two different depths (*d*: 75 and 150 μm), as shown in figure 6.1 (b) and (e), figure 6.2 (c) and (d). The corresponding ratchet depth to period aspect ratios are 0.09 and 0.17, respectively. The main parameter to see was the surface temperature (T_s: 192.7±2.1 ℃ – 298.7±2.1 ℃). All other experimental conditions were kept similar to each other. The radii of all released DI water droplets were around 1 mm right after they left the needle. The needle height to release all droplets was in the range of 2.6 – 3.0 mm. The corresponding impact velocities were ~10 cm/s. Figure 6.12 (a) and (c) display the temperature dependent trajectories obtained from both deep (*d*/*p*: 0.17) and shallow ratchets (*d*/*p*: 0.09). The directional droplet motion with continuous bouncing was observed for both ratchets at the lowest T_s (~193 ℃). Deep ratchets generated more elastic rebounding, as can be seen from the larger amplitude of vertical oscillation. At all other surface temperatures, the droplets rebounded just a few times only near the injection area. After then, they dislocated without bouncing. The droplet trajectories did not significantly vary with the ratchet depth. Therefore, one can conclude that roundness in the shape of ratchet ridges is more responsible for the continuous rebounding which was observed with shallow and rounded ratchets in the previous section. Figure 6.12 (b) and (d) also show the temperature dependent mobility obtained from both ratchets, which is well matched with our previous observation. The fastest mobility was obtained in *L* regime for both ratchets. Less mobile droplet motions were observed with higher T_s. Temperature dependent vapor layer thickness ($\propto \Delta T^{1/3}$), where ΔT is the temperature with respect to the boiling temperature ($\Delta T = T_s - T_b$), dominates the heat transfer between liquid and solid ratchets surface because evaporating vapor is excellent thermal insulator.

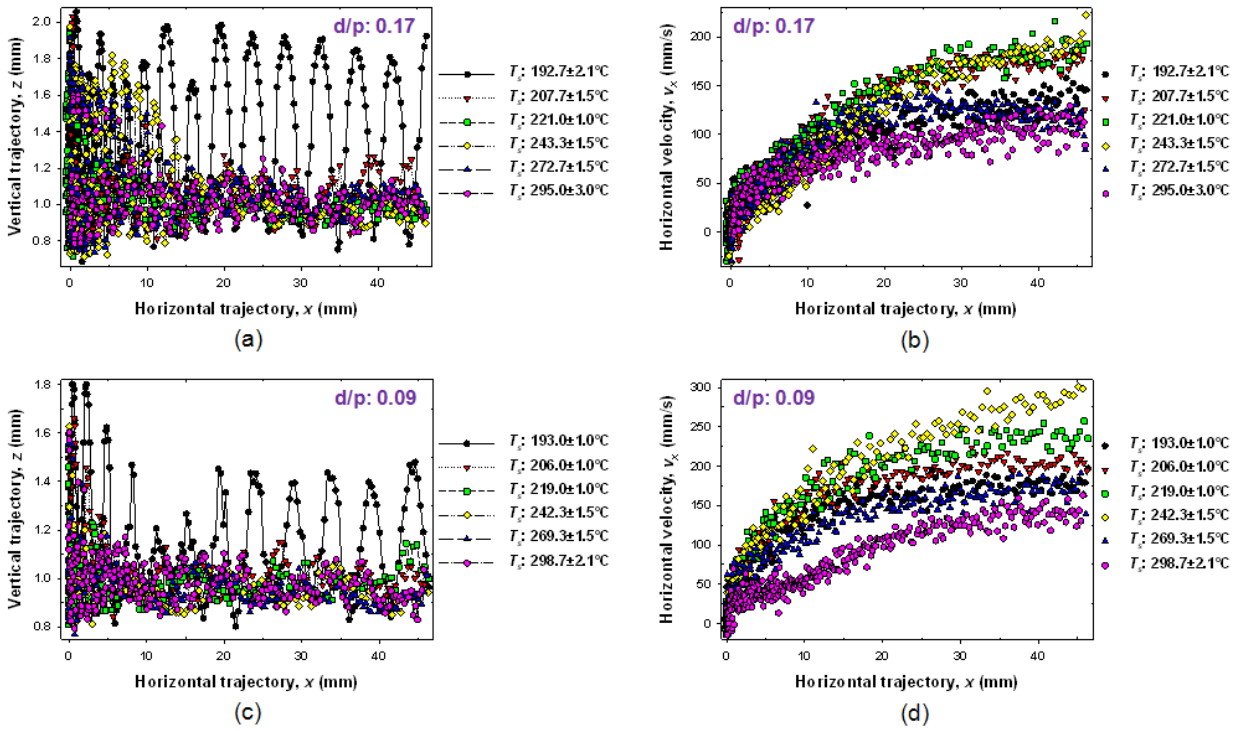

Figure 6.12 Trajectory and velocity profiles of millimetric DI water droplet on two brass microratchets (p: 750 μm) with different aspect ratios and sharp ridges at the varied surface temperatures, which are in the range of 192.7±2.1 ℃ – 298.7±2.1°C. (a) − (b) were obtained from deep ratchets (d/p: 0.17) and (c) − (d) from shallow one (d/p: 0.09).

Figure 6.13 (a) and (b) present measured average terminal velocity and average acceleration value as a function of surface temperature for two different ratchet depths. The droplet motion observed from the lower ratchet depth (d: 75 μm) is always faster than that from the higher ratchet depth (d: 150 μm) regardless the surface temperature in the range of 192 − 299 ℃. The velocity difference between the deep and shallow ratchet depths are more significant in L regime where T_s is lower than ~270 ℃. But they are much less in H regime where T_s is above ~270 ℃. Reminding our previous results about the influence of ratchet period p on the droplet mobility, the horizontal mobility is considerably dependent on p only at relatively lower temperature zone (L regime: ~100 ℃ < ΔT < ~170 ℃). In H regime (~170 ℃ < ΔT < ~260 ℃), however, the droplet velocity does not vary with p due to the thick vapor layer. Note that for the experiments the ratchet aspect (depth to period) ratio was kept almost constant (d/p: ~0.2). Therefore, it is

speculated that the main reason for significant variation of droplet mobility with p is the varied number of ratchets under the droplet in L regime. The smaller p makes the faster motion. For these two ratchets with the same p and different d, however, the number of ratchet beneath the droplet is similar to each other. The driving force by an individual ratchet $F_{ratchet}$ for the motion is given (Linke, Aleman et al. 2006):

$$F_{ratchet} = \frac{h}{2}\frac{dP}{dx} A_{eff} \cos\theta_{ratchet} \tag{6.1}$$

where, h is the vapor film thickness, dP/dx the local vapor pressure gradient (or vapor flow) along the horizontal direction, A_{eff} the area of the droplet bottom surface interacting with a ratchet, and $\theta_{ratchet}$ ratchet angle (refer figure 2.1). When the ratchet aspect ratio is reduced, A_{eff} is the only term which increases and thus increases the ratchet force. The difference in the cosine term is almost negligible ($\Delta cos\theta_{ratchet}$ = 0.014). Since the local pressure difference between the internal pressure of liquid droplet and the vapor pressure could be approximately given by the Laplace pressure $\Delta P = \sigma/R$ (where, σ is the surface tension and R the local radius of curvature), dP/dx can be rewritten as:

$$\frac{\partial P}{\partial x} = \frac{\sigma}{l}\left(\frac{1}{R_B} - \frac{1}{R_A}\right) \tag{6.2}$$

where, l, R_A, and R_B are the effective length, local radius of concave curvature at a ratchet peak, and convex curvature at a ratchet valley, respectively. At a surface temperature, σ values from both ratchets are supposed to be same. Assuming a similar degree of the increase in R_A and R_B with decreasing ratchet aspect ratio, the change in both l and ($1/R_B - 1/R_A$) will decrease the pressure gradient between the ratchet top and bottom edges. Thus, the change in the pressure gradient cannot account for the increase in the horizontal velocity with low aspect ratio ratchets. h would be thicker for the shallow ratchet depth (Prat, Schmitz et al. 1995). Therefore, the enhanced droplet mobility from the shallow ratchets (d/p: 0.09) is attributed to the increased area

between the droplet bottom and the ratchet surface by the geometrical benefit.

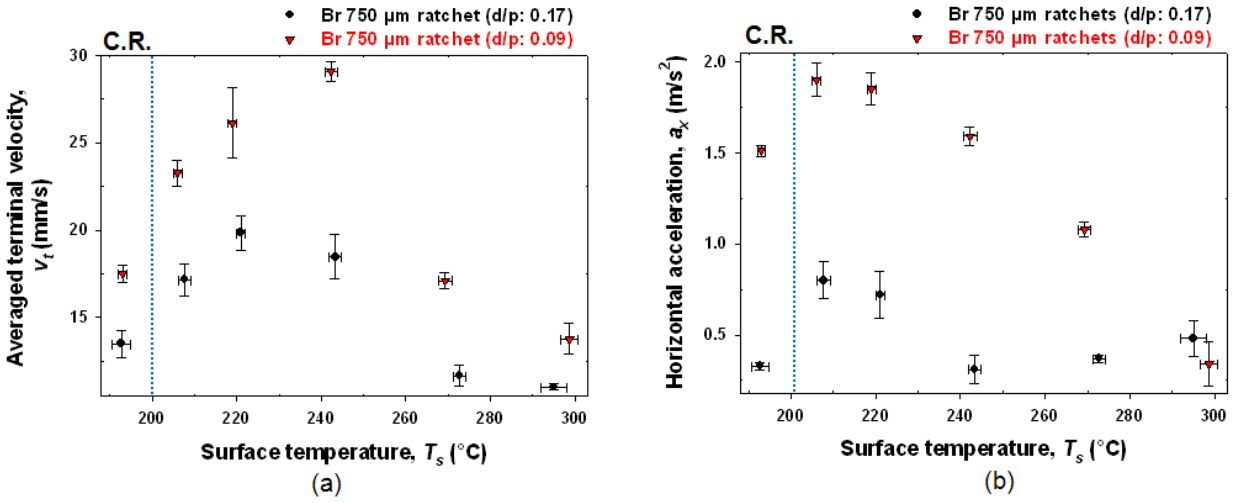

Figure 6.13 Temperature dependence on the horizontal mobility of the millimetric droplet for two brass microratchets (p: 750 μm) with different aspect ratios (d/p: 0.09 and 0.17) and sharp ridges at the varied surface temperatures: (a) averaged terminal velocity, v_t and (b) averaged horizontal acceleration a_x.

In summary, this result clearly indicates that the continuous directional-rebounding motion is caused by round shape of ratchet ridge, not by the lower depth of ratchet.

6.3.5 The Influence of Surface Wettability

According to previous studies, the major influence of surface wettability on Leidenfrost phenomenon is that Leidenfrost temperature (T_L) decreases with higher contact angle (θ), which is caused by less heat transfer due to smaller vapor area underneath the film boiling droplet. It was supported by observing longer evaporation time and smaller heat transfer rate from the solid to liquid droplet (Takata, Hidaka et al. 2005; Hidaka, Yamashita et al. 2006). Our results in Chapter 4.3.4 showed consistent results by observing the decreased threshold temperature for droplet motion (ΔT_{th}: 30 − 45°C) and increased average velocities (Δv_m: 2 – 8 cm/s) in L regime when ratchet surfaces were coated with a fluorinated silane. Here, we aim to have a closer look at the influence of surface wettability on droplet motion by high speed camera imaging and analysis of trajectories and velocity profiles.

6.3.5.1 Effect of a hydrophobic coating on droplet impact at room temperature

First, the injection behavior of water droplets at room temperature was captured by high speed camera with high magnification for three different ratchets after the silane coating: 750 μm deep and sharp ratchets (*p*: 750 μm, *d/p*: 0.17), 750 μm shallow and rounded ratchets (*p*: 750 μm, *d/p*: 0.1), and 750 μm deep and sharp ratchets (*p*: 75 μm, *d/p*: 0.15). The image sequences are shown in figure 6.14, which can be compared with figure 6.9 where no silane coating was treated on ratchet surfaces. Overall, the droplet spreading upon impact was reduced for all cases, due to the low surface energy for the ratchet surfaces. For 750 μm period deep and sharp ratchets, the droplet deformation was significantly while no noticeable changes were observed for the other two ratchets.

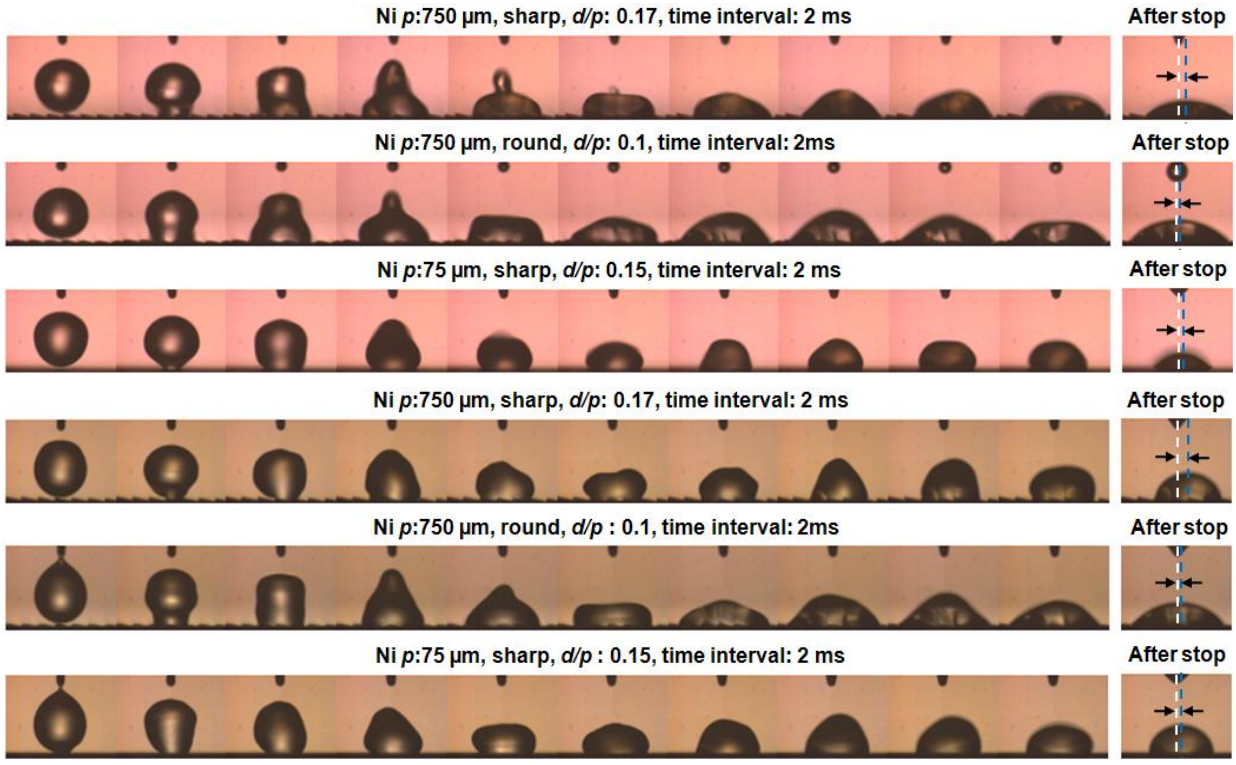

Figure 6.14 High speed camera sequences (magnification: 80 mm spacer, frame rates: 1000 fps and expose time: 1 ms) of droplets on plain ratchets (top three sequence) and fluorinated silane coated ratchets (bottom three sequence) at room temperature.

6.3.5.2 Effect of a Hydrophobic Coating on Droplet Impact at Elevated Temperature

Figures 6.15 and 6.16 show trajectories and velocity profiles of water droplets on 750 μm period ratchets (*d/p*: 0.17) with and without a fluorinated silane coating. Table 6.8 shows parameters related to figure 6.15 and 6.16. Their trajectory profiles look similar to each other, following the characteristic trend, in which a significant decrease in the vertical oscillation amplitude near initial impact is followed by continuous oscillation with low amplitude. The main difference is the average vertical trajectory which increases close to one when the ratchet surface was coated with the silane. This is due to the low surface energy of the silane coated ratchets which reduces the spreading of droplets at each oscillation and thus the center of mass of the droplet is seen at higher vertical location. v_t are similar to each other but v_m from the silane coated ratchets was 1.47 cm/s faster than that from the ratchets without silane coating because initial droplet acceleration upon impact is higher with silane coated ratchets. A similar behavior was also observed with 75 μm period Ni ratchets in *L* regime.

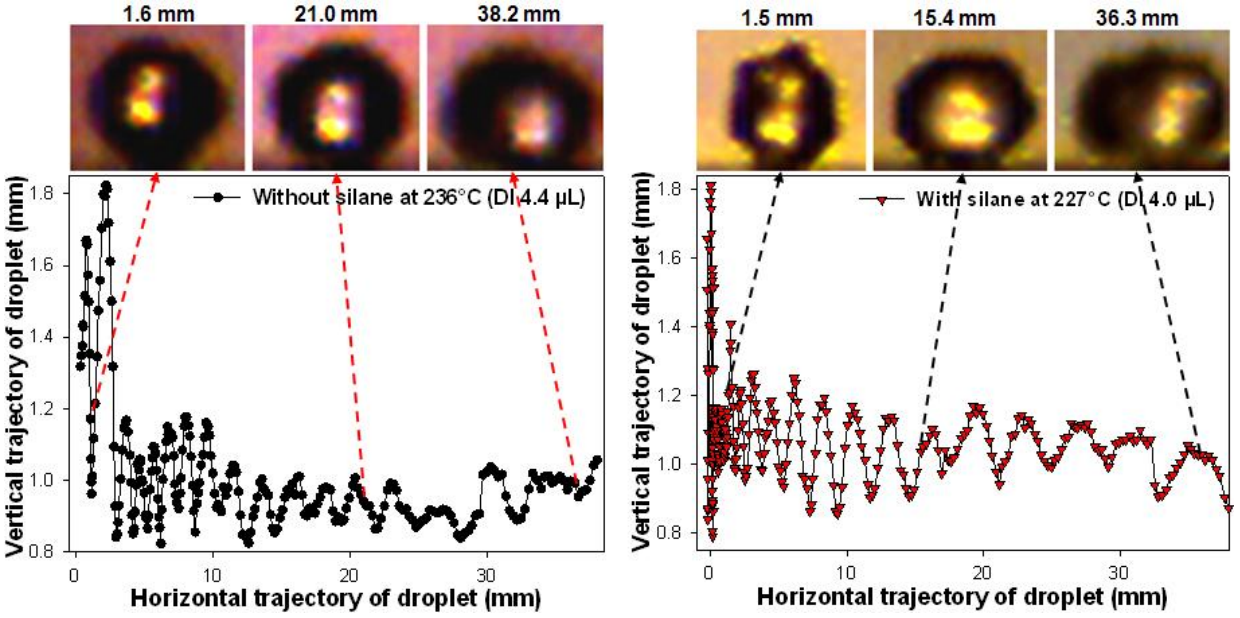

(a) (b)

Figure 6.15 Trajectory of droplet on Ni 750 μm ratchets with and without silane.

In *H* regime, both trajectories and velocity profiles of droplets on Ni micro ratchets with and without silane are similar to each other, consistent with our previous results that the droplet is fully levitating by a thick vapor layer, so that there is no direct contact between the droplet and ratchet surface.

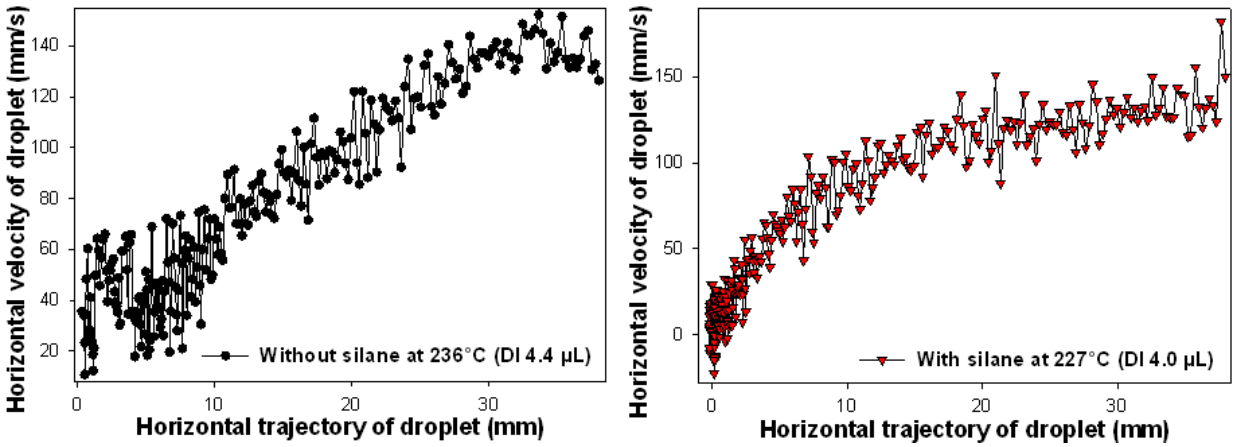

(a) (b)

Figure 6.16 Velocity profiles of droplet on Ni 750 μm ratchets with and without silane.

Table 6.8 The values of relative parameters for figure 6.15 and 6.16 (Ni micro ratchets, *p*: 750 μm with and without silane).

Silane	T_s (℃)	V_0 (μL)	D_0 (mm)	H (mm)	H-D_0 (mm)	v_0 (cm/s)	*We*	t (s)	S (cm)	v_{av} (cm/s)	v_t (cm/s)
w/o	236.0±3.6	4.4	2.03	3.19	1.16	15.08	0.74	0.56	3.8	6.79	13.9±0.8
w/	227.0±2.0	4.0	1.96	3.29	1.33	16.15	0.82	0.46	3.8	8.26	13.5±1.5

In order to check if the silane coating remains on the surface even at an elevated temperature, water contact angles were measured after the experiments. We found that the silane coating was stable even after the ratchet was heated at 306 ℃ for 5 hours. The silence coating was removed only by exposing the surface to O_2 plasma for a few minutes.

6.3.6 Climbing motion over tilted ratchets surface

The Leidenfrost droplet even could climb over the tilted ratchets surface. Figure 6.17 shows the sequence of 4.5 μL DI water droplet moving uphill the 1.3 ° tilted brass microratchets (*p*:

76.7 ±1.1 μm, *d*/*p*: 0.16) at 226.0 ±1.0 ℃. The sequence has 90 ms time interval.

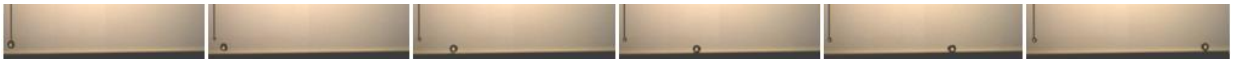

Figure 6.17 Time evolution of millimetric de-ionized water droplet (initial droplet volume, V_0: 4.5 μL) climbing over the 1.3 ° tilted brass microratchets (*p*: 76.7 ±1.1 μm, *d*/*p*: 0.16) at 226.0 ±1.0 ℃, which is recorded at a frame rate of 500 fps and expose time of 100 μs.

The trajectory and mobility of the film-boiling droplet on plain and 1.3 ° tilted brass microratchets were compared as shown in figure 6.18 (a) and (b). The droplets on both surfaces escaped whole ratchets paths by directional and continuous rebounding at this temperature. The vertical fluctuation during bouncing was much less for the droplet motion on the tilted one. Thus, faster horizontal mobility from the tilted one was observed in the range of horizontal trajectory 15 – 45 mm. However, the velocity abruptly decreased due to the gravity. The tilted ratchet surface increases the area of the droplet bottom surface interacting with a ratchet, increasing the ratchet force according to equation 6.1. These results also corroborate with our previous conclusion that the increased area of the droplet bottom surface interacting with ratchets is the main reason in the increase in horizontal velocity for the low aspect ratio ratchets.

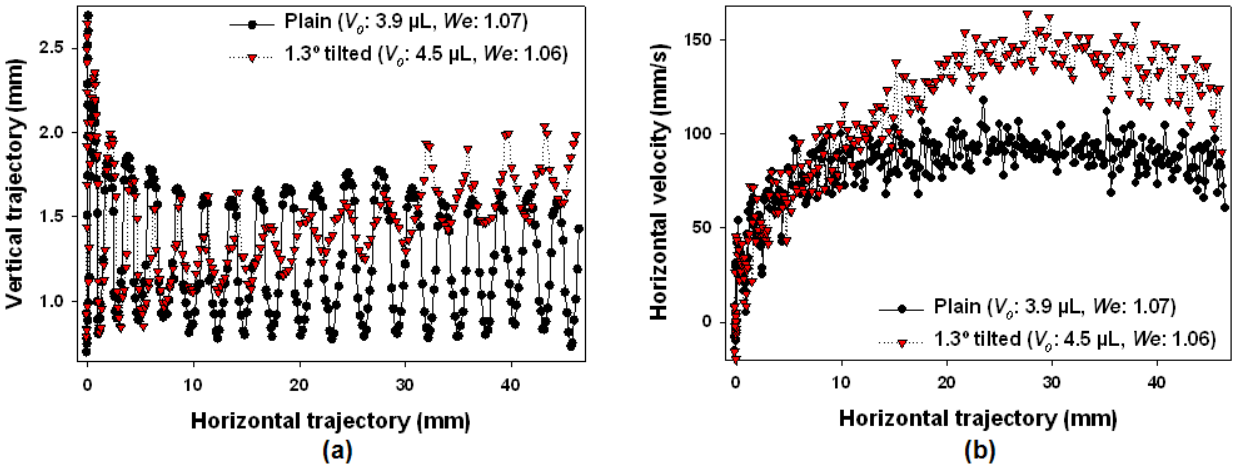

Figure 6.18 Comparison of millimetric droplet motion on plain and 1.3 ° tilted brass microratchets (*p*: 76.7 ±1.1 μm, *d*/*p*: 0.19) at 226.0 ±1.0 ℃: (a) vertical trajectory of droplet and (b) horizontal velocity of droplet as a function of horizontal trajectory of droplet.

6.4 Conclusions

The enhanced experimental setup was used to characterize the millimetric DI water droplet motion on different ratchets under various conditions. The highest acceleration is always observed at the beginning of droplet motion. The vertical oscillation of droplets during horizontal motion was found to be related to how much acceleration the droplet can receive from the ratchet surface. In *L* regime, the terminal velocities (v_t) are at least twice as high as the mean velocities (v_m) obtained by the primitive apparatus. The experiments with different surface temperatures and ratchet dimensions showed the consistent results with those obtained by the primitive setup. For the ratchets with round ridges, continuous rebounds of droplet for whole path were observed. The ratchet depth is another critical factor for the droplet motion. The surface wettability of the ratchets also influences the droplet mobility. The film-boiling droplet even could climb uphill the 1.3 °tilted microratchets.

Chapter 7 Impact and Motion of Droplets on Superhydrophobic Ratchets

7.1 Introduction

Previous chapters focused on the mobility of droplets on miniaturized asymmetric ratchets at an elevated temperature near or above the Leidenfrost temperature. When a liquid droplet is released on a very hot metallic miniaturized asymmetric ratcheted surface far above its boiling point, the droplet shows the remarkable unidirectional mobility due to the absence of actual contact or partial contact between the droplet and ratchet surface, depending on the ratchet surface temperature. Therefore, the vapor layer existing beneath the droplet provides a non-wetting situation with little or no pinning of the droplet into the ratchet surface.

Superhydrophobic surface, which has static water contact angle near 180 ° as well as contact angle hysteresis close to 0 °, is also a non-wetting surface. Due to the technological importance, water repellency (static and dynamic contact angle, as well as rebounding behavior) of superhydrophobic surfaces that have been prepared in a variety of methods has been studied intensively. There has also been an effort to understand the rebounding behavior upon surfaces with engineered non-uniformity (Malouin, Koratkar et al. 2010). In their work, water droplet has a unidirectional rebound on nonuniformly textured silicon micropillars. Therefore, a combination of engineered local non-uniformity provided by a miniaturized ratchet surface with superhydrophobic textures may be an alternative potential method to induce unidirectional motion. In this chapter, rebounding behavior of millimetric water droplets deposited on various superhydrophobic surfaces, which include a natural elephant ear leaf and a biomimetic pyramid array (UV-resin), will be studied. Micro ratchets integrated with superhydrophobic structures and symmetric V-grooves with asymmetric surface roughness prepared into PMMA were used in this

study.

7.2 Biomimetic Superhydrophobic Surfaces in UV-Resin

7.2.1 Preparation and Fabrication of Superhydrophobic Structures

Figure 7.1 shows the process scheme used to fabricate biomimetic UV-resin superhydrophobic surfaces. In the first step PDMS was casted on the surface of an elephant ear leaf or the artificially made superhydrophobic pyramid array template. After curing PDMS it was peeled off from the template and used as a stamp for UV-nanoimprint lithography. After UV exposure it was peeled off from UV imprinted pattern and then printed pattern was coated by fluorinated silane molecules using a vapor deposition method right after surface activation with oxygen plasma. Further detailed procedures are available in chapter 3.2.4. Details on the fabrication methods for the two different superhydrophobic surfaces can be found elsewhere (Farshchian, Choi et al. 2011).

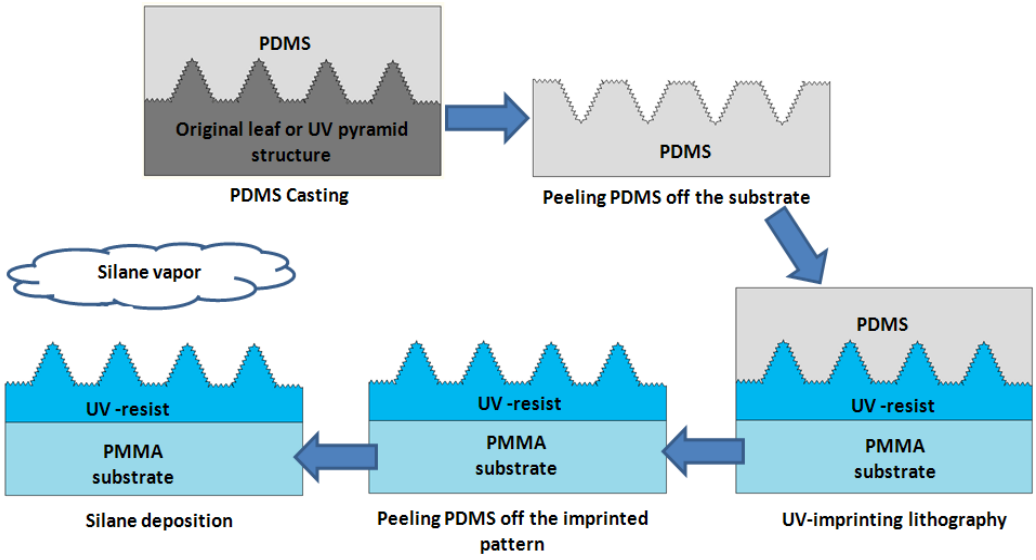

Figure 7.1 Schematic illustration of the process used for the fabrication of superhydrophobic surface using soft UV-NIL and silane deposition. The elephant ear leaf and artificially made superhydrophobic pyramidal surface were used as master mold for replication process.

7.2.2 Structural Analysis and Static Water Contact Angle

Hitachi S-3600N SEM (secondary electron, topographic mode) was used to characterize

microstructures. Figure 7.2 (a) and (b) show SEM images of an elephant ear leaf surface with different magnifications. The surface of the elephant ear leaf is covered by microbumps and each bump is surrounded by a ridge. The bumps and ridges have almost a hexagonal geometry providing a maximum number of ridges and bumps on the surface of leaf. The bumps have an average diameter of 13 μm. The average bump to bump distance and bump to ridge distance are ~40 μm and ~20 μm respectively. The intrinsic nanostructures are textured along the whole leaf surface. Figure 7.2 (c) and (d) show the copied PDMS surface which is a negative replica of the leaf surface structure. This copied PDMS of leaf was used as a transparent stamp for soft UV-nanoimprint lithography. The nanostructures which are in the form of protrusions on surface of leaf will appear in the form of cavities in the negative replica of leaf template. These nanocavities can be blocked in some areas due to collapse and pairing of PDMS, which cause the amount of nanoroughness to decrease on PDMS (Xia and Whitesides 1998). Figure 7.2 (e) and (f) show the positive replica of the leaf template formed in a UV resist via soft UV-nanoimprint lithography. The microbumps and ridges have the same structure like the original template while the amount of nanostructure features on surface has significantly decreased. SEM investigation of silane deposited UV-resin structures proved silane deposition does not change surface topography. In figure 7.3, SEM pictures of superhydrophobic structures fabricated via micromachining techniques are shown. Figure 7.3 (a) and (b) is the Si pyramid master integrated with nanoroughness on the surface. The pyramids had a base with the size of $23 \times 23\ \mu m^2$ and the period of the structure was 50 μm. SEM pictures of negative replica of superhydrophobic template which was made of PDMS is shown in figure 7.3 (c) and (d). This negative replica of superhydrophobic template was used as stamp to transfer patterns to UV-resin to fabricate the positive replica of superhydrophobic template. The SEM images of the replicated structure are

shown in figure 7.3 (e) and (f). The facets of pyramids have a higher curvature and the apex of pyramid is sharper than the template. This is due to shrinkage of UV-resin which occurs during cross linking of the UV-resin polymer.

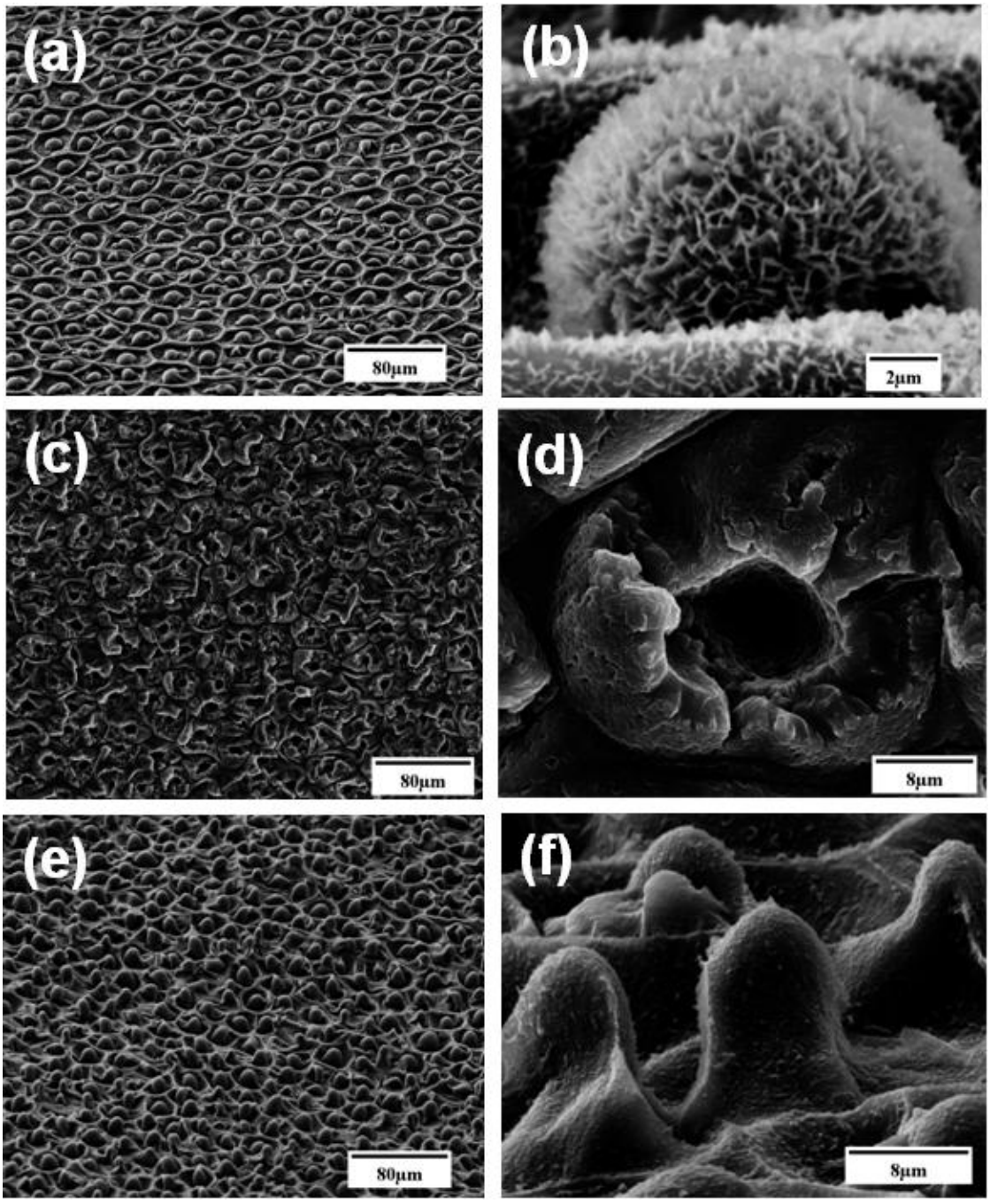

Figure 7.2 SEM pictures of the natural elephant ear leaf template (a) – (b), negative replica of the leaf template made of PDMS (c) – (d), positive replica of the leaf template made of UV-resin (e) – (f).

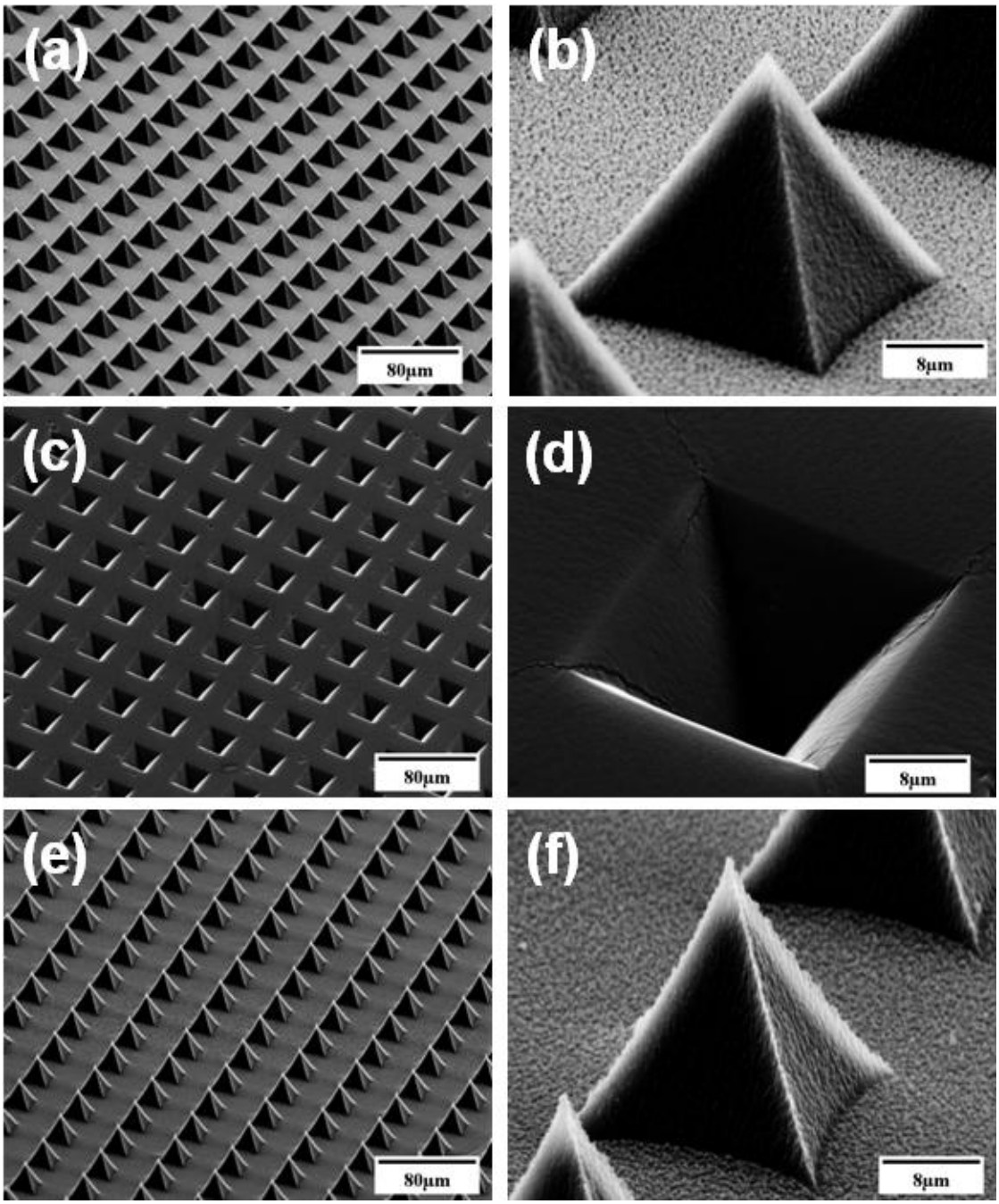

Figure 7.3 SEM pictures of the hierarchical pyramid array (a) – (b), negative replica of the hierarchical pyramid array made of PDMS (c) – (d), and positive replica of the hierarchical pyramid array made of UV-resin (e) – (f).

Figure 7.4 (a) – (h) are typical examples of micrograph images, which show static contact angle for each replication step of the elephant leaf and pyramid array. The static contact angle values for each surface were obtained by observing those at three different positions along the

surfaces.

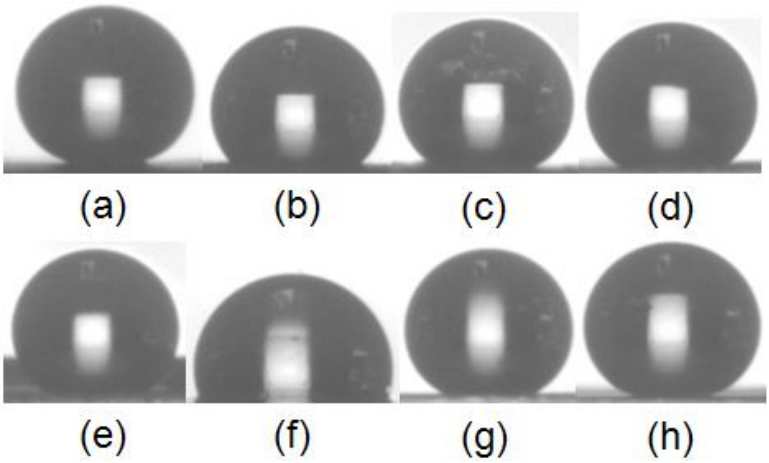

Figure 7.4 Micrograph images of static contact angles for every replication procedures of elephant leaf and pyramid array; (a) elephant ear leaf (θ =165 °), (b) PDMS negative replica of the leaf (θ =125 °), (c) UV-resin positive replica of the leaf without silane (θ =155 °), (d) UV-resin positive replica of the leaf with silane (θ =156 °), (e) Original UV-resin pyramid array with silane (θ =157 °), (f) PDMS negative replica of the pyramid array (θ =103 °), (g) UV-resin positive replica of the pyramid array without silane (θ =145 °), and (h) UV-resin positive replica of the leaf with silane (θ =160 °).

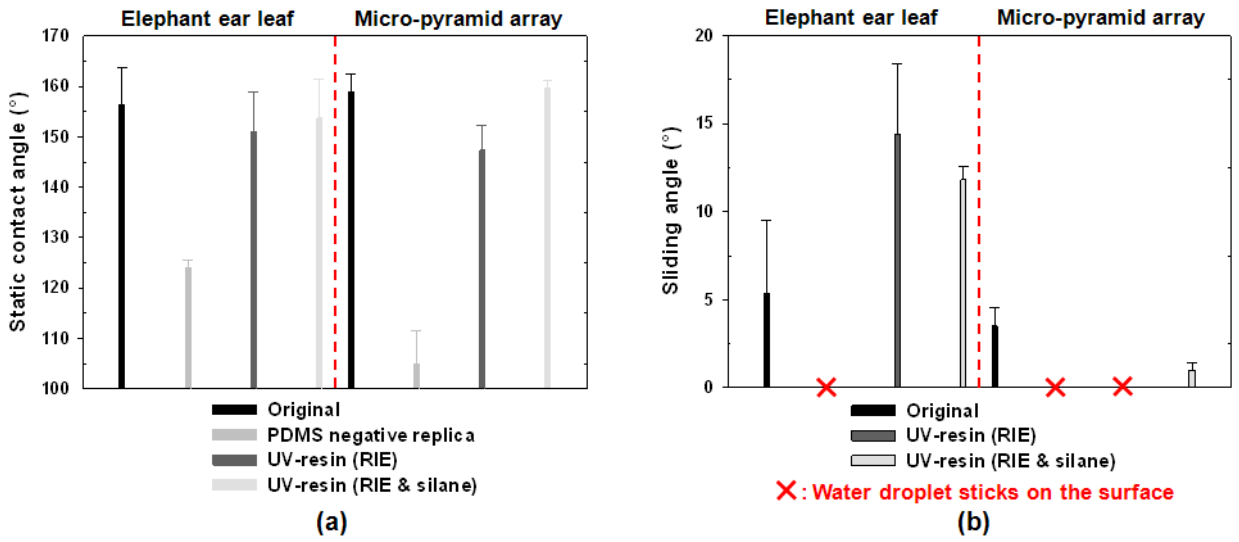

Figure 7.5 (a) Static contact angles and (b) sliding angles of 5 μL DI water droplet on the original template, PDMS negative and UV-resin positive replica of leaf and pyramid array.

Figure 7.5 (a) − (b) show the static contact angles and sliding angles for all surfaces examined in this study. The static contact angle of DI water droplet on the plain UV-resin was 74 ± 1 °. The contact angle for the leaf template is 156 ± 8 ° and the sliding angle is 5 ± 4 °. The

contact angle for the negative replica of leaf template in PDMS was $124 \pm 1°$ while the droplet sticks on the patterned PDMS surface even at $90°$ tilting angle. Positive replicas of leaf template without and with a fluorinated silane coating show static contact angles of $151 \pm 8°$ and $154 \pm 8°$ and sliding angles of $14 \pm 4°$ and $12 \pm 1°$ respectively. The static contact angle of water droplet on UV-resin pyramids without any nanostructures was increased from $74 \pm 1°$ (plain UV-resin) to $99 \pm 2°$ due to the presence of microstructures on surface. Pyramids are unique compared to pillars due to geometrical factors such as large bases and sharp apex; however pyramid structures only cannot provide a superhydrophobic state due to the fact that the Cassie state cannot be maintained with this geometry (Xiu, Zhu et al. 2007). By coating a fluorinated silane on an oxygen plasma treated pyramid array, the surface becomes superhydrophobic with static contact angle of $159 \pm 4°$. In fact, silane molecules form covalent bonds with the OH groups formed on the surface during oxygen plasma etching (Long, Prakash et al. 2006). Due to the simultaneous effect from the presence of the silane molecules on the surface and its high roughness it exchanged to superhydrophobic surface. The static contact angle of water droplet on the PDMS negative replica of pyramid array template was $105 \pm 7°$. The static contact angle of water droplet on the positive replica of the superhydrophobic template which was made of UV-resin before and after silane coating was $147 \pm 5°$ and $160 \pm 2°$ respectively. It was found that water droplet sticks on the surface of positive replica of hierarchical pyramids which were not coated by silane forming a Wenzel state while it slides on surface of the similar UV-resin structures which are coated by silane molecules at low sliding angle of $2 \pm 1°$ forming a Cassie state.

7.2.3 Rebounding

Superhydrophobicity (or water repellency) of the solid surface can be evaluated by investigating the surface reaction to water droplet impact. When the capillary number, the ratio

of viscosity and surface tension, is small enough ($\ll 1$), surface energy dominates viscous force and liquid droplet can rebound like a spring depending on the degree of impact (Reyssat, Richard et al. 2010). However, on extremely high impact speed ($\geq$ 2.8 m/s), splashing occurs. Generally, if liquid droplet rebounds off the surface at lower impact, it could be considered as the more water repellent surface. Based on this background, rebounding of water droplet on both original and copied superhydrophobic elephant ear leaf and pyramid array was investigated by releasing a droplet at two different needle heights (~ 3 mm and ~ 28 mm).

7.2.3.1 Normal Rebounding at Low Impact Speed

Reproducibility of droplet rebounding on all prepared superhydrophobic surfaces was examined after the leveling had been carefully done with a spirit level (Digital Torpedo Level, Craftsman, IL). Three de-ionized water droplets with the volume of 5 μL were released on different surface areas. Vertical trajectories of each droplet on different surface areas were very consistent, showing complete rebounding. Figure 7.6 shows a typical sequence of a DI water droplet impacting on a natural elephant ear leaf surface with a static contact angle of 156 $\pm$ 8°. The image was captured at a frame rate of 1000 fps and at an exposure time of 100 μs. The needle height from the leaf surface is 2.96 mm. The droplet radius is 1.1 mm and the impact velocity is 12.4 cm/s. The corresponding Weber number is 0.46. The droplet first deforms, spreads, then retracts, and finally rebounds off the surface.

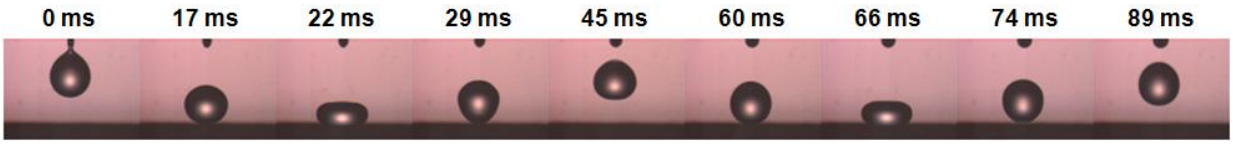

Figure 7.6 A video sequence of a 5.4 μL DI water droplet rebounding on the natural elephant ear leaf at room temperature. The static contact angle of this natural leaf surface was 156 $\pm$ 8°. The sequence shows the deformation time history of the droplet upon impact.

As the rebound repeats, its maximum height of droplet gradually decreases as shown in figure 7.7. As it further repeats, finally the droplet remains completely intact while the self-

oscillation still continues due to its elasticity. Significantly deviated rebounding behavior from copied UV-resin leaf surface is caused by its high sliding angle due to the loss of nanometer scale roughness as shown in figure 7.2 (e) and (f).

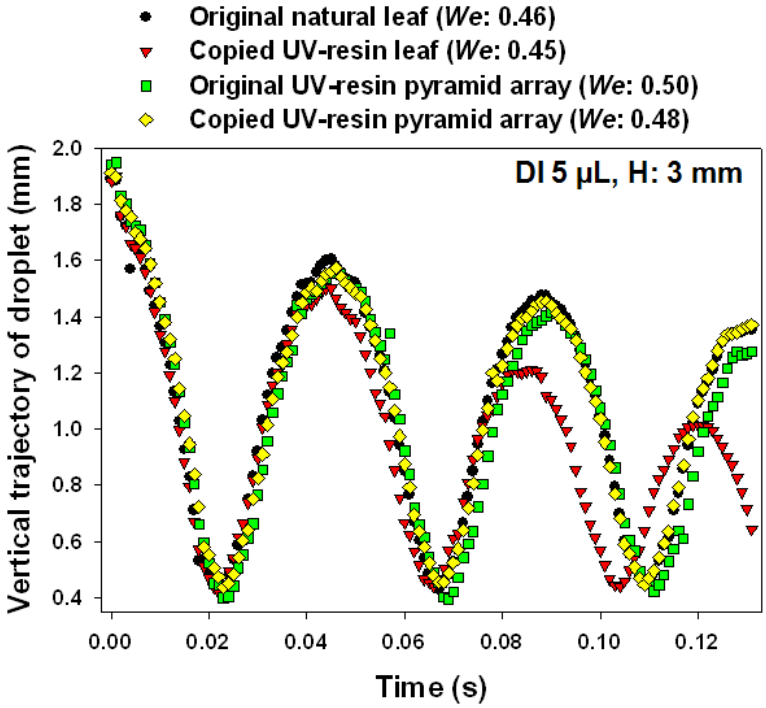

Figure 7.7 Vertical trajectory of DI water droplet impacting four different superhydrophobic surfaces as a function of time (slow impact speed: $v_i \approx 13$ cm/s).

7.2.3.2 Rebounding with Singular Jet at High Impact Speed

Figure 7.8 presents the snapshots of a 4.5 µL water droplet rebounding on the natural leaf with high impact speed (v_i: ~71 cm/s). When a droplet was released at ~28 mm needle height (*We*: ~14.7), rebounding of droplet with jetting was consistently observed on all investigated superhydrophobic surfaces, except on the copied UV-resin leaf. Instead, for two of three rebounding droplets, an air bubble was trapped within the droplet hitting the copied UV-resin leaf. Trapping an air bubble and jetting have strong dependence of impact droplet velocity on multiscale superhydrophobic surface (Bartolo, Josserand et al. 2006; Tsai, Pacheco et al. 2009). Upon impact a surface capillary wave is excited and the shape of droplet deforms like a sharp

cone. Both can be produced due to the development of an air cavity. The cavity restoration dynamics determines the events. At lower impact speed, the surface wave shortly restores and closes the top of cavity. At higher impact speed, a fast jetting is produced due to the fast collapse of the cavity. The shooting jets can be as fine as 60 μm in diameter and as fast as 40 times of the impact velocity. If we remind negligible difference of static contact angles for all superhydrophobic surfaces (2.6° − 6°), the amount of nanometer scale roughness along microstructure would be another important factor of the singular jet formation.

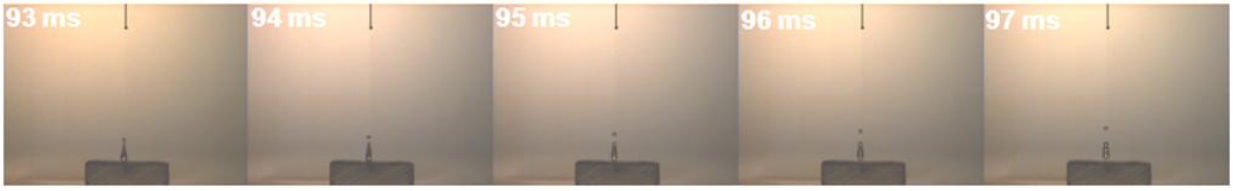

Figure 7.8 Time evolution of the droplet impact event of tiny droplet jetting on the natural elephant ear leaf surface at 156.3±7.5° and *We* = 14.62. The droplet highly elongates before rebounding off and emits singular fast jet.

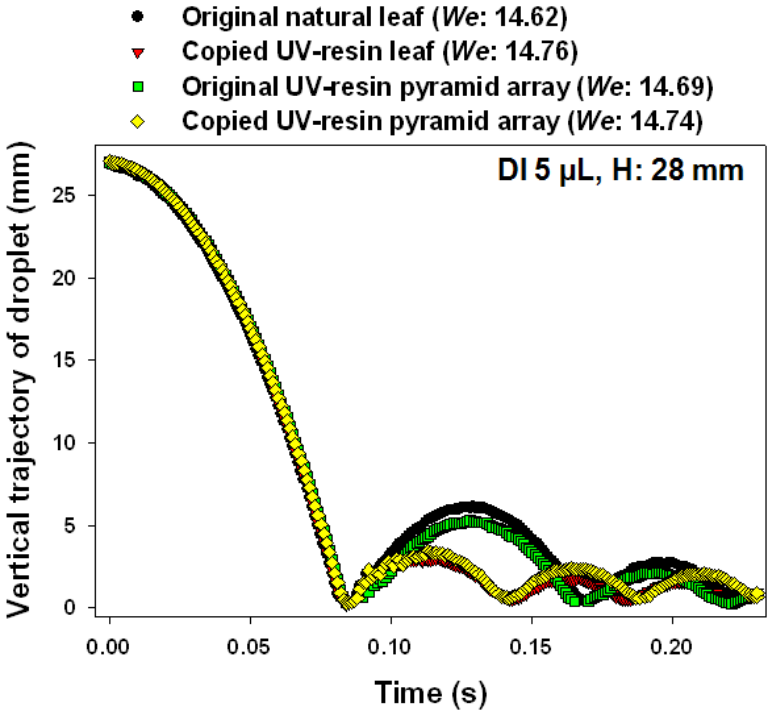

Figure 7.9 Vertical trajectory of rebounding DI water droplet on four different superhydrophobic surfaces as a function of time (fast impact speed: $v_i \approx 70$ cm/s). Tiny droplet jetting was produced for all surfaces.

Significantly reduced droplet elasticity from both copied UV-resin leaf and pyramid array was observed as shown in figure 7.9, comparing with those from natural leaf and original UV-resin pyramid array. This result could be interpreted that the microstructural sharpness also influences the droplet rebounding besides the amount of nanometer scale roughness element.

7.2.3.3 Restitution Coefficient

The restitution coefficient e of rebounding droplet is defined as the take-off velocity to impact velocity ratio ($e = v_t/v_i$). The take-off velocity v_t could be obtained from the time t at which the droplet is detached from the superhydrophobic surface (or the flight time). Since the droplet is subject only to gravity, v_t is $gt/2$. The impact velocity v_i is simply $\sqrt{2gh}$, where h is the distance from bottom of droplet to superhydrophobic surface. Thus, h was simply obtained by subtracting droplet radius ($D_0/2$) from the vertical center of droplet where was at the maximum height. Figure 7.10 displays the variation of the restitution coefficient as a function of droplet impact speed for both original and copied superhydrophobic surfaces, which was obtained from two different needle heights (3 mm and 28 mm). As droplet continues rebounding, e gradually increases for the first 2 ~ 3 bounce because the large viscous loss upon impact at high impact speeds. After reaching a maximum value, e abruptly decreases with further rebounds. Finally the droplet stays on the surface ($e = 0$) with moderate impact speed (v_i < 0.1 m/s). This is caused by the existence of a small adhesion force between the liquid and surface (Biance, Chevy et al. 2006). As the kinetic energy of the droplet becomes very low, pinning on the surface textures renders droplet remain stuck on the surface. As a consequence, the restitution coefficients are the highest at intermediate velocities in the range of 20 – 40 cm/s. The corresponding restitution coefficients are 0.6 – 0.8, which is much lower than those for Leidenfrost droplets. More significant decreases of elasticity are observed at both low and high impact velocities for copied

UV-resin leaf and pyramid array due to the loss of nanoscale roughness or sharpness of micro-pyramid. As well, the maximum values of *e* from copied UV-resin surfaces are much lower than those from original ones.

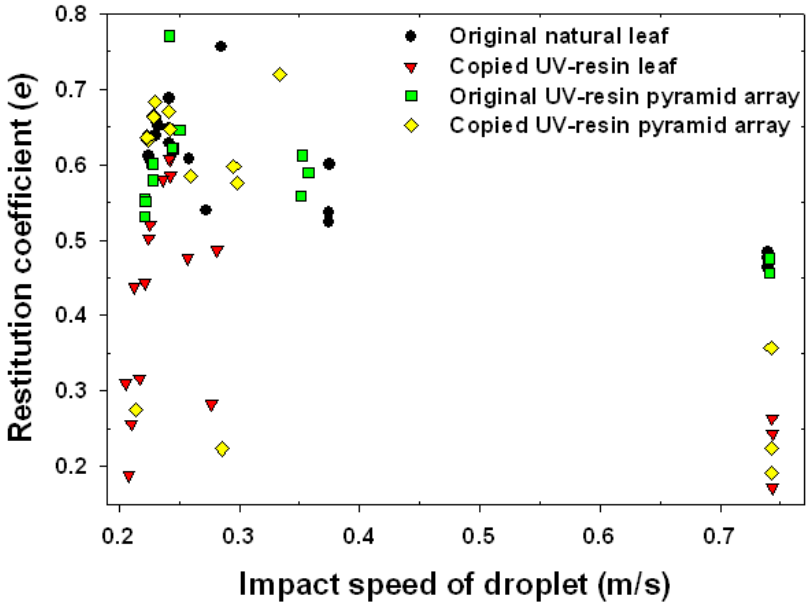

Figure 7.10 Restitution coefficients as a function of droplet impact speed for different superhydrophobic surfaces.

In summary, as respect to water repellency the role of nanoscale roughness is significant at low impact speed of droplet. However, the sharpness of microstructure is only critical for high impact speed. It is not always applicable to superhydrophobic surface that "the smaller impact velocity for rebounding, the better the water-repellent surface".

7.3 PMMA Superhydrophobic Ratchets

7.3.1 Fabrication of PMMA Superhydrophobic Ratchets

Figure 7.11 shows the simple process flow used to fabricate PMMA superhydrophobic ratchets. Various dimensions of brass ratchet molds were fabricated via series of milling process, described in detail in chapter 3.2.1. Short time reactive oxygen plasma etching (30 sec) and fluorinated silane coating on brass molds were followed for easier demolding from the polymer

substrate. Thermal nanoimprint lithography (NIL) process was used to sculpture miniaturized ratchets on 3 mm thick PMMA bulk plain sheet (United States Plastics, Lima). Nanoscale surface roughness was generated by reactive oxygen plasma etching after cut by a band saw into dimensions of 1 × 3 cm^2. Fluorinated silane vapor deposition modified the surface chemistry and exchanged the surface from superhydrophilic (~8 °) into superhydrophobic state (~150 °). Further detailed procedures are described in chapter 3.2.4.

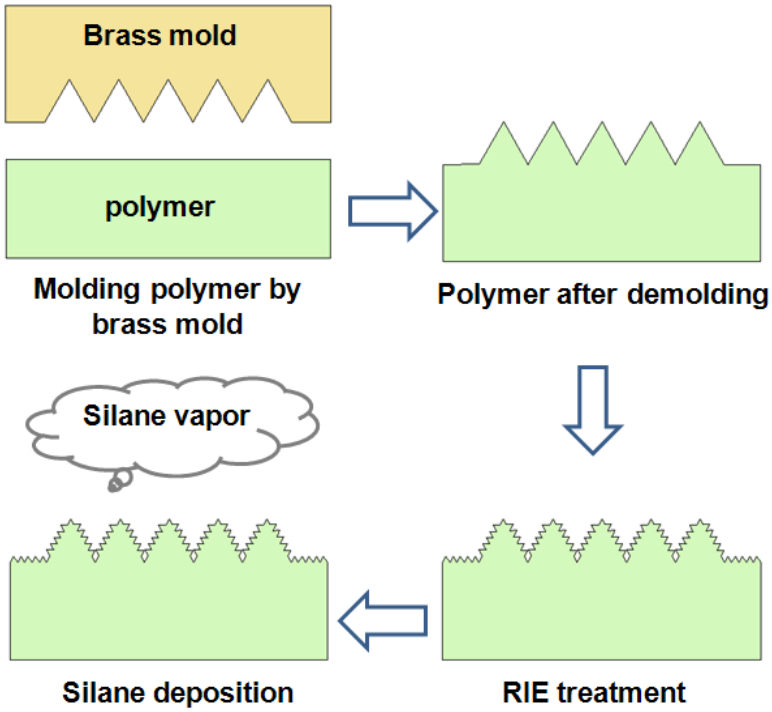

Figure 7.11 Schematic of the process used to fabricate a PMMA superhydrophobic surface by molding.

7.3.2 Structural Analysis and Static Water Contact Angle

Figure 7.12 (a) – (b) and (c) – (d) show PMMA superhydrophobic asymmetric ratchets with ratchet period of 15 μm and 75 μm, respectively. The aspect ratio of both ratchets is around 0.2. Figure 7.12 (e) – (f) show PMMA superhydrophobic symmetric ratchets with different surface roughness along the ratchet face. The period for the symmetric ratchets is 150 μm and the aspect ratio is 0.5. Porous nanoscale surface roughness produced by oxygen plasma is clearly visible in

the higher magnification images of all PMMA ratchets. The change in the ratchet dimensions due to the oxygen plasma process and the fluorinated silane coating is negligible.

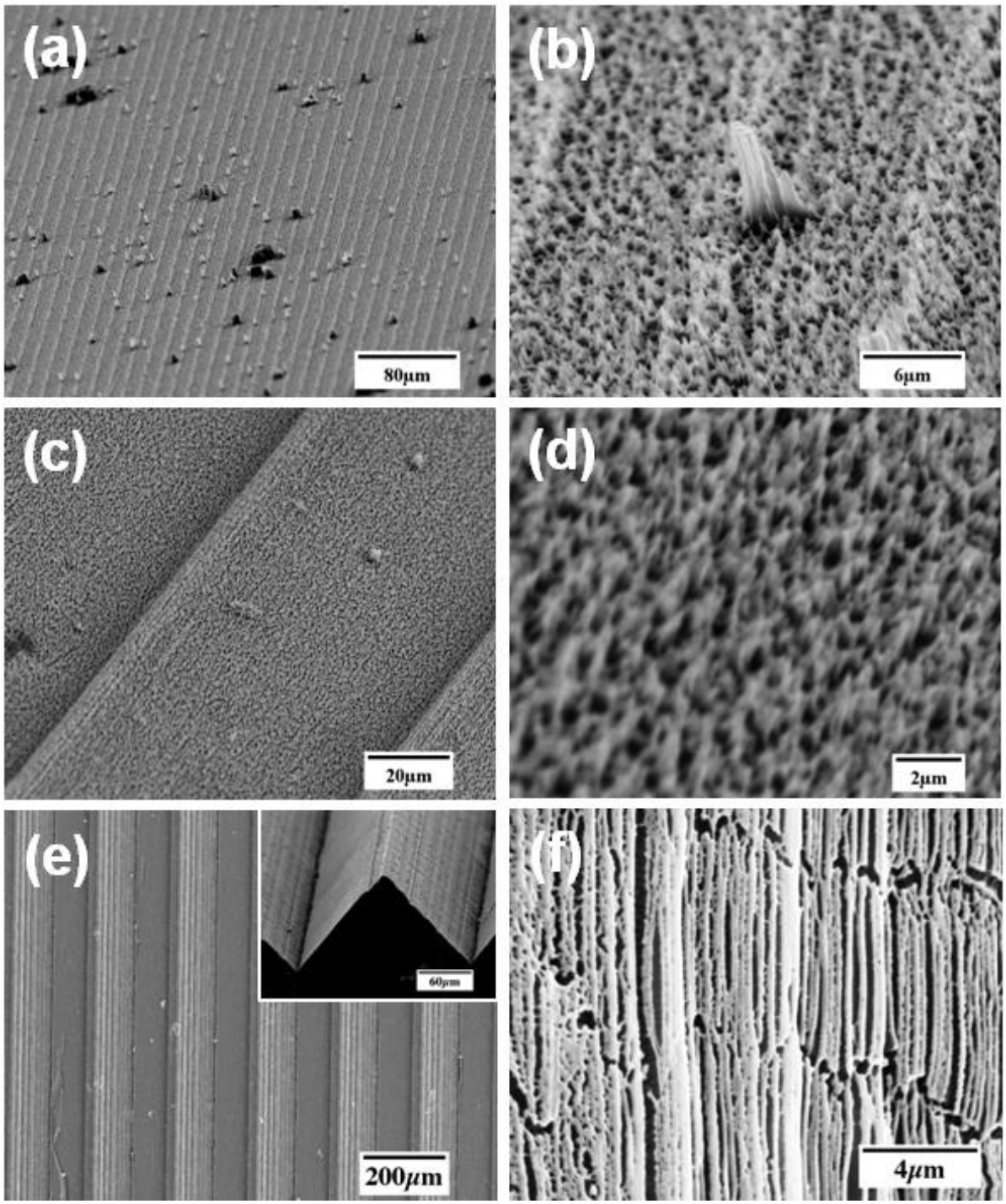

Figure 7.12 Scanning electron micrographs of PMMA superhydrophobic ratchets; (a) − (b) asymmetric ratchets (*p*: 15 µm, *d*/*p*: 0.2), (c) − (d) asymmetric ratchets (*p*: 75 µm, *d*/*p*: 0.2), (e) – (f) symmetric ratchets with different surface roughness (*p*: 150 µm, *d*/*p*: 0.5).

Figure 7.13 displays examples of static water contact angle changes on the 15 μm, 75 μm, and 150 μm period of microratchets before and after superhydrophobic surface treatment. Large contact angle differences between slowly and sharply tapered sides of ratchets are only observed from plain PMMA asymmetric ratchets in the range of 2 − 13°, depending on ratchet size. Figure 7.13 (f) shows that the droplet is only in contact with the top of the ratchet ridges, indicating a Cassie's state.

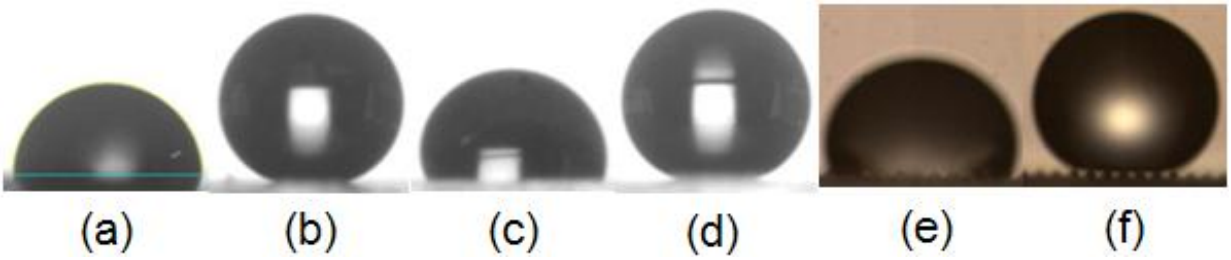

Figure 7.13 Micrograph images of static contact angles for PMMA plain and superhydrophobic (RIE & silane coated) ratchets; (a) − (b) asymmetric ratchets (*p*: 15 μm, *d*/*p*: 0.2), (c) − (d) asymmetric ratchets (*p*: 75 μm, *d*/*p*: 0.2), (e) – (f) symmetric ratchets with different surface roughness (*p*: 150 μm, *d*/*p*: 0.5).

Similar to the metallic ratchets, the geometrical asymmetry of the ratchets leads to different macroscopic contact angles, as shown in figure 7.14 (a), that are measured by assuming a horizontal base line for the solid surface. Microscopically, the contact angle at both sides of the water/air/surface interface should be same. Figure 7.14 (b) shows the static contact angles of DI water droplets on various ratchet surfaces. A significant increase of contact angles was achieved after reactive ion etching and silane coating. The increase of the contact angles are significantly varied in the range of 20° − 60°, depending on the ratchet period. The maximum contact angle of plain polymer ratchets was observed on the 150 μm period of ratchets. For the ratchets of which their period is smaller than 150 μm, the contact angles abruptly decrease as the ratchet period decreases. For the other direction, the contact angles slowly decrease with ratchet period. However, there was no critical relationship between the ratchet period and static contact angle

for superhydrophobic polymer ratchets.

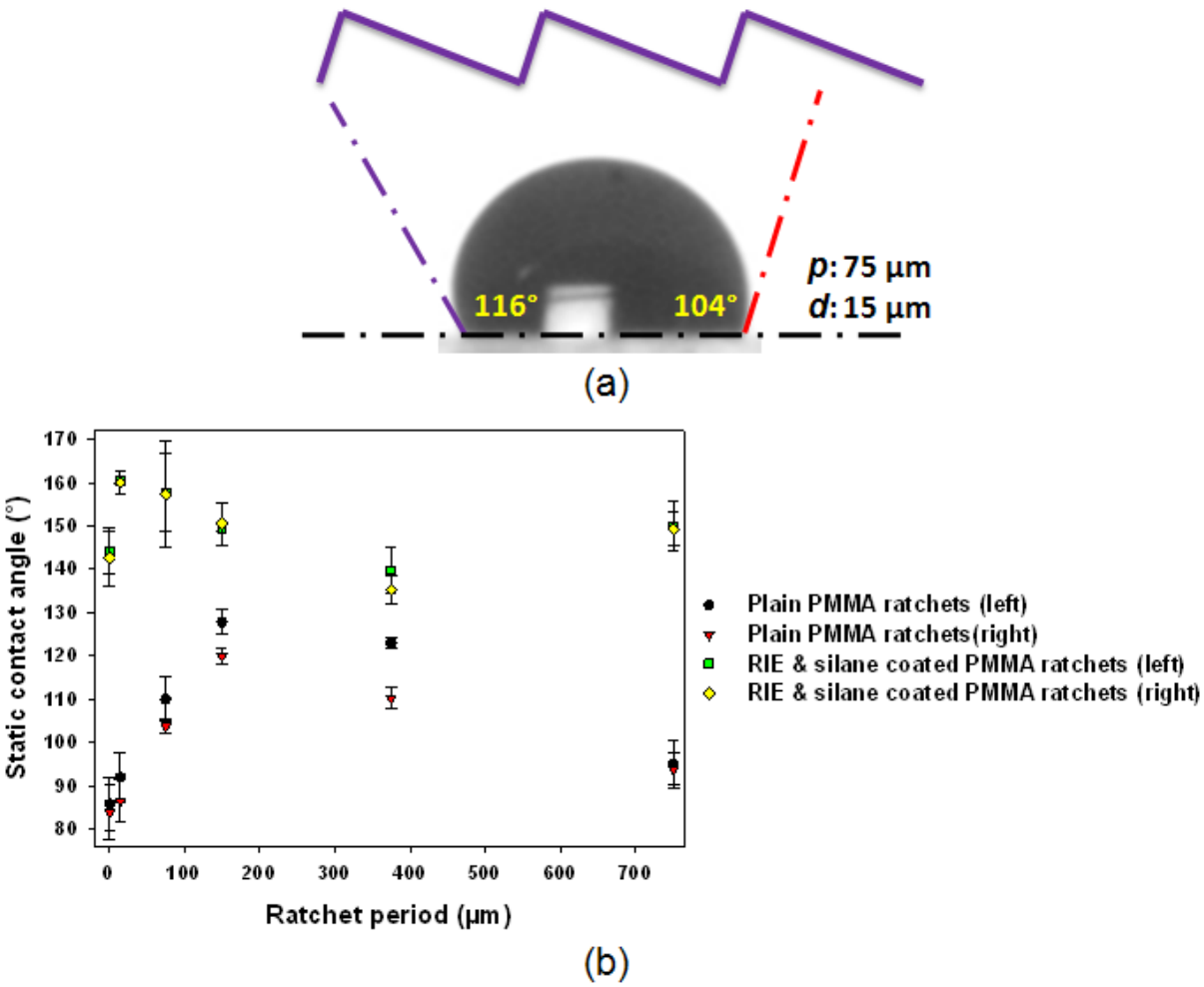

Figure 7.14 (a) Diagram showing typical contact angle difference between left and right side on the asymmetric ratchets (*p*: 75 µm, *d*/*p*: 0.2), and (b) Measured static contact angle values with varied ratchet period (*p*: 800 nm, 15 µm, 75 µm, 150 µm, 375 µm, 750 µm) while keeping depth to period aspect ratio constant (*d*/*p*: 0.2).

7.3.3 The Influence of Impact Velocity on the Motion of Droplet

A systematic study has been carried out to characterize the impact of liquid droplets on polymer superhydrophobic ratchets with different dimensions. The impact velocity of the droplet is simply manipulated by changing the needle height while maintaining a constant droplet size. Three different droplets are released on different surface areas for every sample. The surface condition of superhydrophobic ratchets is changed by using various dimensions of ratchets in

micrometer scale. The nanoscale surface roughness is identical for all the samples used in this study. The droplet size was determined from the captured image right after the droplet is released from the needle. The droplet impact velocity (v_i) was inferred from the height of the released droplet. These parameters are used to obtain dimensionless numbers, such as the Weber number ($We = \frac{\rho R_0 v_i^2}{\sigma}$), Reynolds number ($Re = \frac{\rho R_0 v_i}{\mu}$). Here R_0 is the radius of the liquid droplet, v_i is the impact velocity, ρ is the liquid density, σ is the surface tension, and μ is the liquid viscosity.

Figure 7.15 shows typical video sequences captured as a millimetric DI water droplet impacts three different superhydrophobic surfaces at room temperature. Measured static contact angles (θ_s) on the surfaces are $150° - 160°$. The droplet has a radius R_0 ~1.4 mm and is released from a needle height in the range of 7.2 – 7.5 mm. Corresponding impact velocities and Weber numbers are 29.1 – 30.4 cm/s and 3.31 − 3.56, respectively. More than five times of rebounds were observed for all surfaces. The maximum height from each rebound gradually decreases as time goes. Finally droplet stays on the surface. Droplet deforms significantly due to its elasticity. For plain UV-resin, droplet deforms without breaking the horizontal symmetry as shown in figure 7.15 (a).

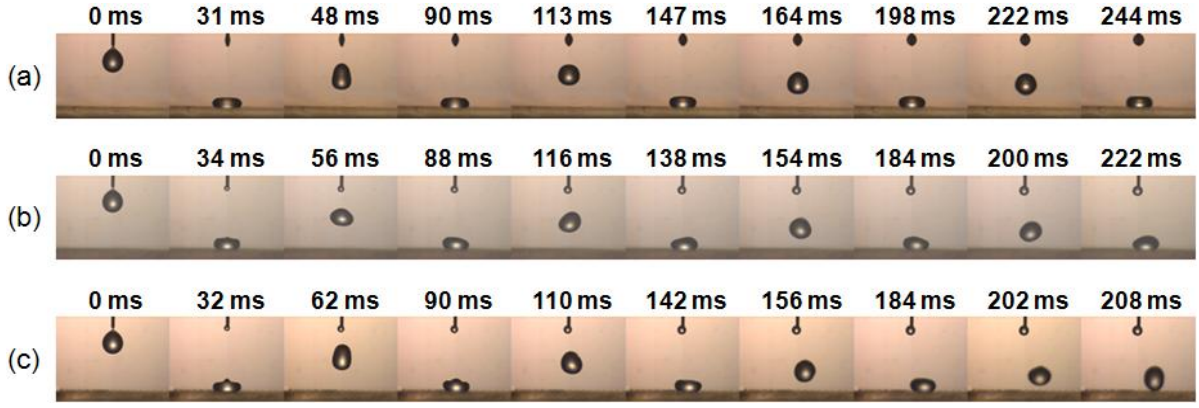

Figure 7.15 High speed camera sequences (magnification: 30 mm spacer, frame rates: 500 fps or 1000 fps and expose time: 100 µs) of droplet on (a) UV-resin RIE & silane coated plain surface (θ_s: 159±4°), (b) PMMA RIE & silane coated asymmetric ratchets (p: 75 µm, d/p: 0.2, θ_s: 158±9°), and (c) PMMA RIE & silane coated asymmetric ratchets (p: 750 µm, d/p: 0.2, θ_s: 150±4°).

For asymmetric superhydrophobic ratchets, the deformation is accompanied by the breakage of the horizontal symmetry. Moreover, droplet horizontally dislocates up to 1.3 – 1.9 mm accompanying rebounds, as shown in Figure 7.16 (a). The moving direction is same as that for the motion of film boiling droplets on hot metallic ratchets, i.e. from the sharply inclined side to the slowly sloped side of a ratchet. The average velocity v_{av} from 75 µm period of ratchets is 4.6 mm/s. For 750 µm period ratchets, droplet moves faster (v_{av}: 8.9 mm/s). The maximum height of droplet by each rebound on the ratchets more abruptly decreases with respect to the rebounding behavior on plain UV-resin as shown in figure 7.16 (b). It is suspected that for the ratchets, the kinetic energy of the droplet is dissipated into both vertical and horizontal directions, following the energy conservation.

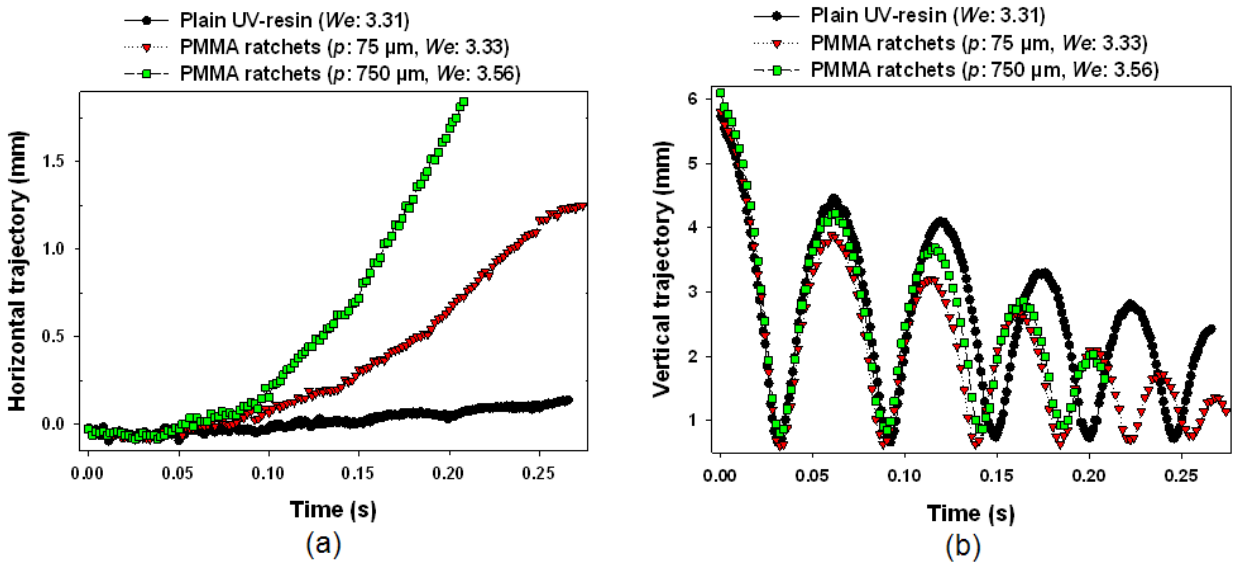

Figure 7.16 Time evolutions of (a) horizontal trajectory and (b) vertical trajectory of millimetric DI water droplet (radius: 1.39 – 1.41 mm) with similar impact speed (*We*: 3.31 – 3.56) on three different superhydrophobic surfaces. The data were obtained from the sequences shown in Figure 7.15.

In the following sections, the influence of droplet impact on three different superhydrophobic surfaces (plain UV-resin, PMMA asymmetric microratchets, and PMMA symmetric microratchets with different surface roughness) will be mainly discussed.

7.3.3.1 Plain UV-Resin

The plain UV-resin superhydrophobic surface was a reference surface to characterize droplet motion on PMMA superhydrophobic ratchets. Figure 7.17 shows the evolutional vertical trajectories of a millimetric DI water droplet hitting the plain UV-resin superhydrophobic surface with a static contact angle $\theta_s = 159 \pm 4°$ for different needle heights in the range of 2.6 mm – 2.65 cm. Figure 7.18 displays the impact scenario map on We and Re axes. In this range of impact speed, three different events were observed; normal rebound (or complete rebounding), rebound with trapped split droplet, rebound with jetting. Complete normal rebounding was observed even at a low *We* of 0.32. This behavior is slightly different from that observed on multiscale rough surfaces of carbon nanofiber jungles (CNFJ) ($\theta_s > 155 \pm 3°$) where four different impact events were distinguished, which include nonbouncing "Fakir" droplet, complete rebound, sticky wetting droplet, and partial rebound with increasing We number (Tsai, Pacheco et al. 2009). When a water droplet is very slowly released, it maintains the "Fakir" state with air trapped underneath the bottom surface of water due to the small kinetic energy. Therefore, higher contact angles between water and solid surface is kept for the entire impact event. A complete rebound can be induced by the nonwetting nature of superhydrophobic surfaces by limiting droplet spreading. When the kinetic energy overcomes the surface energy, the wetting transition such as sticky wetting droplet and partial rebound occurs. For CNFJ surfaces, the wetting transition was observed even from *We* ~1. However, in our case, both the "Fakir" state and sticky wetting droplet state were not observed at the We number of 0.32 and intermediate We number, respectively, indicating a superior water repellency of our superhydrophobic surface to the CNFJ surface.

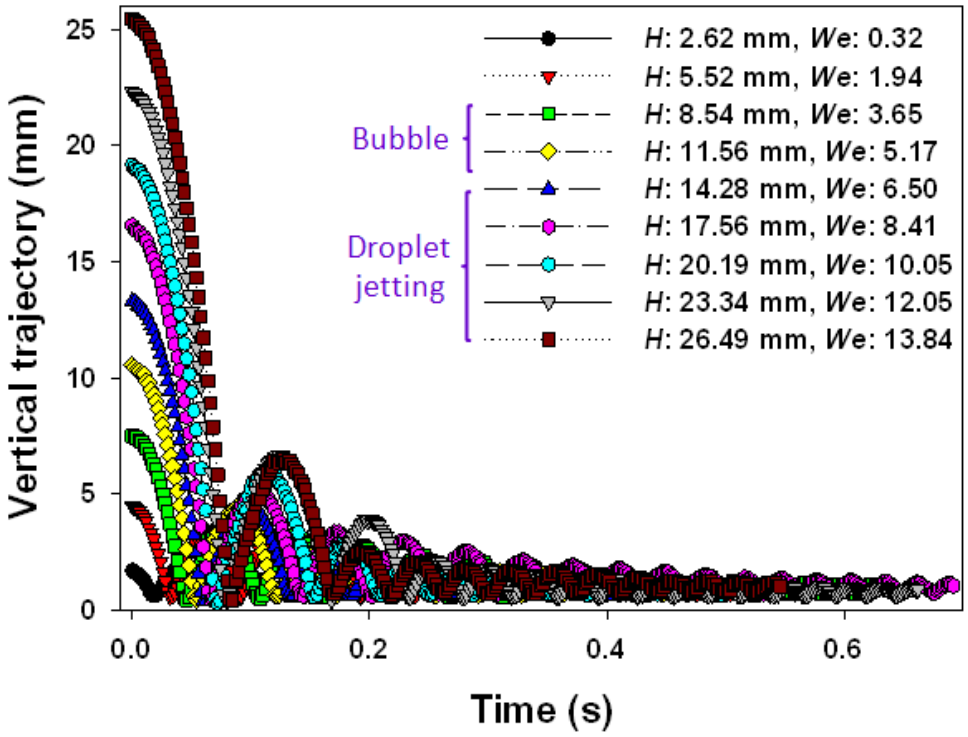

Figure 7.17 Vertical trajectory of 5 µL DI water droplet on UV-resin RIE & silane coated plain surface (θ_s: 159 ± 4°) with varied impact speed (*We*: 0.32 – 13.84). Trapping an air bubble occurred in the Weber number range between 3.65 and 5.17. Fast droplet jet was emitted in the Weber number range between 6.50 and 13.84.

At higher impact speeds, split droplet trapping and jetting happen. In the *We* number range of 3.65 − 5.17, the droplet impact on the superhydrophobic surface leads to a split of the droplet into two small droplets of a similar size. However, the split droplets could not overcome the surface energy of the droplets and as a result could not be separated to each other. This is shown as inset in figure 7.18. In the *We* number range of 6.50 – 13.84, a jet of a tiny droplet was emitted from the droplet. Previous studies reported that the shooting jet could be as fine as 60 µm in diameter and as fast as 40 times of the impact velocity (Bartolo, Josserand et al. 2006; Tsai, Pacheco et al. 2009). Even after a tiny fast jet had been escaped from the original droplet, complete rebounding of the main droplet was consistently observed in this regime. A very similar behavior was observed for the superhydrophobic elephant ear leaf surface and the superhydrophobic surface with an array of UV-resin pyramids previously shown in figure 7.8.

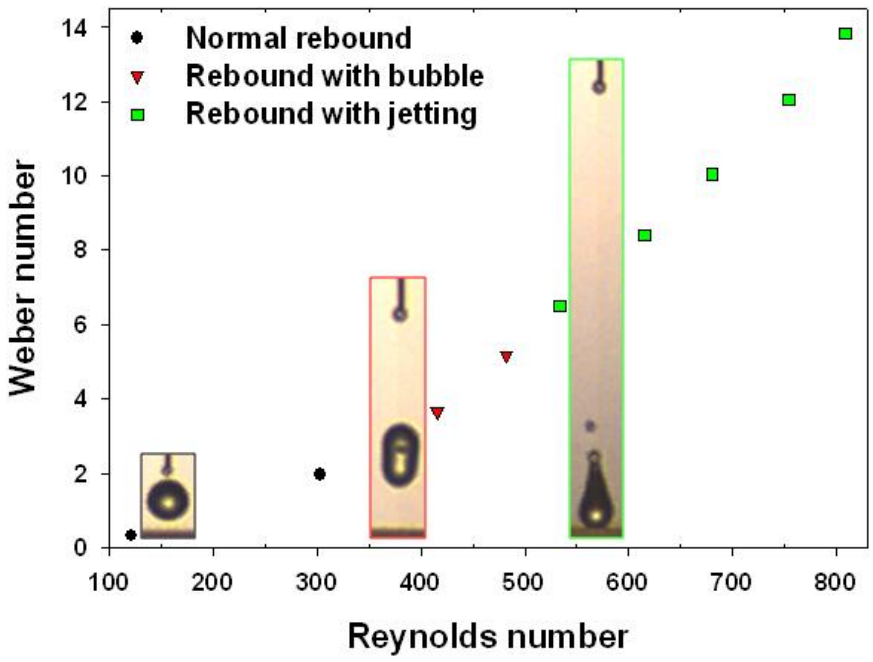

Figure 7.18 Impact dynamics of 5 μL DI water droplet on UV-resin RIE & silane coated plain surface (θ_s: 159 ± 4 °) with varied impact speed (*We*: 0.32 – 13.84). The sequences show three different impact events.

Figure 7.19 (a) shows how the restitution coefficient *e* varies as the droplet rebound progresses for different needle heights. In most of cases, *e* slightly increases for initial several rebounds, and then gradually decreases until it reaches zero. The only exception was observed from the lowest needle height (*H*: 2.62 mm). Instead, *e* just continuously decreased. Number of rebounds increases from 7 to 16 as the needle height increases up to 17.56 mm. After then, the number slightly decreases to 12 until the droplet release height is 26.49 mm. The elasticity significantly decreases as the impact velocity decreases for lower v_i (< 25 cm/s) as shown in figure 7.19 (b). Overall characteristics of restitution coefficient value with varied impact speed are very similar to those observed from natural leaf and original UV-resin pyramid array given in chapter 7.2.3.3.

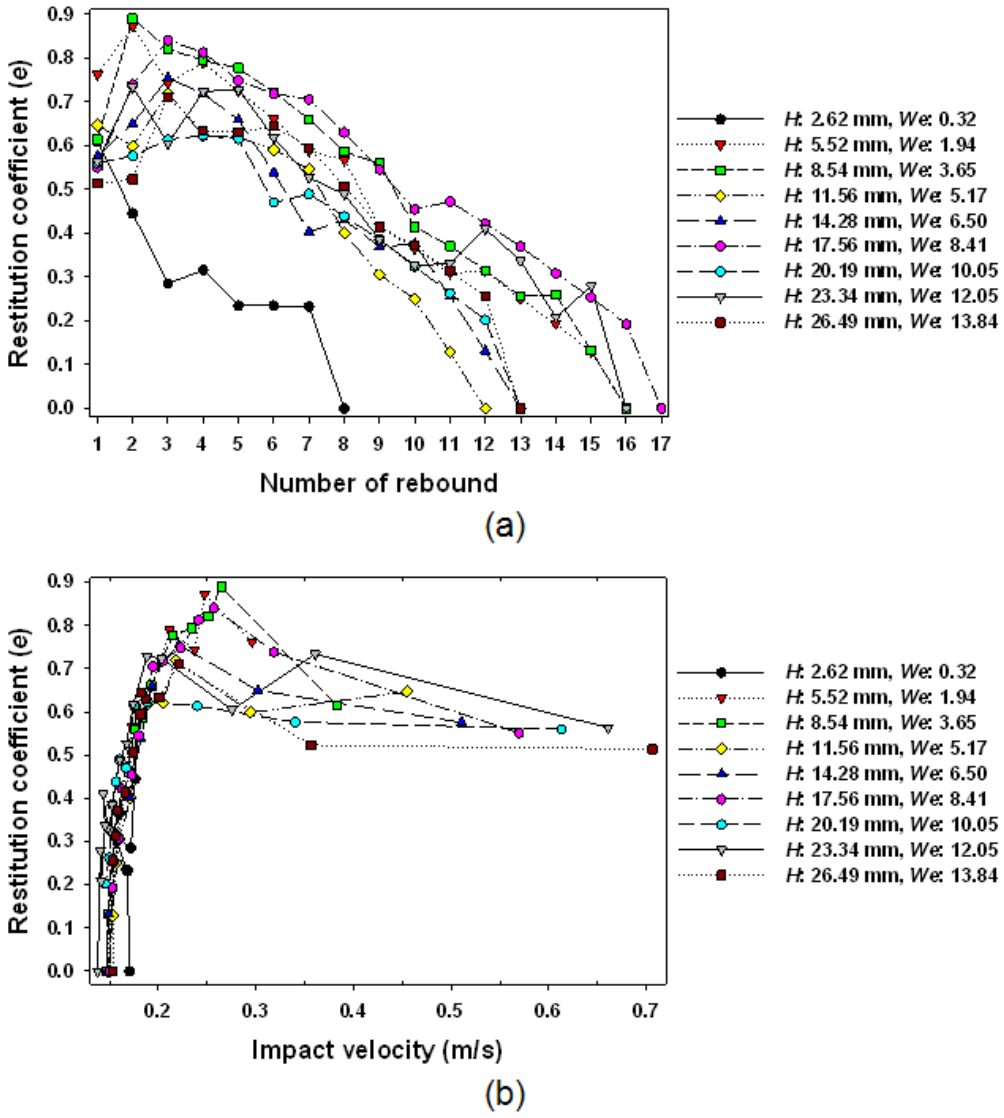

Figure 7.19 Restitution coefficient for 5 μL DI water droplet rebounding on UV-resin RIE & silane coated plain surface (θ_s: 159 ± 4 °) with varied impact speed; as a function of (a) number of rebound and (b) impact velocity (v_i).

7.3.3.2 Asymmetric Ratchets

(1) 750 μm Period of Ratchets

The influence of impact velocity on the motion of droplet was investigated for PMMA superhydrophobic asymmetric microratchets (p: 750 μm, d/p: 0.2, θ_s: 150 ± 4 °). The needle heights to drop DI water droplets were varied from 3.27 mm to 32.75 mm. The corresponding *We* values were 0.67 – 16.23. Figure 7.20 presents the evolutional trajectories for both vertical (a)

and horizontal (b) directions. Directed rebounding of droplet was observed for all conditions. The repulsion between droplet and asymmetric ratchets is the main driving force of a directed rebounding. The slower impact velocity made the longer dislocation as shown in figure 7.20 (b). Due to the lower impact speed, the droplet cannot penetrate into the cavities formed between nanostructures in the superhydrophobic surface, and thus the energy dissipation by adhesion at the droplet/surface interface is lower, which results in a longer displacement before the droplet stops moving. As the impact speed increases, the droplet sinks deeper into the nanostructure cavities. Accordingly, the contact area at the droplet/surface interface increases, giving rise to a shorter dislocation of the droplet.

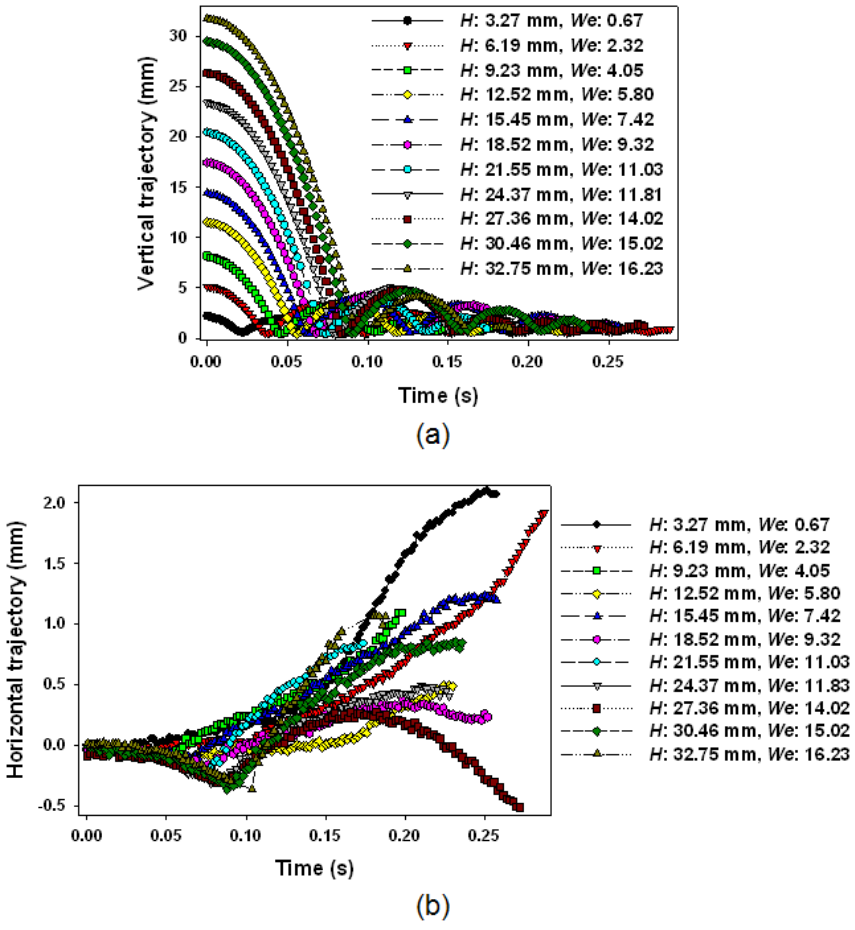

Figure 7.20 Time evolutions of (a) vertical trajectory and (b) horizontal trajectory of 5 μL DI water droplet on PMMA RIE & silane coated asymmetric ratchets (p: 750 μm, d/p: 0.2, and θ_s: 150 ± 4 °) with varied impact speed (We: 0.67 – 16.23).

Figure 7.21 shows the impact scenario map based on *We* and the corresponding *Re* 177.62 – 843.51. Four different events occurred in this range of droplet impact. Comparing the case from the plain UV-resin surface, 'rebound with droplet separation' event was added when *We* was 9.32 and 16.23. This should not be considered as a sign of wetting transition because the escaped tiny secondary droplet was merged with main droplet again and then the merged droplet keep rebounding. This event just seemed that droplet emitted jet to the ratchets surface.

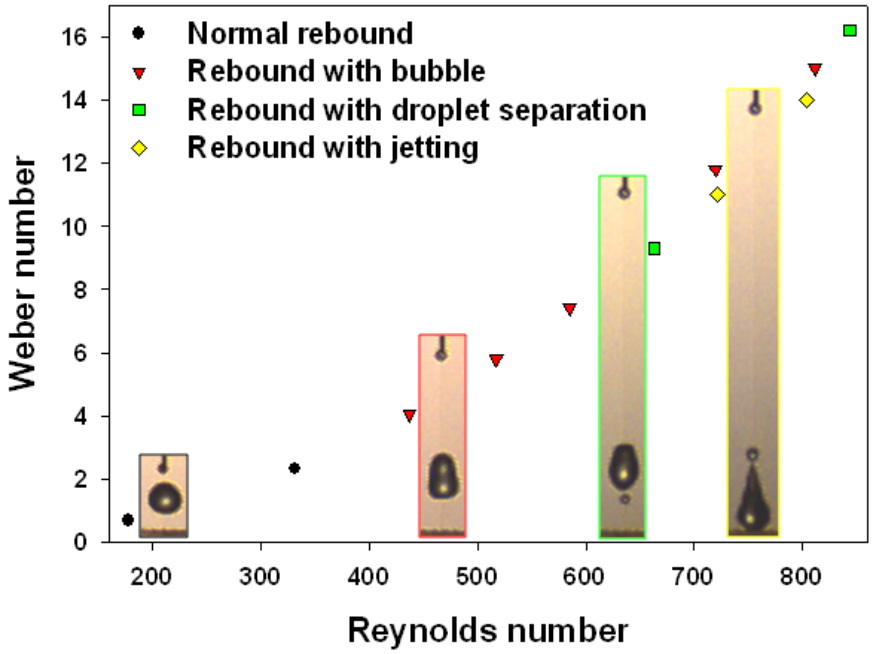

Figure 7.21 Impact dynamics of 5 µL DI water droplet on PMMA RIE & silane coated asymmetric ratchets (*p*: 750 µm, *d*/*p*: 0.2, and θ_s: 150 ± 4 °) with varied impact speed (*We*: 0.67 – 16.23). The sequences show different impact events.

Figure 7.22 (a) and (b) present variation of restitution coefficient *e* of droplet impacting superhydrophobic 750 µm period of ratchets (*d*/*p*: 0.2) for different droplet impact velocity. The number of rebounding for all conditions significantly decreased comparing with those observed from superhydrophobic plain UV-resin surface, indicating significant energy dissipation by the presence of ratchets. Excluding the number of rebounds, all other properties such as static water contact angle and contact angle hysteresis match well with other superhydrophobic surfaces observed.

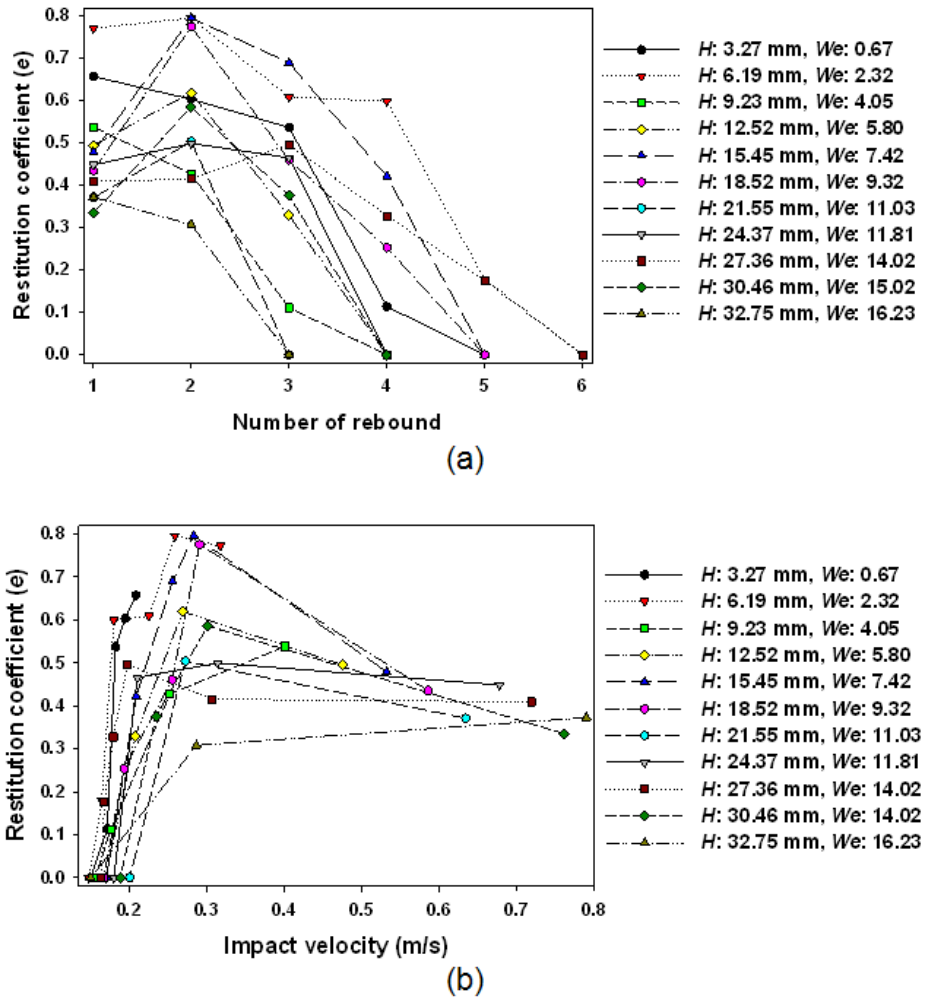

Figure 7.22 Restitution coefficient for 5 µL DI water droplet rebounding on PMMA RIE & silane coated asymmetric ratchets (p: 750 µm, d/p: 0.2, and θ_s: 150 ± 4°) with varied impact speed (We: 0.67 – 16.23); as a function of (a) number of rebound and (b) impact velocity (v_i).

Figure 7.23 presents various dynamic characteristics of droplet motion when it gently releases from the lowest height (H: 3.27 mm). The droplet moved slowly until 15 ms. As the rebounding height decreased, horizontal velocity significantly increased during the next 5 ms (15 – 20 ms) as shown in figure 7.23 (a) and (b). Figure 7.23 (c) shows how the vertical velocities were varied as the droplet vertically moved. Negative values were obtained when the droplet spread upon impact to the surface. Positive values came from when the droplet rises up from the surface. When the droplet rebounded, the absolute values of vertical velocities were between ~50 and ~130 mm/s. The absolute values of vertical velocities caused by self-oscillation of droplet

were less than 40 mm/s. Four rebounds were observed in this condition. Then, the droplet speed abruptly dropped and finally it stopped horizontal dislocation. As shown in figure 7.23 (d), most of droplet dislocation was observed with lower kinetic energy (< 10 nJ).

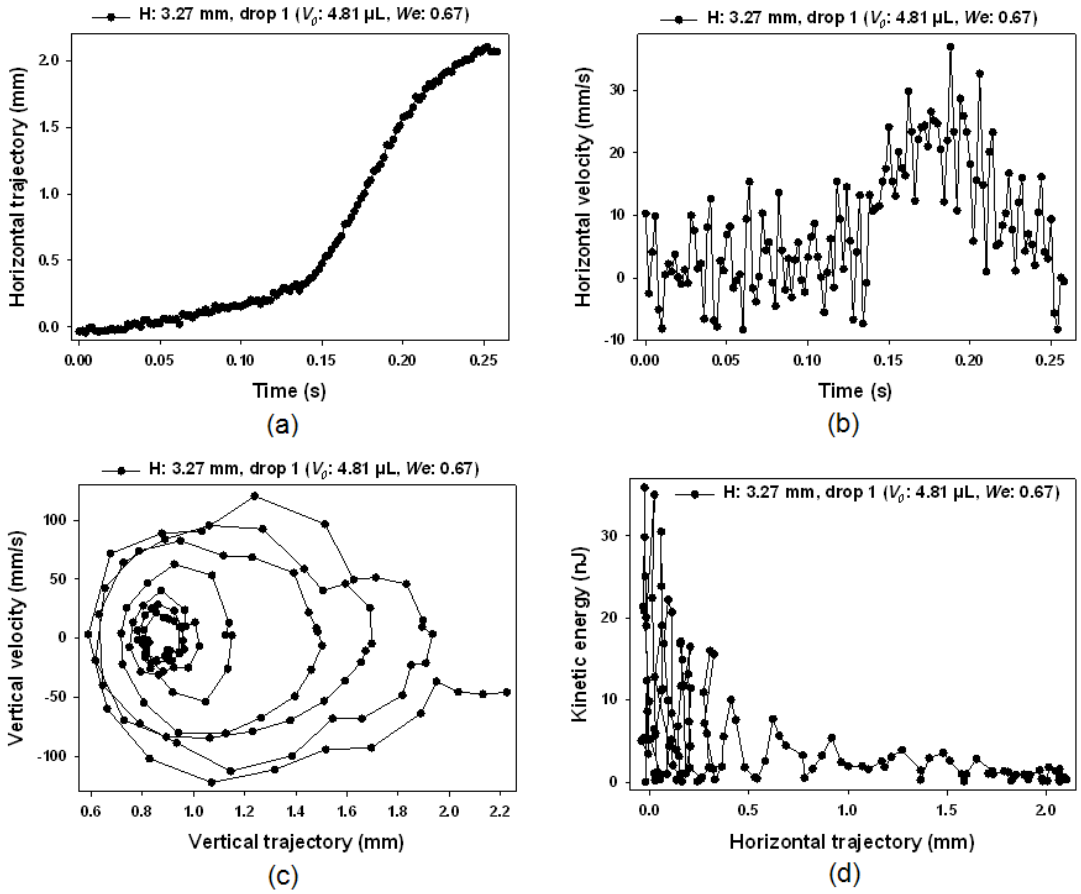

Figure 7.23 Dynamic characteristics of millimetric DI water droplet rebounding and oscillating on PMMA RIE & silane coated asymmetric ratchets (p: 750 µm, d/p: 0.2, and θ_s: 150 ± 4°) at 3.27 mm needle height. The corresponding Weber number is 0.67. (a) time evolution of horizontal trajectory and (b) its velocity, (c) vertical velocity as a function of its vertical trajectory, and (d) kinetic energy as a function of horizontal trajectory.

(2) 15 µm Period of Ratchets

The influence of impact speed on the droplet motion was examined for another PMMA superhydrophobic asymmetric miniaturized ratchets (p: 15 µm, d/p: 0.2, and θ_s: 160 ± 2°), of which SEM images are shown in figure 7.12 (a) and (b). Figure 7.24 displays a typical sequence of a millimetric DI water droplet when it was released from 5.6 mm needle height. The initial

droplet radius is 1.1 mm and the initial impact speed is 26.2 cm/s. The corresponding *We* and *Re* are 1.98 and 305.85, respectively. Directed rebounding induces horizontal dislocation of the droplet along the surface, like the observations from other ratchets (*p*: 75 μm and 750 μm, *d*/*p*: 0.2).

Figure 7.24 High speed camera sequence (magnification: 5 mm spacer, frame rates: 500 fps and expose time: 100 μs) of 4.8 μL DI water droplet on PMMA RIE & silane coated asymmetric ratchets (*p*: 15 μm, *d*/*p*: 0.2, and θ_s: 160 ± 2 °). Droplet was released at 5.6 mm and the corresponding Weber number was 1.98.

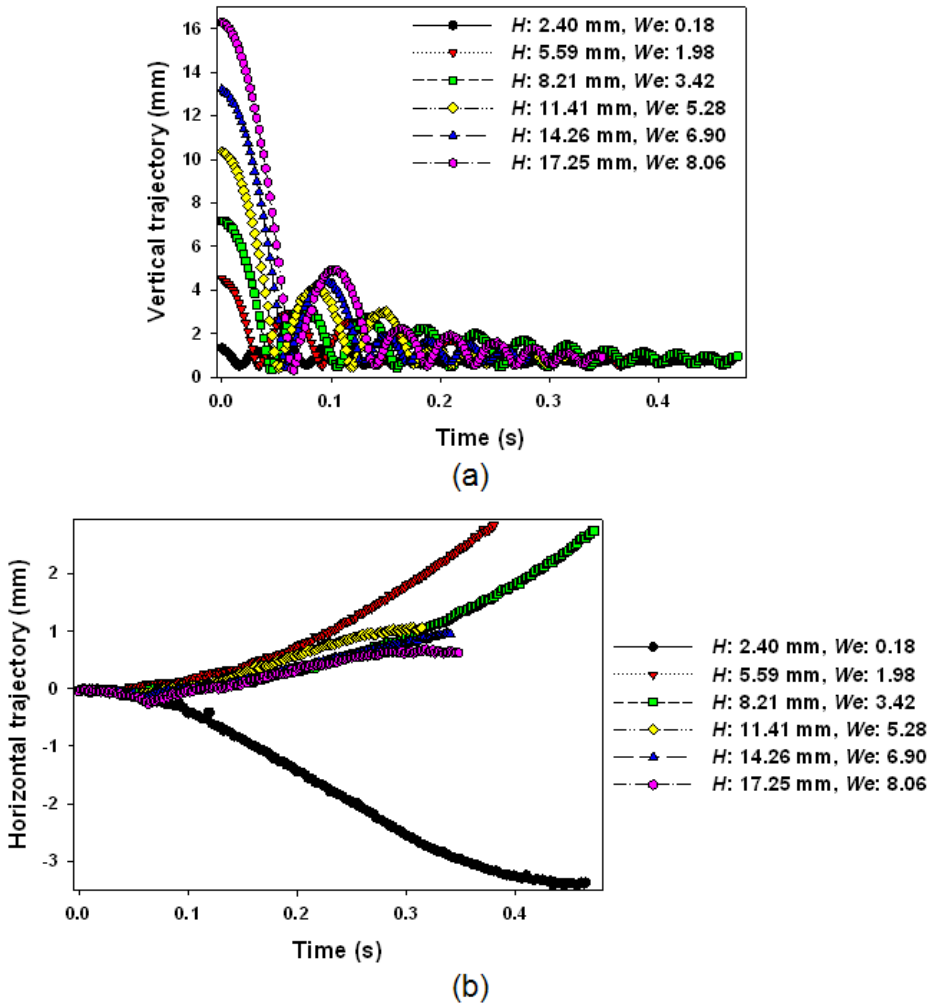

Figure 7.25 Time evolutions of (a) vertical trajectory and (b) horizontal trajectory of 5 μL DI water droplet on PMMA RIE & silane coated asymmetric ratchets (*p*: 15 μm, *d*/*p*: 0.2, and θ_s: 160 ± 2 °) with varied impact speed (*We*: 0.18 – 8.06).

Figure 7.25 shows the evolutional trajectories for both vertical (a) and horizontal (b) directions. Directed rebounding of droplet was observed for all different needle heights. Similar to 750 μm period of ratchets, the slower impact velocity made the longer dislocation. With lower needle heights ($H \leq 8.21$ mm), horizontal displacement larger than 3mm was observed. Exceptionally, reverse motion was observed at the slowest impact (*We*: 0.18) as shown in figure 7.25 (b). The reason for the reverse motion for 15 μm period of superhydrophobic ratchets with very low initial impact velocity is not clear yet. Three different events were observed in the range of *We* 0.18 – 8.06 from 15 μm period of superhydrophobic ratchets as shown in figure 7.26.

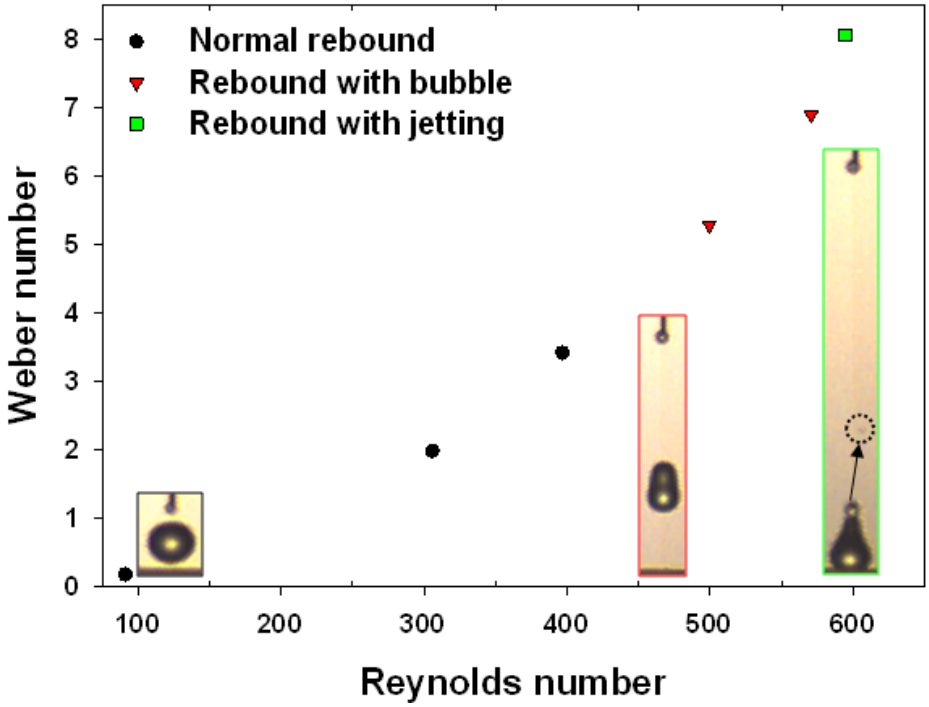

Figure 7.26 Impact dynamics of 5 μL DI water droplet on PMMA RIE & silane coated asymmetric ratchets (*p*: 15 μm, *d*/*p*: 0.2, and θ_s: 160 ± 2 °) with varied impact speed (*We*: 0.67 – 16.23). The sequences show different impact events.

Figure 7.27 (a) and (b) shows the variation of restitution coefficient *e* of droplet impacting superhydrophobic miniaturized asymmetric ratchets (*p*: 15 μm, *d*/*p*: 0.2, and θ_s: 160 ± 2 °) for different droplet impact velocity. Overall the number of rebounds significantly increased comparing with those observed with 750 μm period PMMA superhydrophobic ratchets.

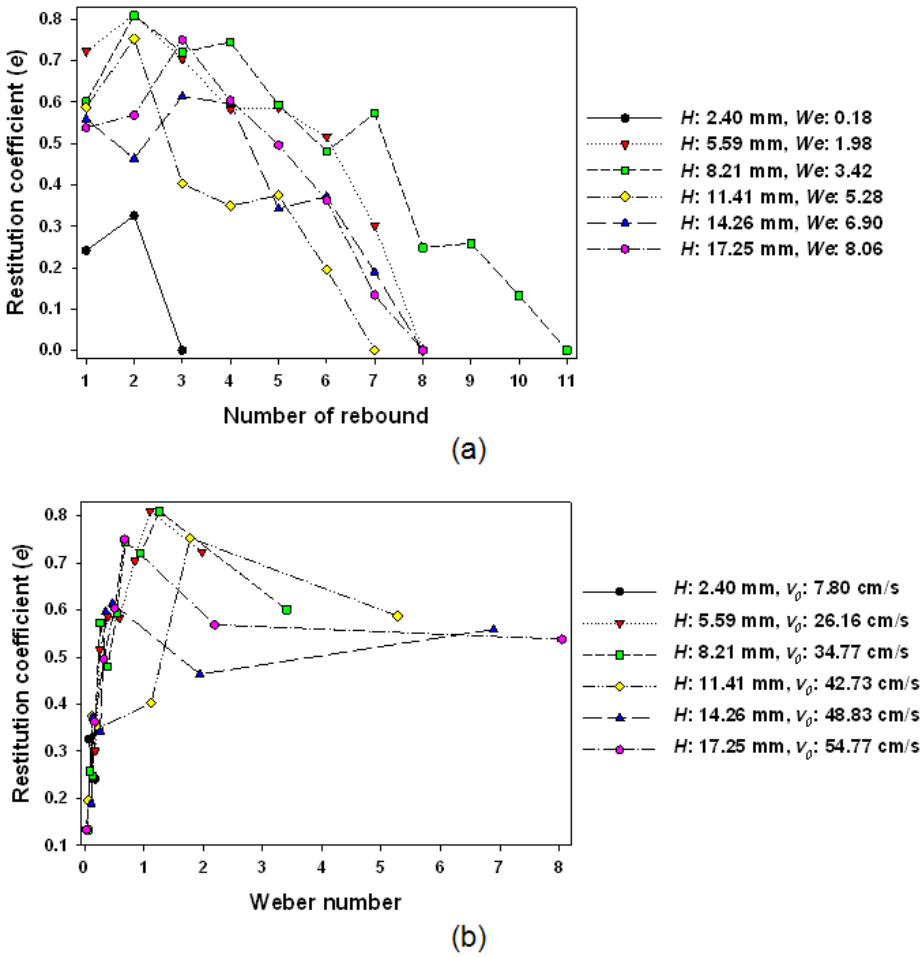

Figure 7.27 Restitution coefficient for 5 µL DI water droplet rebounding on PMMA RIE & silane coated asymmetric ratchets (p: 15 µm, d/p: 0.2, and θ_s: 160 ± 2 °) with varied impact speed (H: 2.40 − 17.25 mm, v_i: 7.80 – 54.77 cm/s); as a function of (a) number of rebound and (b) Weber number.

7.3.3.3 Symmetric Ratchets with Different Local Surface Roughness

A PMMA superhydrophobic symmetric V grooves with asymmetric local surface roughness was also employed to understand rebounding behavior of millimetric droplets. Such asymmetric surface roughness in V grooves was generated in the course of the micromilling of microsteps. The SEM images of the structure is given figure 7.12 (e) and (f). The cross-section of the V grooves in the SEM image shows symmetric structures. However, the difference in surface roughness from the two sides of the V grooves was clearly visible. These PMMA V grooves with asymmetric surface roughness were further treated with O2 RIE and a fluorinated silane coating

to obtain superhydrophobicity Figure 7.28 shows the snapshots a millimetric DI water droplet impacting on the PMMA symmetric grooves with different local surface roughness (p: 150 μm, d/p: 0.5, and θ_s: 154 ± 5 °) with and without O2 RIE and fluorinated silane coating. The right side of each ratchet wall is rougher than that of the left side in figure 7.28. The needle height to drop water was around 3.5 mm and the corresponding *We* was ~0.8. Figure 7.28 (a) shows that there was an apparent air gap between the bottom surface of the droplet and the ratchet valleys in both the spreading and recoiling process of the droplet. In fact, the contacts only occur at the top ridges of the V grooves. Directed rebounding was also observed, which is attributed to the surface tension gradient produced by the local surface roughness difference of the groove surfaces. The rough side of the groove wall has a lower surface energy. Thus, the droplet rebounds toward the smooth surface direction. In case of the V grooves with the surface roughness gradient only, no directional rebounding was observed. The released droplet just sinks and self-oscillates without horizontal dislocation as shown in figure 7.28 (b).

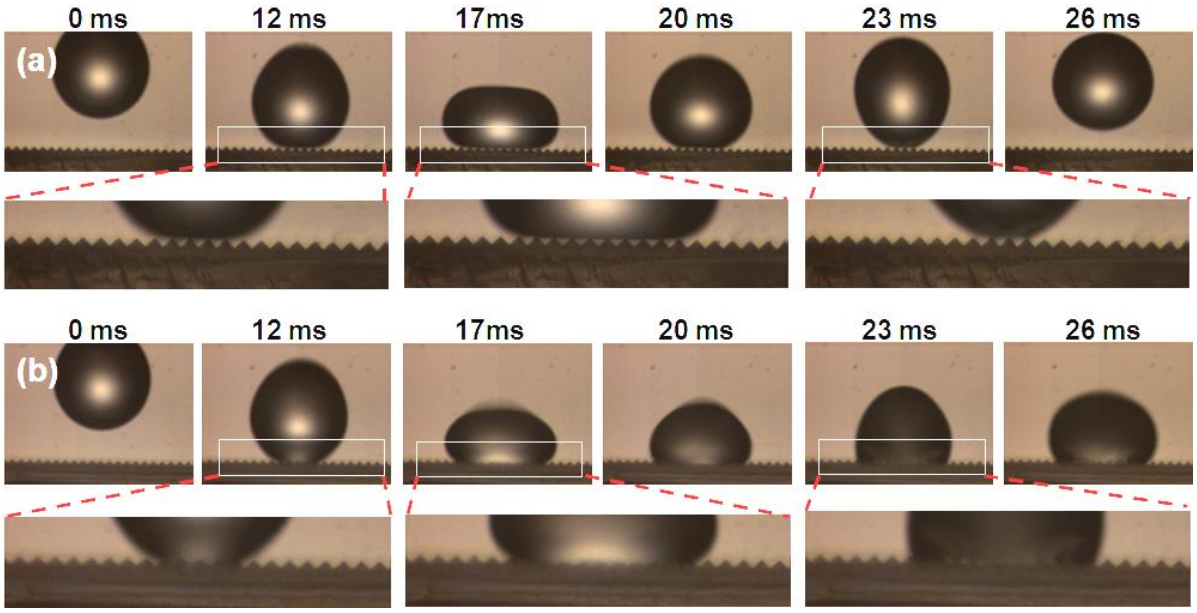

Figure 7.28 The snapshots (magnification: 90 mm spacer, frame rates 1000 fps, and expose time: 100 μs) of ~5 μL DI water droplet impacting PMMA symmetric ratchets with different local surface roughness (p: 150 μm, d/p: 0.5, and θ_s: 154 ± 5 °); (a) RIE & silane coated and (b) plain surface.

Figure 7.29 (a) – (c) display trajectories of millimetric droplets when those are dropped on PMMA superhydrophobic V grooves with different local surface roughness from four different needle heights (*H*: 3.48 – 9.53 mm, *We*: 0.79 – 4.07). Overall directed rebounding behavior of droplet is observed, which is similar to the rebounding on PMMA superhydrophobic asymmetric ratchets. A lower impact speed of droplet results in a longer path of dislocation by directed rebounding. Their impact behavior was also changing with increasing impact velocity Normal complete rebounding occurs only when *We* is 0.79. Trapped split droplet with rebounding was observed in the needle height range of 5.56 – 9.53 mm. Two of three droplets released at 9.53 mm showed the partial rebound events, which made droplet temporary separation while keeping rebounds. No jetting event was appeared.

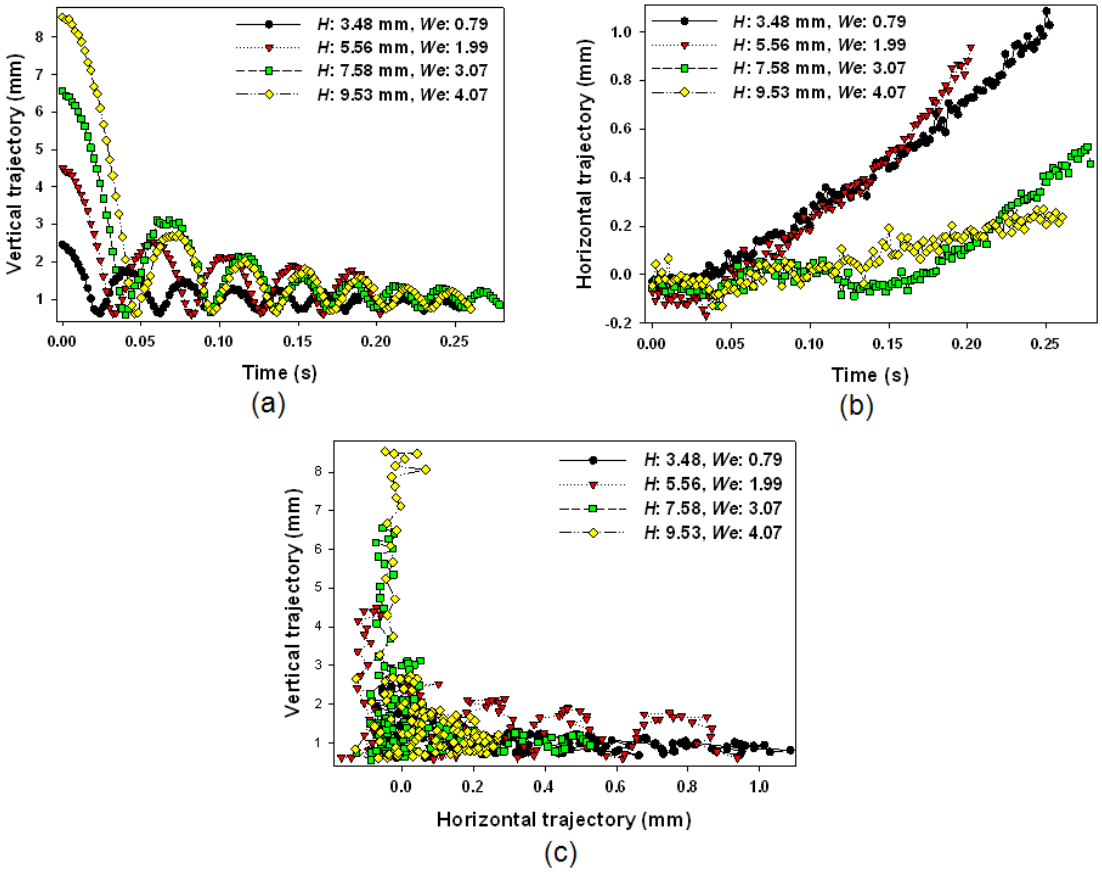

Figure 7.29 (a) – (c) Vertical and horizontal trajectory of ~5 μL DI water droplet rebounding on RIE & silane coated PMMA symmetric ratchets with different surface roughness (*p*: 150 μm, *d*/*p*: 0.5, and θ_s: 154 ± 5 °) for varied needle height (*H*: 3.48 – 9.53, *We*: 0.79 – 4.07).

A similar restitution coefficient variation of millimetric water droplet to that on the superhydrophobic ratchets is shown, with the slight difference in the number of rebounds.

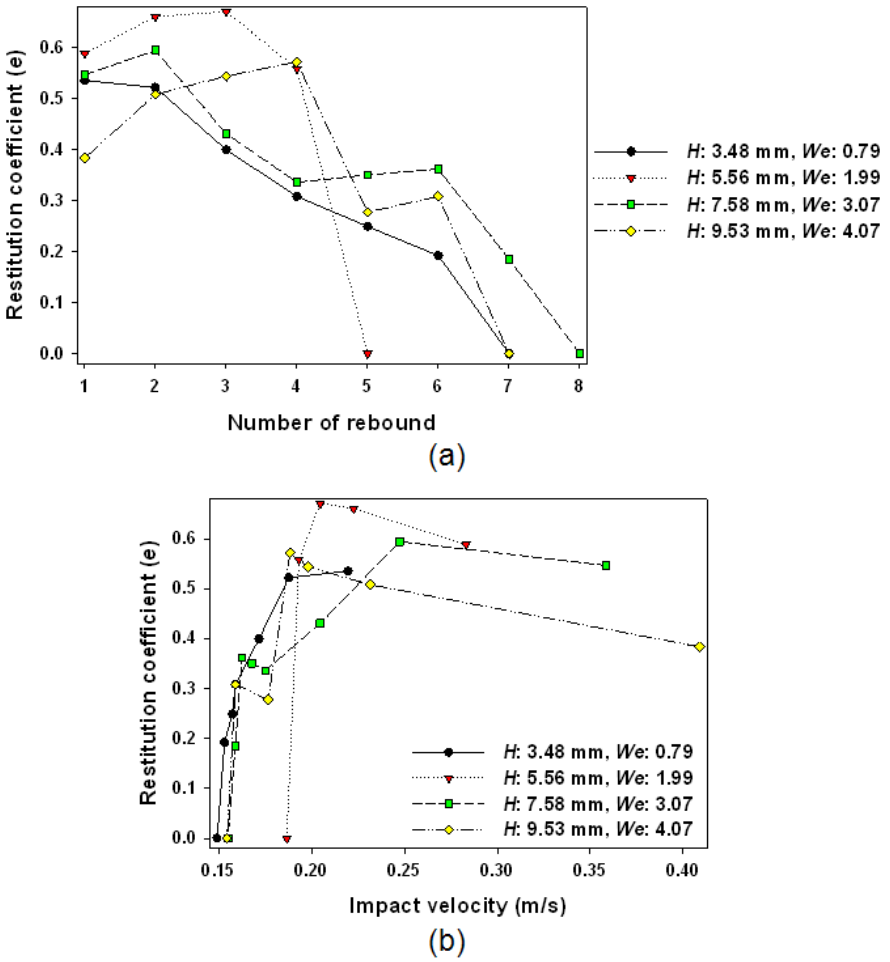

Figure 7.30 Restitution coefficient for ~5 µL DI water droplet rebounding on RIE & silane coated PMMA symmetric ratchets with different surface roughness (p: 150 µm, d/p: 0.5, and θ_s: 154 ± 5 °) for varied needle height (H: 3.48 – 9.53, We: 0.79 – 4.07); as a function of (a) number of rebound and (b) impact velocity (v_i).

Figure 7.31 show the characteristics of the restitution coefficients for millimetric DI water droplet rebounding on various superhydrophobic surfaces. The initial impact velocities are all similar for different superhydrophobic surface (H: 5.33 – 6.19). Micrometer scale surface roughness influences total number of rebounds. More frequency of rebounding tends to be induced by less microscale roughness. There was no strong relevance between ratchets dimensions and horizontal dislocation by directed rebounding.

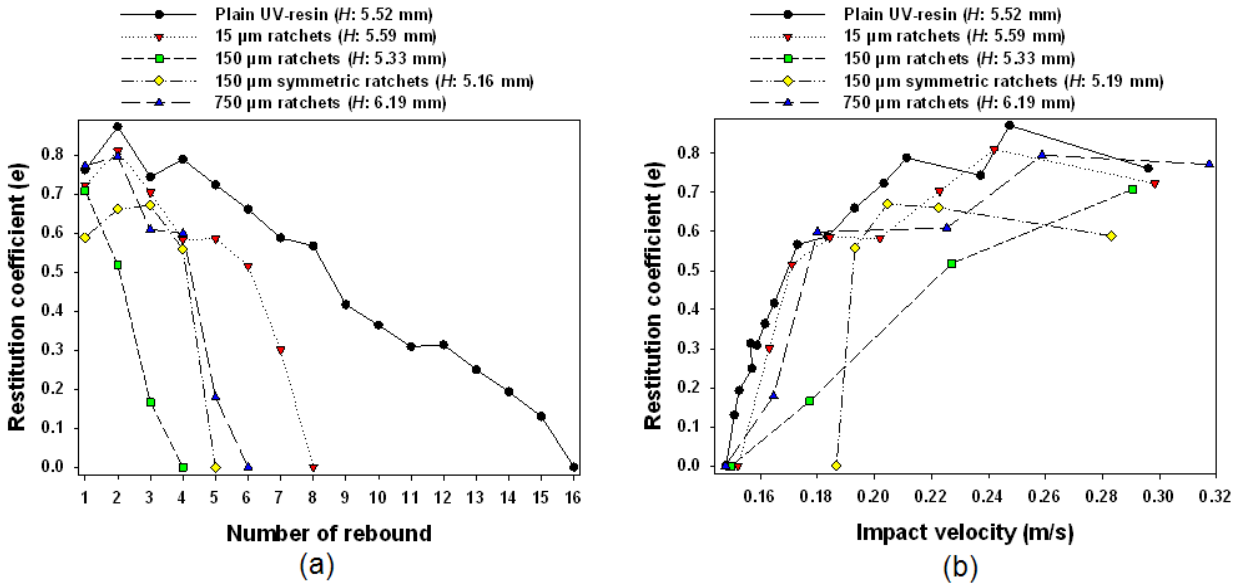

Figure 7.31 Restitution coefficient for 5 µL DI water droplet rebounding on various superhydrophobic surfaces for similar needle height (H: 5.33 – 6.19); as a function of (a) number of rebound and (b) impact velocity (v_i).

7.4 Conclusions

The impact property of millimetric water droplets on various polymer superhydrophobic surfaces was examined. Four different impact events were observed depending on the polymer surface as well as impact speed of droplet. The droplet temporally moves along superhydrophobic asymmetric microratchets and even on the symmetric V grooves with local surface roughness difference. For both of case, the length of moving path is strongly dependent on the droplet impact velocity. This directional rebounding may have in such applications as self cleaning, water harvesting, and turbine blades (Malouin, Koratkar et al. 2010).

Chapter 8 Conclusions and Future Works

8.1 Conclusions

This study aimed to examine the feasibility of using micro and nanoscale asymmetric structures to drive liquid droplets experimentally as well as to understand the driving mechanism. Technically, we have established the fabrication process for large area topological ratchets as well as ratchets integrated with superhydrophobic structures on their surfaces with the period ranging from millimeter down to sub-micrometer via micro/nanomachining techniques. An experimental setup with a high speed camera and an injection system by a syringe pump was built, which enabled capturing details on the droplet motion in a reproducible manner. The image processing tools allowed us to characterize the droplet motion more accurately as well as more efficiently, providing important information such as the droplet size, trajectory, velocity, accelerations, kinetic energy, etc.

When DI water droplets were put on heated miniaturized ratchets near or above the Leidenfrost temperature, two critical temperature regimes were identified. In lower temperature range (*L* regime), which is typically from the threshold temperature for the droplet motion (T_{th}) up to ~ 50 ℃ above T_{th}, the mean droplet velocity (v_m) increases by decreasing ratchet period (p). On the other hand, v_m remains almost constant at a few cm/s regardless the ratchet period in higher temperature range (*H* regime). These clear two regimes were also observed for other liquids such as acetone and IPA. It is also found that a hydrophobic coating on the ratchet surface decreases T_{th} and increases v_m. The different behaviors in the two temperature regimes could be explained by the presence of direct contacts between the bottom of the droplet and the ratchet ridges.

With the enhanced experimental setup equipped with a high speed camera, the influence of

ratchet surface temperature and period was reevaluated and the results were consistent with those observed by the primitive experimental setup, showing the strong dependence of ratchet period only in *L* regime, but not significant in *H* regime. The initial impact velocity of released droplets does not affect the horizontal mobility in both *L* and *H* regime in the We number range of 0.43 – 18.81. Addition of a small amount of polymer additives (200 ppm PEO) to DI water reduced T_{th}, but it also reduced the horizontal mobility significantly. Continuous rebounding behavior of droplets over the entire ratchets path was observed on micro ratchets (*p*: 750 μm) with small aspect ratio (*d/p*: 0.1) and round ridges.

The impact of DI water droplets on various polymer superhydrophobic surfaces was also characterized. Four different impact events such as normal complete rebound, rebound with trapped split droplets, rebound with droplet separation, rebound with jetting, were observed depending on the polymer surface as well as impact speed of droplet. The droplet temporally moves along superhydrophobic asymmetric microratchets and symmetric microratchets with different local surface roughness. For both of case, the length of moving path is strongly dependent on the droplet impact velocity.

The results observed so far present that micro and nano ratchets can potentially be used as a component for micro and nanofluidic devices. An immediate application is envisioned in microscale heat pipes incorporated with micro/nano ratchets for cooling microprocessors that could be powered by waste heat, making them attractive for use closed loop, two-phase cooling systems with no moving parts and no external power. The use of low boiling point materials such as R-134 and liquid nitrogen will also allow room temperature operation. Broader applications are also found as a means of increasing efficiencies for film boiling heat transfer associated with droplets and spray by preventing stationary vapor films between the droplets and hot surface,

such as fuel injection for combustion technology, stream generation for energy conversion in nuclear power energy converters, cooling systems for nuclear reactors, and spray quenching of heat treatable alloys.

However, a critical disadvantage of the Leidenfrost-ratchets system is the requirement of relatively higher operating temperature. The influence of fluorinated silane on the droplet motion indicates that combining ratchets with superhydrophobic treatment (chemically, topologically or the combination thereof) may be able to lower T_{th}, allowing for a broad range of applications, for instance, microchip-based thermal cycling of biopolymers for amplification and ligation. The superhydrophobic ratchets might also keep fluids from fully wetting micro and nanochannel surface. Transport of biomolecules such as molecular motor molecules is another interesting application with nanoratchets because artificial fluctuation force will not be required due to the transduction of chemical energy into mechanical work inherent to the motor molecules (Julicher, Ajdari et al. 1997).

As extended works of this study, it is worth to study about ‘liquid motion within ratcheted microchannel’, ‘the influence of surface roughness’, ‘polymer superhydrophobic ratchets with surface tension gradient’, ‘reverse motion: what is the driving mechanism?’.

8.2 Future Work

8.2.1 Liquid Motion within Ratcheted Microchannel

In this study, the liquid was only transported along open-free surfaces with geometrical asymmetry, not within the microchannel. For further pragmatic applications, it is desired to investigate liquid motion inside the channel with asymmetry. To achieve this goal, the hybrid processes to integrate asymmetric micro/nano structures into 3-D microfluidic devices should be developed. One of the critical challenges of this process is how to fabricate the device with

optically transparent and thermally conductive materials for the appropriate characterization of the liquid motion at higher temperatures. Highly recommended materials are silicon based polymer containing nitrogen (N), carbon (C), and boron (B) since they have been considered as preceramic polymers for various SiC-based non-oxide ceramics (Lee, Yoon et al. 2007). 3-D molding process can shape the desired structure, which can be transformed by heat or UV exposure to form the final dense ceramic solid. SiCN is most candidate material among SiC-based non-oxide ceramics due to the transparency, high thermal conductivity, excellent thermal stability, and high mechanical strength (Yang, Wang et al. 2005). In the stage of material selection, preliminary experiments are necessary to examine how the ceramic porosity influence the Leidenfrost regime with plain fully cured and pyrolyzed one.

8.2.2. The Influence of Surface Roughness

Another important question is the limitation of ratchet dimensions in which directional liquid motion occurs. The significant increase in droplet mobility with decreasing ratchet period suggests that further miniaturization of ratchet period to the real nanoscale (sub-100 nm) may propel the droplet more efficiently until the droplet considers the ratchets as a flat surface (Ok, Lopez-Ona et al. 2010).

Additional surface roughness formed on the ratchet surface may modify the vapor flow underneath droplet and thus the mobility of the droplet. According to the theoretical study by Prat et al., surface roughness significantly influences the vapor flow field between film boiling droplet and impermeable hot flat solid surface (Prat, Schmitz et al. 1995). Three different shapes of surface roughness elements were evaluated: rectangular, semi-cylindrical and triangular. For all cases, vapor flow penetrated into the roughness cavities. However, recirculation regions were existed only for rectangular geometry. As size of droplet increases, in other words, the number of

surface roughness elements underneath droplet increases, the thickness of vapor layer increases. For the Leidenfrost-ratchet system, the recirculation would interfere with the directional vapor flow, produced by local pressure gradient due to topologically asymmetric ratchets. A thinner vapor film would be more efficient for the droplet mobility on ratchets.

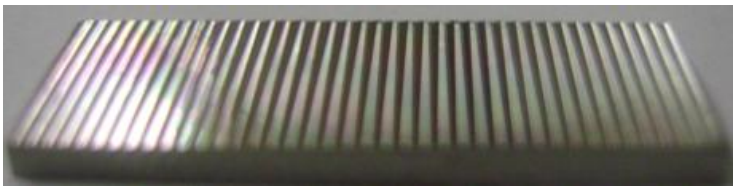

Figure 8.1 Photograph of Ni electroplated micro gratings (grating width *w*: 5 μm, period *p*: 15 μm, and height *h*: 2 μm) on micro ratchets (*p*: 750 μm, size: $3 \times 1 \times 0.25$ cm^3).

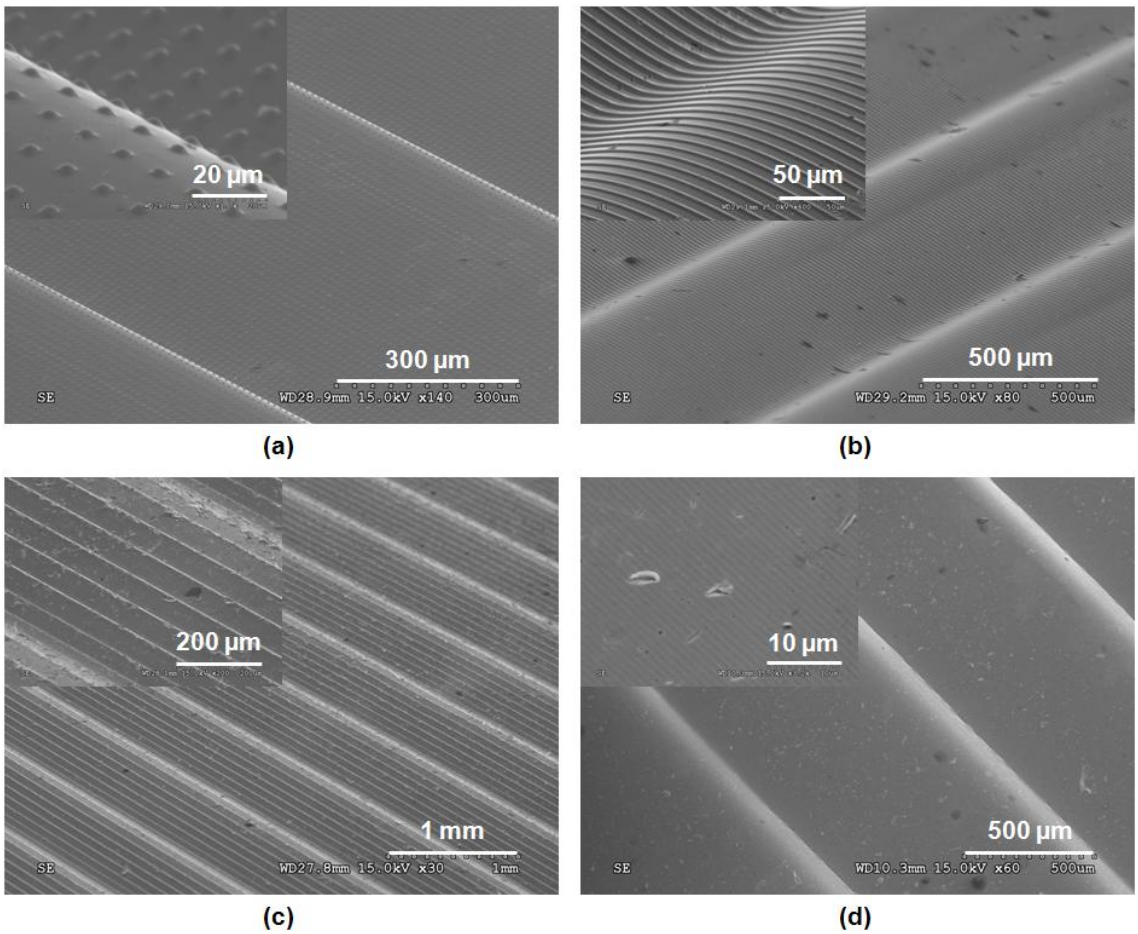

Figure 8.2 SEM images of various miniaturized patterns on micro ratchets (*p*: 750 μm); (a) micro pillars (*w*: 5 μm, *p*: 15 μm *h*: ~2 μm) on micro ratchets (*p*: 750 μm, *d*: ~100 μm), (b) micro gratings (*w*: 5 μm, *p*: 15 μm *h*: 2 μm) on micro ratchets (*p*: 750 μm, *d*: ~70 μm), (c) micro ratchets (*p*: 75 μm and *d*: 15 μm) on micro ratchets (*p*: 750 μm, *d*: ~70 μm), and (d) nano ratchets (*p*: 800 nm and *d*: 200 nm) on micro ratchets (*p*: 750 μm, *d*: ~70 μm).

Therefore, it is interesting to investigate the influence of various shapes of miniaturized structures along the ratchets surface on the motion of droplet. Various micro and nano structures (gratings, pillars and ratchets) on top of the micro ratchets (*p*: 750 μm) can be integrated by 3-D molding process (refer Chapter 3.2.3) that utilizes a thin intermediate PDMS stamp with various micro and nanopatterns. The PMMA micro ratchets produced by 3-D molding will be replicated into nickel via electroplating. Figure 8.1 shows a photograph of an example of electroplated Ni where micrograting with 15 μm period and 2 μm height are integrated into micro ratchets with 750 μm period. Figure 8.2 shows SEM images for electroplated 750 μm period Ni ratchets integrated with various micro and nanostructures. In case the small ratchets are integrated into large ratchets (figure 8.2 (c) and (d)), the directions of the two ratchets are aligned to be consistent. We will investigate the droplet motion on these ratchets at various temperatures and reveal the influence of additional surface roughness.

8.2.3 Reverse Motion: What Is the Driving Mechanism?

We observed both directional motion of droplet on the miniaturized ratchets as shown in figure 8.3. Most droplet motions are in the forward direction. However, for specific conditions, reverse motion has been also observed. For instance, several micro ratchets (*p*: 150, 375, and 750 μm, *d/p*: 0.19) start to generate reverse motion of droplet only when their overall heating times are longer than several hours (5~10 hrs). After cleaning the ratchet surface with metal polish (Brasso, Reckitt Benckiser Inc, NJ) to remove surface metal oxide, forward droplet motion reappeared, indicating that the reverse motion is somehow related to the oxide layer formed upon extended heating of the ratchet surface. This is corroborated by the fact that the reverse motion was not observed from Ni sub-microratchets (*p*: 800 nm), and both Br and Ni macro ratchets (*p*: 1.5 mm). H. Linke et al. also reported that similar behavior could be observed from brass

millimeter scale ratchets, but they did consider this reverse motion as a side effect caused by surface contamination (Linke, Aleman et al. 2006; Taormina 2006).

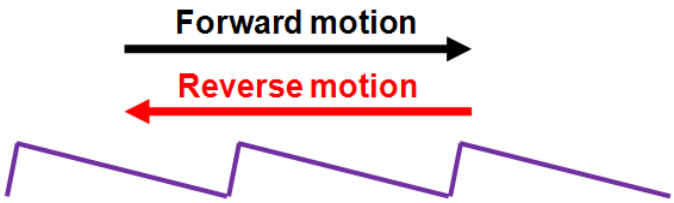

Figure 8.3 Directions of droplet motion along the ratchets.

Figure 8.4 shows droplet velocity as a function of surface temperature for forward and reverse droplet motion, which was obtained from the same brass micro ratchets with the period of 150 μm and aspect ratio of 0.19 aspect ratio. Reverse motion shows a lower threshold temperature as well as much faster droplet velocity compared with those for the forward motion In order to exploit the mechanism of the reverse motion, addition of thermally conductive glitter particles into droplets can help to visualize the motion of droplet. Accurate measurements of local surface temperature by an IR camera as a function of the oxide thickness may also provide hints for the mechanism responsible for the reverse droplet motion.

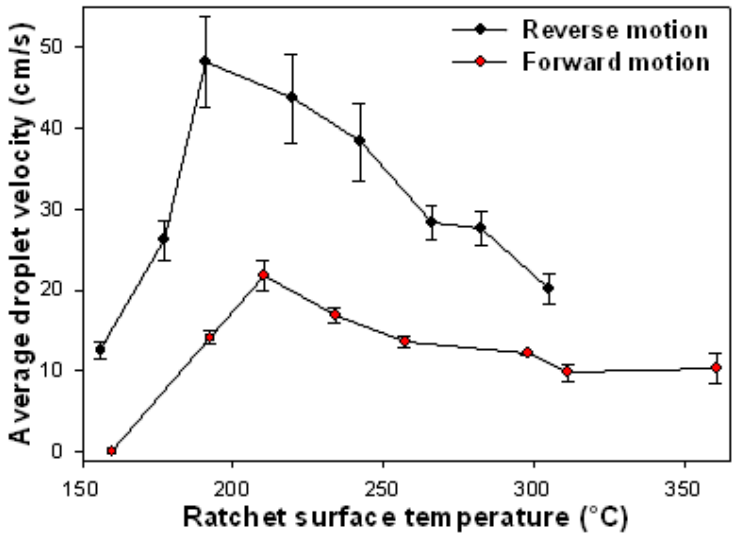

Figure 8.4 Droplet velocity of the forward and reverse motion of millimetric DI water droplet on brass 150 μm ratchets as a function of surface temperature.

References

(2004). HTC-134a Properties, Uses, Storage, and Handling, Dupont.

A. Shastry, D. Taylor, et al. (2007). Micro-Structured Surface Ratchets for Droplet Transport. Transducers '07, Lyon, France.

Acikalin, T., A. Raman, et al. (2003). "Two-dimensional streaming flows induced by resonating, thin beams." Journal of the Acoustical Society of America **114**(4): 1785-1795.

Agrawal, D. C. and V. J. Menon (1994). "Boiling and the Leidenfrost effect in a gravity-free zone: a speculation." Phys. Eudc. **29**: 39-42.

Ajdari, A. (2000). "Pumping liquids using asymmetric electrode arrays." Physical Review E **61**(1): R45-R48.

Ajdari, A. (2002). "Electrokinetic 'ratchet' pumps for Microfluidics." Applied Physics A Materials Science & Processing **75**(2): 271-274.

Amarouchene, Y., G. Cristobal, et al. (2001). "Noncoalescing drops." Physical Review Letters **8720**(20): 046101.

Aussillous, P. and D. Quere (2001). "Liquid marbles." Nature **411**(6840): 924-927.

Austin, M. D., W. Zhang, et al. (2005). "6 nm half-pitch lines and 0.04 mu m(2) static random access memory patterns by nanoimprint lithography." Nanotechnology **16**(8): 1058-1061.

Avedisian, C. T. and M. Fatehi (1988). "An Experimental-Study of the Leidenfrost Evaporation Characteristics of Emulsified Liquid Droplets." International Journal of Heat and Mass Transfer **31**(8): 1587-1603.

Avedisian, C. T., C. Ioffredo, et al. (1984). "Film Boiling of Discrete Droplets of Mixtures of Coal and Water on a Horizontal Brass Surface." Chemical Engineering Science **39**(2): 319-327.

Avedisian, C. T. and J. Koplik (1987). "Leidenfrost Boiling of Methanol Droplets on Hot Porous Ceramic Surfaces." International Journal of Heat and Mass Transfer **30**(2): 379-393.

Bahador Farshchian, Steven Max Hurst, et al. (2010). Simple Fabrication of Hierarchical Structures on a Polymer Surface. NSTI Nanotech 2010, Anaheim, CA.

Barthlott, W. and C. Neinhuis (1997). "Purity of the sacred lotus, or escape from contamination in biological surfaces." Planta **202**(1): 1-8.

Bartolo, D., C. Josserand, et al. (2006). "Singular jets and bubbles in drop impact." Physical Review Letters **96**(12): 124501.

Bartolo, D., C. Josserand, et al. (2006). "Singular jets and bubbles in drop impact." Physical Review Letters **96**(12): -.

Baumeister, K. J., T. D. Hamill, et al. (1966). Film boiling heat transfer to water drops on a flat plate. Chem. Engrg. Progr. Symp.

Bergeron, V. (2003). "Designing intelligent fluids for controlling spray applications." Comptes Rendus Physique **4**(2): 211-219.

Bergeron, V., D. Bonn, et al. (2000). "Controlling droplet deposition with polymer additives." Nature **405**(6788): 772-775.

Bernardin, J. D. and I. Mudawar (1999). "The Leidenfrost point: Experimental study and assessment of existing models." Journal of Heat Transfer-Transactions of the Asme **121**(4): 894-903.

Bernardin, J. D. and I. Mudawar (2002). "A cavity activation and bubble growth model of the Leidenfrost point." Journal of Heat Transfer-Transactions of the Asme **124**(5): 864-874.

Bertola, V. and K. Sefiane (2005). "Controlling secondary atomization during drop impact on hot surfaces by polymer additives." Physics of Fluids **17**(10): 108104.

Bhushan, B., Y. C. Jung, et al. (2009). "Micro-, nano- and hierarchical structures for superhydrophobicity, self-cleaning and low adhesion." Philosophical Transactions of the Royal Society a-Mathematical Physical and Engineering Sciences **367**(1894): 1631-1672.

Biance, A. L., F. Chevy, et al. (2006). "On the elasticity of an inertial liquid shock." Journal of Fluid Mechanics **554**: 47-66.

Biance, A. L., C. Clanet, et al. (2003). "Leidenfrost drops." Physics of Fluids **15**(6): 1632-1637.

Bico, J. and D. Quere (2000). "Liquid trains in a tube." Europhysics Letters **51**(5): 546-550.

Blossey, R. (2003). "Self-cleaning surfaces - virtual realities." Nature Materials **2**(5): 301-306.

Brown, A. B. D., C. G. Smith, et al. (2001). "Pumping of water with ac electric fields applied to asymmetric pairs of microelectrodes." Physical Review E **6302**(2): 016305.

Buguin, A., L. Talini, et al. (2002). "Ratchet-like topological structures for the control of microdrops." Applied Physics a-Materials Science & Processing **75**(2): 207-212.

Castanet, G., T. Liénart, et al. (2008). Measurement of the temperature of droplets interacting with a heated wall. Int. Symp. on Application of Laser Techniques to Fluid Mechanics, Lisbon, Portugal.

Chandra, S. and C. T. Avedisian (1992). "Observations of Droplet Impingement on a Ceramic Porous Surface." International Journal of Heat and Mass Transfer **35**(10): 2377-2388.

Chaudhury, M. K. and G. M. Whitesides (1992). "How to Make Water Run Uphill." Science **256**(5063): 1539-1541.

Chen, H. B., Q. W. Wang, et al. (2005). "Deterministic directed transport of inertial particles in a flashing ratchet potential." Physical Review E **71**(3): 031102.

Chen, L., S. Lee, et al. (2008). "Continuous dynamic flow micropumps for microfluid manipulation." Journal of Micromechanics and Microengineering **18**(1): 013001.

Chiu, S. L. and T. H. Lin (2005). "Experiment on the dynamics of a compound drop impinging on a hot surface." Physics of Fluids **17**(12): 122103.

Choi, K. J. and S. C. Yao (1987). "Mechanisms of Film Boiling Heat-Transfer of Normally Impacting Spray." International Journal of Heat and Mass Transfer **30**(2): 311-318.

Chou, S. Y., P. R. Krauss, et al. (1995). "Imprint of Sub-25 Nm Vias and Trenches in Polymers." Applied Physics Letters **67**(21): 3114-3116.

Chou, S. Y., P. R. Krauss, et al. (1996). "Imprint lithography with 25-nanometer resolution." Science **272**(5258): 85-87.

Cortese, B., S. D'Amone, et al. (2008). "Superhydrophobicity due to the hierarchical scale roughness of PDMS surfaces." Langmuir **24**(6): 2712-2718.

Daniel, S. and M. K. Chaudhury (2002). "Rectified motion of liquid drops on gradient surfaces induced by vibration." Langmuir **18**(9): 3404-3407.

Daniel, S., M. K. Chaudhury, et al. (2001). "Past drop movements resulting from the phase change on a gradient surface." Science **291**(5504): 633-636.

Daniel, S., S. Sircar, et al. (2004). "Ratcheting motion of liquid drops on gradient surfaces." Langmuir **20**(10): 4085-4092.

Darhuber, A. A., J. P. Valentino, et al. (2003). "Thermocapillary actuation of droplets on chemically patterned surfaces by programmable microheater arrays." Journal of Microelectromechanical Systems **12**(6): 873-879.

Deb, S. and S. C. Yao (1989). "Analysis on Film Boiling Heat-Transfer of Impacting Sprays." International Journal of Heat and Mass Transfer **32**(11): 2099-2112.

Degennes, P. G. (1974). "Coil-Stretch Transition of Dilute Flexible Polymers under Ultrahigh Velocity-Gradients." Journal of Chemical Physics **60**(12): 5030-5042.

del Campo, A. and E. Arzt (2008). "Fabrication approaches for generating complex micro- and nanopatterns on polymeric surfaces." Chemical Reviews **108**(3): 911-945.

Delcorio, B. and K. J. Choi (1991). "Analysis of direct liquid-solid contact heat transfer in monodisperse spray cooling." J. Thermophys. Heat Trasfer **5**: 613-620.

Deng, T., K. K. Varanasi, et al. (2009). "Nonwetting of impinging droplets on textured surfaces." Applied Physics Letters **94**(13): 133109.

Ding, Z., W.-B. Song, et al. (2007). Time-Multiplexed Droplet Manipulation Via Vibrating Ratcheted Micro-Channels. IEEE MEMS '07, Kobe, Japan.

Dossantos, D. F. and T. Ondarcuhu (1995). "Free-Running Droplets." Physical Review Letters **75**(16): 2972-2975.

Duncombe, T. A., M. Kumemura, et al. (2009). Integrating EWOD with Surface Ratchets for Active Droplet Transport and Sorting. IEEE MEMS '09, Sorrento, Italy.

Eddi, A., D. Terwagne, et al. (2008). "Wave propelled ratchets and drifting rafts." Epl **82**(4): 44001.

Elbahri, M., D. Paretkar, et al. (2007). "Anti-Lotus effect for nanostructuring at the Leidenfrost temperature." Advanced Materials **19**(9): 1262-1266.

Elleuch, R., K. Elleuch, et al. (2007). "Surface roughness effect on friction behaviour of elastomeric material." Materials Science and Engineering a-Structural Materials Properties Microstructure and Processing **465**(1-2): 8-12.

Engel, A., H. W. Muller, et al. (2003). "Ferrofluids as thermal ratchets." Physical Review Letters **91**(6): 060602.

Fan, L. S., R. Lau, et al. (2001). "Evaporative liquid jets in gas-liquid-solid flow system." Chemical Engineering Science **56**(21-22): 5871-5891.

Farshchian, B., J. Choi, et al. (2011). "Fabrication of superhydrophobic surfaces by soft UV-nanoimprint lithography and surface chemistry modification." Nanotechnology: Under revision.

Farshchian, B., S. M. Hurst, et al. (2011). "3D molding of hierarchical micro- and nanostructures." Journal of Micromechanics and Microengineering **21**(3): 8.

Farshchian, B., J. T. Ok, et al. (2010). Simple Fabrication of Hierarchical Structures on a Polymer Surface. NSTI Nanotech 2010, Anaheim, CA.

Farshchian, B., J. T. Ok, et al. (2009). 3-D integration of micro-gratings into bio-analytical devices. IMECE 09', Lake Buena Vista, FL.

Feng, X. J. and L. Jiang (2006). "Design and creation of superwetting/antiwetting surfaces." Advanced Materials **18**(23): 3063-3078.

Gallardo, B. S., V. K. Gupta, et al. (1999). "ELectrochemical principles for active control of liquids on submillimeter scales." Science **283**(5398): 57-60.

Garnier, N., R. O. Grigoriev, et al. (2003). "Optical manipulation of microscale fluid flow." Physical Review Letters **91**(5): 054501.

Ge, Y. and L. S. Fan (2006). "3-D modeling of the dynamics and heat transfer characteristics of subcooled droplet impact on a surface with film boiling." International Journal of Heat and Mass Transfer **49**(21-22): 4231-4249.

Geng, X., H. Yuan, et al. (2001). "Bubble-based micropump for electrically conducting liquids." Journal of Micromechanics and Microengineering **11**(3): 270-276.

Godleski, E. S. and K. J. Bell (1966). The Leidenfrost phenomenon for binary liquid solutions. Third Int. Heat Transfer Conf., Chicago.

Gorre, L., E. Ioannidis, et al. (1996). "Rectified motion of a mercury drop in an asymmetric structure." Europhysics Letters **33**(4): 267-272.

Gottfrie, B. S., C. J. Lee, et al. (1966). "The Leidenfrost Phenomenon: Film Boiling of Liquid Droplets on a Flat Plate." International Journal of Heat and Mass Transfer **9**(11): 1167-1187.

Groendes, V. and R. Mesler (1982). Measurement of transient surface temperatures beneath Leidenfrost water drops. Int. Heat Transfer Conf., Munich, Hemispher, New Yourk.

Guo, Z. G. and W. M. Liu (2007). "Biomimic from the superhydrophobic plant leaves in nature: Binary structure and unitary structure." Plant Science **172**(6): 1103-1112.

Hardt, S., Schönfeld, F. (2007). Microfluidic Technologies for Miniaturized Analysis Systems, Springer.

Hidaka, S., A. Yamashita, et al. (2006). "Effect of Contact Angle on Wetting Limit Temperature." Heat Transfer-Asian Research **35**(7): 513-526.

Hughes, M. P. (2004). "Numerical simulation of dielectrophoretic ratchet structures." Journal of Physics D-Applied Physics **37**(8): 1275-1280.

Ichimura, K., S. K. Oh, et al. (2000). "Light-driven motion of liquids on a photoresponsive surface." Science **288**(5471): 1624-1626.

Issa, R. J. (2003). Numerical Modeling of the Dynamics and Heat Transfer of Impacting Sprays for a Wide Range of Pressures, University of Pittsburgh. **Ph.D. dissertation**.

J. Yang, G. Mo, et al. (2002). Self-Propelled Drop Movement by Manipulation of Nanoscale Adsorbates through Molecular Self-Assembly, . IEEE-NANO.

Jiang, L., Y. Zhao, et al. (2004). "A lotus-leaf-like superhydrophobic surface: A porous microsphere/nanofiber composite film prepared by electrohydrodynamics." Angewandte Chemie-International Edition **43**(33): 4338-4341.

Julicher, F., A. Ajdari, et al. (1997). "Modeling molecular motors." Reviews of Modern Physics **69**(4): 1269-1281.

Jun, T. K. and C. J. Kim (1998). "Valveless pumping using traversing vapor bubbles in microchannels." Journal of Applied Physics **83**(11): 5658-5664.

Jung, P., J. G. Kissner, et al. (1996). "Regular and chaotic transport in asymmetric periodic potentials: Inertia ratchets." Physical Review Letters **76**(18): 3436-3439.

Jung, Y. C. and B. Bhushan (2008). "Dynamic effects of bouncing water droplets on superhydrophobic surfaces." Langmuir **24**(12): 6262-6269.

Karl, A. and A. Frohn (2000). "Experimental investigation of interaction processes between droplets and hot walls." Physics of Fluids **12**(4): 785-796.

Keller, J. B. and M. J. Miksis (1983). "Surface-Tension Driven Flows." Siam Journal on Applied Mathematics **43**(2): 268-277.

Kettner, C., P. Reimann, et al. (2000). "Drift ratchet." Physical Review E **61**(1): 312-323.

Kim, N., M. C. Murphy, et al. (2008). Investigation of Two-Phase Flow in Rectangular Micro-channels. ASME FEDSM, Jacksonville, FL.

Kulic, I. M., R. Thaokar, et al. (2005). "A DNA ring acting as a thermal ratchet." Journal of Physics-Condensed Matter **17**(47): S3965-S3978.

Lange, K., G. Blaess, et al. (2006). "Integration of a surface acoustic wave biosensor in a microfluidic polymer chip." Biosensors & Bioelectronics **22**(2): 227-232.

Latto, B. (1965). "Viscosity of steam at atmospheric pressure." Int. J. Heat Transfer **8**: 689-720.

Lau, K. K. S., J. Bico, et al. (2003). "Superhydrophobic carbon nanotube forests." Nano Letters **3**(12): 1701-1705.

Laveau, B. L. (2008). Study report: experimental study of droplet motion on a ratcheted surface. Baton Rouge, Louisiana State University**:** 1-70.

Lee, H. J., T. H. Yoon, et al. (2007). "Fabrication of microfluidic channels derived from a UV/thermally cured preceramic polymer via a soft lithographic technique." Microelectronic Engineering **84**(12): 2892-2895.

Lee, J. and C. J. Kim (1998). Liquid Micromotor Driven by Continuous Electrowetting. Proc. MEMS'98, Heidelberg, Germany.

Lee, J., H. Moon, et al. (2002). "Electrowetting and electrowetting-on-dielectric for microscale liquid handling." Sensors and Actuators a-Physical **95**(2-3): 259-268.

Lee, Y. W., S. H. Park, et al. (2007). "Fabrication of hierarchical structures on a polymer surface to mimic natural superhydrophobic surfaces." Advanced Materials **19**(17): 2330-2335.

Leidenfrost, J. G. (1966). "On Fixation of Water in Diverse Fire." International Journal of Heat and Mass Transfer **9**(11): 1153-1166.

Li, D. (2008). Optical manipulation of microscale fluid flow, Springer.

Lide, D. R., Ed. (2006). CRC Handbook of Chemistry and Physics. Boca Raton, FL., CRC Press.

Lindner, B., L. Schimansky-Geier, et al. (1999). "Inertia ratchets: A numerical study versus theory." Physical Review E **59**(2): 1417-1424.

Linke, H., B. J. Aleman, et al. (2006). "Self-propelled Leidenfrost droplets." Physical Review Letters **96**(15): 154502.

Linke, H., T. E. Humphrey, et al. (2002). "Quantum ratchets and quantum heat pumps." Applied Physics a-Materials Science & Processing **75**(2): 237-246.

Linke, H., T. E. Humphrey, et al. (1999). "Experimental tunneling ratchets." Science **286**(5448): 2314-2317.

Liu, L. and S. C. Yao (1982). Heat transfer analysis of droplet flow impinging on a hot surface. Seventh Int. Heat Transfer Conf., Munich, Hemispher, New Yourk.

Long, T. M., S. Prakash, et al. (2006). "Water-vapor plasma-based surface activation for trichlorosilane modification of PMMA." Langmuir **22**(9): 4104-4109.

Luo, J. K., Y. Q. Fu, et al. (2009). "Moving-part-free microfluidic systems for lab-on-a-chip." Journal of Micromechanics and Microengineering **19**(5): 054001.

Mahmud, G., C. J. Campbell, et al. (2009). "Directing cell motions on micropatterned ratchets." Nature Physics **5**(8): 606-612.

Malouin, B. A., N. A. Koratkar, et al. (2010). "Directed rebounding of droplets by microscale surface roughness gradients." Applied Physics Letters **96**(23): 234103.

Mann, R. F. and W. W. Walker (1975). "Vaporization of Small Binary Drops on a Flat Plate at Maximum Heat-Flux." Canadian Journal of Chemical Engineering **53**(5): 487-493.

Marquet, C., A. Buguin, et al. (2002). "Rectified motion of colloids in asymmetrically structured channels." Physical Review Letters **88**(16): 168301.

Matsumoto, H. and J. E. Colgate (1990). Preliminary Investigation of Micropumping Based on Electrical Control of Interfacial Tension. Proc. MEMS'90, Napa Valley, Canada.

Matthias, S. and F. Muller (2003). "Asymmetric pores in a silicon membrane acting as massively parallel brownian ratchets." Nature **424**(6944): 53-57.

Melling, L. (2003). Self-propelled motion of film boiling droplets on ratchet-like surfaces. Physics, University of Oregon. **B.S.**

Muller, F., A. Birner, et al. (2000). "Membranes for micropumps from macroporous silicon." Physica Status Solidi a-Applied Research **182**(1): 585-590.

Nagai, N. and S. Nishio (1996). "Leidenfrost temperature on an extremely smooth surface." Experimental Thermal and Fluid Science **12**(3): 373-379.

Namasivayam, V., R. G. Larson, et al. (2003). "Transpiration-based micropump for delivering continuous ultra-low flow rates." Journal of Micromechanics and Microengineering **13**(2): 261-271.

Nguyen, N. T., A. H. Meng, et al. (2000). "Integrated flow sensor for in situ measurement and control of acoustic streaming in flexural plate wave micropumps." Sensors and Actuators a-Physical **79**(2): 115-121.

Nguyen, N. T. and R. M. White (1999). "Design and optimization of an ultrasonic flexural plate wave micropump using numerical simulation." Sensors and Actuators a-Physical **77**(3): 229-236.

Ok, J. T., E. Lopez-Ona, et al. (2010). "Propulsion of droplets on micro- and sub-micron ratchet surfaces in the Leidenfrost regime." Microfluid Nanofluid: Published online.

Ornatskii, A. P. (1965). "Generalization of experimental data on flow friction in surface boiling." J. Appl. Mech. and Tech. Phys. **6**: 80-82.

Ozaki, K. (1995). Pumping Mechanism Using Periodic Phase Changes of a Fluid. Proceedings of MEMS'95, Amsterdam, The Netherlands.

Pamme, N. (2006). "Magnetism and microfluidics." Lab on a Chip **6**(1): 24-38.

Park, D. S. W., M. L. Hupert, et al. (2008). "A titer plate-based polymer microfluidic platform for high throughput nucleic acid purification." Biomedical Microdevices **10**(1): 21-33.

Park, J. (2007). A liquid lens based on electrowetting. Electrical and Computer Engineering. Baton Rouge, Louisiana State University. **M.S.**

Pedersen, C. O. (1970). "An Experimental Study of Dynamic Behavior and Heat Transfer Characteristics of Water Droplets Impinging Upon a Heated Surface." International Journal of Heat and Mass Transfer **13**(2): 369-381.

Pennathur, S. (2008). "Flow control in microfluidics: are the workhorse flows adequate?" Lab on a Chip **8**(3): 383-387.

Pollock, H. M., D. Maugis, et al. (1978). "Force of Adhesion between Solid-Surfaces in Contact." Applied Physics Letters **33**(9): 798-799.

Prakash, M., D. Quere, et al. (2008). "Surface tension transport of prey by feeding shorebirds: The capillary ratchet." Science **320**(5878): 931-934.

Prat, M., P. Schmitz, et al. (1995). "On the effect of surface roughness on the vapor flow under Leidenfrost-levitated droplets." Journal of Fluids Engineering-Transactions of the Asme **117**(3): 519-525.

Quere, D. (2005). "Non-sticking drops." Reports on Progress in Physics **68**(11): 2495-2532.

Reimann, P. and P. Hanggi (2002). "Introduction to the physics of Brownian motors." Applied Physics a-Materials Science & Processing **75**(2): 169-178.

Rein, M. (1993). "Phenomena of Liquid-Drop Impact on Solid and Liquid Surfaces." Fluid Dynamics Research **12**(2): 61-93.

Ren, H., R. B. Fair, et al. (2004). "Automated on-chip droplet dispensing with volume control by electro-wetting actuation and capacitance metering." Sensors and Actuators B-Chemical **98**(2-3): 319-327.

Reyssat, M., D. Richard, et al. (2010). "Dynamical superhydrophobicity." Faraday Discussions **146**: 19-33.

Richard, D., C. Clanet, et al. (2002). "Surface phenomena - Contact time of a bouncing drop." Nature **417**(6891): 811-811.

Richard, D. and D. Quere (2000). "Bouncing water drops." Europhysics Letters **50**(6): 769-775.

Roach, P., N. J. Shirtcliffe, et al. (2008). "Progess in superhydrophobic surface development." Soft Matter **4**(2): 224-240.

Rothstein, J. P. (2010). "Slip on Superhydrophobic Surfaces." Annual Review of Fluid Mechanics **42**: 89-109.

Rousselet, J., L. Salome, et al. (1994). "Directional Motion of Brownian Particles Induced by a Periodic Asymmetric Potential." Nature **370**(6489): 446-448.

Roychowdhury, A. (2007). Fabrication of perforated polymer membranes using imprinting technology Mechanical Engineering. Baton Rouge, Louisiana State University. **M.S.**

Sandre, O., L. Gorre-Talini, et al. (1999). "Moving droplets on asymmetrically structured surfaces." Physical Review E **60**(3): 2964-2972.

SchimanskyGeier, L., M. Kschischo, et al. (1997). "Flux of particles in sawtooth media." Physical Review Letters **79**(18): 3335-3338.

Shastry, A., M. J. Case, et al. (2006). "Directing droplets using microstructured surfaces." Langmuir **22**(14): 6161-6167.

Shastry, A., D. Taylor, et al. (2007). Micro-Structured Surface Ratchets for Droplet Transport. Transducers '07, Lyon, France.

Slater, G. W., H. L. Guo, et al. (1997). "Bidirectional transport of polyelectrolytes using self-modulating entropic ratchets." Physical Review Letters **78**(6): 1170-1173.

Song, Y. J. and T. S. Zhao (2001). "Modelling and test of a thermally-driven phase-change nonmechanical micropump." Journal of Micromechanics and Microengineering **11**(6): 713-719.

Song, Z. (2007). Study of demolding progress in thermal imprint lithography via numerical simulation and experimental approaches. Mechanical Engineering. Baton Rouge, Louisiana State University. **M.S.**

Stroock, A. D., R. F. Ismagilov, et al. (2003). "Fluidic ratchet based on Marangoni-Benard convection." Langmuir **19**(10): 4358-4362.

Sun, M. H., C. X. Luo, et al. (2005). "Artificial lotus leaf by nanocasting." Langmuir **21**(19): 8978-8981.

T. A. Duncombe, M. Kumemura, et al. (2009). Integrating EWOD with Surface Ratchets for Active Droplet Transport and Sorting. IEEE MEMS '09, Sorrento, Italy.

Takagi, H., R. Maeda, et al. (1994). Transformation Type Micropump. Proc. of Micro Mechatronics and Human Sciences.

Takata, Y., S. Hidaka, et al. (2005). "Effect of surface wettability on boiling and evaporation." Energy **30**(2-4): 209-220.

Taormina, M. J. (2006). Leidenfrost Ratchets. Physics, University of Oregon. **Bachelor of Science**.

Temple-Pediani, R. W. (1970). Fuel drop vaporization under pressure on a hot surface. Instn. Mech. Engrs.

Tessier, F. and G. W. Slater (2002). "Strategies for the separation of polyelectrolytes based on non-linear dynamics and entropic ratchets in a simple microfluidic device." Applied Physics a-Materials Science & Processing **75**(2): 285-291.

Thimbleby, H. (1989). "The Leidenfrost phenomenon." Phys. Eudc. **24**: 300-303.

Tsai, P., S. Pacheco, et al. (2009). "Drop impact upon micro- and nanostructured superhydrophobic surfaces." Langmuir **25**(20): 12293-12298.

Tseng, F. G., K. H. Lin, et al. (2004). "A surface-tension-driven fluidic network for precise enzyme batch-dispensing and glucose detection." Sensors and Actuators a-Physical **111**(1): 107-117.

Tseng, Y. T., F. G. Tseng, et al. (2004). "Fundamental studies on micro-droplet movement by Marangoni and capillary effects." Sensors and Actuators a-Physical **114**(2-3): 292-301.

van Oudenaarden, A. and S. G. Boxer (1999). "Brownian ratchets: Molecular separations in lipid bilayers supported on patterned arrays." Science **285**(5430): 1046-1048.

Wachters.Lh, H. Bonne, et al. (1966). "Heat Transfer from a Hot Horizontal Plate to Sessile Water Drops in Spherodial State." Chemical Engineering Science **21**(10): 923-936.

Wang, S. T., L. Feng, et al. (2005). "Manipulation of surface wettability between superhydrophobicity and superhydrophilicity on copper films." Chemphyschem **6**(8): 1475-1478.

Wang, Z., C. Lopez, et al. (2007). "Impact dynamics and rebound of water droplets on superhydrophobic carbon nanotube arrays." Applied Physics Letters **91**(2): 023105.

Wereley, N. T. N. a. S. T. (2006). Fundamentals and Applications of Microfluidics. Boston, Artech House.

Xia, Y. N. and G. M. Whitesides (1998). "Soft lithography." Annual Review of Materials Science **28**: 153-184.

Xie, Q. D., G. Q. Fan, et al. (2004). "Facile creation of a bionic super-hydrophobic block copolymer surface." Advanced Materials **16**(20): 1830-1833.

Xiu, Y., L. Zhu, et al. (2007). "Hierarchical silicon etched structures for controlled hydrophobicity/superhydrophobicity." Nano Letters **7**(11): 3388-3393.

Xiu, Y. H., D. W. Hess, et al. (2008). "UV and thermally stable superhydrophobic coatings from sol-gel processing." Journal of Colloid and Interface Science **326**(2): 465-470.

Xue, C. H., S. T. Jia, et al. (2010). "Large-area fabrication of superhydrophobic surfaces for practical applications: an overview." Science and Technology of Advanced Materials **11**(3).

Yang, R., W. J. Wang, et al. (2005). "Out-of-plane microlens array fabricated using ultraviolet lithography." Applied Physics Letters **86**(16): -.

Yao, S. C. and K. Y. Cai (1988). "The Dynamics and Leidenfrost Temperature of Drops Impacting on a Hot Surface at Small Angles." Experimental Thermal and Fluid Science **1**(4): 363-371.

Yeo, L. Y. and J. R. Friend (2009). "Ultrafast microfluidics using surface acoustic waves." Biomicrofluidics **3**(1): 012002.

Yokoyama, Y., M. Takeda, et al. (2004). "Thermal micro pumps for a loop-type micro channel." Sensors and Actuators a-Physical **111**(1): 123-128.

Z. Ding, W.-B. Song, et al. (2007). Time-Multiplexed Droplet Manipulation Via Vibrating Ratcheted Micro-Channels. IEEE MEMS ’07, Kobe, Japan.

Zhou, Z. P. and D. Y. Yan (1997). "Mean-square radius of gyration of polymer chains." Macromolecular Theory and Simulations **6**(3): 597-611.

Zhu, X. and E. S. Kim (1998). "Microfluidic motion generation with acoustic waves." Sensors and Actuators a-Physical **66**(1-3): 355-360.

Zhu, X. Y., L. Y. Chu, et al. (2004). "Arrays of horizontally-oriented mini-reservoirs generate steady microfluidic flows for continuous perfusion cell culture and gradient generation." Analyst **129**(11): 1026-1031.

Zsuga, M., J. P. Kennedy, et al. (1988). "The Leidenfrost Reactor - a New General-Purpose Direct-Cooled Reactor and Its Use for Low-Temperature Polymerizations." Polymer Bulletin **19**(2): 201-207.

Vita

Jeong Tae Ok was born on May 14th 1972, in Pusan, South Korea. After completing high school in Seoul, he attended the Sunmoon University in South Korea where he earned his Bachelor of Science in the Department of Mechanical Engineering in February 1995 and his Master of Engineering in the Department of Electronic Engineering in February 1998. He served as an infantry officer of the Korean Marine Corps from March 1999 to June 2002. In August 2004, he entered the Department of Electrical and Computer Engineering at Louisiana State University in Baton Rouge. He earned his Master of Science in May 2007, supervised by Dr. Bingqing Wei. His research topic was on the fabrication of the individual carbon nanotube. He joined the Interdepartmental Program in Engineering Science at Louisiana State University, in January 2007, where he began the research in 'Characteristics of Droplet Motion on Miniaturized Ratchets' under the supervision of Dr. Sunggook Park in the Department of Mechanical Engineering. He is expected to earn the degree of Doctor of Philosophy on May 20, 2011.